HARVARD UNIVERSITY
Graduate School of Arts and Sciences

DISSERTATION ACCEPTANCE CERTIFICATE

The undersigned, appointed by the

Department of Physics

have examined a dissertation entitled

Interlayer Excitons in Atomically Thin van der Waals Semiconductor Heterostructures

presented by Andrew Yunho Joe

candidate for the degree of Doctor of Philosophy and hereby certify that it is worthy of acceptance.

Signature 

Typed name: Professor Philip Kim, Chair

Signature 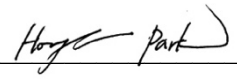

Typed name: Professor Hongkun Park

Signature 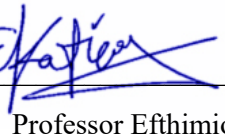

Typed name: Professor Efthimios Kaxiras

Date: May 7, 2021

Interlayer Excitons in Atomically Thin van der Waals Semiconductor Heterostructures

A DISSERTATION PRESENTED
BY
ANDREW YUNHO JOE
TO
THE DEPARTMENT OF PHYSICS

IN PARTIAL FULFILLMENT OF THE REQUIREMENTS
FOR THE DEGREE OF
DOCTOR OF PHILOSOPHY
IN THE SUBJECT OF
PHYSICS

HARVARD UNIVERSITY
CAMBRIDGE, MASSACHUSETTS

MAY 2021

Dissertation Advisor: Professor Philip Kim Andrew Yunho Joe

Interlayer Excitons in Atomically Thin van der Waals Semiconductor Heterostructures

Abstract

Semiconducting transition metal dichalcogenides (TMDs), when reduced to the two-dimensional (2D) limit, exhibit extraordinary excitonic effects that serve as a versatile platform for optoelectronic studies. High-quality, atomically-thin van der Waals (vdW) heterostructures can be constructed to explore rich 2D excitonic physics with these systems. Interlayer excitons, where the electron and hole are in separate layers, form dipolar composite bosons across the atomically-thin type-II heterostructures and are a promising candidate for creating a high-temperature exciton condensate. This dissertation reports on the methods and experimental results of studies on interlayer excitons in high-quality TMD heterostructure devices. We discuss the unique excitonic and material properties of TMDs, and the fabrication techniques required to create highly-tunable optoelectronic devices. We then explore the electrical control of interlayer exciton dynamics, controlling their radiative emission energy, lifetimes, and diffusion characteristics. We observe the three-body charged interlayer excitons, which can be controlled with in-plane fields. We use magnetic fields to explore the interlayer exciton spin-orbit split valley characteristics and electrically generate exclusive spin-singlet or spin-triplet interlayer exciton states. Finally, we electrically generate interlayer excitons that exhibit critical fluctuations, strongly pointing towards evidence of an interlayer exciton condensate. The results presented in this thesis pave the way for future studies on interlayer excitons and their powerful light-matter interactions that can couple to exotic electronic correlated states in vdW heterostructures.

Contents

Author list and Previous publications

Results presented in Chapter 4 were published in:

> "Electrical control of interlayer exciton dynamics in atomically thin heterostructures." Luis A. Jauregui, Andrew Y. Joe, Kateryna Pistunova, Dominik S. Wild, Alexander A. High, You Zhou, Giovanni Scuri, Kristiaan De Greve, Andrey Sushko, Yu, C.-H., Taniguchi, T., Watanabe, K., Needleman, D. J., Lukin,M. D., Hongkun Park, & Philip Kim. Science, 366, 870–875. (2019).

The following authors contributed to Chapter 5:

> Andrés M. Mier Valdivia, Luis A. Jauregui, Kateryna Pistunova, Dapeng Ding, You Zhou, Giovanni Scuri, Kristiaan De Greve, Andrey Sushko, Bumho Kim, Takashi Taniguchi, Kenji Watanabe, James Hone, Mikhail D. Lukin, Hongkun Park, & Philip Kim

Results presented in Chapter 6 were published in:

> "Electrically controlled emission from singlet and triplet exciton species in atomically thin light-emitting diodes." Andrew Y. Joe, Luis A. Jauregui, Kateryna Pistunova, Andrés M. Mier Valdivia, Zhengguang Lu, Dominik S. Wild, Giovanni Scuri, Kristiaan De Greve, Ryan J. Gelly, You Zhou, Jiho Sung, Andrey Sushko, Takashi Taniguchi, Kenji Watanabe, Dmitry Smirnov, Mikhail D. Lukin, Hongkun Park, & Philip Kim. Phys. Rev. B 103, L161411 (2021).

The following authors contributed to Chapter 7:

> Luis A. Jauregui, Andrés M. Mier Valdivia, Dapeng Ding, Kateryna Pistunova, Zhengguang Lu, Giovanni Scuri, Kristiaan De Greve, Ryan J. Gelly, You Zhou, Jiho Sung, Andrey Sushko, Takashi Taniguchi, Kenji Watanabe, Dmitry Smirnov, Mikhail D. Lukin, Hongkun Park, &

Philip Kim.

Some results posted as a preprint:

"Electrically controlled emission from triplet charged excitons in atomically thin heterostructures." Andrew Y. Joe, Luis A. Jauregui, Kateryna Pistunova, Andrés M. Mier Valdivia, Zhengguang Lu, Dominik S. Wild, Giovanni Scuri, Kristiaan De Greve, Ryan J. Gelly, You Zhou, Jiho Sung, Andrey Sushko, Takashi Taniguchi, Kenji Watanabe, Dmitry Smirnov, Mikhail D. Lukin, Hongkun Park, & Philip Kim. arXiv:1912.07678 (2019).

The following authors contributed to Chapter 8:

Andrés M. Mier Valdivia, Dapeng Ding, Trond Anderson, Takashi Taniguchi, Kenji Watanabe, Mikhail D. Lukin, Hongkun Park, & Philip Kim.

Dedicated to my parents, Janet Yi and Yong Joe.

Acknowledgments

The seven years at Harvard have been the most rewarding years of my life. The PhD experience is a daunting task, to learn and then contribute to the vast scientific knowledge that already exists from the countless work of others. However, I realized that, beyond the science, the people I have met have made this such an enriching experience. I am incredibly lucky to have met so many people during my time here that I will cherish for the rest of my life. None of the achievements in this thesis would have been possible without them.

First, I need to thank my advisor, Philip. As many before me have said, Philip is a kind advisor who is incredibly patient and genuinely cares about his students. Philip gave me the space and time to grow as both a person and a researcher. He would always take the time to meet with me about any of the problems that would be on my mind. As a research advisor, Philip could not have been more supportive. He trusts his students in their research directions and encourages them to explore them. Even as I pursued optics experiments in a primarily transport-driven lab, Philip's belief in my abilities to build an expensive optical setup was an extremely validating feeling that I am still thankful for today. Discussing research with Philip is also a joy, because he gives you very insightful advise from his wealth of knowledge and asks difficult questions to really understand the experiments to push

them forward. When I joined his lab, I knew Philip was a leader in his field, but it is only as I leave that I am beginning to understand how broad and deep that knowledge must be in order to lead a field. When giving advise, he always suggested me to be mindful of the bigger picture and seven years later, I can finally begin to see why. The long-term goals in both life and in research are what matter in the end. I am unbelievably lucky to have worked with Philip and I am very thankful that he accepted me into his group.

Next, I need to thank Luis, the postdoc who taught me everything. I had the privilege to be mentored by Luis for four years during my PhD, during which he taught me everything from device fabrication to transport and optical techniques. Luis was always willing to explain and reexplain any of the details in our experiments and it is because of his patience and care that I was able to learn everything that I did. His most defining characteristic is the passion that he showed for our research. His dedication to our experiments was something that I could not understand at the time, but something I am lucky to have subconsciously learned while working with him. Now I can understand his excitement of staying in the lab late into the night and how every physics discussion is spun immediately into the experiments we are trying to perform. I feel fortunate to have spent the time working with him and even today, I am able to message him anytime for advise and discussions. Luis taught me to be passionate about my work and I will be able to carry that wherever I go.

I also need to thank Kate, an undergrad that seemed closer to a graduate student. Kate and I learned device fabrication and measurement techniques together and it felt like having another graduate student working alongside me. Her motivation and drive helped me stay focused during my earlier years and her friendship is one I still value today. She has now moved on to become an actual graduate student and I look forward to her achievements in whatever she pursues.

After Luis and Kate left the lab, I was lucky to have a new team to work with in Andrés and Dapeng. Andrés has been an absolute pleasure to work with and his patience and consistent work ethic are a large part of why we have been able to make such great progress together. Dapeng arrived later but

brought very valuable optics expertise, which was particularly important for the final parts of this thesis. I want to specifically thank them for listening to me during lengthy brainstorming sessions about our research directions, some which would run later into the evening as we tried to figure things out. It has been wonderful to work with them and I know I am leaving the optics setup in very capable hands for the future research directions in the Kim lab.

I want to thank the rest of the Kim lab and the many labmates I have had during my time here. I have very fond memories of the summer BBQs, the fall hiking trips, and the end of the year winter parties where we could relax and just chat about life. Jesse, Jayakanth, Hiroshi, Xiaomeng, Austin, Jing, Frank, Katie, Gilho, Young Jae, Si Young, Ke, Kwabena, Luis, Kate, Nicola, Youngjo, Hoseok, Hyobin, Laurel, Rebecca, Alex, James, Zeyu, Önder, Antti, Joon Young, Isabelle, Mehdi, Yuval, Artem, Jonah, Tom, Zhongying, Qi, Andrés, Dapeng, Jonathan, and Andrew - thank you for being such fun and wonderful labmates. It is only at the end that I realized how special the Kim lab community really is. The lab really takes after Philip in that people are kind and always willing to help. I cannot remember a single person in the lab that I could not go to for help or advice, and I can say I have learned something from every person here. In addition, I got to hang out with my labmates outside of the lab - board game nights with the group, discussing pizza currency with Qi, rock climbing with Rebecca, volleyball with Mehdi, late night dinners with Xiaomeng and Kate, cat discussions with Isabelle or Zhongying, and many many more. In particular, I need to thank Katie and Hyobin. Katie began her time in the lab around the same time as me. During our first year, we did marathon overnight cleanroom sessions trying to pool our collective knowledge to figure out the equipment together. It was nice to have a friend to share the experience of struggling as a young graduate student. She is someone I will always enjoy having a conversation with and I am very thankful to have met her during my time here. As for Hyobin, he was such a fun person to talk to. The blend of Korean and Korean-American humor while chatting in his office helped break down many of the Korean cultural barriers for me. Our conversations usually ended up having a Korean lesson, an English lesson, and a physics

discussion all in one. I have made many wonderful friends in the lab and I am thankful for them all.

I need to thank Professor Hongkun Park and his lab members, who I interacted closely with throughout my graduate career. All of the optics knowledge that I have today is through collaborations I had with the Park lab. Since many experiments were performed on their experimental setups, Hongkun paid careful attention to my work and provided a contrasting, but very helpful, mentoring style in comparison to Philip. I appreciate his care for my research and the opportunity to have worked with him. Finally, I would like to thank the rest of the Park group - Gio, Ryan, Alex, Kristiaan, Jiho, You, Elise, and Sasha - for the helpful discussions and many fun memories.

The Harvard physics staff provided so much support during my time here. Lisa and Jacob created a strong foundation for the physics graduate students and I am so thankful to have had them to lean on during difficult times. I want to give special thanks to Hannah, who started as the Kim lab administrator and has subsequently joined the Harvard physics staff. Being at the interface between the graduate students and the faculty, she had a very unique perspective on the PhD experience and was a helpful person to talk to during times of frustration. I often stopped by to drop off paper work and we ended up talking for hours. I am very thankful to have had her support during my time here and the physics department is incredibly lucky to have her now.

I am grateful for the entire physics graduate student cohort from my year and the community that we fostered. In particular, "Triple A" - Anj, Anne, and Ana - was a constant source of friendship, support, and fun banter. Aaron still inspires me to have an adventurous spirit and seek out new experiences. Lastly, I want to thank Tyler, who is a big part of my graduate school experience. Having been my roommate for nearly three years, Tyler has always been there to celebrate the successes and to cheer me up during the frustrations. The board games, hikes, sports, and many fun parties kept me sane outside of the lab. I have been blessed to have met friends here that will last a lifetime.

My family is such an important part of me, and the major reason that I am here today. Whenever I visited my family at home, I was always refueled to return to my research and they gave me so much of

the strength to persevere. I want to thank my parents and my brother, Kevin, for their never-ending support and encouraging words.

Finally, I need to thank Catherine. I met Catherine during my second year and ever since then she has been such an important person to keep me grounded. Catherine stood by me through the stress-induced ups and downs and is someone I could always count on. She has been my best friend and it was impossible to not feed off of her positive energy. I am so glad to have been able to share many of the exciting PhD experiences with her, including traveling around the world to various conferences. My achievements would not have been possible without her support. I am very excited about our life together and I cannot wait for what the future holds for us.

No one any longer pays attention to - if I may call it - the spirit of physics, the idea of discovery, the idea of understanding. I think it's difficult to make clear to the non-physicist the beauty of how it fits together, of how you can build a world picture, and the beauty that the laws of physics are immutable.

Hans Bethe

1

Overview

This dissertation discusses optoelectronic studies of interlayer excitons. The concepts of coupled two-dimensional electron gases and indirect excitons existed before the discovery of two-dimensional (2D) materials. In the era of the high quality gallium arsenide (GaAs) 2D quantum wells, many exciting theoretical proposals for dipolar excitons in 2D system were discussed, including the famed optically-generated exciton condensate. The introduction of monolayer semiconducting

transition metal dichalcogenides (TMDs) led to a naturally 2D material system for attempting similar experiments, while also adding unique spin-valley properties and extremely large binding energies. The work and results in this thesis lay the foundations for using van der Waals (vdW) heterostructures to study novel physics of optically and electrically generated interlayer excitons, which can be electrically tuned.

Chapter 2 discusses the fundamental concepts needed to understand the results in this thesis. We delve into the material properties of TMDs and discuss the basic properties of excitons, trions, and interlayer excitons. We provide an overview of some of the interesting physics that can be explored with the interlayer excitons in TMD heterostructures. We finally describe the main optical techniques used to prepare the reader for the subsequent chapters.

Chapter 3 discusses the fabrications steps required to create a vdW heterostructure device compatible with optoelectronic studies. Fabricating our novel devices required solving the unique challenge of creating both optically accessible and electrically transparent devices. We also briefly describe the second harmonic generation technique, which is vital for aligning the crystallographic edges of the separate layers.

Chapter 4 presents the results from studies on the electrostatic control of the interlayer exciton dynamics. We discuss interlayer excitons and the electrostatic control of their long lifetimes and emission energies. We discuss long-range charge neutral interlayer exciton diffusion and also the control of charged interlayer exciton diffusion. Finally, we present the dynamics of the electrically generated interlayer excitons.

Chapter 5 adds to the foundations in the previous chapter to further control the interlayer exciton movement. We design patterned gates to create spatially varying electric fields to increase the interlayer exciton density. The increased density allows us to cross the Mott transition, giving an upper bound interlayer excitons in our search for a condensate phase.

Chapter 6 discusses the spin and valley characteristics for the interlayer excitons. While the previous

chapters establish the interlayer nature of the excitons, the separation of the layers requires special consideration for the alignment of the K valleys. We discuss the modified selection rules and show the brightening of both singlet and triplet-type interlayer exciton transitions. This allows us to electrically generate different spin-aligned interlayer excitons, paving the way for valleytronic interlayer exciton devices.

Chapter 7 builds on the discussions in the previous chapter and explores the magnetic field response of the interlayer excitons. We are able to extract details of the band structure and interlayer exciton energetics with the magnetic field, but observations leave open questions about the effect of the free carriers.

Chapter 8 further explores the interesting transport behavior found in Chapter 6. When performing similar measurements with an increased spacing between the layers, we are able to clearly show enhancements in the electrically generated interlayer excitons. The electrically generated interlayer excitons show preliminary evidence for coherent interlayer exciton emission.

Finally, the conclusion will provide outlook on the interlayer excitons in TMDs. This final chapter of this thesis shows that we are tantalizingly close to an interlayer exciton condensate. The demonstration of the interlayer exciton combined with the new understanding of the moiré effects in the TMD heterobilayers should open up many exciting directions to explore Bose-Einstein condensates in a condensed-matter system.

The appendices comprise of additional details on the experiments and theory. They include fabrication details, the optical setups, specifics on the main devices, details on the electrostatic calculations, and further theoretical discussions. Lastly, they include the supplemental data figures.

The beginning seems to be more than half of the whole.

Aristotle

2

Excitons in Transition Metal Dichalcogenides

An entirely new field of two-dimensional (2D) materials emerged when a single layer of graphite, or graphene, was first isolated and experimentally confirmed in 2004 [1,2,3]. Bulk van der Waals (vdW) materials have their electronic properties mostly governed in a 2D plane with weaker

out-of-plane vdW forces between them. By using a scotch tape mechanical exfoliation method, single layers (monolayers) could be cleaved from bulk crystals with properties ranging from semi-metals, semiconductors, superconductors, and topological insulators. The monolayers themselves are stable structures on their own and are atomically flat, not having any dangling bonds. Lack of either of these properties is a large reason that many other bulk materials cannot be thinned down to a few atomic layers. In addition, since single layers of the material can be isolated, they can be stacked into exotic heterostructures, limited only by the imagination. The field of 2D materials rapidly opened up accessibility to low-dimensional, condensed matter physics with just bulk crystals and scotch tape. Specifically, high-quality, thin-film heterostructures could be constructed without the complications of growth seen in single-crystal or molecular beam epitaxial (MBE) techniques.

While studies on bulk semiconducting transition metal dichalcogenides (TMDs) date back to at least the mid 1900s[4,5,6], it was not until 2010 when monolayer TMDs and their direct band gap properties were experimentally measured[7,8]. Since then, the field expanded to explore the many exciting excitonic properties in monolayers. Results such as observing the dark, spin-forbidden excitons in tungsten diselenide (WSe_2)[9,10] or utilizing the spin-valley degrees of freedom to make an excitonic switch[11] were all realized within a decade. Two different monolayer TMDs could be stacked to form semiconducting heterostructures, forming p-n junctions[12]. Since they can form a type-II heterojunction, excitons with the electron and hole in separate layers could also form[13,14]. These excitons, also known as interlayer excitons, form the basis for the majority of the studies in this thesis.

This chapter will delve into the basic concepts for understanding the remainder of this thesis. We will introduce TMD materials and their general properties. Then we will discuss excitons in TMDs and why the choice of material is particularly useful and exciting for these studies. We will then discuss the unique optical selection rules for excitons in the TMDs. We will briefly discuss the charged excitons (most often referred to as trions or exciton-polarons), which are three-body complexes that emerge with increasing free-carrier density. We will then discuss the interlayer exciton in TMDs and

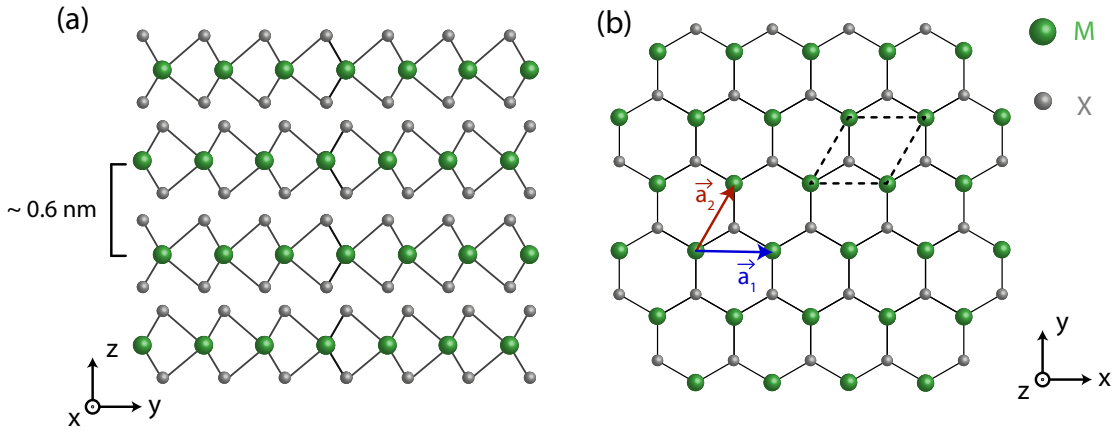

Figure 2.1: TMD structures. (a) Side view of the 2H bulk crystal structure with the green and silver atoms being metal (M) and chalcogen (X) atoms, respectively. Each layer has a thickness of 0.6 nm. (b) Top-down view of a monolayer TMD. $\vec{a_1}$ and $\vec{a_2}$ are lattice vectors with the dashed line outlining the primitive unit cell.

motivate why they are useful for the search of the exciton condensate. Finally, we will end the chapter with an introduction to the optical techniques used in the remainder of the thesis.

2.1 Monolayer transition metal dichalcogenides

TMDs are a class of vdW materials, similar to graphene or hexagonal boron nitride (h-BN), which have most of their electronic properties in-plane. Since the layers are held by weak vdW forces, they can be cleaved from the bulk via mechanical exfoliation. The lack of covalent bonds between the layers also means the resulting thin layers do not have dangling bonds on their interface. The surface is atomically flat!

We will focus on the group VI semiconducting TMDs which have the form MX_2, where M (= Mo, W) is the metal atom and X (= S, Se, Te) is the chalcogen atom. Figure 2.1(a) shows the bulk structure of the TMD. In the natural bulk system, the semiconducting TMDs generally form 2H stacking structures, where the layer orientation flips every other layer. The layer thickness is $\sim$ 0.6 nm with a repeating structure every two layers in the vertical direction. A top down view of a single

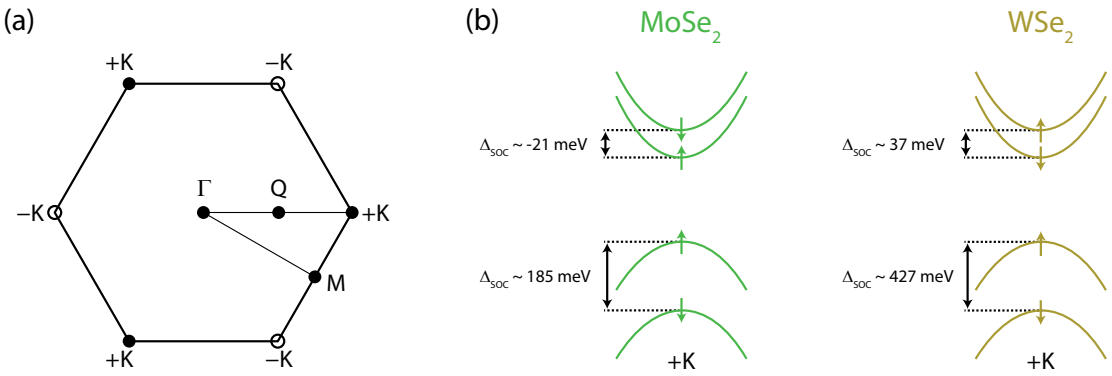

Figure 2.2: (a) The Brillouin zone in TMD monolayers where the +K and -K points are related via time-reversal*. (b) The band structure of monolayer TMDs and theoretically calculated values from Kormányos, A. et al.[15]. The molybdenum-based TMDs are known to have smaller spin orbit coupled splittings (Δ_{SOC}) than tungsten-based TMDs. The splitting also has opposite signs resulting in opposite ordering of the spins in the conduction band.

layer reveals a hexagonal lattice, much like graphene and h-BN, but with alternating M and X atoms at the hexagonal points (Fig. 2.1(b)). The dashed lines map out the primitive unit cell with lattice vectors $\vec{a_1}$ and $\vec{a_2}$. The lattice constant, $a_0 = |\vec{a_1}| = |\vec{a_2}| \approx 3$ Å, varies for the different materials, depending mostly on the chalcogen atom.

When reduced to a monolayer, the indirect gap bulk TMDs become direct band gap materials[7,8]. This direct band gap emerges at the $+K$ and $-K$ (also referred to as K and K') points (Fig. 2.2(a)), which are related to each other via time-reversal symmetry. Density functional theory (DFT) calculations show that the band gap at the K valleys do not shift much with layer thickness. Instead, the Q^* point in the conduction band and the Γ point in the valence band move significantly with layer thickness[8]. This is a strong indication that the electronic bands that govern the monolayer do not have a significant layer dependence.

The K-valleys in TMDs have spin-split conduction and valence bands due to strong spin-orbit coupling. The orbital characteristics of the conduction band and valence band are predominantly characterized by the d-orbitals in the metal atom: for the the conduction band, $d_{m=0} \equiv d_{z^2}$ for the

*The Q point is not a high symmetry point, but it is relevant in discussions about the conduction band in multi-layer structures.

conduction band and $d_{m=\pm 2} \equiv d_{x^2-y^2} \pm d_{xy}/\sqrt{2}$ for the valence band [15,16]. Thus, to the lowest order, we see that a spin-orbit term, $\vec{L} \cdot \vec{S}$, will result in negligible spin-orbit splitting in the conduction band and a larger splitting in the valence band. More detailed theoretical studies, however, show that the conduction band also has a small splitting, with opposite signs in the molybdenum or tungsten based materials [15,16]. Optical studies on the two materials confirmed this assignment, which showed the ordering of the spin-flip transition in WSe_2 [9,10] and $MoSe_2$ [17]. Figure 2.2(b) summarizes the spin-orbit coupling splittings (Δ_{SOC}) for $MoSe_2$ and WSe_2 at the $+K$ valley, using theoretically calculated values. The spin-orbit splitting is particularly exciting when discussing the optical selection rules in Section 2.3, because the bright transition in each valley is coupled to a spin. This phenomena is referred to as spin-valley locking. Thus, by using circularly polarized light to address a specific valley, one can also extract information about the spin in the system. Furthermore, one can use this to create devices that transport spin via its valley curvature [18], or study spin and orbital splitting g-factors by using magnetic fields [19]. The latter is the basis for the studies in Chapters 6 and 7.

Another important property of the TMD monolayer bands is their effective mass, which is large compared with III-V semiconductors such as GaAs. The effective mass, which describes the curvature of the electronic bands, will have a strong effect on the energy scales in the system. Depending on the material and on the theoretical or experimental study, the effective mass values range from $0.3m_0$ [15] to as large as $0.8m_0$ [20], where m_0 is the bare electron mass. This is in comparison to the GaAs light hole mass of $\sim 0.06m_0$ and heavy hole mass of $\sim 0.45m_0$.

We summarize the important values discussed in this section along with the dielectric constants in Table 2.1. This table is not comprehensive in terms of citations, but can rather be used as a reference for quickly estimating energy and length scales in other parts of this thesis.

	$MoSe_2$	WSe_2
a_0 (Å)	3.319 [15]	3.316 [15]
Δ^c_{SOC} (meV)	−21 [15]	37 [15]
Δ^v_{SOC} (meV)	185 [15]	427 [15]
m_e (m_0)	0.56 [15], 0.8 [20]	0.3 [15]
m_h (m_0)	0.6 [15]	0.35 [15], 0.35[unpublished], 0.45 [21,22]
$\varepsilon_\perp$ (ε_0)	7.2 [23]	7.4 [23]
$\varepsilon_\parallel$ (ε_0)	17.4 [23]	15.6 [23]

Table 2.1: Theoretically calculated and experimentally measured values for $MoSe_2$ and WSe_2.

2.2 Excitons in TMDs

Excitons are electron-hole pairs in a crystal that bind due to their attractive Coulomb interaction [24]. They can be viewed similarly to positronium, an electron and positron bound state. Since they comprise of two fermions, they form a composite boson. Excitons can move around the crystal and transport their properties (energy, heat, spin, etc.). However, since they are charge neutral, they do not transport charge. Excitons will form at critical points in k-space, or when the conduction band (c) and valence band (v) are parallel. At this condition, singularities in the joint density of states will appear. Trivially, this also occurs at the bottom (top) of the conduction (valence) bands.

There are two limiting approximations for describing an exciton. The Frenkel exciton describes a tightly bound exciton state where its size is on the order of the lattice constant and is strongly localized near an atom. The Mott-Wannier exciton describes the opposite extreme: a weakly bound exciton where the exciton size is much larger than the lattice constant that can move freely through the crystal. For excitons in semiconducting TMDs, the estimated size of the Bohr radius is about 1 to a few nm, which spans over a few lattice periods as shown in Figure 2.3. Although the semiconducting TMDs

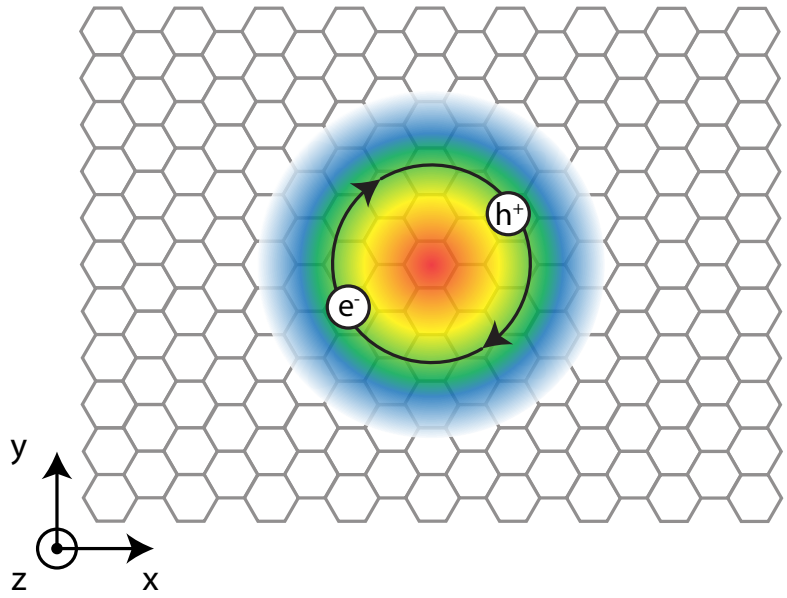

Figure 2.3: An exciton, an electron-hole bound pair, in a hexagonal lattice. Size is approximately to scale with the lattice size.

have strongly bound excitons, since the Bohr radius of excitons are several times the lattice constant, the Mott-Wannier picture appropriately describes the excitonic behavior in TMDs[25].

For Mott-Wannier excitons, the exciton binding energy can be treated as the hydrogen atom problem with the lattice acting as a dielectric background. We begin with the Hamiltonian,

$$H = \frac{-\hbar^2 \nabla_r^2}{2\mu} + V(r), \tag{2.1}$$

where the $1/\mu = 1/m_e + 1/m_h$ is the reduced mass of the exciton, m_e (m_h) is the electron (hole) mass, r is the radial distance in the 2D plane, and $V(r)$ is the attractive electron-hole interaction. In the simplest picture, we can solve for the binding energy using the locally screened Coulomb potential

$$V_{Coulomb}(r) = -\frac{1}{4\pi\varepsilon_0}\frac{e^2}{\varepsilon_{eff} r}, \tag{2.2}$$

where e is an electron charge, ε_{eff} is the effective dielectric constant of the lattice, and ε_0 is the vacuum permittivity. Solving for the energy eigenvalues in 2D, the binding energy of the exciton and its corresponding Rydberg series with quantum number n are

$$E_b^{(n)} = \left(\frac{1}{4\pi\varepsilon_0}\right)^2 \frac{\mu e^4}{2\hbar^2 \varepsilon_{eff}^2 (n-1/2)^2}. \tag{2.3}$$

Note that this formula is different from the usual Rydberg series in 3-dimensional excitons as n is replaced by $n-1/2$, reflecting the 2D nature. The binding energy can be understood as the energy scale of the excited state with respect to free electrons and holes. This is the energy required for exciton disassociation, or the return of the electron and hole to the free particle conduction band and valence band, respectively. The emission energy is the energy of the emitted photon during the radiative recombination process and is dictated by the difference between the band gap (E_{gap}) and the binding energy. Thus, the emission energy of an excitons is given by

$$E_{exciton}^{(n)} = E_{gap} - E_b^{(n)}. \tag{2.4}$$

Most discussions on the excitons consider the 1s exciton state ($n = 1$), and thus, is used to describe the overall binding energy ($E_{binding}$) of the exciton. In Figure 2.4(a) we illustrate this picture, showing the binding energy and exciton energy with respect to the conduction and valence bands. The additional exciton resonances for $n > 1$ (2s, 3s, etc.) are shown approaching the band gap. Figure 2.4(b) shows a schematic of the expected exciton absorption resonances, which eventually give way to the absorption of free electron and holes.

We use the above discussion to estimate the binding energy (Eq. (2.3)) and corresponding Bohr radius

$$a_B = \frac{4\pi\,\varepsilon_{eff}\,\varepsilon_0 \hbar^2}{\mu\, e^2} \tag{2.5}$$

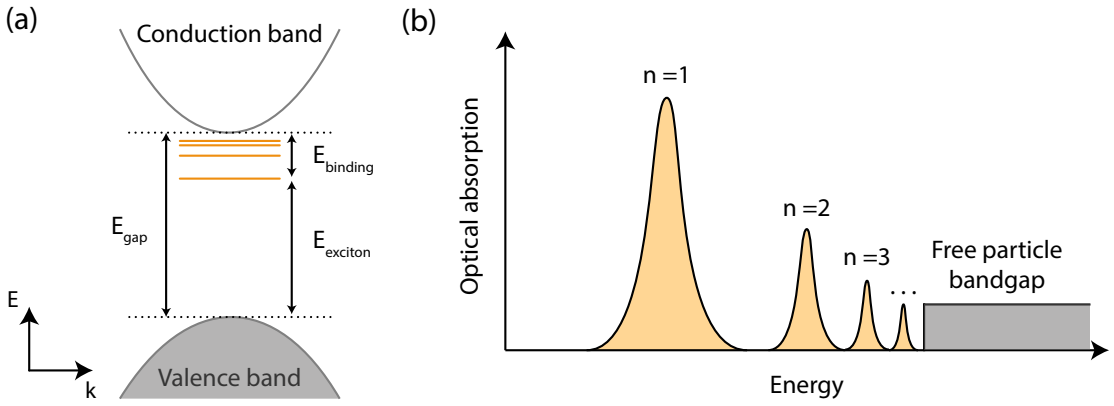

Figure 2.4: The exciton binding energy (a) The exciton emission lines (orange) with respect to the binding energy and band gap. Lines above the binding energy represent the additional excitonic states. (b) A schematic of the optical absorption of the different excitonic states and their relative energies approaching the free particle band gap. The image is adapted from Wang, G. et al.[25].

for the TMD excitons. We can see now that the large effective mass of the electrons and holes in TMDs help create strongly-bound excitons in these materials. If we use equal electron and hole masses of $\sim 0.5m_0$ and $\varepsilon_{eff} \sim 10$, we can approximate a binding energy of $E_{binding} \approx 270meV$, and a Bohr radius of $a_B \approx 1.5$ nm. The large binding energy means temperatures exceeding thousands of Kelvin are required to thermally dissociate the exciton. Similarly, the small Bohr radius indicates a tightly bound exciton which can reach higher densities before quantum dissociation at the Mott density[26,27]. We discuss this later in the chapter during our discussion about the interlayer excitons.

While the Coulomb potential makes sense in a 3D bulk crystal where the dielectric environment is close to uniform and isotropic, it does not sufficiently describe the non-uniform dielectric environment for a 2D TMD layer. One can see this in Figure 2.5 where the electric field lines for the 1s and 2s excitons experience a combination of large dielectric screening in the TMD material and lower dielectric screening outside. To correct for this, we can replace the Coulomb potential with a non-locally screened Keldysh potential with substrate screening effects[28,29,30]

$$V_{Keldysh}(r) = -\frac{\pi e^2}{2 r_0}\left[H_0\left(\frac{(1+\varepsilon_s)r}{2 r_0}\right) - Y_0\left(\frac{(1+\varepsilon_s)\, r}{2 r_0}\right)\right], \tag{2.6}$$

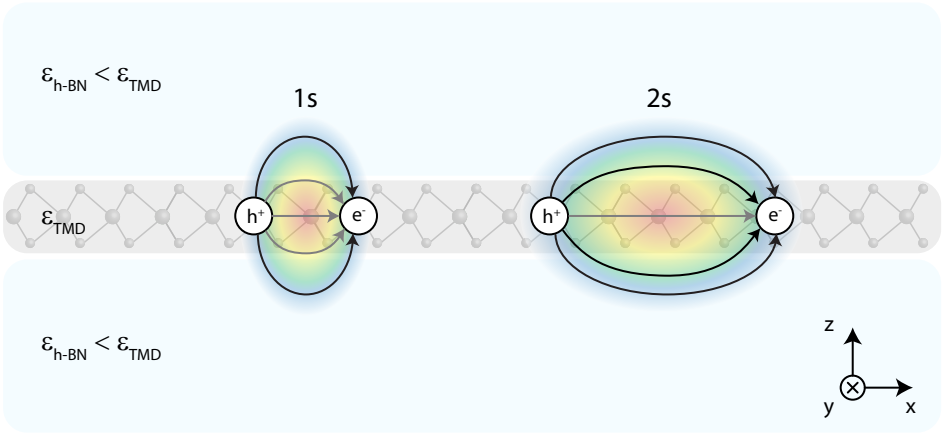

Figure 2.5: TMD screening in 1s and 2s excitons. The arrows show the electric field lines in the exciton. Short-range interactions are heavily screened by the high TMD dielectric constant (ε_{TMD}) and scales as $\log(r)$ whereas long range attraction is less screened in the h-BN substrate layer ($\varepsilon_{h-BN} < \varepsilon_{TMD}$) and scales as $1/r$. The image is adapted from Chernikov, A. et al.[30].

where H_0 and Y_0 are the Struve and Bessel functions and ε_s is the dielectric constant for the substrate. The screening length r_0 indicates the crossover from the $1/r$ potential (stronger attraction) at long length scales to $\log(r)$ scaling (weaker attraction) for shorter length scales[30]. This modified Keldysh potential also approximately accounts for the substrate dielectric (rather than assuming vacuum), which returns to a r/r_0 scaling when the substrate dielectric is vacuum ($\varepsilon_s = 1$). The Keldysh potential correction is especially important for the 1s and 2s states, where the electric field between the electron and hole can experience large variations in the effective dielectric screening and the electron-hole separation is much smaller (Fig. 2.5).

Another consequence of the large binding energies is the very short radiative lifetime of the exciton. In a simple approach, the radiative lifetime can be written as[31,32]

$$\tau_{rad} = \frac{1}{2\Gamma_0} = \frac{\varepsilon_0\,\varepsilon_{eff}}{2\,\hbar\,k_0}\left(\frac{E_{exciton}}{e\,v}\right)^2 (a_B)^2 \tag{2.7}$$

where Γ_0 is the radiative decay rate, $k_0 = E_{exciton}\sqrt{\varepsilon_{eff}}/\hbar c$ is the light wave-vector, and $v = \sqrt{E_{gap}/2m_e}$

is the approximated Kane velocity in a two-band model. In this model, using $E_{gap} = 2$ eV, $E_{exciton} = 1.7$ eV ($E_{binding} \approx 0.3$ eV), and similar estimated values from our calculation for the binding energy above, we can estimate the exciton radiative lifetime to be $\tau_{rad} \approx 0.3$ ps. This value turns out to be a good estimate of the radiative lifetime in comparison to experimental and theoretical reports [33,34,35]. Since only a small number of the excitons can be within the light cone ($k < k_0$) though, the effective lifetime is closer to $\tau_{eff} \approx 3$ ps for low temperature measurements [33]. These lifetimes are still incredibly fast and result in bright exciton emission in an atomically thin material.

Finally, we note that excitons are traditionally seen as existing in insulating materials where the excited electron in the conduction band will bind with the free hole in the valence band as discussed above. In this description, the excitons themselves are not a stable ground state and their lifetime will be dictated by the electron-hole recombination rate. Especially in direct band gap materials, the recombination or absorption can be very efficient allowing optical detection of the excitonic states. Therefore, the excitons need to be constantly generated via photons or by electrical injection. There are other methods for creating and detecting excitons. Semi-metals such as 1T-$TiSe_2$ can have an equilibrium density of both electrons and holes that form excitons [36]. Furthermore, in double-layer graphene or GaAs double quantum wells, magnetic fields can create excitons in half-filled Landau levels in separate layers, given a sufficient thickness of insulating spacer layers suppress the tunneling current [37,38,39]. In this thesis, we will discuss the optically active excitons as they can give a clean signature of the local behavior and a reliable way to both generate and detect the excitons. Future work could utilize equilibrium exciton densities in the semiconducting TMD materials to create a more stable ground state exciton.

2.3 Optical selection rules

The symmetries of the material and knowledge of the conduction and valence band orbital characteristics are sufficient for calculating the optically allowed transitions in the monolayer TMDs. We closely follow the arguments in Yu, H. et al.[40] to present this symmetry-based proof for the optical selection rules. Their work shows more detailed theoretical arguments and numerical calculations for the selection rules and their transition strengths.

We start by defining a Bloch function at the K points, ψ_{n,K,S_z}, where $n = c, v$ is the relevant conduction (c) or valence (v) band, $\pm K$ is the relevant K point, and $S_z = \pm\frac{1}{2}$ is the spin quantum number. For our derivation, we consider only a single K point so that we can define the Bloch function as ψ_{n,S_z} and the $-K$ valley can be obtained by time reversal. The Bloch function must be eigenfunctions of the symmetries of our lattice. The monolayer TMD is symmetric under $\hat{C}_3$ and $\hat{\sigma}_h$ as seen in Figure 2.6, where $\hat{C}_3$ denotes a rotation by 120° and $\hat{\sigma}_h$ is a mirror reflection. The Bloch functions then satisfy

$$\hat{C}_3\psi_{n,S_z} = e^{-i\frac{2\pi}{3}(C_3(n)+S_z)}\psi_{n,S_z} \tag{2.8}$$

$$\hat{\sigma}_h\psi_{n,S_z} = \sigma_h(n)\, e^{-i\pi S_z}\psi_{n,S_z} \tag{2.9}$$

where $C_3(n) = 0, \pm 1$ and $\sigma_h(n) = \pm 1$ are the quantum numbers for $\hat{C}_3$ and $\hat{\sigma}_h$, respectively, and n is the electron band. As is evident from Eq. (2.8), the quantum number $C_3(n)$ is only defined up to the addition of multiples of 3. The conduction bands (CB1 and CB2) and valence band (VB) have primarily metal atom d-orbital characteristics, $d_{m=0} \equiv d_{z^2}$ and $d_{m=\pm 2} \equiv d_{x^2-y^2} \pm d_{xy}/\sqrt{2}$, respectively. Since the Bloch states are extensions of the orbital characteristics, when rotating about the metal atoms (M), we know the $\hat{C}_3$ quantum numbers for the two bands will be $C_3(c, M) = 0$ and $C_3(v, M) = +2\,(-1)$. We can also see that the monolayer TMD is symmetric with a mirror reflection

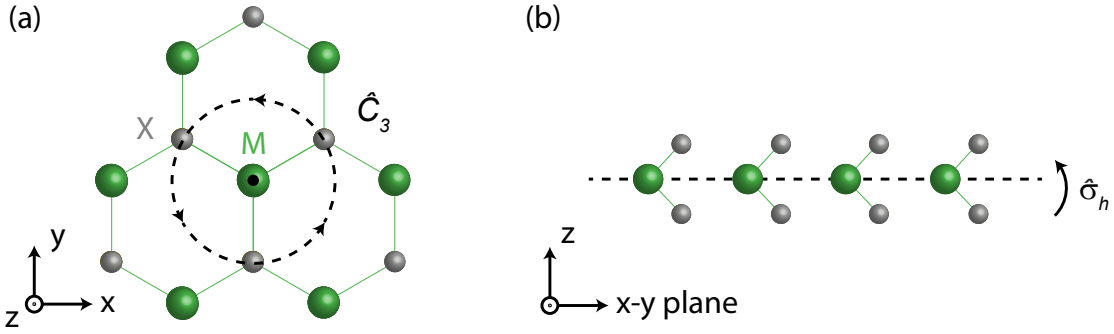

Figure 2.6: Symmetries for a monolayer $MoSe_2$ layer showing (a) the $\hat{C}_3$ rotational symmetry and (b) the $\hat{\sigma}_h$ mirror symmetry.

and thus $\sigma_z(n) = +1$. Finally, the spin quantum numbers can be extracted from the established band structure for the monolayer TMDs in Fig. 2.2(b). For our discussion here, we will consider the band structure of $MoSe_2$, but a similar calculation can be done for other monolayer semiconducting TMDs. We summarize the quantum numbers for the case above in Table 2.2.

$n =$	v	c_1	c_2
$C_3(n, M)$	-1	0	0
$\sigma_z(n)$	$+1$	$+1$	$+1$
$S_z(n)$	$+\frac{1}{2}$	$+\frac{1}{2}$	$-\frac{1}{2}$

Table 2.2: The quantum numbers associated with the first valence band, and first two conduction bands of a monolayer TMD. Note that CB1 (c_1) and CB2 (c_2) here are the spin-split conduction band due to spin-orbit coupling so they only differ in their spins.

To calculate interband transitions at the K point, we define the momentum operator as $\hat{\mathbf{p}} = \hat{p}_+ e_+ + \hat{p}_- e_- + \hat{p}_z e_z$, where $e_\pm \equiv \left(e_x \pm i e_y\right)\sqrt{2}$ and e_x, e_y, and, e_z are the three Cartesian unit vectors. We can interpret $\hat{p}_\pm$ and $\hat{p}_z$ as the components that couple to $\sigma_\pm$ circularly polarized light and out-of-plane, z polarized light, respectively. We can write out equations for the momentum operator with respect to

the $\hat{C}_3$ symmetry as

$$\begin{aligned} \hat{C}_3 \hat{p}_\pm \hat{C}_3^{-1} &= e^{\mp i \frac{2\pi}{3}} \hat{p}_\pm, \\ \hat{C}_3 \hat{p}_z \hat{C}_3^{-1} &= \hat{p}_z, \end{aligned} \tag{2.10}$$

and the $\hat{\sigma}_h$ symmetry:

$$\begin{aligned} \hat{\sigma}_h \hat{p}_\pm \hat{\sigma}_h^{-1} &= \hat{p}_\pm \\ \hat{\sigma}_h \hat{p}_z \hat{\sigma}_h^{-1} &= -\hat{p}_z. \end{aligned} \tag{2.11}$$

Using the momentum operator and Eqs. 2.8 - 2.11, we evaluate the optical matrix elements with respect to the two symmetries:

$$\begin{aligned} \left\langle \psi_{n\prime,S_z'} \middle| \hat{p}_\pm \middle| \psi_{n,S_z} \right\rangle &= \left\langle \psi_{n\prime,S_z'} \middle| \hat{C}_3^{-1} \hat{C}_3 \hat{p}_\pm \hat{C}_3^{-1} \hat{C}_3 \middle| \psi_{n,S_z} \right\rangle \\ &= e^{i\frac{2\pi}{3}(C_3(n\prime)+S_z')} e^{-i\frac{2\pi}{3}(C_3(n)+S_z)} e^{\mp i\frac{2\pi}{3}} \left\langle \psi_{n\prime,S_z'} \middle| \hat{p}_\pm \middle| \psi_{n,S_z} \right\rangle \\ &= e^{i\frac{2\pi}{3}(C_3(n') - C_3(n) + S_z' - S_z \mp 1)} \left\langle \psi_{n',S_z'} \middle| \hat{p}_\pm \middle| \psi_{n,S_z} \right\rangle, \end{aligned} \tag{2.12}$$

$$\begin{aligned} \left\langle \psi_{n\prime,S_z'} \middle| \hat{p}_\pm \middle| \psi_{n,S_z} \right\rangle &= \left\langle \psi_{n\prime,S_z'} \middle| \hat{\sigma}_h^{-1} \hat{\sigma}_h \hat{p}_\pm \hat{\sigma}_h^{-1} \hat{\sigma}_h \middle| \psi_{n,S_z} \right\rangle \\ &= \sigma_h(n\prime)\, e^{i\pi S_z'} \sigma_h(n)\, e^{-i\pi S_z} \left\langle \psi_{n\prime,S_z'} \middle| \hat{p}_\pm \middle| \psi_{n,S_z} \right\rangle \\ &= \sigma_h(n\prime)\, \sigma_h(n)\, e^{i\pi(S_z'-S_z)} \left\langle \psi_{n\prime,S_z'} \middle| \hat{p}_\pm \middle| \psi_{n,S_z} \right\rangle \end{aligned} \tag{2.13}$$

and

$$\begin{aligned} \left\langle \psi_{n',S_z'} \middle| \hat{p}_z \middle| \psi_{n,S_z} \right\rangle &= \left\langle \psi_{n',S_z'} \middle| \hat{C}_3^{-1} \hat{C}_3 \hat{p}_z \hat{C}_3^{-1} \hat{C}_3 \middle| \psi_{n,S_z} \right\rangle \\ &= e^{i\frac{2\pi}{3}(C_3(n')+S_z')} e^{-i\frac{2\pi}{3}(C_3(n)+S_z)} \left\langle \psi_{n',S_z'} \middle| \hat{p}_z \middle| \psi_{n,S_z} \right\rangle \\ &= e^{i\frac{2\pi}{3}(C_3(n') - C_3(n) + S_z' - S_z)} \left\langle \psi_{n',S_z'} \middle| \hat{p}_z \middle| \psi_{n,S_z} \right\rangle, \end{aligned} \tag{2.14}$$

$$\begin{aligned} \left\langle \psi_{n\prime,S_z'} \middle| \hat{p}_z \middle| \psi_{n,S_z} \right\rangle &= \left\langle \psi_{n\prime,S_z'} \middle| \hat{\sigma}_h^{-1} \hat{\sigma}_h \hat{p}_z \hat{\sigma}_h^{-1} \hat{\sigma}_h \middle| \psi_{n,S_z} \right\rangle \\ &= \sigma_h(n\prime)\, e^{i\pi S_z'} \sigma_h(n)\, e^{-i\pi S_z} (-1) \left\langle \psi_{n\prime,S_z'} \middle| \hat{p}_z \middle| \psi_{n,S_z} \right\rangle \\ &= -\sigma_h(n\prime)\, \sigma_h(n)\, e^{i\pi(S_z'-S_z)} \left\langle \psi_{n\prime,S_z'} \middle| \hat{p}_z \middle| \psi_{n,S_z} \right\rangle \end{aligned} \tag{2.15}$$

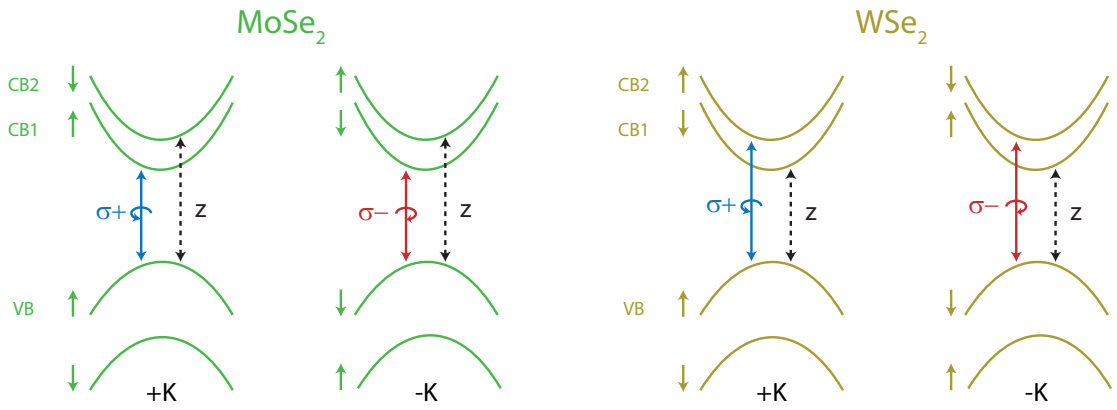

Figure 2.7: Selection rules for $MoSe_2$ and WSe_2 for both valleys. The colored arrows denote the spin of each band.

This results in the following selection rules:

$$\sigma\pm \text{ transition} = \begin{cases} C_3(n') - C_3(n) + S_z' - S_z = 3N \pm 1 \\ \text{and} \\ \sigma_h(n\prime)\,\sigma_h(n)\,e^{i\pi(S_z'-S_z)} = +1 \end{cases} \tag{2.16}$$

$$z \text{ transition} = \begin{cases} C_3(n') - C_3(n) + S_z' - S_z = 3N \\ \text{and} \\ \sigma_h(n\prime)\,\sigma_h(n)\,e^{i\pi(S_z'-S_z)} = -1 \end{cases} \tag{2.17}$$

where N is an integer. We find that the allowed transitions depend on the $\hat{C}_3$ quantum numbers as well as the spin. We can take two important conclusions from this calculation. In the K valley, only $\sigma+$ transitions that are spin conserving will be coupled to far-field emission. With time-reversal symmetry ($C_3 \rightarrow -C_3$ and $S_z \rightarrow -S_z$), it can then be shown that the $-K$ valley couples to $\sigma-$ circularly polarized light. We also see that transitions to the c_2 are allowed but with z-polarized light. A similar calculation can be done for WSe_2, but with the flipped spin ordering in the conduction band. Figure 2.7 shows the selection rules for $MoSe_2$ and WSe_2, which forms the basis for optically addressing each

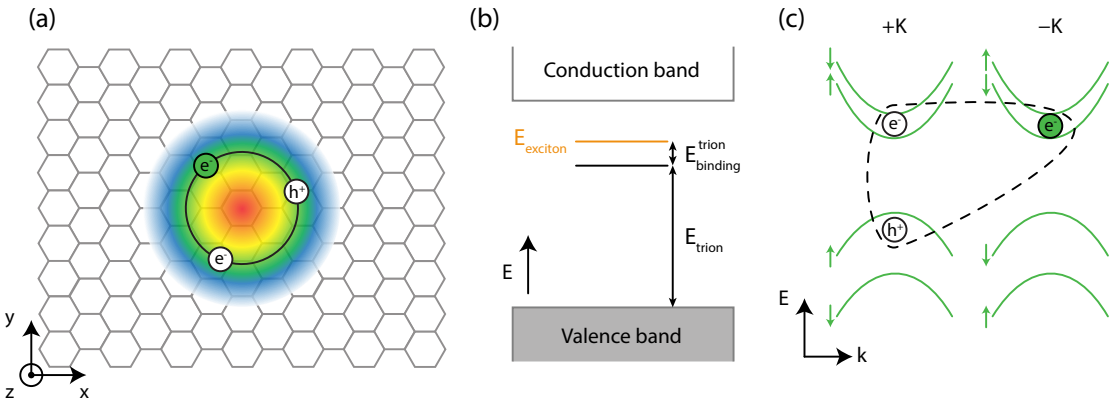

Figure 2.8: (a) Schematic of a three-particle trion state using an additional negative charge as an example. (b) Schematic of trion binding energy and emission. (c) Example of a trion state where the exciton is in the +K valley. The green arrows indicate the electron spins of the bands. The free carrier must obey Pauli exclusion principle.

valley for the two different layers. These selection rules have led to a multitude of exciting results that make use of the unique coupling of circularly polarized light to the degenerate valleys[9,10,17,41], which are locked to specific spins due to their large spin orbit coupling.

In the initial studies of interlayer excitons, these same selection rules were assumed to be true, which led to confusing results in the exciton community. We will later see in Chapter 6 that the selection rules are modified for the interlayer excitons due to the interlayer atomic registry that contributes a quasi-angular momentum in the interlayer transitions. This is essential when considering how the interlayer excitons form and emit in our studies of $MoSe_2/WSe_2$ heterostructures.

2.4 Charged excitons

When excitons are in the presence of free carriers, an exciton and free charge can form a three-particle bound state called the trion (Fig. 2.8(a)). The formation of a trion lowers the energy of the exciton state and thus can be described to have a binding energy with respect to the exciton energy,

$$E_{trion} = E_{exciton} - E_{binding}^{trion}, \tag{2.18}$$

where E_{trion} is the trion emission energy (Fig. 2.8(b)). The trion binding energy is reported to be $20-30$ meV[42,43], which makes trions in TMDs relevant up to room temperatures. Since the free carrier density in atomically thin layers can easily be tuned using a gate, trion formation can be electrically modulated. Due to the Pauli exclusion principle, the extra free carrier cannot come from the same state (spin or valley) as the charges in the exciton. Thus, given an exciton state in the $+K$ valley, the bound free carrier must come from the spin-split band or the $-K$ valley (Figure 2.8(c)). Trions are observed in the presence of both positive and negative charges, with interesting exchange and interaction effects that can arise[44,45].

While the exciton is a composite boson, the three-particle trion is treated as a fermion with net charge. This allows charge transport driven by an optically active particle via in-plane electric fields[46,14]. It also has important physics consequences for exploring how fermionic statistics will compete with the bosonic statistics of an exciton gas. In Chapter 4, we will discuss the first discoveries of the charged interlayer excitons and their electrically controllable movement. In Chapter 7, we will learn more about the charged interlayer excitons and discuss open questions about their behavior in magnetic fields.

We also note here that the features observed in the optical measurements can also be explained using a polaron picture[47,48]. In the polaron theory, the exciton interacts with or is dressed by the entire Fermi sea of electrons, rather than a single electron. When charges are introduced into the layer, an attractive polaron and a repulsive polaron branch emerge, which correspond to increases or decreases in the exciton energy. The attractive polaron is analagous to the trion picture above, but current experiments cannot distinguish between the two theories. Acknowledging this issue, we discuss the charge dressing of excitons as a "charged exciton" in most discussions in this thesis.

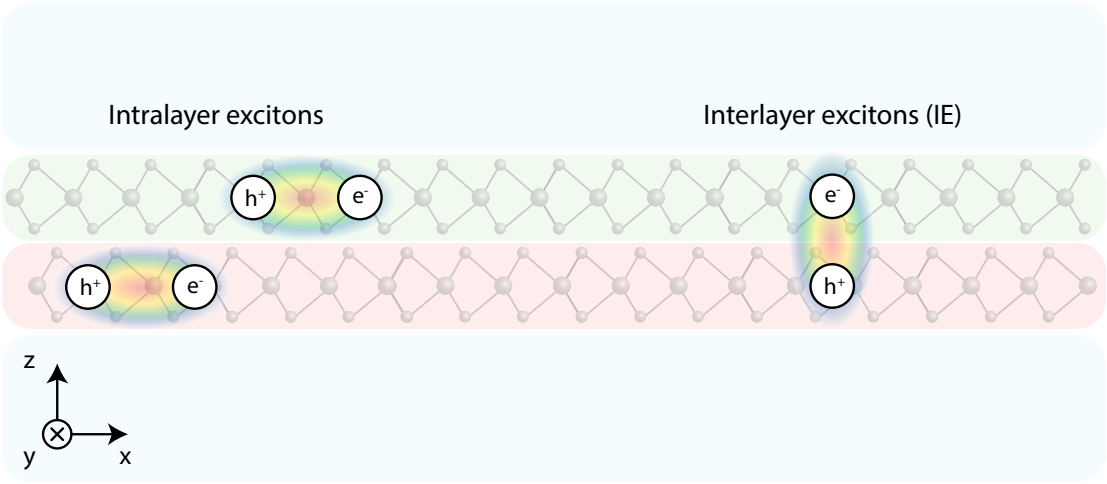

Figure 2.9: Schematic of the intralayer and interlayer excitons. The red and green layers represent $MoSe_2$ and WSe_2 layers while the blue capping layers represent h-BN.

2.5 Interlayer excitons

Excitons in monolayer TMDs exist entirely in the plane of a single atomic layer. When two of these layers are stacked on top of one another, we can now have bound states that exist vertically across two layers. We distinguish these two types of excitons as intralayer excitons, where the electron and hole are localized in a single layer, or interlayer excitons (IEs), where the electron and hole are localized on separate layers[†] (Fig. 2.9). Since the orientation of its electric dipole is always out-of-plane, the interlayer exciton's most distinguishing feature is its interaction with an out-of-plane electric field ($\vec{E} = E\hat{e_z}$). For a permanent dipole moment, the interlayer exciton energy will shift according to the linear Stark effect,

$$\Delta E_{IE} = \vec{p} \cdot \vec{E}, \tag{2.19}$$

[†]Note that this picture is only valid for excitons that form near the K points, where the orbitals at the conduction and valence bands are strongly localized on the metal atoms. Other points in the Brillouin zone can have the electron or hole wavefunctions can be spatially delocalized.

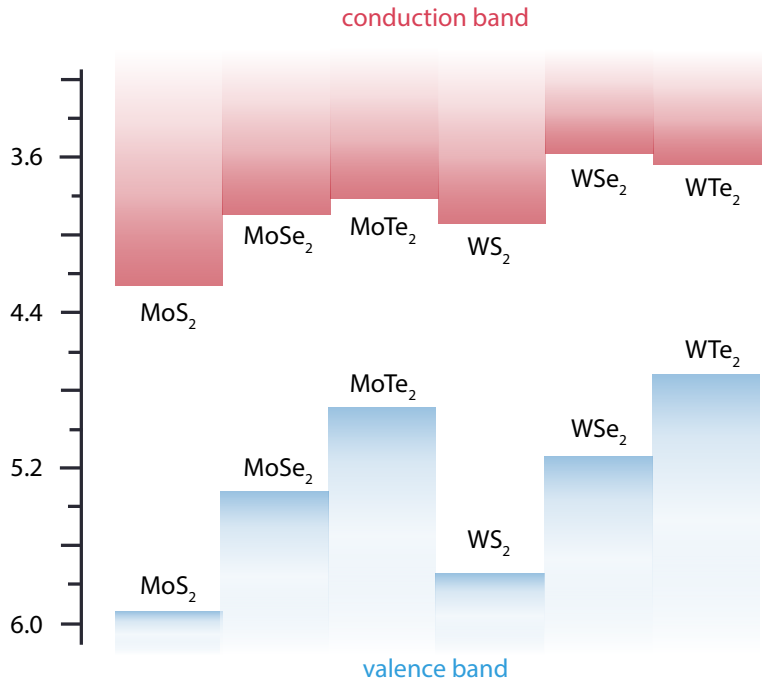

Figure 2.10: Monolayer band alignments of various semiconducting TMDs. Adapted from Liu, Y. et al.[49].

where ΔE_{IE} is the energy shift of the interlayer exciton, $\vec{p} = e\vec{d}$ is the electric dipole moment of the interlayer exciton, e is an electron charge, and $\vec{d}$ is the vector connecting the electron and hole that is dictated by the interlayer separation. This is in contrast to intralayer excitons that do not have a preferred electric dipole orientation and therefore can only be tuned by the significantly weaker second order (quadratic) Stark effect. This interaction allows tuning of the interlayer exciton properties, such as emission energy and the radiative lifetime, as we will show in Chapters 4 and 5.

Since there are several semiconducting TMDs to choose from, we can pick the layers that we stack on top of each other. Figure 2.10 shows the various semiconducting TMDs. Depending on the selected layers, the newly formed structure will have different relative band alignments to each other. To encourage the formation of interlayer excitons, we want to choose a pair of materials with a staggered band alignment, which creates a built-in electric field to layer polarize the electrons

and holes. This will form a type-II heterostructure so that one layer has the lowest energy conduction band and the other layer has the highest energy valence band. The resulting heterostructure will then have a new effective band gap (E_{gap}^{HS}) (Fig. 2.11). Thus, another way to recognize the interlayer exciton states is to find emission at lower energy than the expected direct band gap transitions in the individual monolayers. Depending on the choice of materials, this band gap can range from near infrared (NIR) into infrared (IR) wavelengths. There are several pairs that form this staggered band alignment, including MoS_2/WS_2 [50,51,52], WS_2/WSe_2 [53], MoS_2/WSe_2 [54,55], or our material choice $MoSe_2/WSe_2$ [14,13,56,57,58,59,60,61,62,63,64,65,66,67], which all have experimental reports of interlayer excitons. The layer separation of the electron and hole happens on a rapid time scale, $\sim$ 50 fs[68,69], which is faster than the exciton radiative lifetime.

It should be noted that other structures could be formed as well. If we choose to stack two of the same layers (homobilayer), the conduction and valence bands for the two layers would be aligned. The formation of intralayer and interlayer excitons would then be sensitive to the interactions between the layers which would determine the built-in electric field. By using external electric fields, the relative band alignment can be tuned to exceed the difference in the binding energy of the intralayer and interlayer excitons to make interlayer exciton formation favorable[70,71].

Since the electrons and holes are spatially separated, the recombination process becomes more difficult, significantly increasing the lifetime of the interlayer exciton. In Chapters 4 and 5, we show that the measured lifetimes can range from 1 to 500 ns, or almost 3 to 5 orders of magnitude longer than the intralayer excitons. Studies have predicted the lifetime can be determined by the relative twist angle between the layers[72]. Also, depending on the alignment of the K valleys in the two layers, the spin-valley properties can be modified, which will be shown in Chapter 6. Finally, the binding energy is still very large. The interlayer exciton will experience larger dielectric screening because the electric field lines are almost entirely within the TMD layers (Fig. 2.9), but still have estimated binding energies of $\sim$ 150 meV[73,74]. Thus, by using interlayer excitons, we have a longer-lived, electrically tunable

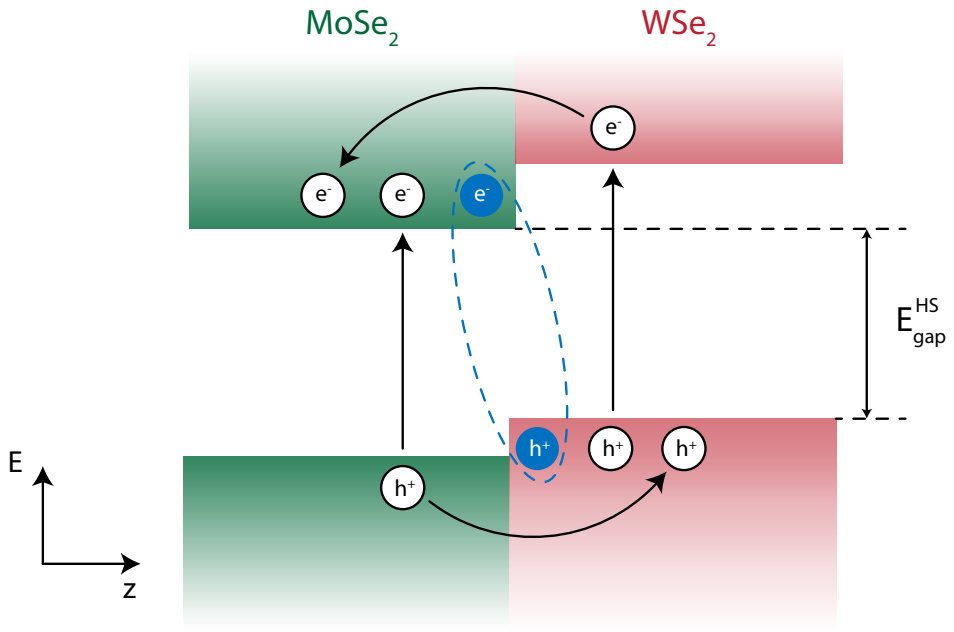

Figure 2.11: Schematic of the band alignment for a $MoSe_2/WSe_2$ heterostructure. Electrons and holes are created in each layer and quickly move into the opposite layers to form interlayer excitons (blue). E_{gap}^{HS} is the new effective band gap of the heterostructure.

quasi-particles that preserve the large binding energies and unique spin-valley properties of intralayer excitons. This gives the potential for many exciting applications such as exciton routers[75,76] or tunable light emitting diodes (LEDs)[66,77,78].

2.6 Exciton BEC

The large motivation for studying interlayer excitons is the search for a high temperature Bose-Einstein condensate (BEC). The BEC is a state of matter where an unlimited number of bosons, governed by Bose-Einstein statistics, occupy a single ground state, resulting in macroscopic quantum behavior such as superfluidity. In a 3D non-interacting gas, this occurs at a critical temperature of

$$k_B T_C = \frac{1}{\zeta(3/2)} \frac{\hbar^2 n^{2/3}}{m}, \tag{2.20}$$

where k_B is the Boltzmann constant, ζ is the Riemann zeta function, n is the particle density, and m is the particle mass. The first experimental evidence of a BEC was realized in cold Rubidium atoms at 100 nK in 1995[79]. However, the large mass of atoms equates to a low T_C. A similar thermodynamic calculation for a non-interacting 2D gas will reveal that long-range condensation cannot exist above $T = 0$ K. However, for a fixed particle density and finite sample size, a similar transition should occur even for reduced dimensionality[80].

Realization of a 2D condensate at higher temperatures was later shown with indirect excitons in GaAs double quantum wells. In these systems, coherent exciton emission was observed at $T \approx 2$ K[81,82]. In TMDs, predictions of an exciton condensate are at even higher temperatures[73,83]. Phase diagrams have been mapped out for interlayer excitons showing critical temperatures as high as 100 K[73]. In these calculations, the degeneracy temperature can be written as a function of the total exciton density (n_{IE})

$$k_B T_D = \frac{2\pi\hbar^2}{\nu\, m_{IE}} n_{IE}, \tag{2.21}$$

where ν is the exciton degeneracy considering the spin and valley symmetry in TMDs, and $m_{IE} = m_e + m_h$ is the exciton mass. Thus, T_D is only limited by the largest sustainable exciton density before dissociation. Exciton dissociation is determined by the Mott criterion[26] and will occur at at a critical density

$$n_{Mott}\, a_B^2 \approx 0.04, \tag{2.22}$$

where a_B is the exciton Bohr radius. So although the mass of the exciton is larger ($0.6m_0 - 1.2m_0$ compared to only $0.22m_0$, where m_0 is the bare electron mass), the significantly larger binding energies in the TMD excitons equate to a significantly larger sustainable exciton density and a higher achievable degeneracy temperature. Also discussed is the Berezinskii–Kosterlitz–Thouless (BKT) transition temperature

$$k_B T_{BKT} = \frac{1.3\,\hbar^2}{\nu\, m_{IE}} n_{IE}, \tag{2.23}$$

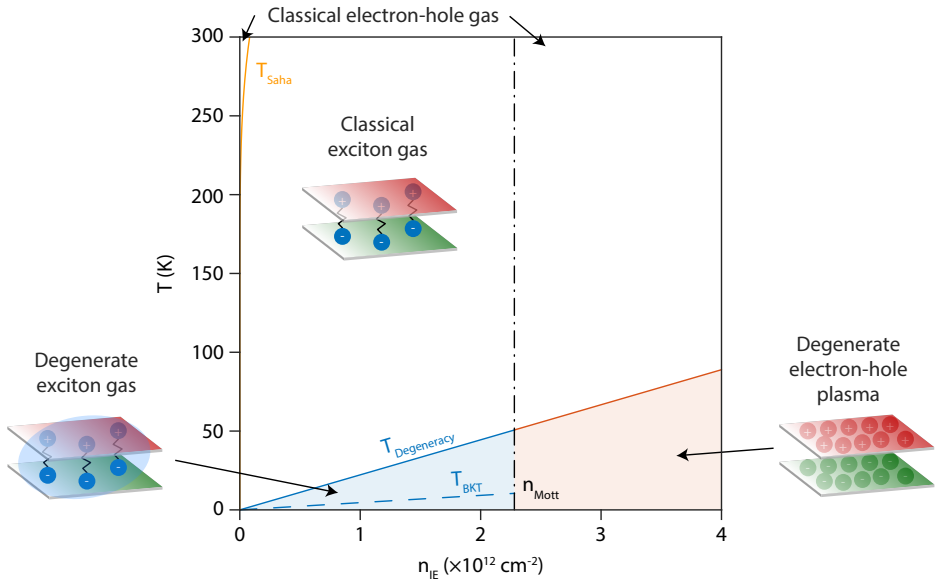

Figure 2.12: Interlayer exciton phase diagram using equations from Fogler, M. et al.[73]. The blue solid and dashed lines corresponds to the degeneracy and BKT temperatures, respectively. The black dashed line correspond to the Mott density, switching to a degenerate electron-hole plasma. The yellow line corresponds to thermal dissociation, which occurs above the Saha temperature.

corresponding to the temperature below which macroscopic superfluidity can exist.

Finally, out of completeness, we also mention the thermal disassociation of the exciton, which occurs above the Saha temperature

$$k_B T_{Saha} = \frac{\pi \hbar^2}{\nu m_{IE}} n_{IE} e^{E_{binding}/k_B T_{Saha}}, \tag{2.24}$$

where $E_{binding}$ is the interlayer exciton binding energy. Due to the large interlayer exciton binding energy, thermal disassociation requires very high densities and is mostly irrelevant for the work in this thesis. The high temperature disassociation of excitons in TMDs have been studied in the intralayer excitons[73,84,85,86].

In Figure 2.12, we map out the phase diagram for the $MoSe_2/WSe_2$ interlayer excitons based on the discussions above. Using theoretically calculated values, we approximate a maximum $T_D \approx 50$

K for $n_{Mott} \approx 2.2 \times 10^{12}$ cm^{-}2. While the exact values are strongly dependent on the effective mass and Bohr radius, we use this phase diagram as both a guide and motivation for Chapters 5 and 8.

While both intralayer and interlayer excitons in TMDs are composite bosons and can form a condensate, there are a few considerations we should make. First, in order to form a condensate, a large steady-state density of excitons must exist - for a given generation rate, the interlayer excitons with their longer lifetimes can more easily reach these higher exciton densities. Second is the avoidance of the excitation position. While the laser generates the excitons, it can also induce coherence in the light emission and be a source for heating. To avoid these issues, probing the exciton gas away from the excitation position is an important step to searching for a condensate. For both problems, the interlayer exciton is a better candidate than the intralayer exciton. The long lifetime should allow for a large density of excitons to be generated. Also, the longer lifetime and permanent dipole moment gives them time to move away from the excitation spot via dipole-dipole repulsion and thermally cool. In the analogous indirect excitons in GaAs double quantum wells, spontaneous coherence from an exciton condensates was observed by probing away from the excitation spot, either by diffusion or by trapping[81,82].

An alternative method for generating the high densities is via electrical generation. This removes the concerns about laser induced coherence completely. Unlike lasers or other cavity induced coherence, free electrons and holes that are electrically injected into the system will only emit coherent light if the recombination mechanism is itself coherent, e.g. an exciton condensate forms. The difficulty lies in injecting an equal density of electrons and holes. In Chapter 8, we will expand on the efforts towards electrically generating an exciton condensate.

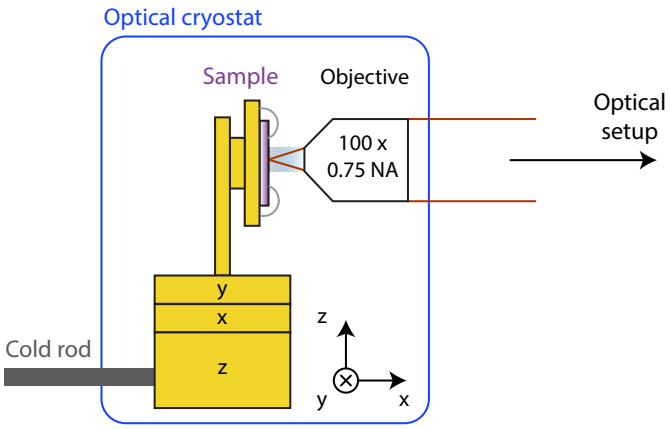

Figure 2.13: Schematic of the cryostat and sample mount. The objective focuses light onto the wire-bonded sample, which sits on top of three piezo stages. The sample is cooled by mechanically damped cold rod. Light is coupled into and out of the cryostat via the rest of the optical setup outlined in Appendix B.

2.7 The optics techniques

In the final section of the introduction, we briefly discuss the experimental concepts and details used in this thesis. We use a 4f confocal microscope in a closed-loop 4K optical cryostat to perform low-temperature photoluminescence (PL) and absorption measurements. The sample sits on three piezo stages, which allow the area of interest to be centered under the microscope objective (Fig. 2.13). The collection position can then be scanned using mirrors that move our diffraction limited spot (red cone in Fig. 2.13). This allows us to select positions on our sample and measure the optical response of the device. The basic concept can then be expanded to measure time-resolved PL, scanning diffusion, electroluminescence, and polarization dependent PL. Here, we will discuss the basic absorption and PL measurements and leave the optical setups and further measurement details in Appendix B.

The majority of the optical data presented in this thesis will be from PL or absorption measurements. Both techniques involve using a light source in order to excite free carriers from the valence band to the conduction band. Since excitons have well-defined transitions, we can extract information from either the wavelength of light at which there is resonant absorption in the material, or the

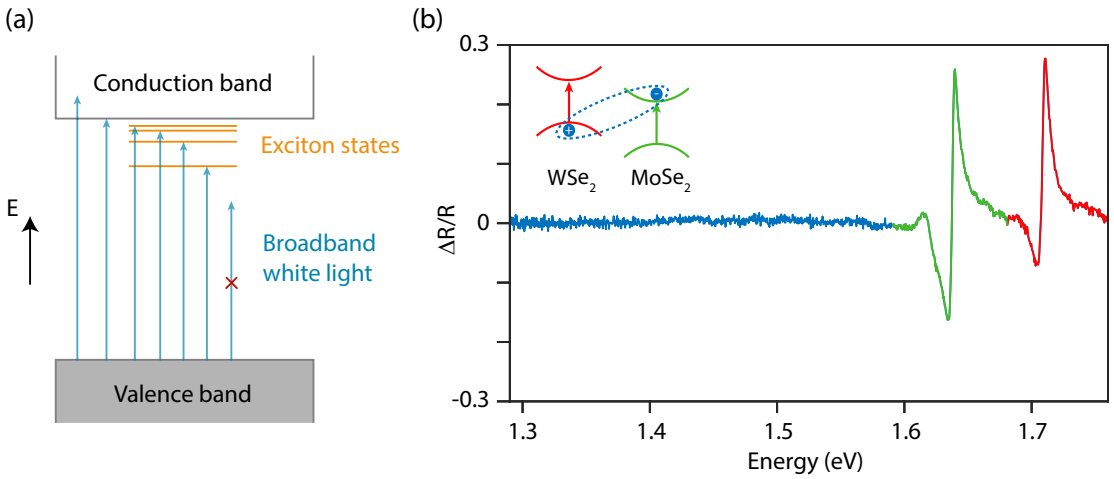

Figure 2.14: (a) Schematic of absorption measurements where broadband light spanning all energies is incident on the sample. Only available transitions will show absorption features. (b) Absorption spectra in the $MoSe_2/WSe_2$ heterostructure area showing strong absorption of the monolayer intralayer excitons (red and green), but no absorption in the interlayer exciton energy range (blue). Inset: band diagram of the heterostructure.

wavelength of light that emits from the material.

The absorption measurement is an optical technique which provides information on the optical transition energies and their relative strengths in a given material. When a photon is incident on the sample with a given energy, $\hbar\omega$, or wavelength, $\lambda = 2\pi c/\omega$, the photon will be absorbed given the existence of a transition with the corresponding energy. Figure 2.4(b) showed a schematic of the expected exciton resonances and simple expectation for the free-particle density of states in 2D.

Experimentally the measurement can be performed in two ways. A broadband light source (white light or supercontinuum laser) can be used to get a continuous and broad range of excitation wavelengths which are incident on the sample. When the photon wavelength is resonant with an allowed transition, the photon will be absorbed (Fig. 2.14(a)). With a transparent substrate, the light will continue through the sample and can be spectrally resolved in a spectrometer. By comparing the incident light intensity ($I_0(\lambda)$) and the transmitted light intensity ($I_t(\lambda)$), the absorption at a given wavelength

can be calculated as

$$A(\lambda) = \frac{I_0(\lambda) - I_t(\lambda)}{I_0(\lambda)}. \tag{2.25}$$

This measurement can be done with different light polarization to resolve the polarization dependent absorption as well.

Unfortunately, as shown in Figure 2.13, the geometry of the optical setup and the non-transparent Si/SiO_2 substrate that our devices are fabricated on do not allow for a transmission measurement and require slightly different considerations. Since the substrate is reflective, we instead measure the reflected light ($I_r(\lambda)$). To first order, the measurements are comparable as the reflected light should be the incident light intensity minus the absorbed photons,

$$I_r(\lambda) = I_0(\lambda)(1 - A(\lambda)). \tag{2.26}$$

Thus to extract the absorption, we measure the normalized differential reflectance $\Delta R/R$,

$$A(\lambda) = \frac{I_0(\lambda) - I_r(\lambda)}{I_0(\lambda)} = \frac{\Delta R}{R}. \tag{2.27}$$

In Figure 2.14(b), we show the normalized differential reflectance spectrum from a $MoSe_2/WSe_2$ heterostructure and observe features at 1.64 and 1.71 eV, corresponding to the $MoSe_2$ and WSe_2 intralayer exciton resonances. We also observe an additional dip in reflectance, unexpected from just the exciton absorption spectrum (Fig. 2.4(b)). This is attributed to interference between the exciton reflection and the substrate reflection. A π-phase shift across the exciton resonance gives rise to destructive interference from the light reflected from the substrate[35]. We also notice a lack of absorption features at lower energy where we expect the interlayer exciton resonance. The weak optical dipole strength of the interlayer excitons, approximately 3 orders of magnitude smaller than the intralayer excitons, makes absorption measurements very difficult to observe[78,87]. So to detect the interlayer excitons,

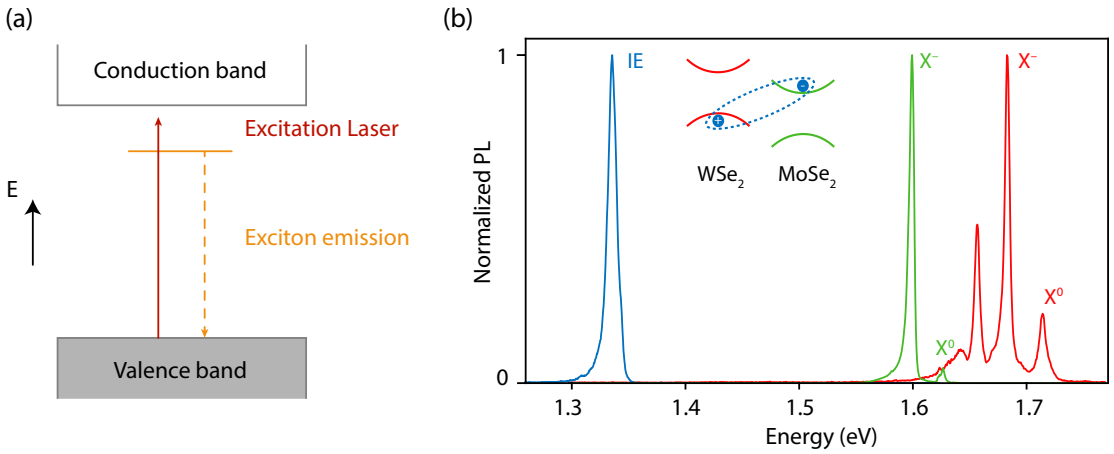

Figure 2.15: (a) Schematic of photoluminescence (PL) measurements where broadband light spanning all energies are incident on the sample. Only available transitions will show absorption features. (b) PL spectra of intra- and interlayer excitons (IE) in the individual monolayer regions (red and green) and the $MoSe_2/WSe_2$ heterostructure region (blue). Inset: band diagram of the heterostructure.

we perform PL measurements, where we take advantage of the efficient absorption at the intralayer exciton transitions to observe interlayer exciton emission.

PL is a useful technique because it generally probes the lowest emitting energy transitions. For the PL measurements, we co-align our diffraction limited excitation and collection spots (red cone in Fig. 2.13), which allows us to excite and probe the exciton emission at any position. Figure 2.15(a) shows a schematic of the PL technique. We excite above the exciton resonance of interest and collect the emitted light while spectrally filtering the laser wavelength. The optically excited electron-hole pairs will relax into the lowest energy states before emitting, allowing weaker optical transitions (such as the interlayer exciton) to be probed. Figure 2.15(b) shows representative PL spectra from the $MoSe_2$ monolayer (green), WSe_2 monolayer (red), and the $MoSe_2/WSe_2$ (blue) heterostructure regions of a sample. In our experiments, we use a 660 nm (1.88 eV) laser to excite the TMD, which can excite all of the relevant excitonic states. In each monolayer region, we observe PL from the exciton (X^0) and trion (X^-) states, which are the two highest emission energy peaks. In WSe_2, there are additional peaks below which are related to defect peaks. In the $MoSe_2/WSe_2$ heterostructure region, we only observe

the interlayer exciton emission at around 1.34 eV with the intralayer excitons strongly suppressed. For the case of the $MoSe_2/WSe_2$ heterostructures, since the time scale for electrons and holes to tunnel across the layers (50 fs) is faster than the exciton lifetime, we are able to observe predominantly interlayer exciton emission [68,69]. PL emission spectra cannot be as easily understood as optical absorption because the microscopic details of the electron relaxation in the bands can be difficult to model. The eventual PL emission is usually dominated by the lowest energy states, although the emission will always be a competition of the relaxation and radiative rates. For example, the lowest energy states in WSe_2 are difficult to detect in far-field measurements such as PL due to the selection rules [10,9], and thus, a higher energy exciton state will dominate PL emission. In Chapter 6, we will discuss how we can brighten some dark states in PL by quenching the relaxation via band filling. With PL, we can extract information about the interlayer exciton emission energy, valley characteristics, spin, and even charge information. In this thesis, we will demonstrate our ability to modulate the interlayer exciton properties and extract this information via optical spectroscopy.

The best investment is in the tools of one's own trade.

Benjamin Franklin

3

Creating an Optoelectronic Device

Our devices are designed to be more electrically controllable than any previously measured TMD heterostructures. We owe this to many of the established fabrication methods for high-quality graphene devices[88,37]. Figure 3.1 provides a schematic for our typical multi-terminal and multi-gate device structure. We create a $MoSe_2/WSe_2$ heterostructure (red and green atomic layers) encapsulated by thicker h-BN insulating layers (light-blue layers). Each layer has elec-

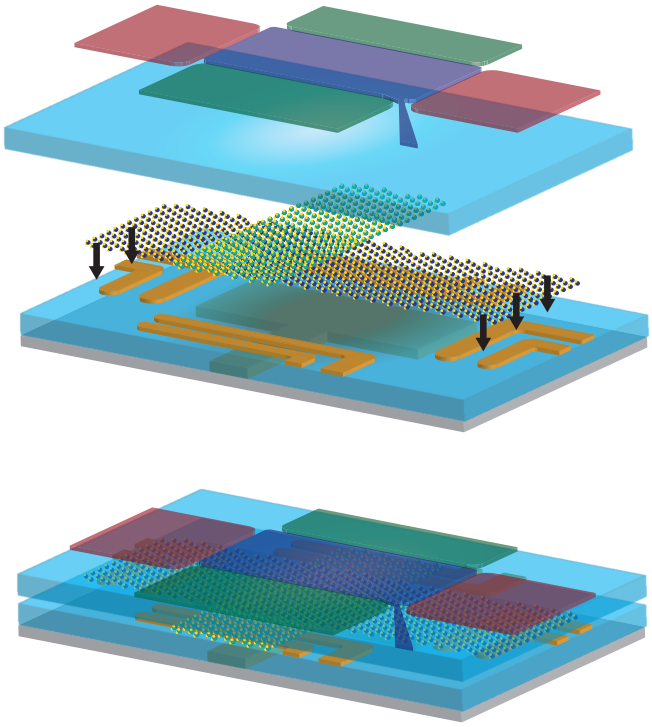

Figure 3.1: A device schematic of the highly electrically tunable TMD heterostructure device. The red (green) top gates correspond to the contact gates for WSe_2 ($MoSe_2$). The blue gate is the heterostructure gate which controls the $MoSe_2/WSe_2$ overlap region. The gold colored leads on the bottom h-BN layer are the pre-patterned Pt contacts. The TMD layers are depicted as atomic layers. The light blue slabs are the encapsulating h-BN layers. The large rectangle beneath the lower h-BN layer is the PdAu bottom gate. These are stacked together to create our device.

trical contacts, shown as yellow electrodes, which are pre-patterned 20 nm thick platinum (Pt). Each contact region is covered by a matching contact gate (red and green top gates respectively), which activate the contacts to gives us electrical access to the active layers. The heterostructure region has matching top (blue) and bottom (gold-colored below the bottom h-BN layer) gates for applying out-of-plane electric fields and to tune the free carrier densities. In this chapter, we outline the steps required to fabricate such a device, going through only the essential details. Specific lithography recipes and additional details can be found in Appendix A.

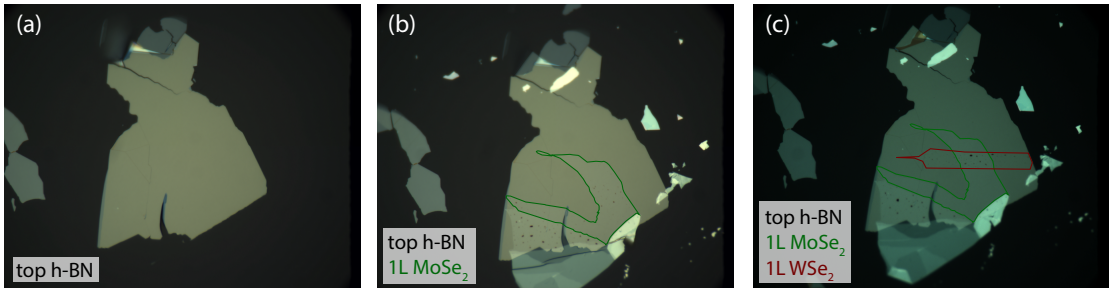

Figure 3.2: Optical images of the top stack at 100x magnification on a PC / PDMS stack. (a) Top h-BN layer. (b) After picking up the $MoSe_2$ layer, outlined with a green line. (c) After picking up the WSe_2 layer, outlined with a red line.

3.1 Stacking the active layers

We begin by preparing the top half of the device so that the bottom substrate and contacts can be designed based on the active TMD layers. The top stack will consist of everything above the Pt contacts, which is usually the top h-BN layer and the active TMD layers (either the $MoSe_2/WSe_2$ heterostructure or just a single TMD). All heterostructures are stacked with the polycarbonate (PC) stacking method (details in Appendix A.1). In Figure 3.2, we show the steps for picking up each layer. We begin by picking up the top h-BN layer using our (PC) / polydimethylsiloxane (PDMS) stamp (Fig. 3.2(a)). We then pick up the two active TMD layers (Fig. 3.2(b)-(c)) with the top h-BN layer. Since the layers will interact via the van der Waals force, the electrically and optically active layers will not need to be exposed to the polymer. For the $MoSe_2/WSe_2$ heterostructures, this gives a clean interface between the two layers. It should be noted that although the heterostructure interface is clean with this method, in single layer WSe_2 devices, it only guarantees a clean top surface.

When stacking the TMD heterostructures, the layers are aligned so that the angle between the crystallographic edges of the $MoSe_2$ and WSe_2 is at an angle modulo 60° degrees, which matches the rotational symmetry of the K valleys in momentum space. This can be done in two ways. The first method is to align the layers based on the naturally defined edges of the exfoliated crystals. While crude, this method is faster if the exfoliated layers have well-defined edges. In Fig. 3.3(a), we can see that all of the

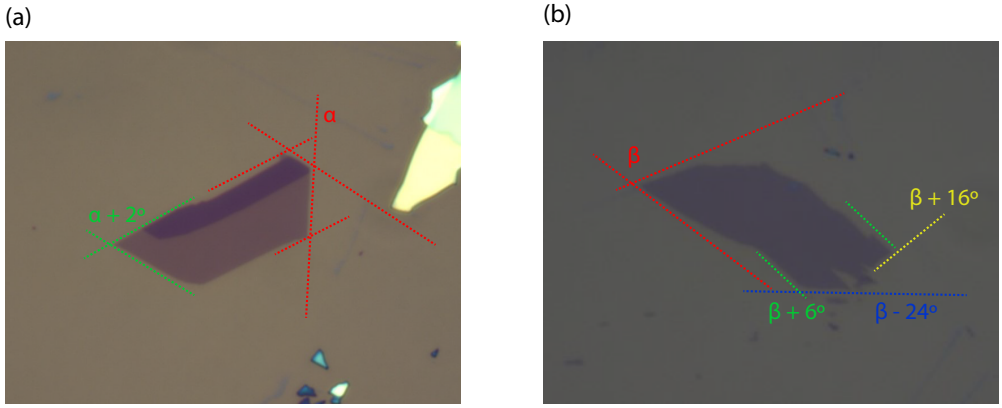

Figure 3.3: Zoomed in optical images of TMD flakes. (a) An exfoliated WSe_2 layer with well-defined edges that are at 60 degree angles. The difference in angle between the red lines (α) and green lines ($\alpha + 2$) is the source of some of the error in determining the stacking angle. (b) An exfoliated WSe_2 layer without well-defined edges. The red lines (β) are at angles not divisible by 60 degrees from the other defined edges (yellow, blue, and green lines) making it difficult to determine the true crystallographic edge.

edges are relatively well defined and do not differ greatly in angle. However, some crystals will have conflicting edges (clean edges that are at an angle that is not divisible by 60 degrees) or no clear edges. Fig. 3.3(b) shows an example where there could be multiple edges that define the crystallographic edge. In this case, we use second harmonic generation (SHG) as a tool for detecting the angle of the crystallographic edges of the monolayer. We will expand on the SHG method in the next section.

Once the layer alignment can be determined the top stack can be created by picking them up in the orientations determined in the above step. Since at this point, 0-degree and 60-degree alignment cannot be distinguished, we can choose to rotate the layers with 60 degree intervals to either maximize the overlap or create an optimal overlap region while leaving space to align the monolayers to electrical contacts. The TMD layers can be picked up at temperatures below the glass transition temperature of PC, because the stickiness of the PC layer is less important when picking up via the van der Waals forces between the layers (details in Appendix A.1). Once the top stack is prepared, we move on to the bottom stack.

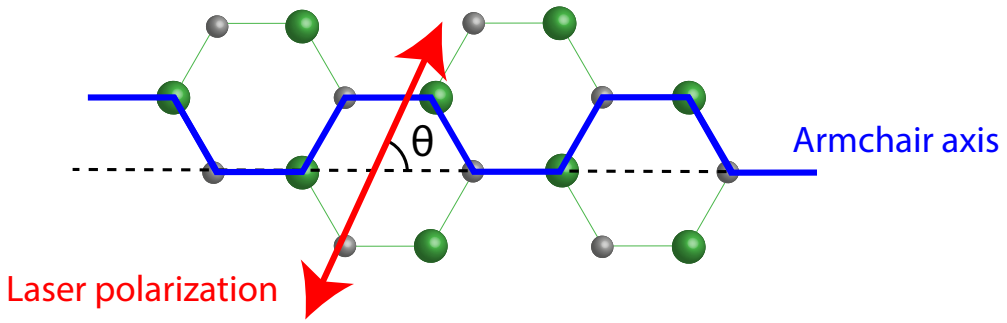

Figure 3.4: The armchair axis of the monolayer crystal. The angle θ is defined as the angle between the laser polarization and the armchair axis of the crystal.

3.2 Second harmonic generation

Second harmonic generation (SHG) is a nonlinear optical process where the frequency of the output is double that of the input. For the case of monolayer TMDs, the intensity of the SHG signal is dependent on the angle difference between the linearly polarized femtosecond pump laser and the monolayer material's crystallographic edges (further details can be found in Li, Y. et al.[89]). The expected polarized intensity of the sample is:

$$\begin{aligned} I_{\parallel} &= I_0 \cos^2(3\theta) \\ I_{\perp} &= I_0 \sin^2(3\theta) \end{aligned} \tag{3.1}$$

where $I_{\parallel}$ and $I_{\perp}$ are measuring the linearly co- and cross-polarized SHG signal from the sample and θ is the angle between the excitation linear polarization and the armchair axis of the monolayer (Fig. 3.4). Thus, we can use the SHG signal to determine a crystallographic edge of different samples, which we then use for alignment during stacking. Figure 3.5 shows SHG images of a TMD monolayer where we observe a minimum and maximum in the SHG signal as the sample is rotated by an angle $\Delta\theta$. We observe a 6-fold symmetry in the signal (minimum at both $\Delta\theta = 0°$ and $\Delta\theta = 60°$). While this method can find the 6-fold degenerate armchair crystallographic axis, it cannot distinguish between

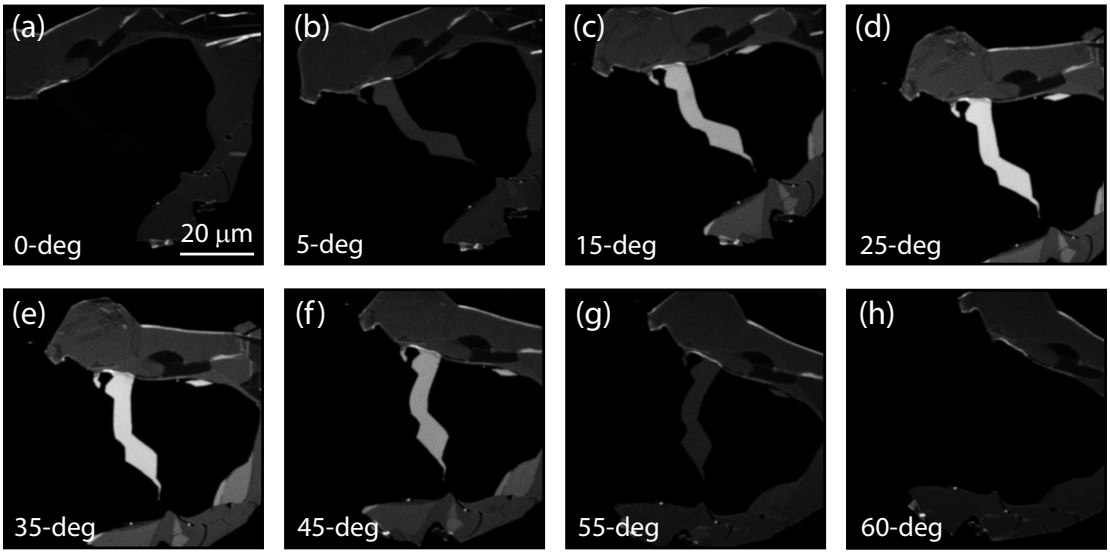

Figure 3.5: SHG intensity for a monolayer $MoSe_2$ flake at various rotation angles where $\Delta\theta$ is with respect to the starting rotation position. All images are normalized to the same scale. $\Delta\theta$ = (a) 0°, (b) 5°, (c) 15°, (d) 25°, (e) 35°, (f) 45°, (g) 55°, and (h) 60°.

aligning the two layers' *K* valleys at 0- or 60-degrees (or equivalently 180°). Thus, every device must be initially characterized once the device is complete to determine whether the heterostructure is a 0- or 60-degree stacked device.

There has been work showing that SHG can be used to determine the stacking angle of the TMD heterostructure once it is stacked[90]. Hsu, W. et al. observed enhancement or suppression of the SHG signal at the hetero-interface depending on the stacking orientation. Figure 3.6 shows SHG images of a stacked heterostructure at different rotations where we found the SHG signal in the heterostructure was neither enhanced nor suppressed. However, the intensities of individual monolayers do not seem to have a maximum at different rotation angles, implying good alignment of the layers. In the end, we were unable to use this technique to reliably distinguish the 0- and 60-degree alignment in the heterostructures. Later in Chapter 6, we expand on how the selection rules can be a clearer indication of the stacking orientation.

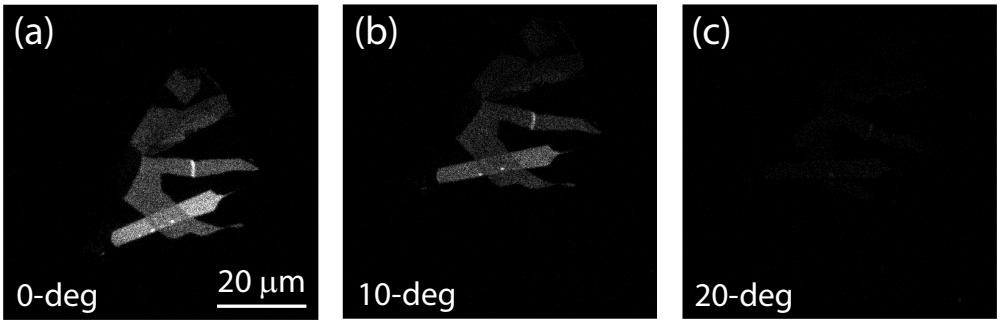

Figure 3.6: SHG intensity from a $MoSe_2/WSe_2$ heterostructure for a few rotation angles where $\Delta\theta$ is with respect to the starting rotation position. All images are normalized to the same scale. (a) $\Delta\theta = 0^\circ$, (b) 10°, and (c) 20°.

3.3 Preparing the bottom stack

The bottom stack is designed based on the top stack with the active TMD layers. We design the bottom gate and Pt contact locations to match the location of the TMD layers. We then deposit the Cr (1 nm)/PdAu (9 nm) bottom gate defined by electron beam (e-beam) lithography onto a Si substrate coated with 285 nm SiO_2 (exact recipe in Appendix A.2.3). These metal gates are annealed in a vacuum annealer at a pressure below 5×10^{-7} Torr and a temperature of 350° C for at least 15 minutes before proceeding. We use thin (< 10 nm) PdAu alloy gates because our experience has showed that they create the most uniform and flat surfaces (in comparison to gold or palladium), which is important for maintaining as close to an atomically-flat surface for the active TMD heterostructure. Graphite gates are known to have even lower disorder and are atomically flat, but we use the metal gates due to the convenience of creating very fine, e-beam lithography defined features (details in Appendix A.2.3). In Figure 3.7(a)-(b), we show an optical image and an atomic force microscope (AFM) image of a typical bottom gate structure made with the PdAu alloy. We are typically able to get surfaces with roughness less than 1.5Å, or 1/2 the thickness of an h-BN layer.

The bottom h-BN layer is then transferred by the PC dry transfer method (Appendix A.1) onto the bottom gate electrode (Fig. 3.7(a)). We anneal the transferred stack with the vacuum annealer again.

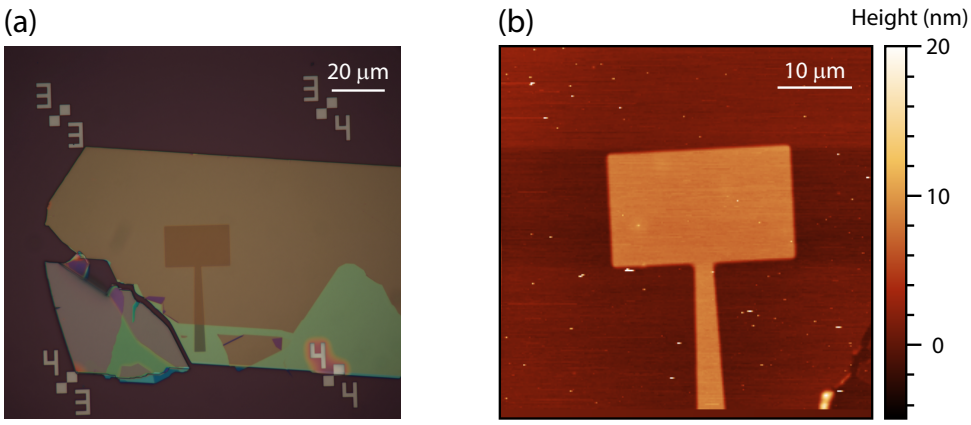

Figure 3.7: The backgate with bottom h-BN transferred on top. (a) Optical image at 100x magnification. (b) Atomic force microscope (AFM) image of the bottom gate structure. The white dots could be PC or PMMA residue but are relatively sparse.

We then evaporate Cr (1 nm)/Pt (19 nm) for the TMD contacts (exact recipe in Appendix A.2.4). We again aim for flat surfaces but typically get surface roughnesses rougher than the gates. In Figure 3.8(a), we show an AFM image of the contacts evaporated on top of h-BN. Figure 3.8(b) shows a higher contrast version of the same image to distinguish smaller roughness variations. The roughness quality of the Pt contacts can vary from lead to lead with some leads having large edges or "bunny ears", while others being flat across the entire surface. The recipe in Appendix A.2.4 aims to maximize the chances for producing the flat contacts, but variations are often seen. These contacts are optimized for the WSe_2 layer as Pt has a high work function [49], but work sufficiently for both WSe_2 and $MoSe_2$ when driving a diode, where low-voltage excitations are not as critical. Some devices were made with Cr (1 nm)/Pt (9 nm) for the $MoSe_2$ contact as we found the work function with the thinner Pt contact was slightly lower, but ultimately the improvement was minimal in comparison to the added fabrication steps. Whether separate thickness Pt contacts were made or a single thickness was chosen, the stack is annealed between each lithography step to clean the surface of contaminants.

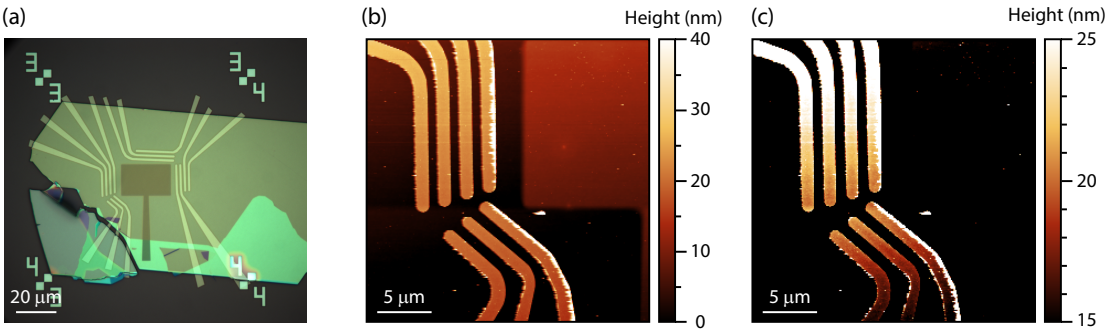

Figure 3.8: (a) Optical image of the bottom stack with the bottom gate, bottom h-BN, and Pt contacts prepared. (b-c) AFM image of sets of Pt contact leads on the bottom h-BN layer with lower contrast (b) and higher contrast (c) scale bars. Some leads are flatter than others with "bunny ear" heights ranging from 30 nm to not present at all.

3.4 Finishing the device

Once the bottom half of the device is prepared (bottom gate, bottom h-BN, and Pt contacts), we stack the top half of the device (Fig. 3.9(a)). The final step involves aligning the top stack to the bottom stack and releasing the stack from the PC polymer layer (Appendix A.1). After the stack is completed, the PC is removed with chloroform.

Importantly, we do not anneal the final stack as we find that annealing the TMD heterostructure has mixed results. Traditionally, h-BN encapsulated, graphene devices will be annealed to remove bubbles and other defects that may be trapped in between the layers. Sometimes these bubbles will combine into certain areas of the sample, but since these devices are typically etched into small regions, the device area can be defined away from these defect sites. In the TMD heterostructures, we do not have a reliable recipe for etching the device as the heterostructure is often damaged in the process. In addition, we note that in TMD heterostructures, bubbles and defects can become larger in lateral area and in height after annealing, which can make any clean areas even smaller. This issue in TMDs could be attributed to the differing sign in the thermal expansion coefficients of TMDs[91] (positive) versus h-BN[92,93] or graphene[91,94] (negative). Despite these concerns, we found that the process of spinning PMMA (typically at 4000 RPM) and baking the resist at 180° C aids in flattening bubbles. This seems

to happen quite reliably and can be repeated multiple times before proceeding. When comparing the images after finishing the stack (Fig. 3.9(a)) and evaporating the top gate (Fig. 3.9(b)), we see greater uniformity in the sample with only one of the large bubbles remaining.

We now discuss the final lithography steps. We deposit top gates that match the monolayer only regions and the heterostructure region separately (Fig. 3.9(b)). The gates above the monolayer TMDs (and their contacts) are designated as contact gates, which can be set to large positive (negative) voltages to electron (hole) dope the region. This doping scheme allows us to have efficient electrical contacts and to inject current into the heterostructure. The heterostructure gate is designed to only be above the overlap between the $MoSe_2/WSe_2$ region, which gives us independent control of the region. These top gates are either Cr (1 nm)/Pd (9 nm) or Cr (1 nm)/PdAu (9 nm), depending on the device. They are thick enough to be continuous films, but thin enough for optical access, with an approximate transmittance of 10%. Once again, graphite gates could be used to improve the optical access and uniformity, but with less resolution in feature sizes. Improvements on graphite gate feature sizes are being developed in the Kim lab and future devices will likely make use of these techniques[95]. Specifically, the gates can be etched by designing fine lines in PMMA. The etched lines are confirmed via a probe station as the two leads on the gate will no longer conduct once a physical gap has been opened.

Finally, any extraneous areas of h-BN or thick parts of TMD can be removed with an etching step before proceeding to evaporating Cr (5 nm) / Au (> stack height) leads and bonding pads (Fig. 3.9(c)-(d)). The bonding pads allow the contacts and gates to be connected to the external electronics racks via wire bonds. Palladium (Pd) layers of around $10 - 30$ nm can be evaporated between the Cr and Au layers for added mechanical sturdiness, which allow for many more wire bonds before requiring repair. However, Pd is much harder to remove (both Cr and Au have available wet etch recipes) and thus, can be less forgiving for device designs.

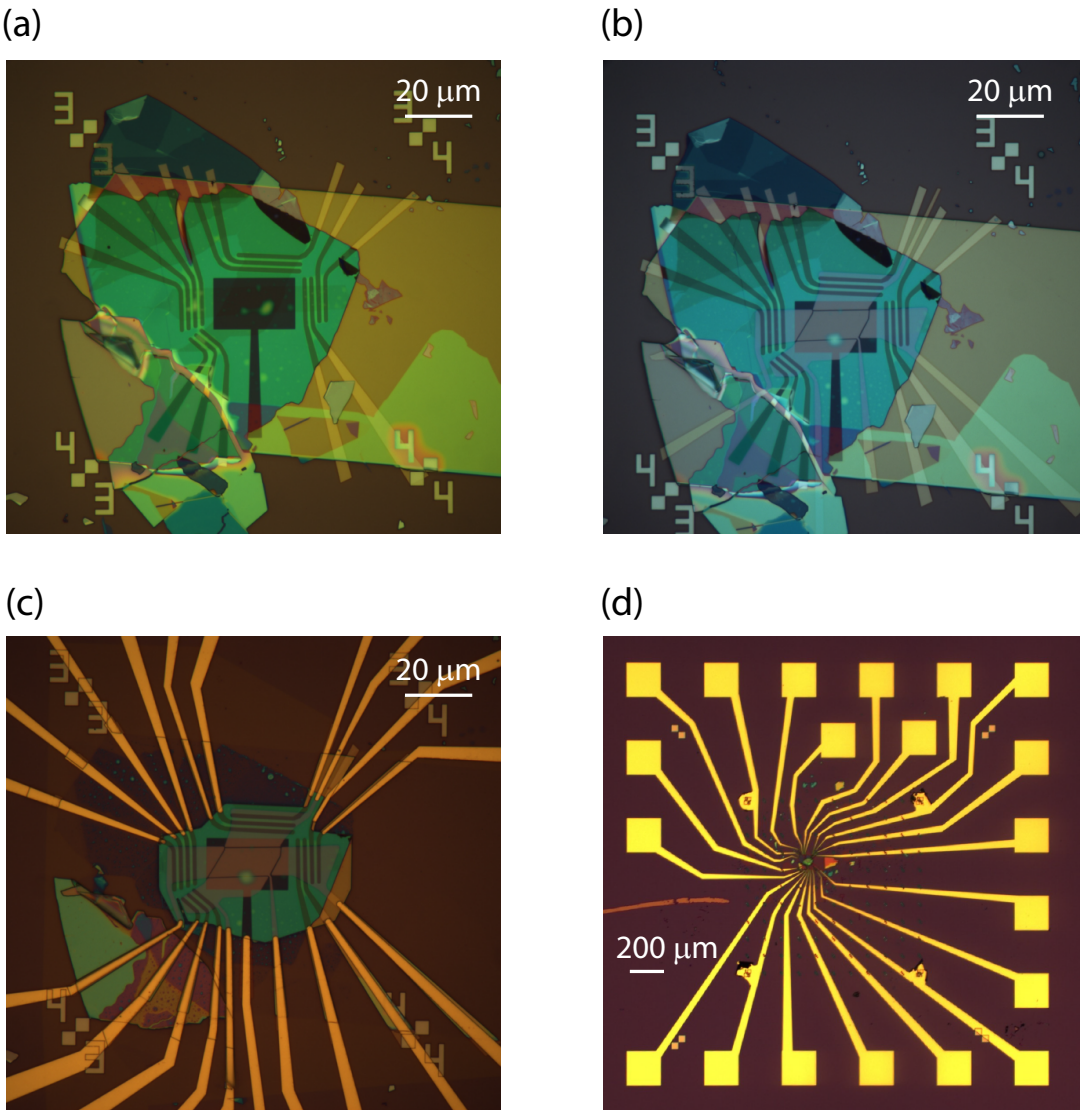

Figure 3.9: Optical images of the stacks during the final steps. (a) The top stack is placed on the prepared bottom stack and the PC film is removed. (b) After evaporating the top gate structures. (c) After final etching and bonding pad evaporation steps. (d) Zoomed out version (2.5x) of the final stack with bond pads.

All for one and one for all.

Alexandre Dumas, *The Three Musketeers*

4

Electrical Control of Interlayer Exciton Dynamics

Long-lived excitons can be potentially utilized for the realization of coherent quantum many-body systems[96,73,97] or as quantum information carriers[98,99]. In conventional semiconductors, the exciton lifetime can be increased by constructing double quantum well

(DQW) heterostructures, where spatially separated electrons and holes form interlayer excitons (IEs) across the quantum wells[81,82,100,101,102,103,104]. Strongly bound IEs can also be formed by stacking two single atomic unit cells of TMDs into a van der Waals (vdW) heterostructure. TMD heterostructures, such as $MoSe_2/WSe_2$, MoS_2/WS_2, and MoS_2/WSe_2 have shown ultrafast charge transfer[68], the formation of IEs with a large binding energy of approximately 150 meV[13], and diffusion over long distances[76]. Moreover, the tight binding and small exciton Bohr radius potentially allow for quantum degeneracy of these composite bosons, which may lead to exciton condensation at significantly elevated temperatures compared to, e.g., conventional BECs of cold atoms[73].

We fabricate individually electrically contacted optoelectronic devices using hexagonal boron nitride (h-BN) encapsulated vdW heterostructures of $MoSe_2$ and WSe_2[37,105]. Optically transparent electrical gates and Ohmic electrical contacts realized for the individual atomic layers allow us to have complete control of the carrier densities in each TMD of the DQW while maintaining full optical access. The top and bottom insets of Fig. 4.1(a) show an optical image of a representative device with false-colored top gates and a schematic cross-section, respectively (details on fabrication and the device are in Chapter 3 and Appendix C). The green and red false-colored gates depict the contact gates for doping the $MoSe_2$ and WSe_2 regions, respectively. These contact gates together with the pre-fabricated Pt electrodes provide Ohmic contacts in the WSe_2 p-channel[21].

Employing these heterostructures, we realize optical and electrical generation of long-lived neutral and charged interlayer excitons. We demonstrate that neutral interlayer excitons can propagate across the entire sample and that their propagation can be controlled by excitation power and gate electrodes. We also realize the drift motion of charged interlayer excitons using Ohmic-contacted devices. The electrical generation and control of excitons provides a route for realizing quantum manipulation of bosonic composite particles with complete electrical tunability.

4.1 Electrical gate modulation of interlayer exciton properties

The presence of the top (optically transparent) and bottom electrical gates, in addition to the separately contacted TMD layers, allows us to control the carrier density in the individual TMD layers as well as the electric field across the TMD heterostructure, E_{hs}, using the voltage V_{tg} (V_{bg}) applied to the top (bottom) gate. For intrinsic TMD layers (i.e., no free carriers and the chemical potential located within the semiconducting gap), where the heterostructure can be approximated by a thin dielectric slab, E_{hs} is controlled by a gate operation scheme where we apply opposite gate polarity $V_{tg} = \alpha V_{bg}$, where $\alpha = t_{top}^{h-BN}/t_{bottom}^{h-BN} = 0.614$ is the voltage ratio (details in Appendix D). We calculate:

$$E_{hs} = \left(\frac{\varepsilon_{h-BN}}{\varepsilon_{TMD}}\right) \cdot \frac{V_{tg} - V_{bg}}{t_{total}} \tag{4.1}$$

where $t_{top}^{h-BN} = 70$ nm and $t_{bottom}^{h-BN} = 114$ nm are the top and bottom h-BN thicknesses, respectively, t_{total} is the total h-BN thickness. We use $\varepsilon_{h-BN} = 3.9$ and $\varepsilon_{TMD} = 7.2$ for the h-BN and TMD permittivity, respectively, taken from literature [106,23]. Figure 4.1(a) shows the photoluminescence (PL) spectrum measured at temperature $T = 4$ K as a function of E_{hs}, keeping both TMD layers intrinsic. We observe a linear shift of PL peak energy with E_{hs}, suggesting a first order Stark shift caused by the static electric dipole moment across the vdW heterostructure. By fitting the linear PL peak shift with the linear Stark shift formula $-e\,d\,E_{hs}$, where $e\,d$ is the dipole moment, we estimate $d \approx 0.6$ nm, in good agreement with the expected vdW separation between WSe_2 and $MoSe_2$. This analysis strongly suggests that the observed PL peak indeed corresponds to the IE emission of the $WSe_2/MoSe_2$ heterostructure with out-of-plane oriented electric dipoles. There is around 10% of non-linearity in the energy shift dependence vs. E_{hs}, which, combined with weak variations of the absorption intensity (as shown in Fig. 4.1(b)), might be attributed to the charging effect caused by uncompensated gating. Similar to a previous study [13], we also note that the PL from the intralayer ex-

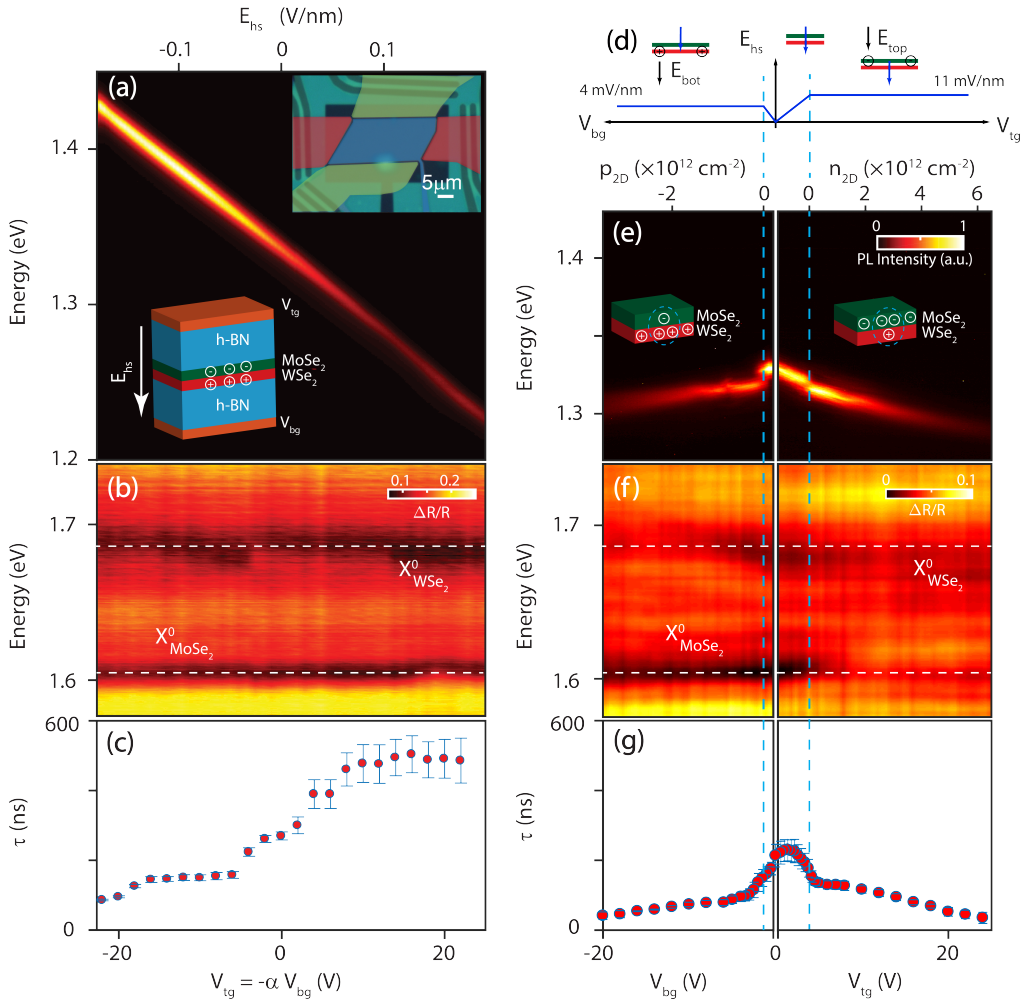

Figure 4.1: Electric field and carrier density control of interlayer excitons. (a) IE PL spectra vs. electric field applied to the heterostructure (E_{hs}). Right inset: optical image of a representative device with the top gates false colored. Left inset: schematic of the heterostructure cross section, showing electrons (holes) accumulate on the $MoSe_2$ (WSe_2) layers, forming IEs. The white arrow represents the positive direction of E_{hs}. (b) Normalized reflectance vs. E_{hs}. (c) IE lifetime τ vs. E_{hs}. Error bars are obtained by adjusting the fitting range. (d) Calculated E_{hs} vs. V_{tg} and V_{bg}. The field E_{hs} remains constant once a given layer is doped. The top cartoons represent the heterostructure for different applied gate voltages. The fields E_{hs} and E_{BN} (electric field on the top and bottom h-BN layers) are depicted as blue and black arrows, respectively. (e) Single gate dependence (V_{tg} or V_{bg}) of the PL shows formation of charged IEs with varying carrier density obtained from the gate operation scheme in (d). Left (right) inset: cartoon of hole (electron)-doped IEs with V_{bg} (V_{tg}). (f) Normalized reflectance vs. carrier density. The horizontal dashed lines in (b) and (f) represent the neutral excitons for WSe_2 ($X^0_{WSe_2}$) and $MoSe_2$ ($X^0_{MoSe_2}$). (g) Neutral and charged IE lifetimes τ vs. carrier density. The vertical light blue dashed lines in (d)–(g) mark the intrinsic region. Data in (e)-(g) were taken in different thermal cycles from (a)-(c). Thus, small shifts in the energy spectrum or lifetime occur owing to different disorder configurations and measurement positions at low temperatures.

citons is strongly suppressed compared to that of IEs in the $WSe_2/MoSe_2$ heterostructure region (see Fig. 2.15(b)), suggesting a fast dissociation of intralayer excitons and an efficient conversion to IEs in this system. We further confirm from the constant normalized reflection $\Delta R/R$ at the intralayer exciton resonances [35,9,107] that our gate operation scheme only varies E_{bs} while keeping the layers intrinsic (Fig. 4.1(b)).

The IEs in the vdW heterostructure can live longer than intralayer excitons thanks to the spatial separation of electrons and holes in the heterostructure. Figure 4.1(c) shows the IE lifetime τ as a function of E_{bs}, measured using time-dependent PL after pulsed laser illumination. We measure the lifetime at low laser power (20 nW) to ensure a single exponential PL decay. The lifetime τ increases as E_{bs} increases, reaching $\approx$ 600 ns for $E_{bs} > 0.1$ V/nm, an order of magnitude larger than in previous studies [13,56]. The observed dependence of τ on E_{bs} can be explained by changes in the overlap between the electron and hole wavefunctions. The lifetime of the interlayer excitons has a strong dependence on the overlap of the electron and hole wavefunctions. The wavefunctions are expected to stretch due to an external electric field, which can be expected to change the tails of the wavefunctions. An electric field anti-parallel to the IE dipole moment is therefore expected to reduce the recombination rate as it pulls the two carriers apart, consistent with our measurements. We note that even a slight change of the tails of the electron and hole wavefunctions is sufficient to significantly affect the IE lifetime owing to the strong localization of the carriers to separate layers. This explains why the IE dipole moment remains constant over the entire range of electric fields, as evidenced by the linear Stark shift, despite the large change in the IE lifetime. Our argument further suggests that a quantitative description of this effect requires an accurate solution of the Bethe-Salpeter equation, which may be the topic of future theoretical studies.

The electrostatic condition in our heterostructures is greatly modified if we change the gate operation scheme such that one of the TMD layers is doped electrostatically, introducing free charge carriers. Figure 4.1(e) shows the IE PL spectrum following the gating scheme depicted in Fig. 4.1(d).

In this scheme, as shown in the normalized reflection $\Delta R/R$ at the intralayer exciton resonances (Fig. 4.1(f)) the carrier density of $MoSe_2$ (WSe_2), n_{2D} (p_{2D}), changes with positive V_{tg} (negative V_{bg}) while the WSe_2 ($MoSe_2$) layer remains intrinsic, keeping E_{hs} constant (Appendix D). We note the normalized reflection spectrum from the top $MoSe_2$ is brighter than that from the bottom WSe_2 due to the dominant direct reflection of the top layer, which provides a simpler normalization scheme. We observe several drastic changes in the IE emission spectrum as V_{tg} (V_{bg}) increases (decreases) and $n_{2D} > 0$ ($p_{2D} > 0$). First, the IE PL peaks exhibit a sudden red shift for n- (p-) doping of $MoSe_2$ (WSe_2). Second, the PL peaks continuously red-shift as doping increases for both n- and p- sides. Note that in this regime, E_{hs} is fixed as discussed above, thus these shifts cannot be explained by the Stark effect. Lastly, the PL intensity diminishes rapidly as doping increases.

Our measurements in the doped regime can be explained by the formation of charged IEs (CIEs) [108]. As shown in the normalized reflection measured with the same gating scheme, we can identify (i) intrinsic/p, (ii) intrinsic/intrinsic, and (iii) n/intrinsic regions by the disappearance of the absorption dips for intralayer excitons in $MoSe_2$ and WSe_2 [109], which are well aligned with the sudden red shift observed in IE PL (vertical dashed lines). Thus, this jump in energy can be related to the CIE. We note that charged excitons can be referred to as trions [43,110,111,112], three-body bound states, or alternatively, attractive polarons, excitonic states dressed by a polarized fermionic sea [48,47], similar to those in monolayer TMDs. The value of the observed jump $\approx$ 10 meV (15 meV) for positive (negative) CIEs is in good agreement with the calculated binding energy of CIEs [108]. The lifetime of CIEs is $\approx$ 100 ns near the band edge, decreasing with increasing doping presumably owing to additional decay channels enabled by scattering with free carriers (Fig. 4.1(g)).

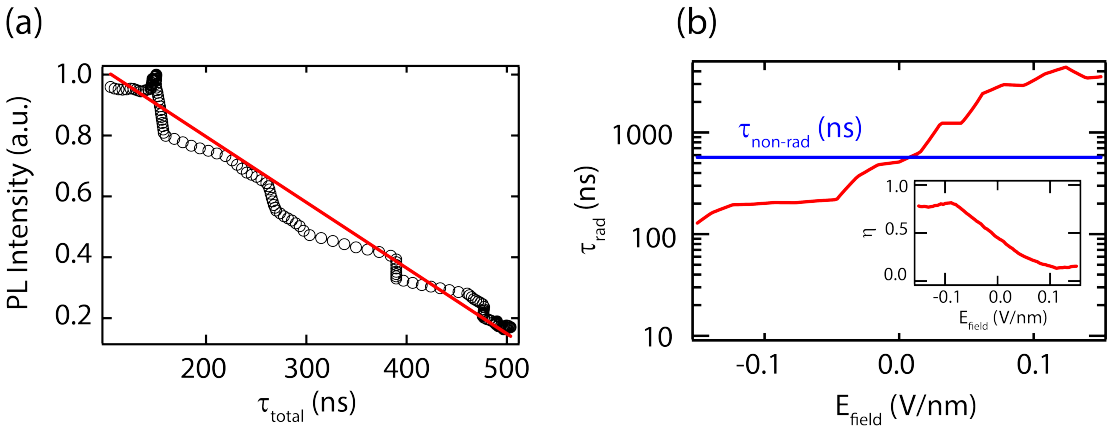

Figure 4.2: (a) I_{PL} vs. lifetime, extracted from Figs. 4.1(a) and 4.1(c) for varying electric fields (E_{bs}). (b) Extracted radiative lifetime (τ_{rad}) and non-radiative lifetime ($\tau_{non-rad}$) vs. E_{bs}. Inset: extracted quantum efficiency (η) vs. E_{bs}.

4.2 Modulating the quantum efficiency

Considering the PL intensity modulation shown in Fig. 4.1(a) together with the measured τ (Fig. 4.1(c)), we demonstrate that the emission efficiency (η) can be tuned with E_{bs}. Based on the definition of quantum efficiency (η) and the total decay rate ($1/\tau_{total} = \gamma_{total} = \gamma_{rad} + \gamma_{non-rad}$):

$$\eta = \frac{\gamma_{rad}}{\gamma_{total}} = 1 - \frac{\gamma_{non-rad}}{\gamma_{total}} = 1 - \gamma_{non-rad}\,\tau_{total}, \tag{4.2}$$

where $\gamma_{non-rad}$ and γ_{rad} are the non-radiative and radiative decay rates, respectively. The quantum efficiency is proportional to the photoluminescence (PL) intensity (I_{PL}) and so we can replace Eq. (4.2) with I_{PL} to get

$$I_{PL} = A(1 - \gamma_{non-rad}\tau_{total}), \tag{4.3}$$

here A is an arbitrary scaling factor and $\gamma_{non-rad}$ is the non-radiative decay rate. Now when applying an electric field, we can tune both the I_{PL} and the τ_{total}. If we plot intensity vs total lifetime (Figure 4.2(a)), we find that the dependence is linear and so the $\gamma_{non-rad}$ can be extracted using Eq. (4.3)

by extrapolating the fit to the limit of $I_{PL} = 0$. We find a non-radiative lifetime of 577 $\pm$ 12 ns. Using the non-radiative decay rate and Eq. (4.2), we extract both the electric field dependent radiative lifetime (Figure 4.2(b)), ranging from 100 ns to 4 μs, as well as the electric field dependent quantum efficiency (Figure 4.2(b) inset). We find that for negative electric fields (E_{bs} is aligned against the IE dipole moment), our radiative lifetime is shorter than the non-radiative lifetime, allowing us to achieve large quantum efficiencies up to $\sim$ 80%. For large positive electric fields (E_{bs} is aligned with the IE dipole moment), our total lifetime plateaus near the non-radiative lifetime (Fig. 4.1(c)) and results in a much lower quantum efficiency.

4.3 Extracting the exciton density

We create high densities of IEs by increasing laser power. In particular, for neutral IEs, we observe that the PL emission is shifted to higher energy with increasing power (Fig. 4.3), consistent with a mean-field shift stemming from the repulsive dipole-dipole interaction between oriented IEs. In the mean-field approximation, where the average distance between the excitons is much larger than the separation between the layers, we use the parallel plate capacitor model to estimate this energy shift[113,114]. Equal number of electrons in one TMD layer and holes in the other layer will create potential difference $\Delta\varphi = \frac{n\,e\,d}{\varepsilon_{TMD}\,\varepsilon_0}$, where n is the interlayer exciton density, e is the electric charge, d is the separation between the layers. Adding one more interlayer exciton will increase the energy by $e\Delta\varphi$, resulting in a "plate capacitor formula",

$$\Delta E = \frac{ne^2 d}{\varepsilon_{TMD}\,\varepsilon_0} \tag{4.4}$$

We can now extract interlayer exciton density:

$$n = \frac{\varepsilon_{TMD}\,\varepsilon_0}{e^2 d}\Delta E \tag{4.5}$$

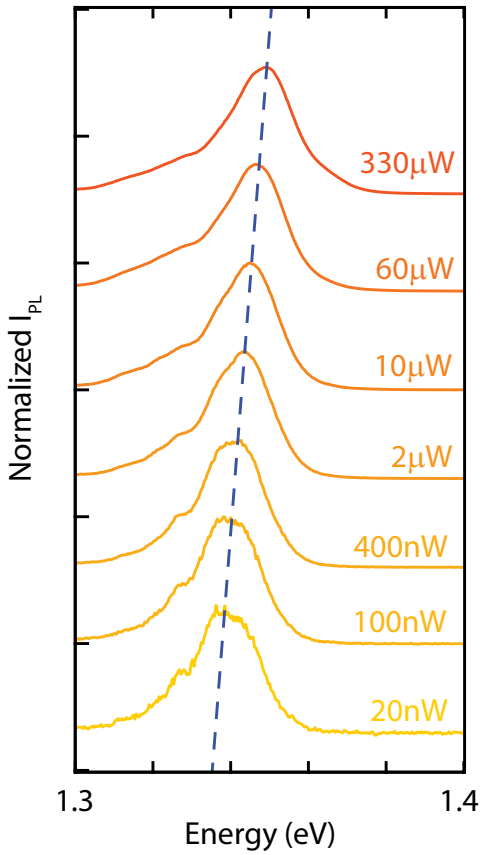

Figure 4.3: Power (P) dependence of the normalized PL spectra collected from the same spot as the excitation. The blue dashed line corresponds to the PL peak position vs. power.

where $d = 0.6$ nm, $\varepsilon_{TMD} = 7.2$, and ΔE is the energy shift from the lowest emission energy. Following the analysis based on a parallel plate capacitance model used for GaAs DQW IEs [113], we obtain a lower bound for the IE density $n \approx 5 \times 10^{11}$ cm^{-2} for $\Delta E = 10$ meV at $P = 1$mW.

The parallel plate capacitor model is known to underestimate the interlayer exciton density because the model does not account for a reduction in interaction energy due to the rearrangement of the interlayer excitons. This reduction in interaction energy as the excitons avoid each other means a higher density of excitons will be required to achieve the same energy shift [115]. However, it should be noted that the model also assumes a linear relation of energy shift and interlayer exciton density,

which may break down when the exciton separation approaches the layer separation. The Mott critical density of interlayer excitons has been predicted to occur around $\sim 4\times10^{12}$ cm^{-2} based on the critical ratio of the exciton size and inter-exciton distance of 0.3, taking into account valley degeneracy[73]. These considerations allow us to provide a lower and upper bound for the interlayer exciton densities.

4.4 Long-range interlayer exciton diffusion

The high density of long-lived IEs and the large τ observed in our heterostructures can enable transport of IEs across the samples. Figures 4.4(a)-(c) show the spatial map of the IE PL intensity at different laser powers. The PL signal can be detected far away from the diffraction-limited focused laser spot ($< 1\mu$m in diameter). At the highest power, PL can be observed many microns away from the excitation spot, strongly suggesting transport of IEs across the sample. From these maps, we obtain the normalized, radially-averaged PL intensity, $I_{PL}^{norm}(r)$, where r is measured from the center of the diffraction-limited steady state laser spot. Here, the PL intensity is normalized by the value obtained at $r = 0$. As shown in Fig. 4.4(d), away from the laser spot, $I_{PL}^{norm}(r)$ decreases rapidly as r increases. We note, however, that at a given r, $I_{PL}^{norm}(r)$ increases with P even at a position far away from the laser spot. The characteristic length L_D for the decaying behavior of $I_{PL}^{norm}(r)$ can be obtained from fitting

$$I_{PL}^{norm}(r) \sim \frac{1}{\sqrt{r/L_D}} e^{-r/L_D} \tag{4.6}$$

away from the laser excitation spot (dashed lines in Fig. 4.4(d)), following the 2D diffusion model with a point source (Appendix E.1). As shown on the left axis of Fig. 4.4(f), we find that L_D increases as P increases, suggesting increased diffusion at high IE density possibly due to exciton-exciton interactions.

We also measured the temporal decay of the PL intensity using a diffraction-limited focused pulsed laser. Figure 4.4(e) shows an estimate of the time-dependent exciton population (integrated PL signal

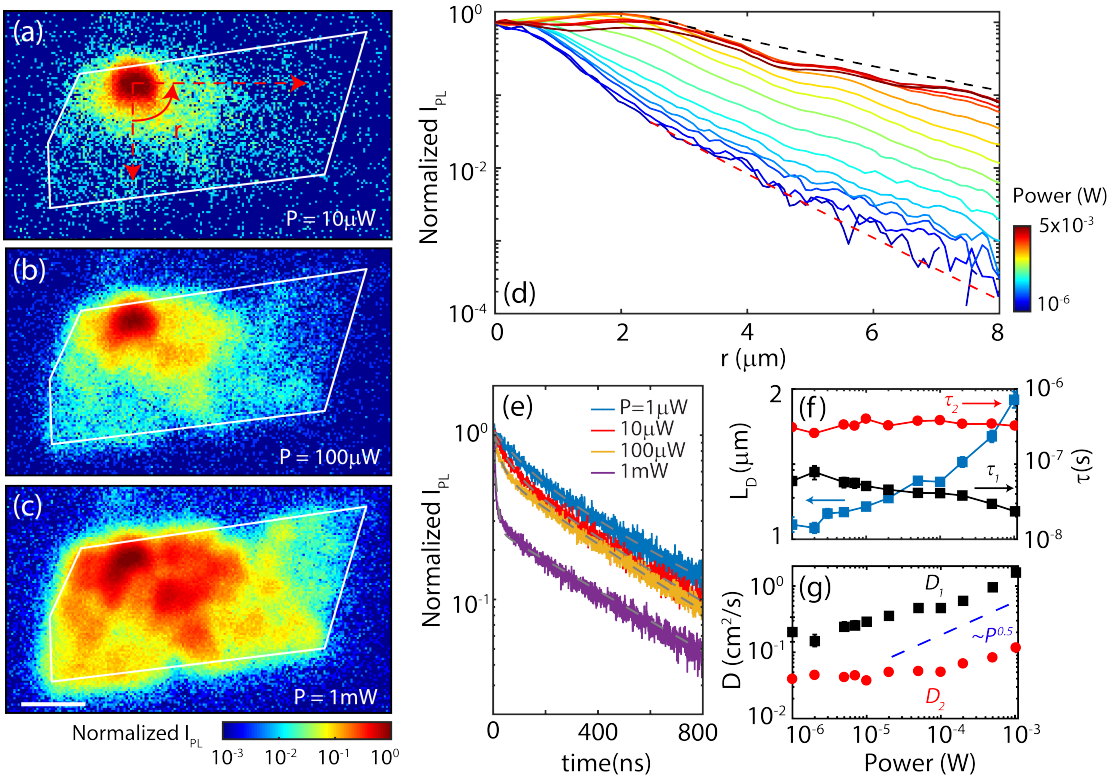

Figure 4.4: Power dependent diffusion of neutral interlayer excitons. (a)-(c) Spatial dependence of the intensity of the normalized PL for P = 10, 100, and 1000 μW, respectively. The white lines depict the heterostructure area. The continuous wave laser excitation (λ = 660 nm) is fixed at the top left of the sample. The scale bar corresponds to 5 μm. All the measurements were performed at 4 K. The red curve and the dashed lines represent the radial averaging. (d) Power dependence of normalized radially averaged I_{PL} (normalized I_{PL}) vs. r with the excitation fixed at the center of the sample. The red and black dashed lines represent $e^{-r/L_D}/\sqrt{r/L_D}$ for L_D = 1.1 and 3.2 μm, respectively, where L_D is the diffusion length. (e) Time-dependent PL normalized at t = 0 for different ON powers P. For this measurement we use a pulsed 660 nm diode laser with a 100 kHz repetition rate and 1μs ON time. The power we quoted is the ON power or peak power. Dashed gray lines correspond to double exponential fits. (f) L_D vs. P extracted from the data in (d). Right axis: lifetime (τ) vs. P with two values of τ extracted from the double exponential decay fit. (g) Diffusion constant ($D = L_D^2/(\tau)$) vs. P extracted from (h) using the two different values of τ. Dashed line corresponds to $D \sim P^{1/2}$, expected from the non-linear diffusion model (Appendix E.1).

along the heterostructure weighted by r^2) after a laser pulse with peak power P. The time-dependent PL exhibits a faster decay process with characteristic time scale $\tau_1 \sim 10$ ns initially, followed by a slower decay process occurring on the time scale $\tau_2 \sim 100$ ns, suggesting that there are two different mechanisms for the PL intensity decay. The value of L_D estimated above can be converted to a diffusion constant according to $D = L_D^2/\tau$. Two values D_1 and D_2 are obtained using the short (τ_1) and long (τ_2) decay times, respectively (Fig. 4.4(g)). Because our lifetime measurement uses a pulsed laser where the interaction driven IE diffusion occurs just after the pulse is off when the IE density remains high, τ_1 could be more relevant for the IE diffusion than τ_2. The value of L_D, however, measured in steady state, would be dominated by τ_2. Figure 4.4(g) shows that D_2 is in the range of $0.01 - 0.1$ cm^2/s, whereas D_1 changes from 0.1 to 1 cm^2/s. Both D_1 and D_2 are increasing with increasing P, providing upper and lower bounds for non-linear IE diffusion caused by dipolar repulsive interaction (Appendix E.1), respectively.

Similar maps can be taken while changing E_{bs}. Figures 4.5(a)-(b) shows spatial maps of the IE PL intensity for $P = 1$mW for the two extremes in E_{bs} where we observe a stark change in the PL intensity distributions. We take the same radial averaging as Fig. 4.4(d) and show $I_{PL}(r)$ at various E_{bs} (Fig. 4.5(c)), where r is the radial distance from the excitation spot. We observe that $I_{PL}(r > 2\,\mu\text{m})$ is larger with increased E_{bs} (increased τ), while at the excitation spot $I_{PL}(r = 0)$ reduces with increasing E_{bs} (as extracted in Fig. 4.2(a)). The increase of $I_{PL}(r)$ away from the excitation spot confirms that we are increasing the density of IE at the excitation spot and therefore IE move away from larger density areas. In contrast, if we would be observing the tail of a non-Gaussian shaped laser excitation, the $I_{PL}(r)$ across the sample should be modulated proportionally with the $I_{PL}(r = 0)$ at the excitation spot. The latter observation is consistent with exciton transport, as longer-lived IEs may travel farther. Additional measurements of IE diffusion at higher temperatures show a smaller spatial extension of PL around the excitation (Fig. F.1). While the single particle diffusion constant is expected to rise as a function of temperature, a sharp decrease in lifetime has been shown at temperatures above 50 K[116],

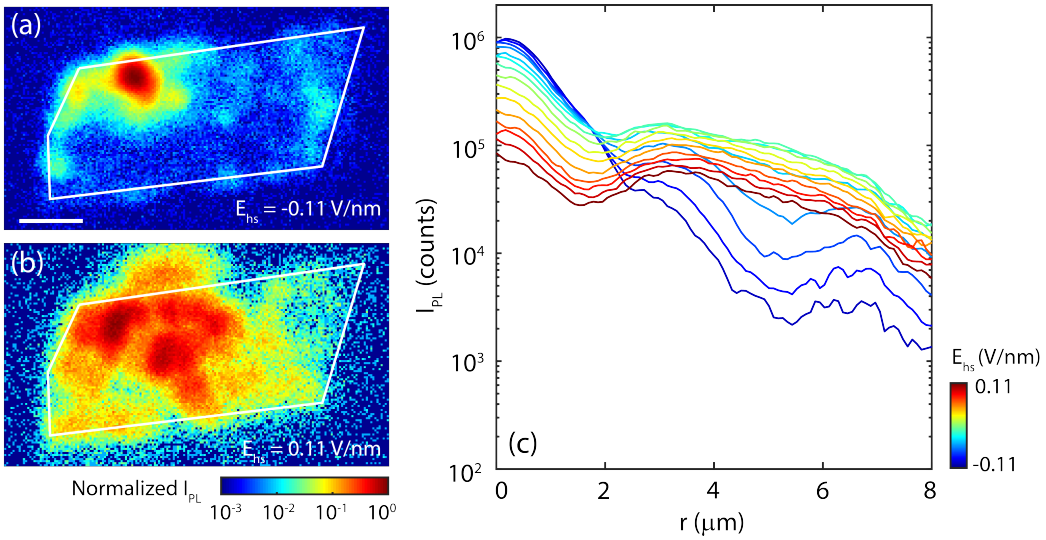

Figure 4.5: Electric field dependent diffusion of neutral interlayer excitons. (a)-(b) Spatial dependence of the intensity of the normalized PL for E_{hs} = -0.11 and 0.11 V/nm. The white lines depict the heterostructure area. The continuous wave laser excitation (λ = 660 nm) is fixed at the top left of the sample. The scale bar corresponds to 5 μm. (c) E_{hs} dependence of radially averaged I_{PL} vs. r with the excitation fixed at the center of the sample.

which can explain the change in diffusion behavior. These measurements provide additional support for an exciton transport mechanism.

We obtain further evidence for IE transport from time-dependent spatial PL maps with a pulsed laser illuminating the center of the sample. We measure the IE PL intensity $I_{PL}(r,t)$ as a function of distance r (referenced to the laser illumination spot) and time t (referenced to the falling edge of the laser pulse). Figures 4.6(a) and (b) show the normalized time-dependent PL, $I_{PL}^{norm}(r,t) = \frac{I_{PL}(r,t)}{I_{PL}(r=0,t)}$ at different laser peak powers. The time-dependent root-mean-square radius, $r_{rms}(t) = \sqrt{\langle r^2 \rangle}$, computed from $I_{PL}^{norm}(r,t)$ (white lines) increases rapidly when the laser is on, reaching a steady state within $\sim$ 200 ns. Interestingly, $r_{rms}(t)$ increases again rapidly within 100 ns after the laser is turned off. Although the observed two decaying time scales and the dynamics of IEs can be explained by the diffusion of IEs driven by interaction and their recombination, we also note that an alternative scenario involving the diffusion of photoexcited free carriers [117] is also possible [14]. Future experimental stud-

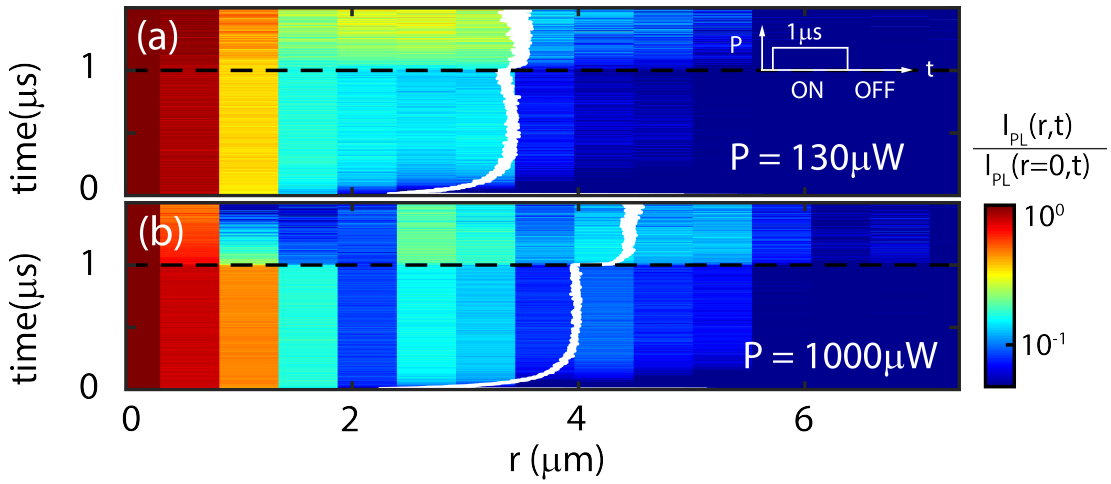

Figure 4.6: Time-dependent spatial photoluminescence (PL). (a)-(b) Normalized I_{PL} vs. time and distance from the laser spot. $I_{PL}(r,t)$ was estimated by averaging over a line cut through the laser spot. We normalize I_{PL} at each time by $I_{PL}(r,t)/I_{PL}(r=0,t)$. Overlaid white lines represent $\sqrt{\langle r^2 \rangle}$ obtained from the experimental PL map assuming rotational symmetry of the sample. Top right inset: The pulsed laser diode is turned ON at t = 0 μs with powers of 130 μW (a) and 1000 μW (b) and turned OFF at t = 1 μs (also marked with dashed black lines).

ies using spatially resolved resonant excitation of IEs can be potentially utilized to distinguish these scenarios.

4.5 Electrically driven charged interlayer exciton diffusion

Unlike the neutral IEs discussed above, CIEs can be manipulated by an in-plane electric field (V_{ds}). We aim to keep the carrier density the same as we change the in-plane electric field, but observe the undoped regime shifts in the PL spectra with applied V_{ds} vs either V_{tg} or V_{bg} (Figures 4.7). We maintain the same carrier density for the different V_{ds} by compensating with either the V_{bg} or V_{tg} for the p-type or n-type CIE, respectively. We, thus, apply $V_{bg} = 2.13V_{ds} - 5\text{V}$ and $V_{tg} = 1.6V_{ds}$ for the p-type and n-type CIE, respectively.

Figure 4.8(a) shows the spatial map of I_{PL} overlaid with the device image when CIEs are optically excited at the center of the sample ($V_{ds} = 0$ V, $V_{bg} = -5$ V). Similar to neutral IEs, CIEs generated

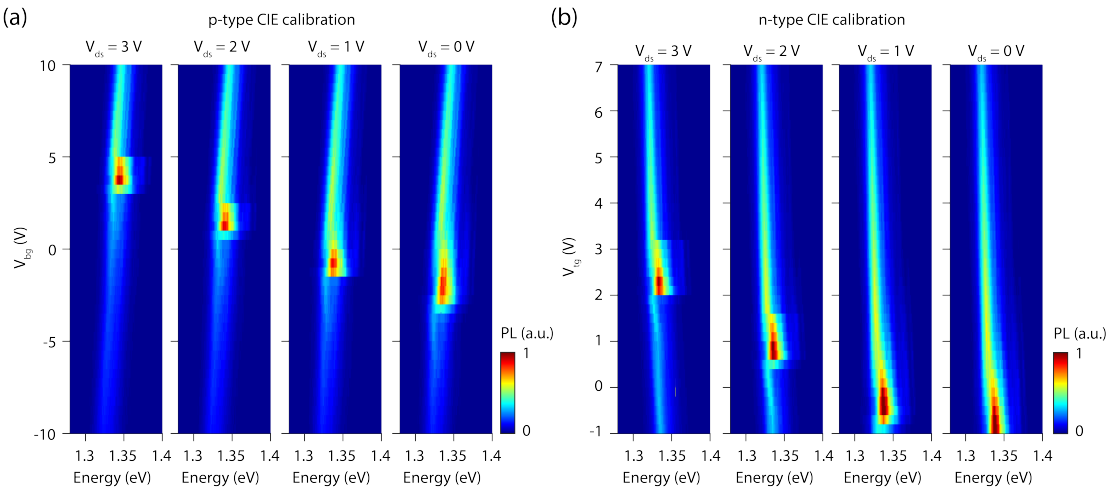

Figure 4.7: (a) PL spectra taken near the center of the sample with P = 500 μW as a function of V_{ds} (applied in the left to right sample direction) and V_{bg}. Note that the interlayer exciton regime shifts with V_{ds}, requiring an adjusted V_{bg} to maintain the same doping in the sample for the p-type CIEs. (b) Same as (a) but for V_{ds} and V_{tg} to calibrate the n-type CIEs.

at the laser illuminated spot can diffuse across the entire sample. We note that both the WSe_2 and $MoSe_2$ layers in our device have multiple electrical contacts away from the heterostructure edge ($\sim$ 10 μm away) that are used to control the lateral electric field while avoiding any local Schottky barrier effects. Figure 4.8(b) shows the spatial map of the PL intensity normalized as $I_{PL}(V_{ds})/I_{PL}(V_{ds} = 0)$ when applying a bias voltage of $V_{ds} = 3$ V across the WSe_2 layer. We observe that the grounded edge of the sample becomes brighter with increasing V_{ds} (also see Fig. 4.8(c) for the normalized average emission intensity along the heterostructure channel). This increase in PL at the boundary between the heterostructure and highly-doped monolayer region can be explained by drift of CIEs under the applied bias voltage in the channel. The applied bias V_{ds} creates an electric field to tilt the band structure in the direction of the WSe_2 channel, driving positive (+) CIEs along the same direction as shown in the schematic diagram in Fig. 4.8(d). At the boundary of the heterostructure, however, the +CIE cannot be transported to the WSe_2 p-channel because current across the boundary must be preserved. Therefore, the transported +CIEs recombine to turn into a hole in the WSe_2 p-channel. In Figs. F.2

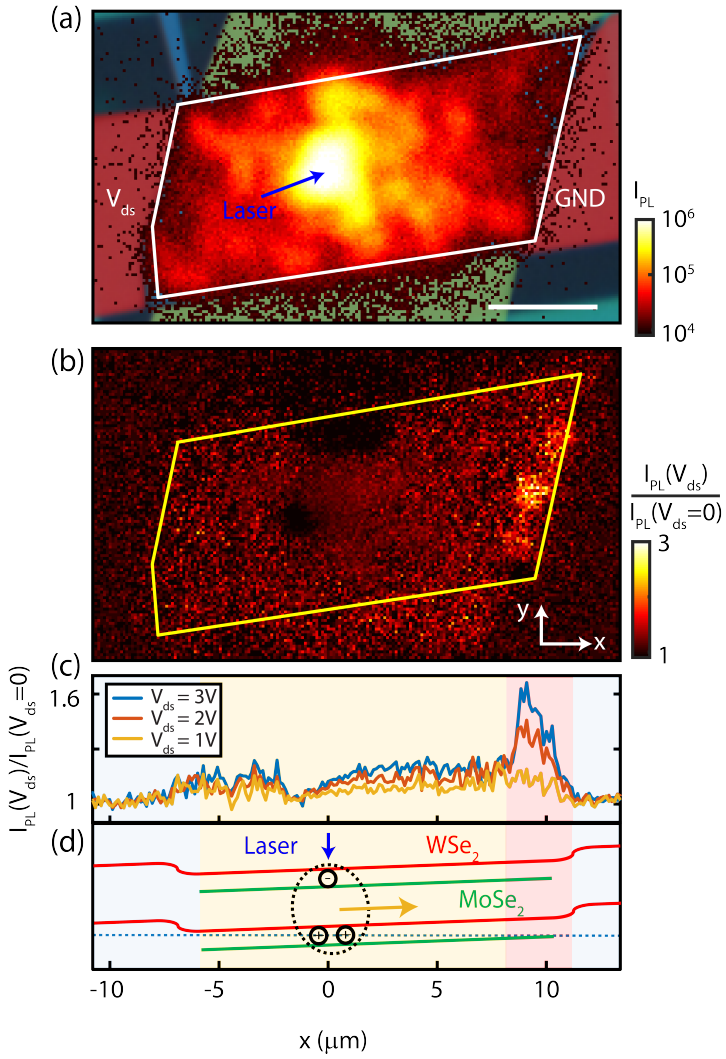

Figure 4.8: Spatial control of charged interlayer excitons. (a) Spatial dependence of I_{PL} with the laser excitation fixed at the center of the heterostructure (arrow). An optical image of the device with false colored top gates that cover the WSe_2 and $MoSe_2$ contacts is overlaid. An in-plane electric field is applied by a voltage in one of the WSe_2 contacts (V_{ds}) while keeping the other contact grounded. (b) Spatial dependence of I_{PL} normalized according to $I_{PL}(V_{ds})/I_{PL}(V_{ds}=0)$ for $V_{ds}=3$ V. We observe a larger population of charged IEs near the right WSe_2 electrode by increasing V_{ds}. The yellow arrow in (d) represents the current direction. (c) Normalized I_{PL} averaged over the y-axis vs. x (depicted in (b)) for different V_{ds}. (d) Schematic of the heterostructure bands with applied V_{ds}. The red (green) bands correspond to WSe_2 ($MoSe_2$). A positive V_{ds} is applied, while the chemical potential (indicated by a blue dotted line) is kept inside the WSe_2 valence band to form positively charged IEs. Under positive V_{ds}, the CIEs drift towards the grounded contact. The emission mainly occurs near the grounded contact, because the charged exciton cannot move beyond the heterostructure.

and F.3, we further confirm this picture of CIE transport by changing the doping polarity and V_{ds} direction.

We note that the observed experimental evidence can be due to a few alternative mechanisms such as free carriers aiding the transport of the CIEs or the CIEs upconverting to IEs while traveling towards the edge of the heterostructure. Additionally, thermal gradients and coupling to phonons may also play an important role for CIE diffusion in TMDs as described in reference[29]. Further experiments such as pump-probe measurements and systematic photocurrent measurements might be required for clarification in a future study.

4.6 Electrically generated interlayer excitons

Finally, we demonstrate the electrical generation of IEs by free carrier injection using Ohmic contacts in individual TMD layers. Because our heterostructure forms type-II aligned *p*- and *n*- layers, the charge transport across the WSe_2 to $MoSe_2$ is expected to show diode-like rectifying behaviors[78,12]. Figure 4.9(a) shows interlayer current (I_{ds}) versus interlayer bias (V_{ds}) curves, whose characteristic can be modulated by V_{tg} and V_{bg}. Changing (V_{tg}, V_{bg}) adjusts the band offset in the type-II heterojunction and their filling. The inset to Fig. 4.9(a) shows a map of the forward bias current at a fixed bias voltage. One can identify the region in which both WSe_2 and $MoSe_2$ layers remain intrinsic, consistent with the absorption spectrum discussed in Fig. 4.1. Interestingly, we find that this p-n device generates detectable electroluminescence (EL) at sufficiently high bias. A particularly interesting EL condition occurs when both TMD layers are intrinsic, thus, allowing electrons and holes to recombine through the formation of IEs. Figures 4.9(b) and (c) show the EL maps of the heterostructure region. The local EL intensity in the heterostructure depends on the local recombination current density, which can be controlled by (V_{tg}, V_{bg}) (Fig. F.4).

We find that the EL spectrum resembles the PL spectrum in the same (V_{tg}, V_{bg}) configuration[78].

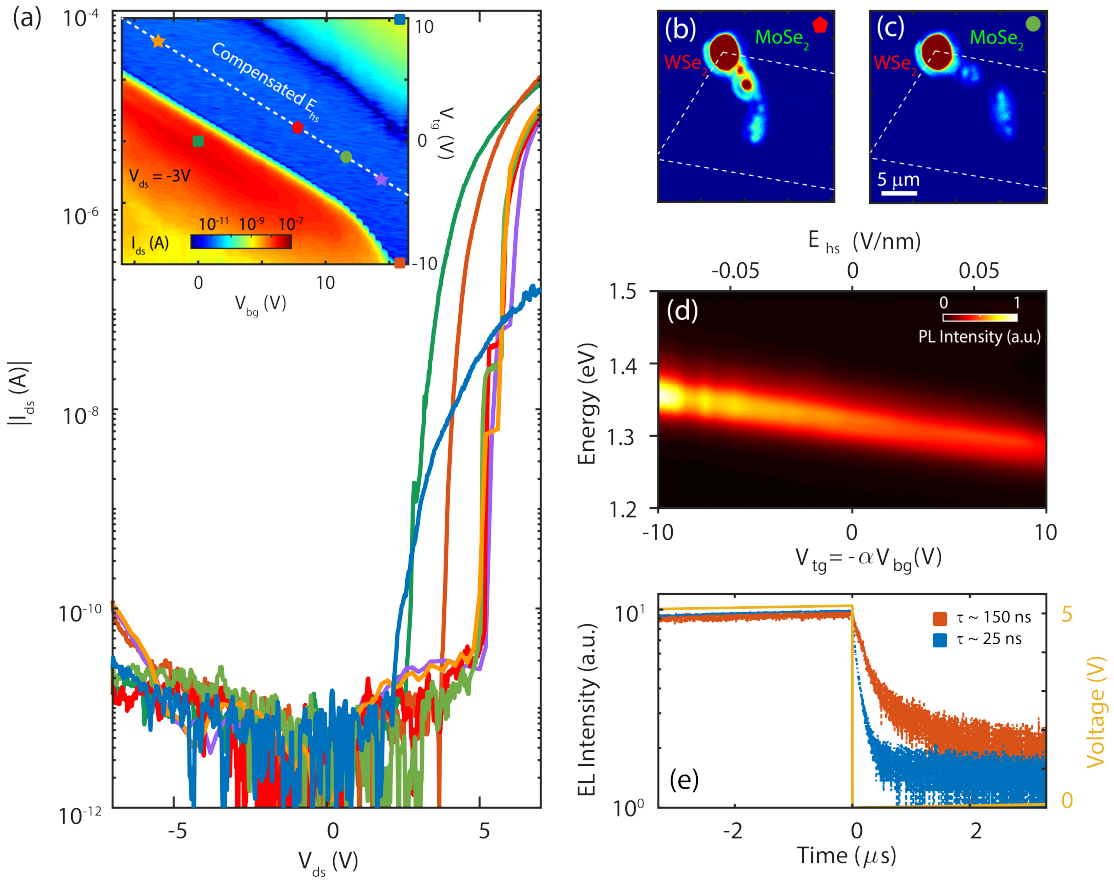

Figure 4.9: Electrical generation of interlayer excitons. (a) I-V curves at various top (V_{tg}) and bottom (V_{bg}) gate configurations with corresponding indicators in the inset. Inset: Ids vs. V_{tg} and V_{bg} (with $V_{ds} = -3$ V on $MoSe_2$ and grounded WSe_2). The white dashed line represents the compensated electric field where $V_{bg} = 10.37$ V - αV_{tg}. The markers represent the gate voltages used in (a)-(c) and (e). (b)-(c) are spatially dependent electroluminescence (EL) maps for $V_{tg} = -1$ V (1 V) and $V_{bg} = 12$ V (8.75 V) at $V_{ds} = 7$ V, respectively. The white dashed lines indicate the heterostructure area. (d) Electric field (E_{hs}) dependence of the interlayer exciton EL. The electron-hole separation ($d \approx 0.55$ nm) obtained from the slope agrees reasonably with the electron-hole separation extracted from PL. (e) Time-dependent EL intensity for two different gate configurations: blue (orange) curve uses $V_{tg} = 10$ V (-10 V) and $V_{bg} = 16.28$ V. The yellow line represents the pulsed sawtooth voltage applied to V_{ds}. The measured EL lifetime is gate-tunable, as in the PL case, and of comparable magnitude to the PL lifetime.

Figure 4.9(d) shows EL vs. E_{bs}. Similar to the PL shown in Fig. 4.1(a), the EL spectrum shifts linearly with E_{bs}, which can be attributed to the IE Stark effect. More direct evidence that the EL process in our heterostructure is mediated through the IE formation by carrier injection is provided by the EL lifetime. Figure 4.9(e) shows the EL intensity as a function of time when we pulse V_{ds} at a fixed (V_{tg}, V_{bg}). We measured the EL at the falling edge of the pulse. Long and short lifetimes of $\approx$ 150 ns and $\approx$ 25 ns were obtained for the gate voltages of $V_{tg} = 10$ V and -10 V with $V_{bg} = 16.3$ V, corresponding to the neutral IE and charged IE formation regime, respectively (see Fig. 4.9(a) inset). We note that the measured EL lifetime is much longer than the RC time ($\tau_{RC} < 10$ ns) of the biasing pulse.

Our initial EL experiments showed tunable emission and demonstrations of the interlayer exciton nature in a *p-n* diode, but further EL experiments are performed in the later chapters of this thesis. In Chapter 6, we will show tunability between singlet and triplet excitons. In Chapter 8, a more fundamental understanding of the forward-bias current and EL emission will be revealed, where V_{ds} and the gate voltages are carefully tuned to match electron and hole densities.

4.7 Conclusion

The electrical generation of long-lived interlayer excitons provides an electrically driven near-infrared light source with an energy tunability that ranges over several hundreds of meV and spatial control of the emission. Achieving high density IEs without optical excitation could pave a way to realize quantum condensates in solid-state devices. Large valley polarization [56,118] strongly coupled to the spin may also lead to optoelectronic devices based on electrically driven CIEs. The spin degree of freedom in such devices could be potentially utilized for both classical and quantum information processing.

Quantum theory thus reveals a basic oneness of the universe.

Fritjof Capra

5

Gate-defined Interlayer Exciton Traps

Optically generated excitons, bound pairs of excited electrons and holes, in monolayer transition metal dichalcogenides (TMDs) are an exciting system for exploring two-dimensional (2D) bosonic gases because of their large binding energies [30] and spin-valley locking properties [119,18]. In type-II TMD van der Waals (vdW) heterostructures, the energetically favorable interlayer exciton (IE), where the electron and hole are localized on separate lay-

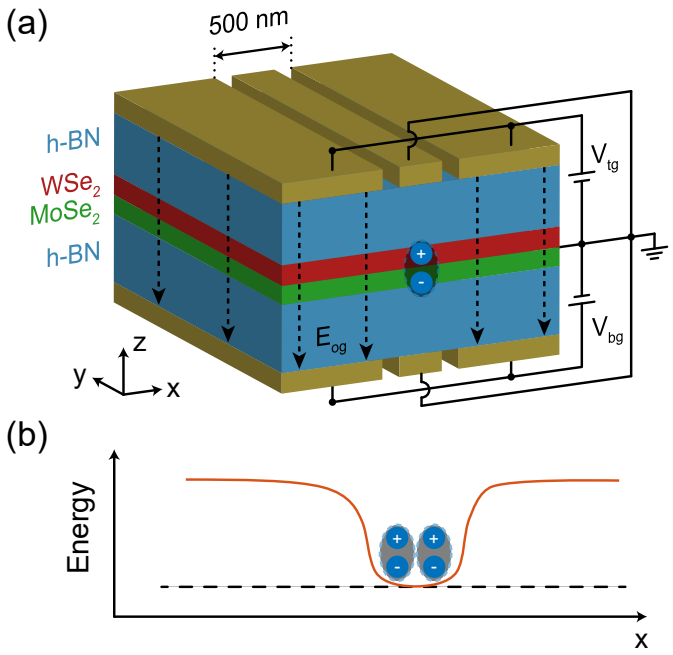

Figure 5.1: Concept for the interlayer exciton traps (a) Device schematic showing the wire gate and large outer gates on either side. V_{tg} and V_{bg} are applied to create electric fields in the outer gate (E_{og}) regions while the wire gates kept grounded. (b) Interlayer exciton (IE) energy schematic as a function of x position perpendicular to the wire gate. The red (black dashed) curves represent the electric field profile felt by the IEs with (without) E_{og}.

ers, forms with a permanent out-of-plane dipole moment[14,77,13,120], extended lifetime[14,57,63], and long diffusion lengths[14,76,120], while maintaining large excitonic binding energies[74,121,73]. Their long lifetimes allow for the generation of high densities of IEs, which have been shown in GaAs double quantum wells (DQW) to condense into a degenerate exciton gas[81,82,122] or undergo a Mott transition[123,124,125]. In TMD heterostructures, the large binding energies also allow for much larger densities before dissociating upon reaching the Mott density[73,63,126]. The large exciton mass combined with larger sustainable densities could be used to realize high-temperature condensates that are electrically tunable[73,66,67]. In order to sweep over the substantial range of exciton densities though, large laser excitation powers are required, leading to heating or non-linear Auger recombination that compete unfavorably with the exotic IE phases[127,128]. Electrostatic traps can be a useful tool for "collect-

ing" the diffusive excitons away from the laser excitation spot, allowing the generation of cold high density IE systems and removing local laser-induced coherence effects that can hinder the unambiguous identification of a condensate[82].

In this chapter, we design a multi-gated structure to create electrostatic traps that allow us to generate high densities of IEs. Figure 5.1(a) shows a schematic of the device design. A high-quality, h-BN encapsulated $MoSe_2/WSe_2$ heterostructure is fabricated with matching top and bottom metal gates (detailed images in the Section 5.1). The IE energy in the trap area can be controlled by a matching set of wire gates (width of $\sim$ 250 nm) that are kept grounded. On either side of the wire trap, there are two sets of top and bottom gates (separation width of $\sim$ 500 nm) that control the IE energy in the outside region. By applying voltages on the outer gates, we create an electric field in the neighboring area,

$$E_{og} = \frac{\varepsilon_{hBN}}{\varepsilon_{TMD}} \cdot \frac{V_{tg} - V_{bg}}{t_{total}}, \tag{5.1}$$

where ε_{hBN} and ε_{TMD} are the h-BN and TMD dielectric constants, V_{tg} and V_{bg} are the top and bottom gate voltages, and t_{total} is the total h-BN thickness. Applying positive E_{og} raises the IE energy in the outer gate region due to the linear Stark effect in IEs[14,77,13,120]. This creates a trapping potential so that a high density of IEs can accumulate in the trap without escaping (Fig. 5.1(b)).

5.1 One-dimensional exciton traps

Figure 5.2(a) shows our h-BN encapsulated $MoSe_2/WSe_2$ heterostructure with electrical contacts to each layer. In order to create the trapping potentials in our device, we need to fabricate matching top and bottom gates. We write and evaporate the bottom gates following the PdAu gate recipe (Appendix A.2.3) and use scanning electron microscopy (SEM) to characterize the gate separations. Although designed for 300 nm wire gate width, the most reliably flat bottom gates had 250 nm gate width. Any wider wire gate width or narrower separation between the wire gates and outer gates usually resulted

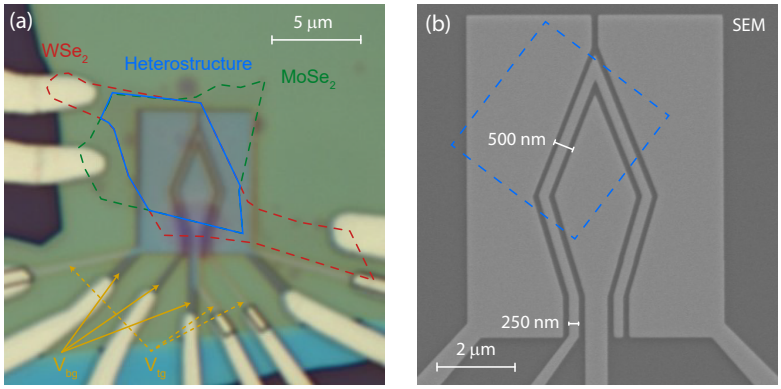

Figure 5.2: (a) Optical image of the device. Red and green dashed lines outline the WSe_2 and $MoSe_2$ regions, respectively. Blue line outlines the heterostructure region. Gold arrows identify the relevant top gate and bottom gate structures. (b) SEM image of the Cr/PdAu bottom gates with the wire gate width and outer gate widths identified. The red dashed square indicates the approximate location for the PL diffusion measurements.

in a failed liftoff. The matching top gate is fabricated after the heterostructure is placed down. Since both use the same alignment marks and use electron beam lithography, the margin for alignment error is quite small. However, since the image is aligned optically, there can be small offsets, which cause some effects that we discuss later in our diffusion measurements and in Appendix E.2.

5.2 Spatial energy modulation

We demonstrate our gate modulated trapping potential by performing scanning photoluminescence (PL) spectroscopy at various E_{og} across the wire gate region (details in Appendix B). All PL measurements are performed at $T = 4$ K, unless otherwise stated, and with an excitation wavelength of 660 nm (1.87 eV) with a diffraction limited spot. In Figure 5.3(a), we measure the PL spectra with a power (P) of 50μW at the edge of the wire gate as a function of E_{og}. As E_{og} increases, two peaks emerge, with only the higher energy peak shifting linearly with the applied external field. We extract a dipole separation of $d \approx 0.6$nm from the slope of the shift ($\Delta E = e\vec{d} \cdot \Delta\vec{E_{og}}$, where ΔE is the energy shift and e is an elementary charge), matching the expected interlayer separation between the electron and hole wavefunctions in the TMD layers. In Figures 5.3(b)-(c), we excite the heterostructure with $P = 500\mu$W at

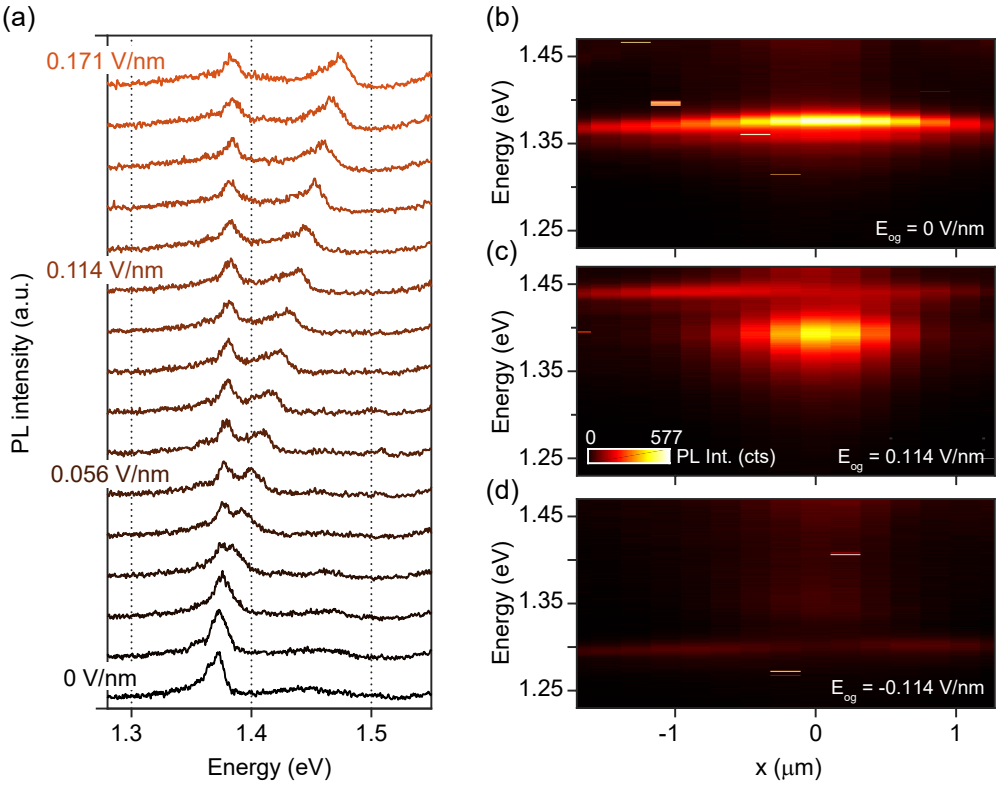

Figure 5.3: Modulating the interlayer exciton energy with electric fields (a) IE emission as a function of E_{og}. The linearly shifting peak at higher energy is from the outer gate region while the lower energy peak is from within the wire gate region. (b)-(d) Scanning PL spectroscopy, where the laser excites at $x = 0\mu$m and the spectra is collected across the wire gate at E_{og} =0, 0.114, and -0.114 V/nm, respectively, showing spatially modulated IE energy.

the wire gate location ($x = 0$) and measure the PL spectra across wire gate (x as shown in Fig. 5.5(a)) for two representative electric fields, $E_{og} = 0$ V/nm and 0.114 V/nm. When $E_{og} = 0$ V/nm, the PL emission energy is constant at $\sim$ 1.38 eV across the spatial linecut, matching the expected electric field profile. When $E_{og} = 0.114$ V/nm, the PL energy in the outer gate region is elevated to $\sim$ 1.44 eV, matching the gate dependent spectra, while the wire gate region still displays emission at a lower energy. Thus, we conclude the higher energy peak originates from IEs outside of the trap, and we can identify the lower energy peak as the trapped IEs (IE_{trap}). Independent of the trapping potential, we notice that the high-energy free IE emission extends out almost 3 μm from the wire. This is due to

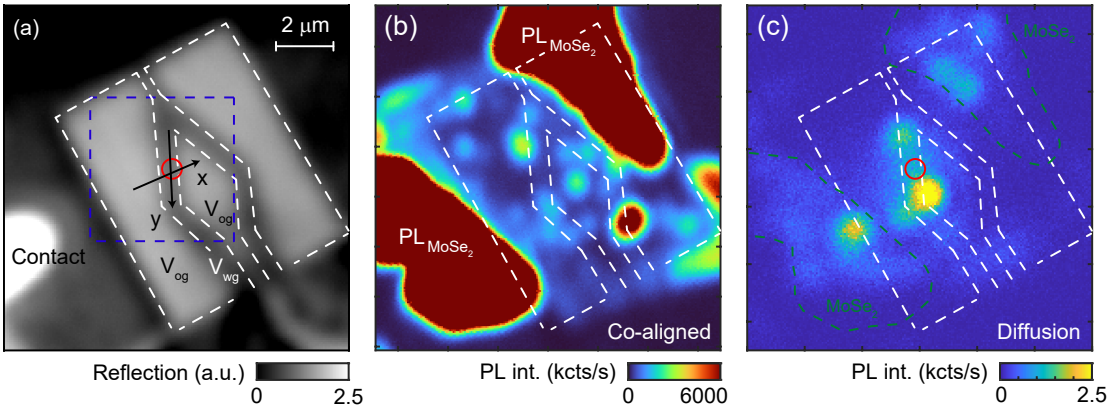

Figure 5.4: (a) Reflection image of the device over larger scanning range. The outer gate and the wire gate areas are outlined (white dashed line) and labeled V_{og} and V_{wg}, respectively. Black arrows indicate positive x and y direction for line cuts. Red circle indicates the excitation spot for diffusion measurements. The blue dashed square shows the region of interest in Fig. 5.5(a)-(c). (b) Co-aligned PL measurements without filtering for interlayer exciton emission. Bright regions on the top and bottom areas are from the monolayer $MoSe_2$ regions. (c) Diffusion map at $E_{og} = E_{wg} = 0$ V/nm on a larger scale.

dipole-dipole interactions and the resulting long diffusion lengths exhibited by IEs in TMDs [14]. However, we note that the high-energy emission is darker when the trapping potential is active, hindering the IE diffusion perpendicular to the trap, while favoring localization in the wire. We also demonstrate anti-trapping potential shapes where the emission is significantly darker because the IEs quickly diffuse away from the excitation spot (Fig. 5.3(d)).

5.3 Shaping the exciton diffusion

We show representative scanning maps over a larger range of the sample. Figure 5.4(a) shows a reflection scanning map, where the entire sample is flooded with a broadband white light lamp. We can see the strong reflection from the outer gate regions and the contacts. The wire gate is harder to see given the size (250 μm) is smaller than the diffraction limit. In this image, we also indicate the x and y directions used for defining the x and y line cuts (discussed later in this section). The blue dashed square indicates the area of this larger image that is used in Figures 5.5(a)-(c). Figure 5.4(b) is a co-

aligned scanning photoluminescence (PL) map over the same area. We can see there are brighter and darker regions on the sample, creating a natural landscape. The PL counts in this measurement do not filter the intralayer excitons which are brighter in comparison to the interlayer exciton emission, hence the bright, saturated regions in the upper right and and lower left of the sample. Figure 5.4(c) shows the diffusion map at $E_{og} = E_{wg} = 0$ V/nm over the same larger region. The diffusion of IEs is mostly localized to the trap area, near the excitation spot. We also note that bright emission appears in the monolayer region. This behavior is similar to the IE diffusion behavior observed in a room temperature exciton switch[76].

To further understand the diffusive behavior when forming a trapping potential, we take PL intensity maps at the IE energy. Figure 5.4(a) shows a reflection image of the sample, where the outer gate regions (V_{og}) and the wire gate region (V_{wg}) are labeled. Figures 5.5(a)-(c) show diffused IE PL emission for anti-trap, flat, and trapping potential when the heterostructure is excited at the wire gate with $P = 550$ μW (red circle). For $E_{og} = -0.023$ and 0 V/nm, we observe emission around the laser spot size, but also at naturally occurring bright spots on the sample. In the absence of the externally applied trapping potential, the IEs diffuse and localize in these naturally-occurring trap sites (Figs. 5.4(b)-(c)). However, when we apply $E_{og} = 0.114$ V/nm, we observe uniform and elongated emission along the wire gate, implying that the IE diffusion is constrained along the wire gate. In Figure 5.5(d), we take take line cuts along x of the normalized PL emission, averaged across the uniform area between the natural bright spots, as a function of E_{og}. We observe a narrowing of the spatial IE cloud width when the trapping potential is active, and broadening when the an anti-trap is created. We show characteristic line cuts along the red, black, and yellow dashed lines in Figure 5.5(e), which clearly show the spatially narrowed (broadened) distribution for $E_{og} = 0.114$ V/nm (-0.023 V/nm) when compared to 0 V/nm.

We perform similar linecuts along the wire gate (y as shown in Fig. 5.4(a)) to quantify when the IE PL intensity becomes uniform in the trap. Figure 5.6(a) shows linecuts, averaged perpendicular to the

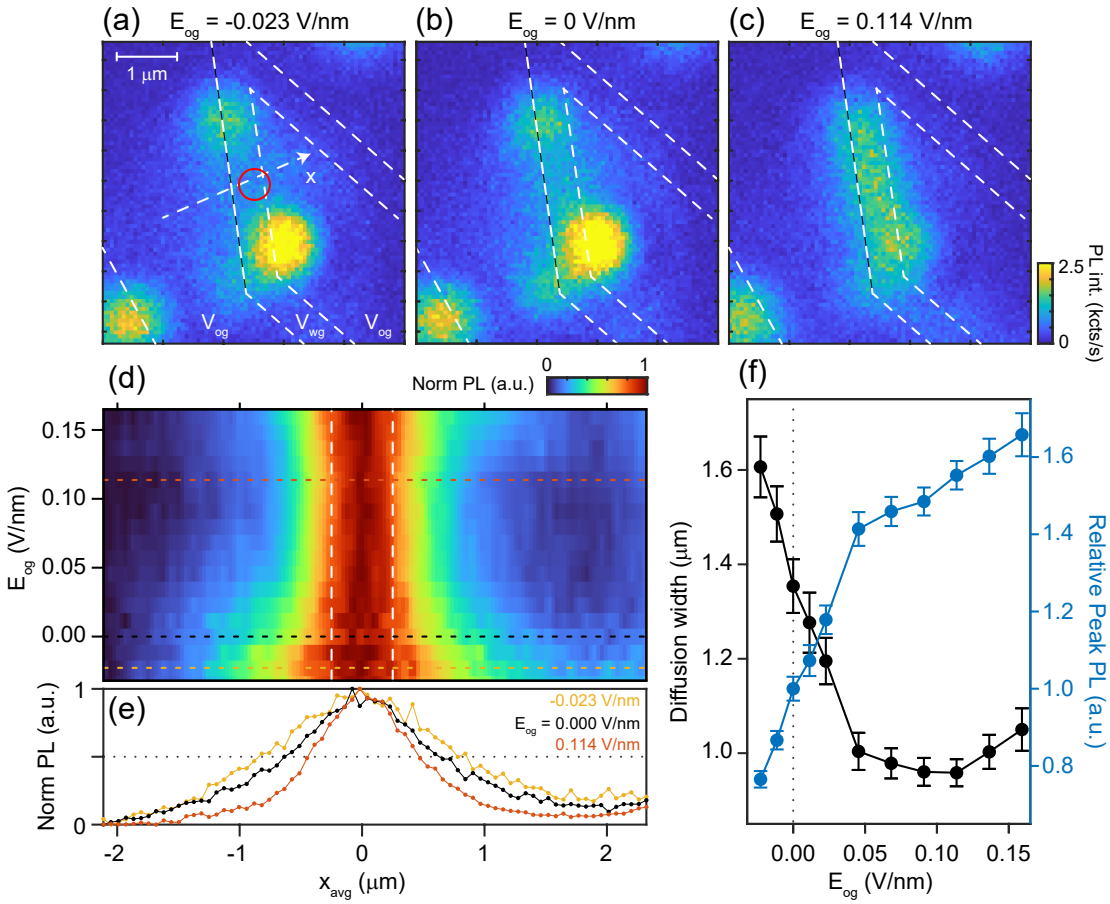

Figure 5.5: Controlling the diffusion behavior (a)-(c) Spatial mapping of the diffused interlayer exciton (IE) photoluminescence (PL) emission at $E_{og} = -0.023$, 0, and 0.114 V/nm. The outer gate and the wire gate areas are labeled V_{og} and V_{wg}, respectively. White dashed arrow indicates positive x direction. Red circle is the excitation position. Bright spots that naturally occur on the sample are reduced with the trapping potential. (d) Normalized PL along the x direction, averaged over the uniform trap region, as a function of E_{og}. The dotted lines correspond to the E_{og} line cuts in (e). The white dashed lines indicate the expected trap width of $\sim$ 500 nm. (e) Line cuts at E_{og} = -0.023, 0, and 0.114 V/nm showing narrowing (broadening) of the diffusion width when forming a trap (anti-trap). (f) Extracted diffusion width and relative peak intensity ($\text{PL}_{\text{peak}}(E_{og})/\text{PL}_{\text{peak}}(E_{og} = 0)$) as a function of E_{og}. We observe the trap saturates near $E_{og} \approx 0.04$ V/nm.

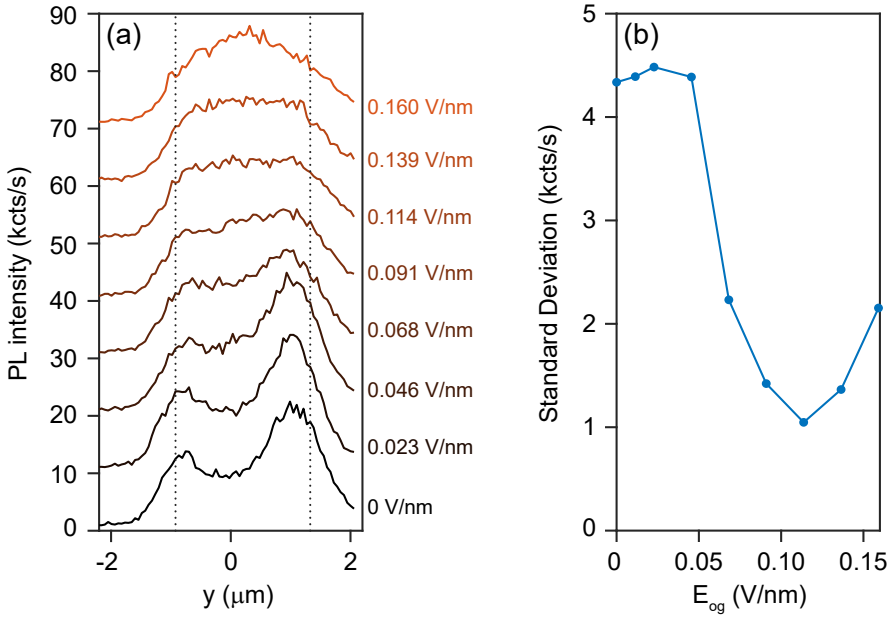

Figure 5.6: Linecuts along the trap (a) Averaged linecuts along the trap length offset by 10 kcts/s for each E_{og}. The black dotted lines indicate the range used for calculating the standard deviation of the points in (b). (b) The standard deviation of the PL intensity along the y-linecutas a function of E_{og}.

trap region, as a function of E_{og}, where $y = 0$ is approximately where the x-linecuts were performed. We see the two larger intensity regions corresponding to natural traps. As we increase E_{og}, the emission becomes more uniform. We quantify this by taking the standard deviation of the PL intensity in the trap region (indicated by the black dotted lines) as shown in Figure 5.6(b). The standard deviation of the emission in the trap saturates around $E_{og} \approx 0.09$ V/nm, reaching the noise floor (1 kct/s) for these measurements. $E_{og} \approx 0.09$ V/nm corresponds to a trap depth of ~ 55 meV, which is consistent with the energy scale in reports of defect or strain trapped IEs in these heterostructures [129,130]. The increase in the standard deviation again at $E_{og} > 0.114$ V/nm corresponds to a brightening in the trap region due to the trapping potential.

In Figure 5.5(f), we fit the averaged non-normalized PL x line cuts to a Gaussian distribution and extract the peak PL intensity height and diffusion full-width half-maximum (FWHM) as a function

of E_{og}. We observe the trap diffusion width saturates near $E_{og} \approx 0.04$ V/nm at around 0.95μm. The FWHM is broader than the expected trap size, which could be explained by an imperfect alignment of the top and bottom gates convoluted with the diffraction limited beam shape (Appendix E.2). We also note that the FWHM increases slightly for $E_{og} > 0.12$ V/nm, which could be due to a shortened lifetime at larger electric fields and therefore, greater emission outside the trap[14]. The relative peak PL (normalized to emission at $E_{og} = 0$ V/nm) also increases rapidly until $E_{og} \approx 0.04$ V/nm, before increasing at a slower rate. We also observe the longest IE lifetime in the trap area when the trapping potential is applied, increasing by up to 20% at the largest E_{og} (Fig. 5.7). These signatures point towards the strong confinement of higher IE densities in the trap region.

5.4 Lifetime modulation with the trap

We perform time-dependent PL (TDPL) measurements across the trap at different trapping potentials. We fix the excitation ($\lambda = 660$ nm with $P_{avg} = 5\mu$W and 80 Mhz repetition rate) at one spot near the edge of the wire gate and move our separate collection spot. Figure 5.7(a) shows the TDPL counts in the trap without the trapping potential and obtain an exciton lifetime $\tau_{IE} = 1.22 \pm 0.03$ ns. We take lifetime measurements across different spatial locations for three representative outer gate electric fields $E_{og} = 0$, 0.068, and 0.138 V/nm (Fig. 5.7(b)-(d)) to see the effects of the trapping potential. We note that even at $E_{og} = 0$ V/nm, τ_{IE} is not spatially uniform, which could be due to the natural traps or variations across our sample. However, as we increase the trapping potential, we begin to observe τ_{IE} be peaked near $x = 0$. In Figure 5.7(e), we choose two representative positions, $x = 0$ and 0.432 nm, and plot the IE lifetime as a function of E_{og}. We find that the lifetime inside (outside) the trap increases (decreases) with higher E_{og}. We also observe the lifetime decreases in the trap for $E_{og} < 0$ V/nm.

When we increase the IE density in the trap there could be multiple competing effects. At higher

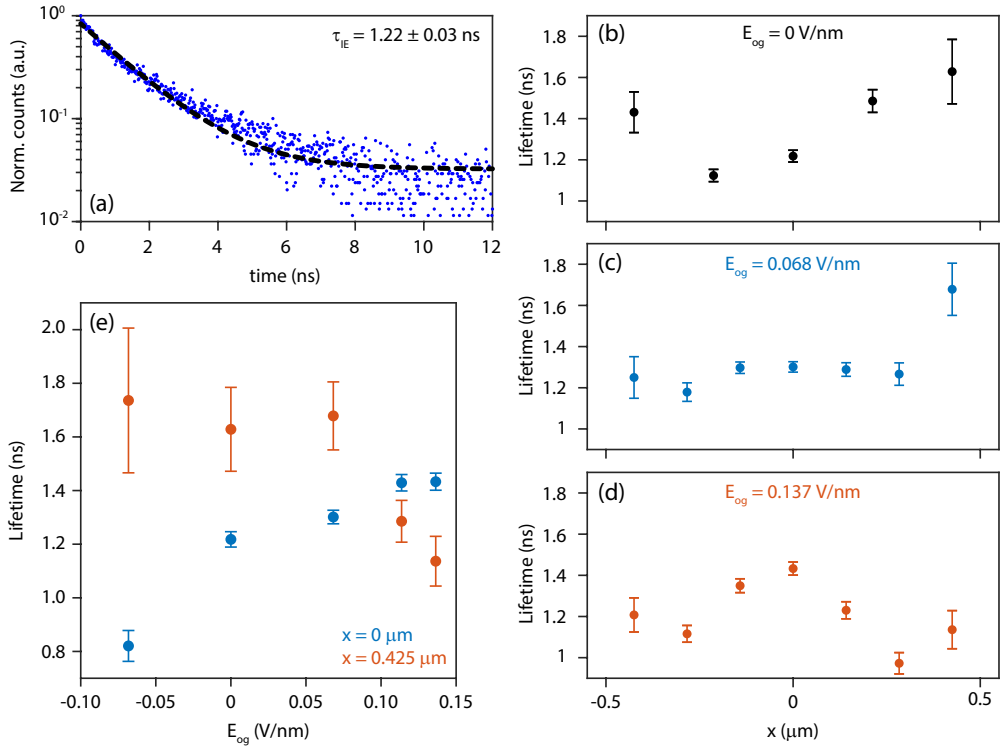

Figure 5.7: (a) Time-dependent PL measurements in the trap at $E_{og} = 0$ V/nm. The lifetime is extracted with a single exponential fit. (b)-(d) Lifetime (τ_{IE}) as a function of x for $E_{og} = 0$, 0.068, and 0.138 V/nm. (e) Lifetime at two representative spots as a function of E_{og}.

trapping potentials, the trap confines the IEs from diffusing away, increasing the PL lifetime. However, the higher IE density could result in more scattering mechanisms and non-radiative decay channels which could decrease the lifetime. When creating an anti-trap ($E_{og} < 0$ V/nm), we expect the lifetime to decrease as the IEs are pushed out of the trap area, as we observe. Overall, the order of magnitude of the lifetime, $\tau_{IE} \sim 1$ ns, is shorter than some previous reported interlayer exciton lifetimes, which could be due to the twist angle[72] or other non-radiative processes such as Auger or defect mediated recombination.

5.5 Extracting the interlayer exciton density

Since the trapping potential funnels the IEs into a smaller area, we expect a higher steady-state IE density to exist in the wire trap. Figure 5.8(a) shows the normalized power dependence of the IE emission at $E_{og} = 0$ V/nm. We observe a blue shift in the PL energy with excitation power due to dipole-dipole interactions as the IE density increases [14,58,77,63,131,124,125]. We can model this blue shift with a simple parallel-plate capacitor model where the energy shift,

$$\Delta E = \frac{(n_{IE} - n_0)\, e^2\, d}{\varepsilon_{TMD}\, \varepsilon_0}, \tag{5.2}$$

where n_{IE} is the IE density, n_0 is the starting density, and ΔE as the PL energy difference. The same relation can be found by considering a classical dipolar exciton using a mean field approach, although both methods underestimate the IE density [113]. Thus, we treat the ΔE as an indication of increasing density. Interestingly, when we apply the trapping potential of $E_{og} = 0.114$ V/nm (Fig. 5.8(b)), we observe a greater blue-shift for the same P range. In fact, the IE energy at the highest powers is limited by the trap depth, where $\mathrm{IE}_{\mathrm{trap}}$ and the peak corresponding to IEs outside of the trap (~ 1.44 eV) merge. We extract the IE density (right axis) at each P by using the blue-shift ΔE at each P as shown in Fig. 5.8(c).

For the lowest excitation power, since we do not have an energy to compare with, we get an IE density (n_{IE}) of 0 when there is clearly PL emission. To account for this, we calculate an upper bound starting density n_0 based on the excitation power, similar to Wang, et al. [63]. We can calculate the steady-state n_{IE} if we know the lifetime (τ) and generation rate (G). As pointed out in Wang, et al. [63], both quantities will depend on n_{IE}, giving us:

$$n_{IE} = G(n_{IE})\tau(n_{IE}). \tag{5.3}$$

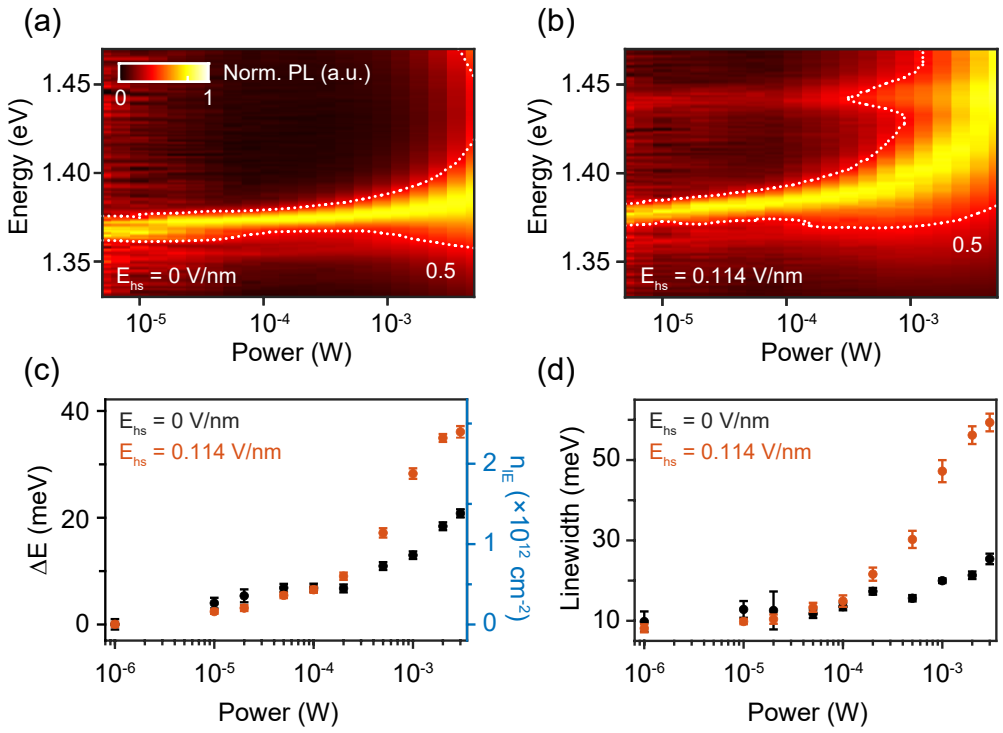

Figure 5.8: Tuning the interlayer exciton density (a) Normalized power dependent PL emission from the wire gate region at $E_{og} = 0$ V/nm, when the excitation laser is slightly outside the region. The dotted white line shows a contour of half the intensity of the IE_{trap}. (b) Same as (a) for $E_{og} = 0.114$ V/nm. (c) The blue-shift energy, ΔE, for $E_{og} = 0$ and 0.114 V/nm as a function of power. Right axis (blue) shows the corresponding calculated IE density, n_{IE}. (d) Fitted IE_{trap} linewidth for $E_{og} = 0$ and 0.114 V/nm as a function of power. The error bars in (c) and (d) are from the fitting of the spectral peaks.

However, since we are only concerned about a single density to normalize our curve, we consider G and τ for this specific case. The generation rate at the lowest power used in our experiments will be

$$G = \frac{P \cdot \sigma}{A \cdot h\nu}, \tag{5.4}$$

where σ is the absorbance of the sample, A is the area of the beam spot, and $h\nu$ is the excitation photon energy. First, we calculate the absorbance from $\sigma \approx 0.11$ at our excitation energy of 1.87 eV (wavelength, $\lambda = 660$ nm)[63], scaled by the approximate losses due to the metallic top gates ($\sim 5\%$

transmission). We assume a diffraction limited spot size with a Airy ring radius, $r = 0.61\frac{\lambda}{NA} = 536$ nm, to get $A = \pi r^2 \approx 0.9\mu\text{m}^2$. We take $\tau \approx 1$ ns in this device (Section 5.4). Using these values we can obtain

$$n_{IE}(P) = P \times (2.04 \times 10^9)\ \text{cm}^{-2}/\mu\text{W}, \tag{5.5}$$

assuming that there is minimal non-radiative decay processes. Thus, for ($P = 1\mu$W), we can add $n_0 = 2.04 \times 10^9$ cm^{-2} to the starting density. Since our calculated n_0 and the energy shift at low powers is small, this assumption only contributes a small error at higher densities.

At lower excitation powers, the densities are comparable, presumably because the trap area is large compared to the exciton density. At higher powers, we can see that a sharp increase in the IE density occurs earlier for $E_{og} = 0.114$ V/nm, indicating the trapping potential increases the IE density for the same generation rate. Without any trapping potential applied, we can achieve a maximum $n_{IE} = 1.3 \times 10^{12}$ cm^{-2}, in agreement with previous measurements[14]. With the trapping potential we can reach almost twice this density, $n_{IE} = 2.3 \times 10^{12}$ cm^{-2}. We note that the enhanced blue-shift only occurs for trapped IEs and does not occur for IEs outside of the trap even at $E_{og} = 0.114$ V/nm. The measured blue shifts outside of the trap at the largest excitation power (P) are $\Delta E \approx 12.7$ and 10.6 meV for $E_{og} = 0$ and 0.114 V/nm, respectively, corresponding to IE densities of 8.4×10^{11} cm^{-2} and 7.0×10^{11} cm^{-2} (Fig. 5.9). Neither measurement in the outer gate region show dramatic changes in the blue-shifting energy. This confirms that the blue-shift enhancement is a consequence of enhanced dipolar interactions due to the generation of higher IE densities. In addition to shifts in the peak energy, we also observe linewidth broadening as shown in the contour lines of half maximum IE_{trap} normalized intensity (Figs. 5.8(a)-(b)). Figure 5.8(d) shows the fitted linewidth as a function of power for $E_{og} = 0$ and 0.114 V/nm. At lower excitation powers, we have a linewidth of ~ 10 meV in both cases. At higher P, we observe an earlier increase in the linewidth with the trapping potential, similar to the deviations in n_{IE}. We rule out heating as the main mechanism because the linewidth broadening

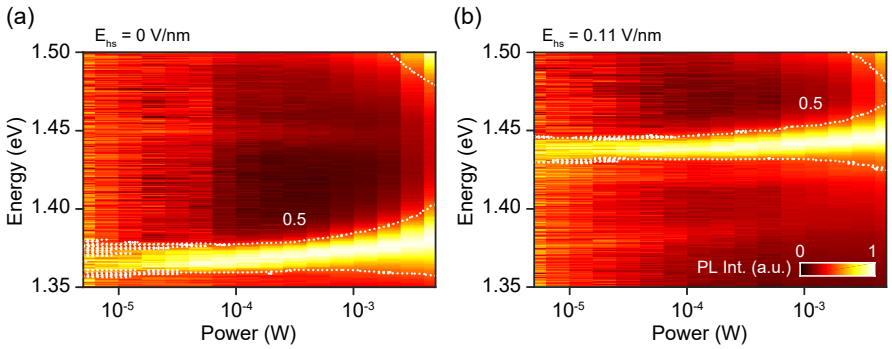

Figure 5.9: Power dependence outside the wire gate (a) Power dependent PL spectra of the interlayer excitons outside of the trap area with $E_{og} = 0$ V/nm. (b) Same measurement with $E_{og} = 0.114$ V/nm shows similar blue shifts and linewidth broadening to $E_{og} = 0$ V/nm.

would occur at the same power, independent of E_{og}.

5.6 The interlayer exciton Mott transition

The interlayer exciton linewidth should broaden as it approaches the Mott transition, regardless of the trap depth. We plot all linewidth versus density curves for various E_{og} on a scatter plot, which appears to scale linearly on a semi-log scale for the y-axis (Fig. 5.10). Phenomenologically, we fit the n_{IE} versus linewidth curve with an exponential,

$$w(n_{IE}) = w_0 \, e^{n_{IE}/n^*_{IE}} \tag{5.6}$$

to extract the critical density n^*_{IE}. Figure 5.11(a) shows the linewidth as a function of IE density for various E_{og} in a scatter plot with the density on a semi-log scale. Amazingly, we find that the data points fall onto a universal curve, which suggests a transition occurs at critical density n^*_{IE}, independent of the local electrostatic environment. We extract a characteristic $n^*_{IE}(T = 4\text{K}) = 1.20(\pm 0.05) \times 10^{12}$ cm^{-2} (Fig. 5.10). Similar measurements were performed at two other temperatures, $T = 30$ and 50 K (Fig. 5.11(b)-(c)), showing a trend towards higher critical density for higher temperatures (Fig.

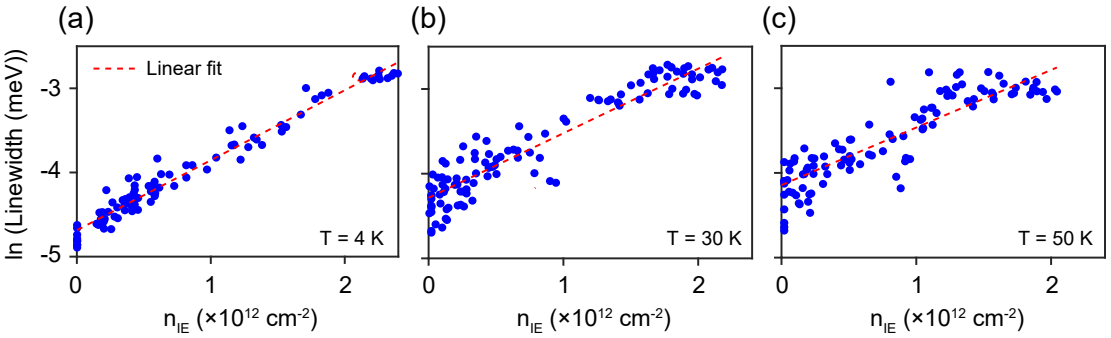

Figure 5.10: Exponential fits of the linewidth as a function of density on a semi-log plot which correspond to a linear function at T = (a) 4 K, (b) 30 K, and (c) 50 K.

5.11(d)).

Broadening in IE linewidth as a function of n_{IE} was previously observed in indirect excitons in GaAs double quantum wells[131,124] as well as in IEs in $MoSe_2/WSe_2$ heterostructures[63]. Similar to previous studies, we attribute this broadening to a Mott transition, or the quantum dissociation of excitons at a critical density. The Mott transition occurs when the ratio of n_{IE} approaches the size of the exciton, or $n_{IE}\,a_{IE}^2 \sim 0.04$[26,73,132]. For intralayer excitons, the Bohr radius, $a_{Bohr} = 4\pi\varepsilon_0\varepsilon_{\mathrm{TMD}}\hbar^2/\mu e^2 \approx 1$ nm (where μ is the exciton reduced mass), can be used as the exciton size, yielding a Mott density of $n_{\mathrm{Mott}}^{\mathrm{intra}} \approx 4 \times 10^{12}\ \mathrm{cm}^{-2}$[84]. For the IEs, we estimate the Bohr radius to be $a_{IE} \approx 1.6$ to 2.7 nm[73,74]. This gives a range for $n_{Mott}^{IE} \approx 0.5 - 1.6 \times 10^{12}\ \mathrm{cm}^{-2}$. Here we take $n_{Mott}^{IE} \approx 1.6 \times 10^{12}\ \mathrm{cm}^{-2}$ similar to Wang, et al.[63,126] (black line in Fig. 5.11(d)). The extracted n_{IE}^* are in reasonable agreement with the Mott density as shown in the IE phase diagram (Fig. 5.11(d)).

To understand the temperature dependence, there are a few considerations. A quasi-2D Saha's equation relates the degree of ionization with the interlayer exciton density and temperature[133,134], but more aptly describes purely thermal disassociation, which occurs at much higher temperatures. Alternatively, one can consider the Mott transition as the plasma-gain-onset density in 2D, which reduces to a linear dependence between the Mott density and temperature[135]. Both predict an increase in n_{Mott} with increasing temperature, consistent with a Debye-screening model. However, in the case

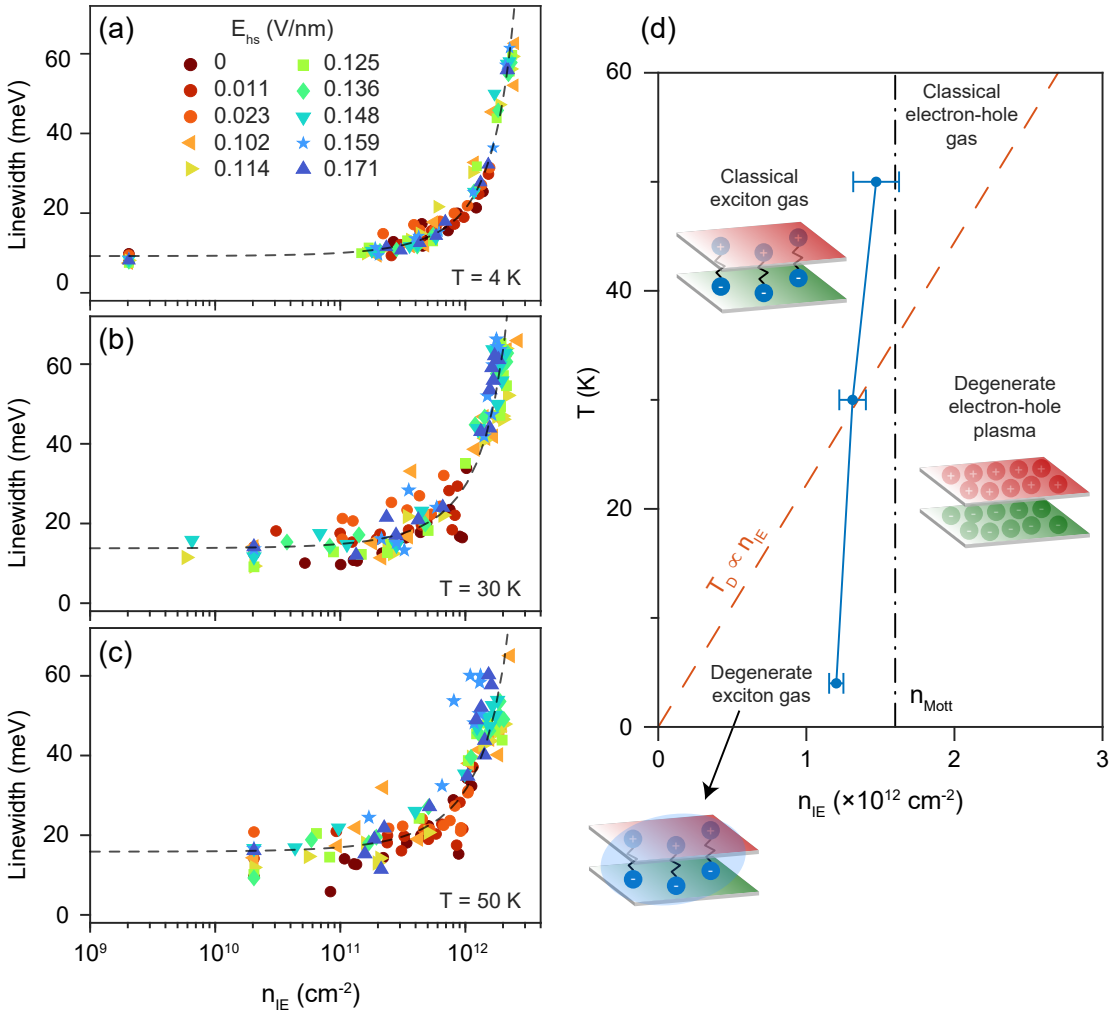

Figure 5.11: Interlayer exciton Mott transition (a) Scatter plot of linewidth vs IE density for various trap depths. A universal critical density $n^*_{IE}(4\text{K}) = 1.20(\pm 0.05) \times 10^{12}$ cm^{-2} is extracted. (b)-(c) Same as (a) but at 30 K and 50 K with $n^*_{IE}(30\text{K}) = 1.31(\pm 0.09) \times 10^{12}$ cm^{-2} and $n^*_{IE}(50\text{K}) = 1.47(\pm 0.15) \times 10^{12}$ cm^{-2}. (d) The IE phase diagram and the extracted $n^*_{IE}(T)$ at different temperatures. The red dashed line follows the degeneracy temperature (T_D) and the black dashed line is the Mott density, n^{IE}_{Mott}.

of an IE condensate, strong correlations could change these pictures and further studies are required to have an accurate understanding of the expected Mott transition density behavior. We note that although the observed transitions occur below the degeneracy temperature T_D, there is no evidence of an exciton condensate in this sample. The natural defects and the fragility of the condensate state could hinder formation of coherent condensate state.

5.7 Conclusion

Our capability to create IE traps via finely patterned electrostatic gates allows us to increase the maximum achievable IE densities and control their diffusion profile. We can modulate the IE density with the trap depth, demonstrating electrical tunability across the IE phase diagram. We show evidence for the IE Mott transition, which occurs universally at the same density across various trapping potentials. Our gate tunable IE traps can be designed for novel optoelectronic devices such as exciton transistors [136,76,75]. Finally, depth-tunable traps are an important step towards reliably creating a controlled density of cold dipolar excitons away from the excitation spot, removing any laser-induced heating or coherence effects that could prevent unambiguous identification of a condensate. The realization of the coveted high-temperature IE condensate would open the way for practical on-chip coherent electronics.

To see the world for a moment as something rich and strange is the private reward of many a discovery.

Edward M. Purcell

6

Spin-Singlet and Triplet Interlayer Excitons

Not everything is well understood in a burgeoning field. With the ability to stack TMD layers due to their van der Waals nature, heterostructures were constructed and studied without a thorough understanding of the interlayer band structure that would arise. In early studies, the optical selection rules for the interlayer excitons were assumed to directly follow that of the monolayer TMDs. However, we would find that high symmetry twist angles and the resulting preferential stack-

ing registries would play an important role in the most often observed optical selection rules in these systems.

Specifically, we would find that both the singlet and triplet transitions in $MoSe_2/WSe_2$ heterostructures are allowed. The singlet and triplet interlayer exciton states, with opposite spin characteristics, could be used as the basis for polarization switches [58] in excitonic quantum devices. However, since the optical selection rules differ for different atomic registries of the TMD heterostructure, the IE emission spectra, even qualitatively, vary between studies without consistent observation of both singlet and triplet states or specifications of the heterostructure stacking configuration [64,65,137]. Theoretical studies have predicted selection rules for TMD heterostructures based on the stacking orientation, either 0-degree aligned or 60-degree aligned, and atomic registry, which provide a quasi-angular momentum to brighten singlet and triplet optical transitions [138,40,87]. While singlet and triplet interlayer excitons have been observed in 60-degree aligned heterostructures [64,65,137], the observation of these states in 0-degree aligned heterostructures has not been reported so far. The 0-degree aligned heterostructures are predicted to have flipped polarization coupling to the lower and upper transitions, giving an additional degree of freedom for valleytronic devices.

We will first delve into the initial experimental observations. Then we will discuss the symmetry arguments for the selection rules which will explain the initially mysterious behavior of spin-singlet and triplet interlayer excitons. We will finally present experiments where we electrically control the emission between the singlet and triplet states in both 0- and 60-degree $MoSe_2/WSe_2$ heterostructures.

6.1 Singlet and triplet interlayer excitons

Our experiments employ h-BN encapsulated $WSe_2/MoSe_2$ devices with top and bottom gates, and electrically transparent contacts (Fig. 3.1), as described in Chapter 3. We use a dual-gating scheme where the top-gate voltage (V_{tg}) and the back-gate voltage (V_{bg}) have the same polarity, achieving

higher carrier densities than in previous IE studies [58,14,13] (details in Appendix D). Furthermore, separate electrical contacts made for $MoSe_2$ and WSe_2 layers allows operating the device as an atomically-thin PN diode where the current can flow across the heterostructure interface. Below we focus on two representative devices with 0-degree (called device A) and 60-degree (called device B) stacking orientations.

Figs. 6.1(a)-(b) show a comparison of the photoluminescence (PL) spectrum for device A and B at neutral doping with circularly co- and cross-polarized exciton emission (I_{co} and I_{cross}, respectively). We discuss the details for taking these measurements in Appendix B. In device A, we observe only a single peak at $\sim$ 1.34 eV. For device B, there are two peaks, one at $\sim$ 1.39 eV and the other at $\sim$ 1.41 eV, with a separation of $\sim$ 25 meV. As shown in Figs. 6.1(c)-(d), the degree of circular polarization (DOCP), computed from $\frac{I_{co}-I_{cross}}{I_{co}+I_{cross}}$, of the lower energy peak at 1.39 eV in device B is positive, suggesting the chirality of the light emitted remains unchanged, unlike the higher energy peak in device B and the peak in device A. The observation of two peaks with opposite DOCP in device B is consistent with previous experimental results for 60-degree aligned heterostructures [64,65] and their selection rules [40,87]. Thus, we tentatively identify the lower and higher energy peaks as triplet (X_T) and singlet excitons (X_S), respectively, while the emission energy and DOCP for device A are consistent with a 0-degree heterostructure [59].

The PL spectrum can further be modified by applying gate voltages on the devices. Figures 6.1(e)-(f) show the PL spectrum from devices A and B as a function of $V_{tg} = \alpha V_{bg}$, where $\alpha = 0.617$ or 1.4 for the two devices (based on each device's h-BN thicknesses), respectively. In this gate voltage configuration, we can maximize our achievable two-dimensional (2D) carrier density n_{2D}. We identify four distinct gate regions, marked by I-IV, from the electrostatic doping of the heterostructure (Fig. 6.1(g)). We verify the doping of the layers by measuring the intralayer exciton absorption spectra as a function of the gate voltage (Fig. 6.2).

The gate dependent PL shows strong atomic stacking registry dependence. For device A (Fig.

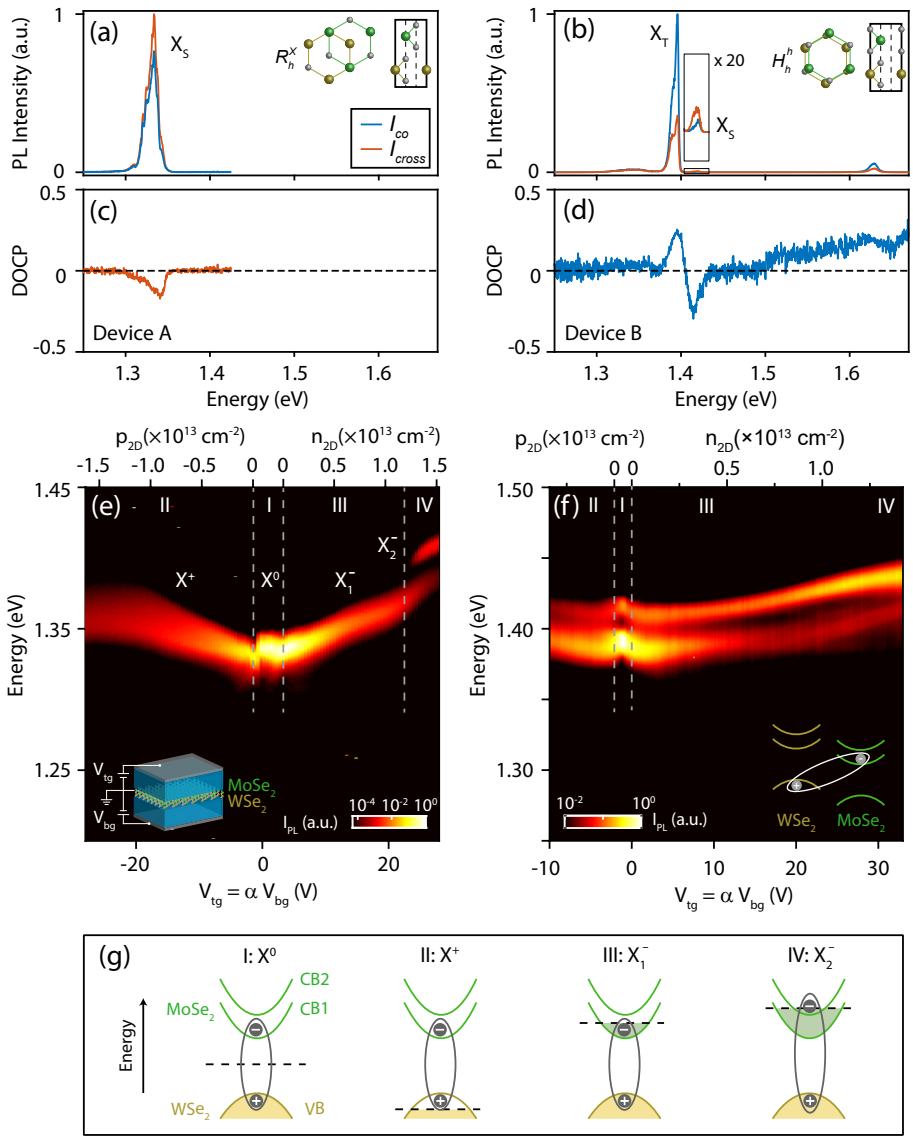

Figure 6.1: Photoluminescence (PL) of interlayer excitons in $MoSe_2/WSe_2$ heterostructures. (a)-(b) Polarization resolved PL from devices A and B, respectively. Excitation power, $P = 0.5$ μW and 100 μW, respectively, are used to compare all existing exciton species. Inset: Lowest energy stacking configuration for 0- and 60-degree heterostructures. (c)-(d) Degree of circular polarization (DOCP) extracted from (a)-(b). (e)-(f) PL vs. $V_{tg} = \alpha V_{bg}$, where α is based on the h-BN thicknesses, for devices A and B, respectively. Left inset: device schematic and direction of applied gate voltages. Right inset: band schematic of an interlayer exciton between the conduction band of $MoSe_2$ and valence band of WSe_2. (g) Reduced band diagrams of the $MoSe_2/WSe_2$ heterostructure showing the upper (CB2) and lower (CB1) conduction bands of $MoSe_2$ and the valence band of WSe_2 (VB). The exciton and Fermi energy (black dashed line) are drawn for each regime marked in (e)-(f). The green ($MoSe_2$) and yellow (WSe_2) shaded areas indicate filled electron bands.

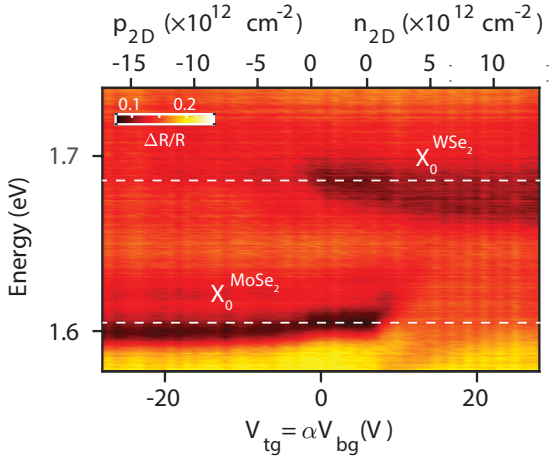

Figure 6.2: Dual gate-dependent reflection spectrum in the same doping regime as Fig. 6.1(e).

6.1(e)), only neutral interlayer excitons labeled as X^0 appear in region I. In region II (III), the Fermi energy crosses the valence band of WSe_2 (lower conduction band (CB1) of $MoSe_2$) and we begin to *p*-dope (*n*-dope) the heterostructure forming charged interlayer excitons (CIEs), X^+ (X_1^-). The discontinuities in the PL energy between regions I/II and I/III are attributed to CIE binding energies of $\sim$ 15 meV and $\sim$ 10 meV, respectively, as discussed in Chapter 4 [14]. In region IV, when the electron density is further increased, an additional PL peak, X_2^-, appears $\sim$ 25 meV above the X_1^- peak, which overtakes in intensity with increasing n_{2D}. This additional exciton feature is likely related to reaching the upper conduction band of $MoSe_2$ (CB2). For device B (Fig. 6.1(f)), we observe a similar discontinuity in emission energy when entering regions II and III due to CIE formation but find the higher energy peak to always be present as we tune the carrier density.

To understand the angular momentum characteristics of the interlayer excitons, we measure PL under magnetic fields to determine the effective Zeeman splitting of the exciton species. We perform polarization-resolved PL measurements as a function of magnetic field (B) using a cross-polarized measurement scheme (Appendix B.4.2). Figs. 6.3(a)-(c) show the normalized $\sigma+$ (blue) and $\sigma-$ (red) PL spectra measured in device A at $n_{2D} = 0, 1.02\times10^{13}$ cm^{-2}, and 1.57×10^{13} cm^{-2}, respectively. From

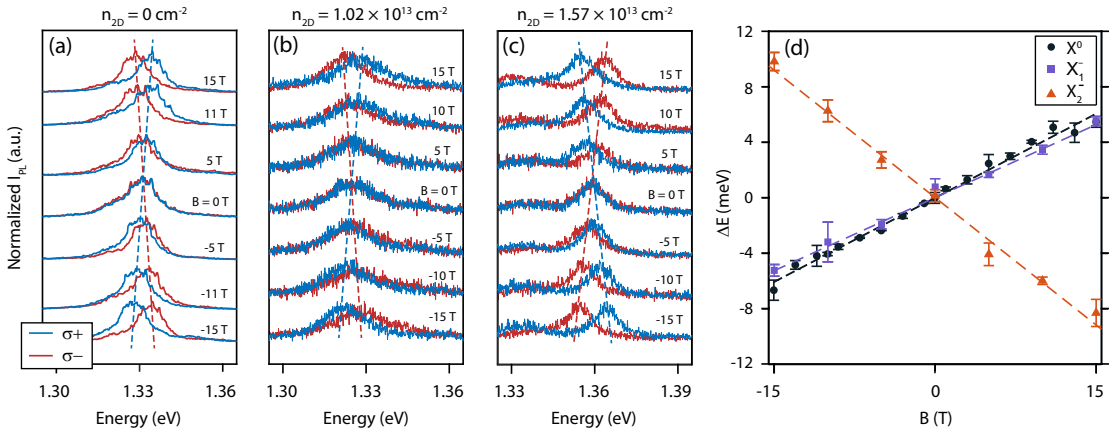

Figure 6.3: Experimental evidence of spin-singlet and spin-triplet excitons via magnetic field in device A. (a)-(c) Polarization-resolved photoluminescence (PL) spectra at $n_{2D} = 0, 1.02 \times 10^{13}$ cm^{-2}, and 1.57×10^{13} cm^{-2}, respectively, for characteristic magnetic fields (B) using a cross-polarized measurement scheme (Appendix B.4.2). Blue (red) curves are $\sigma+$ ($\sigma-$) collection. The dashed lines serve as a guide to the eye. (d) PL energy splitting ($\Delta E = E_{\sigma+} - E_{\sigma-}$) as a function of magnetic field for X^0, X_1^-, and X_2^-. Error bars are calculated from the fitting of the peak position. The dashed lines are linear fits to the energy splitting giving $g_0 = 6.99 \pm 0.35$, $g_1 = 6.06 \pm 0.58$, and $g_2 = -10.6 \pm 1.0$.

these polarization-resolved spectra, we obtain the PL energy splitting between the circularly polarized light ($\Delta E = E_{\sigma+} - E_{\sigma-}$) as a function of B. Fig. 6.3(d) shows the measured energy difference follows a linear relation $\Delta E = g\mu_B B$, where g is the effective g-factor and μ_B is the Bohr magneton. From the slope of the measured relation between ΔE and B, we obtain the effective g-factors for X^0, X_1^-, and X_2^-: $g_0 = 6.99 \pm 0.35$, $g_1 = 6.06 \pm 0.58$, and $g_2 = -10.6 \pm 1.0$, respectively. Interestingly, the g-factor for X_2^- is greater than and has the opposite sign of g_0 and g_1, implying X_2^- has an additional Zeeman splitting contribution and that the chiral light coupling to the K valleys is flipped compared to X^0 or X_1^-. The observation of a higher energy emission in region IV also suggests that transitions between the highest WSe_2 K-valley valence band and both spin-split $MoSe_2$ K-valley conduction bands are allowed. This would indicate that the higher energy peak is an emissive triplet transition with an in-plane dipole moment, evidenced by far-field emission, unlike dark triplet excitons in monolayers [9,10,139].

6.2 Interlayer exciton selection rules

We established the selection rules for monolayer TMDs in Chapter 2, where we used symmetry arguments to determined the allowed same layer, interband transitions. In interlayer excitons, the optical transition is from a valence band in one layer (WSe_2) to the conduction band of another layer ($MoSe_2$). The relative shifts between the layers then play an important role in the newly allowed selection rules.

Modified selection rules arise from the space group symmetry of the atomic configuration of $WSe_2/MoSe_2$ heterostructures – as opposed to being purely determined by the symmetry of any individual, constituent layer, as discussed in Section 2.3. Theoretical calculations[40,138] have shown there are 6 high symmetry atomic registries for the two layer system: 3 for 0-degree aligned (Fig. 6.4(a)) and 3 for 60-degree aligned (Fig. 6.4(b)). We use the same naming convention as in previous works[40,140], where R_h^μ (H_h^μ) represents an R-type (H-type) or 0-degree (60-degree) stacked sample with the $\mu = h, X, M$ sites on the top layer overlapping with the h site on the bottom layer. We will work through the optical selection rules for the 0-degree aligned heterostructures here and a similar calculation can be done for the 60-degree aligned heterostructures.

When discussing the selection rules, we must select a single point of reference. In the monolayer case, this can be arbitrary and we selected the metal (M) point for convenience. In the heterostructures, the interlayer, interband transition can occur across two different points in the lattice (M, h, X) and so the quantum numbers must be calculated for each symmetry point. Thus, the optical selection rules for interlayer recombination involve the phase difference from the translation of the Bloch wave function between the two rotation sites in addition to the orbital angular momentum quantum number of each individual layer. This induced phase from the atomic registry translation can be regarded as an additional quasi-angular momentum in the optical transition, altering the resulting selection rules.

To get the quantum numbers at different rotation centers, we can consider the same rotation about

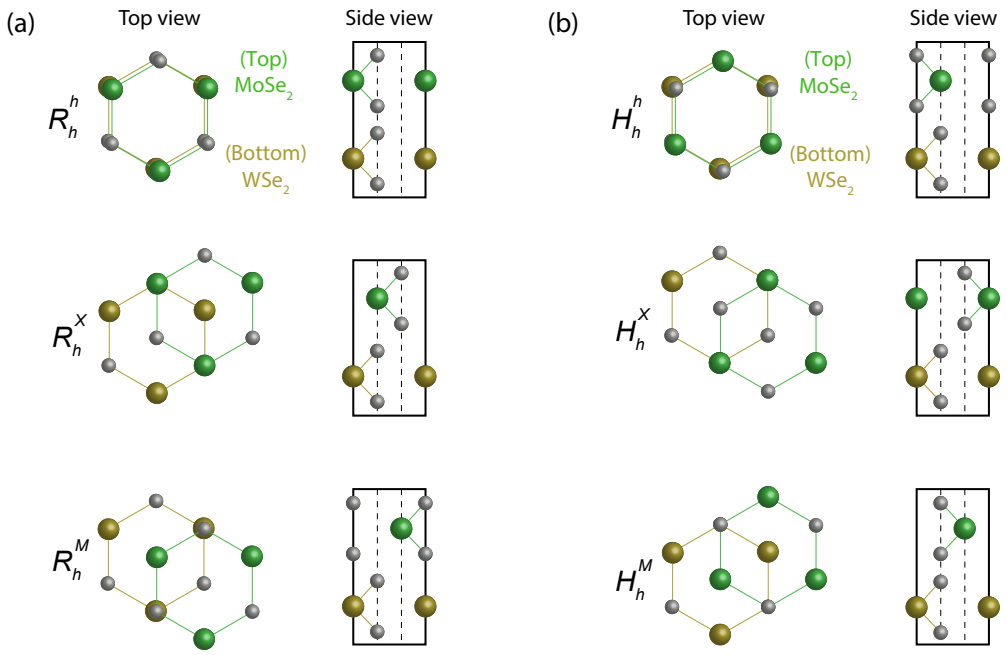

Figure 6.4: (a) The top and side views of the three 0-degree stacking conventions, R_h^{μ}, where $\mu = h,\ X,\ M$ is the top layer's center of rotation when rotating about the bottom layer's h site are shown. The top layer is the $MoSe_2$ (green) layer and the bottom layer is the WSe_2 (yellow) layer. (b) The top and side views of the three 60-degree stacking conventions, H_h^{μ}, where $\mu = h,\ X,\ M$ is the top layer's center of rotation when rotating about the bottom layer's h site are shown.

M followed by a translation vector. In Figure 6.5(b), we show that the $\hat{C}_3$ rotations can all be written in terms of the $\hat{C}_3(M)$ rotation followed by a translation, $T(d_1)$ or $T(d_2)$. The translations $T(d_1)$ and $T(d_2)$ can be written as a linear combination of the lattice vectors. Translating a Bloch wavefunction by a lattice vector will only add a phase but not change the wavefunction itself. Since the high-symmetry points (M, h, X) can be written as displacement from the M site by a lattice vector, the translation will only result in an additional phase of $\pm\frac{2\pi}{3}$. Taking the axis convention from Yu, H., et al.[40] where $K = \frac{4\pi}{3a}(1, 0)$, one can show that the $\hat{C}_3$ quantum numbers, when rotating around the h and X sites, will be $C_3\ (n, M) + 1$ and $C_3\ (n, M) - 1$, respectively. In Table 6.1, we show the $C_3\ (n)$ quantum numbers for the three different centers of rotations for the first conduction band's two spin states (c_1 and c_2) and the top most valence band (v), as well as the $S_z\ (n)$ and $\sigma_h\ (n)$ quantum

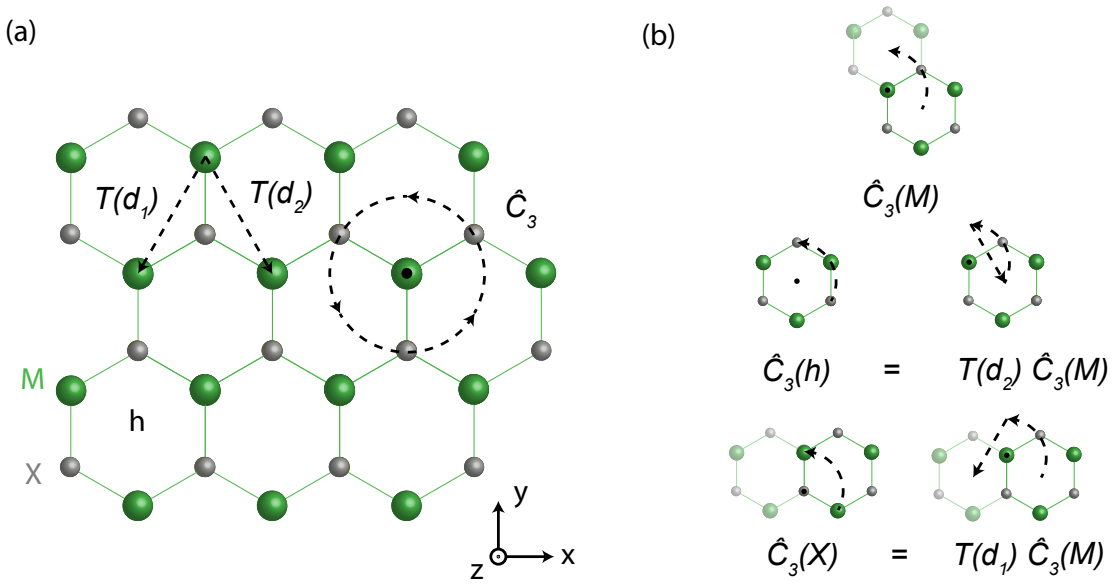

Figure 6.5: (a)The $\hat{C}_3$ rotation operator and $T(d_1)$ and $T(d_2)$ translation operators demonstrated on a TMD lattice. Lattice locations $\mu = h, X, M$ are also shown. (b) Visual representation of writing the rotation operator at different centers of rotation with respect to $\hat{C}_3(M)$, $T(d_1)$, and $T(d_2)$.

numbers.

$n =$	v	c_1	c_2
$C_3(n, M)$	-1	0	0
$C_3(n, h)$	0	$+1$	$+1$
$C_3(n, X)$	$+1$	-1	-1
$\sigma_z(n)$	$+1$	$+1$	$+1$
$S_z(n)$	$+\frac{1}{2}$	$+\frac{1}{2}$	$-\frac{1}{2}$

Table 6.1: The quantum numbers associated with the first valence band, and first two conduction bands of a monolayer TMD at different rotation centers at the K point. Note that CB1 and CB2 here are the spin-split conduction band due to spin-orbit coupling, so they only differ in their spins.

From here, we can follow the same procedures in Chapter 2 to calculate the allowed transitions for the various interlayer shifts with one caveat. In the heterobilayer case, the $\hat{\sigma}_b$ symmetry no longer holds,

removing Eq. (2.9) as a constraint. We still have the same $\hat{C}_3$ rotational symmetry at high-symmetry interlayer offsets shown in Figure 6.4(a). This results in the following selection rules:

$$C_3\left(n'\right) - C_3\left(n\right) + S_z' - S_z = \begin{cases} 3N \pm 1 & \sigma\pm \text{ transition} \\ 3N & z \text{ transition} \end{cases} \tag{6.1}$$

where N is an integer. We find that the allowed transitions depend on the $\hat{C}_3$ quantum numbers as well as the spin. However, when the two layers are displaced relative to each other within the plane, the rotation axis for the two layers will no longer be the same, resulting in different allowed transitions depending on the offsets of the layers (Fig. 6.4(a)). In addition, if one of the two layers are rotated 60° from the axis convention in Figure 6.5(a) (resulting in 60 degree aligned stacking), then the rotated quantum numbers, $\hat{C}_3'$, will be related by to $\hat{C}_3$ by a factor of -1, as discussed in previous theory work[40].

It was theoretically and experimentally shown that for $WSe_2/MoSe_2$ heterostructures, the lowest energy atomic stacking registry in 0-degree aligned heterostructures is R_h^X, representing an R-type stacking (0-degree aligned) with the X site of the top $MoSe_2$ layer above the h site of the bottom WSe_2 layer[40,138,59]. We check the allowed transitions from the first valence band (v) to the first two conduction bands (c_1 and c_2) using these $\hat{C}_3$ quantum numbers and find:

$$\begin{aligned} C_3\left(c_1, X\right) - C_3\left(v, h\right) + S_z'\left(c_1\right) - S_z\left(v\right) &= (-1) - 0 + \tfrac{1}{2} - \tfrac{1}{2} = -1 = 3N - 1, \\ C_3\left(c_2, X\right) - C_3\left(v, h\right) + S_z'\left(c_2\right) - S_z\left(v\right) &= (-1) - 0 + \left(-\tfrac{1}{2}\right) - \tfrac{1}{2} = -2 = 3N + 1. \end{aligned} \tag{6.2}$$

Thus, from symmetry arguments we see that the first transition (CB1) has $\sigma-$ circular polarization and the second transition (CB2) has $\sigma+$ circular polarization. These selection rules show that a transition from c_2 is optically allowed and consistent with our experimental observations. Moreover, they predict spin-singlet and spin-triplet IEs that have opposite circular light polarization coupling to the

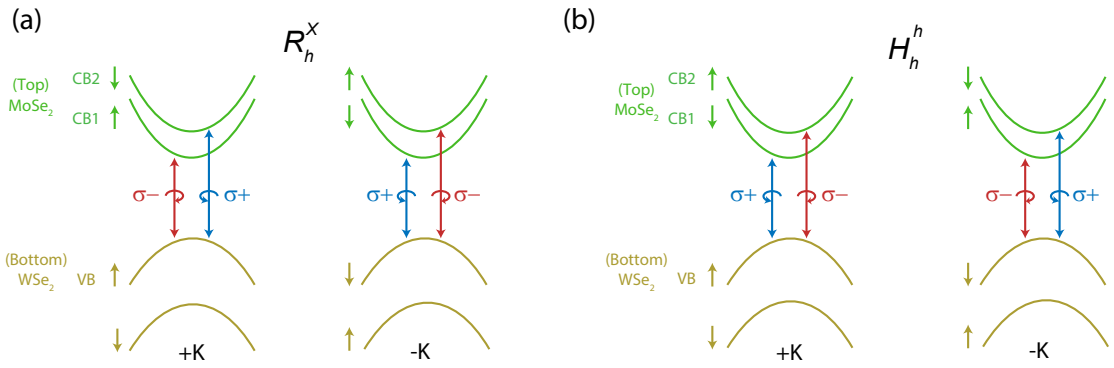

Figure 6.6: Interlayer exciton selection rules for (a) R_b^X and (b) H_b^b. Note that they have opposite polarization coupling to each conduction band, but the circular polarization is the same for singlets or triplets in a given valley.

K valleys (Fig. 6.6(a)). These rules flip in the $-K$ valley due to time-reversal symmetry ($C_3 \rightarrow -C_3$ and $S_z \rightarrow -S_z$). A similar calculation can be done for the 60-degree aligned heterostructure and its lowest energy stacking configuration, H_b^b, as shown in Figure 6.6(b). We summarize all of the transitions for any stacking angle and atomic registry in Table 6.2. A more comprehensive derivation and quantitative analysis can be found in previous theoretical studies[40,138].

	R_b^b	R_b^X	R_b^M	H_b^b	H_b^X	H_b^M
$v \rightarrow c_1$	$\sigma+$	$\sigma-$	z	$\sigma+$	z	$\sigma-$
$v \rightarrow c_2$	z	$\sigma+$	$\sigma-$	$\sigma-$	$\sigma+$	z

Table 6.2: The selection rules for R-type and H-type heterostructures with different atomic registries.

6.3 Expected g-factor for 0-degree heterostructures

The theoretical selection rules agree well with our observations. To quantify the magnetic field response, we look at the expected g-factors for the 0-degree band alignment. Upon applying a magnetic field, the bands involved in the two transitions will shift (Fig. 6.7) with three main contributions: the spin, the atomic orbital, and the valley moment. The atomic orbital contribution is only significant

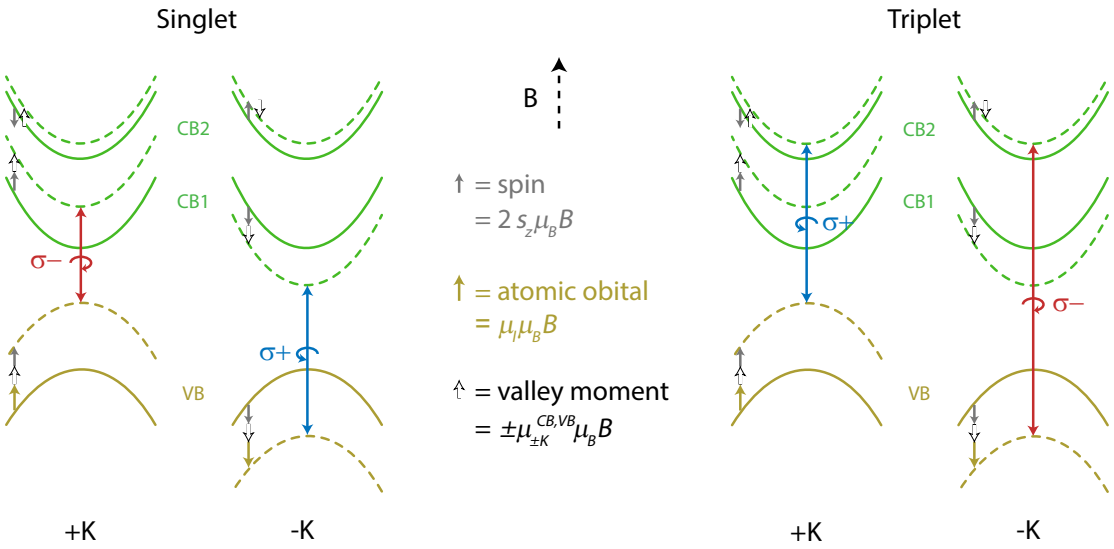

Figure 6.7: Cartoons of the singlet and triplet interlayer exciton transitions with B > 0T for 0-degree alignment. The solid green/yellow lines show the bands at B = 0T and the dotted green/red lines show the bands under magnetic field with the spin (grey), atomic orbital (yellow), and valley moment (white/black) directions indicated for each band. Band splittings are exaggerated to clarify the magnetic field response.

for the WSe_2 with a value of $\mu_l = \pm 2$ depending on the valley. The spin contribution is from the spin 1/2 of the electrons, $2s_z = \pm 1$, which cancel in the X^0 and X_1^- case, but provide an additional contribution of 4 for the X_2^-. Finally, the valley magnetic moment, $\mu_{\pm K} = \pm \frac{m_0}{m^*}$, comes from the self-rotation of the Bloch wavepackets [57] and has contributions from both the conduction and valence bands. Each of these contributions will shift each band with an effective g-factor:

$$\begin{aligned} g_{\sigma+} &= g_{\sigma+}^{CB} - g_{\sigma+}^{VB}, \\ g_{\sigma-} &= g_{\sigma-}^{CB} - g_{\sigma-}^{VB}. \end{aligned} \tag{6.3}$$

We then combine each of the shift for each circular polarization to determine estimated g-factors for the spin-singlet and spin-triple transitions:

$$g_{singlet}^{0-theory} = g_{\sigma+} - g_{\sigma-} = \left(4 + 2\left(\frac{m_0}{m_h} - \frac{m_0}{m_e^{(1)}}\right)\right) \approx 7.05, \tag{6.4}$$

$$g_{triplet}^{0-theory} = g_{\sigma+} - g_{\sigma-} = -\left(4 + 2\left(\frac{m_0}{m_h} - \frac{m_0}{m_e^{(2)}}\right) + 4\right) \approx -11.05 \tag{6.5}$$

where we use effective mass values $m_e^{(1)} = m_e^{(2)} = 0.8\, m_0$ [20] and $m_h = 0.36 m_0$ [15]. The expected g-factor is based on the Zeeman shift of each electron band (Fig. 6.7) without considering any additional excitonic effects under magnetic field. This model assumes the single-particle bands will fully determine the Zeeman splitting of the exciton energies. Although studies suggest there are corrections to this picture, the good agreement between the detailed theoretical studies and our simplified model shows that it uses reasonable assumptions [87,141,142]. Since we do not account for any effects associated with doping, such as free carrier screening and band renormalization, our model expects $g_{X^0}^{theory} = g_{X_1^-}^{theory}$. The main difference between the g-factors for the two transitions are the sign of the g-factor and the spin configuration. The sign differs because of the opposite selection rule described above. The spin of the upper conduction band is the opposite of the valence band, giving an enhancement of the g-factor by 4 for the upper interlayer exciton transition.

We use the experimentally measured lower conduction band effective mass [20] for all calculations. The measured value differs significantly from the theoretically calculated values of $m_e^{(1)} = 0.5\, m_0$ and $m_e^{(2)} = 0.58\, m_0$ [15]. We use this value for both conduction bands because of the inconsistency with the condition that $m_e^{(2)} > m_e^{(1)}$ when combining the experimental and theoretical values. DFT calculations predict a 15% larger effective mass for $m_e^{(2)}$, which can be considered a small change to the already simplified g-factor calculation.

6.4 Revealing the triplet state in 0-degree heterostructures

The experimental observations of $\sim 25meV$ splitting between X_2^- and X_1^- as well as the opposite polarization characteristics are consistent with spin-singlet and -triplet transition selection rules in the 0-degree aligned heterostructure. Quantitative evidence for the singlet and triplet states and opposite

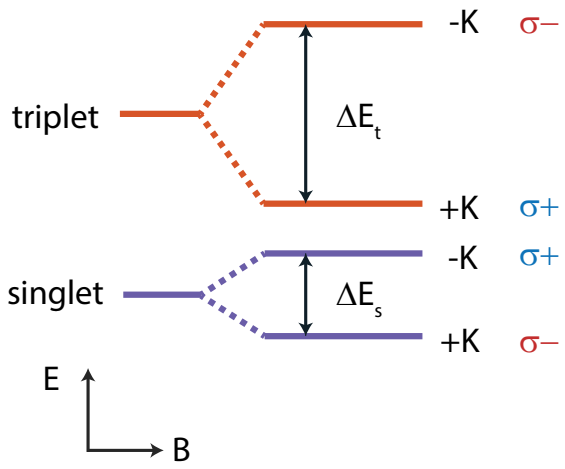

Figure 6.8: Zeeman splitting for the singlet and triplet excitons in the exciton particle picture and the circular polarization light coupling.

circular polarization coupling is revealed by comparing the expected exciton g-factors (calculated in the previous section) with our measured values. From this model, we calculate the singlet and triplet g-factors to be $g_{singlet}^{0-theory} \approx 7.1$ and $g_{triplet}^{0-theory} \approx -11.1$, respectively. These calculated g-factors are in excellent agreement with experimentally observed values both in terms of sign and magnitude. Thus, we confirm X_1^- and X_2^- as singlet and triplet excitonic transitions, respectively. We note that unlike the traditional picture of singlet and triplet states, the degeneracy of interlayer exciton singlet and triplet states is already broken due to spin-orbit coupling. These states split differently under magnetic field as shown in Fig. 6.8 in the exciton particle picture. Thus, we confirm the emission of triplet excitons in 0-degree heterostructures occur, but only at high n_{2D}.

From this analysis, we can now assign the peaks in the PL spectra (Fig. 6.1(e)) as either singlet or triplet states. In regions I-III, X^0, X^+, and X_1^- all have transitions from CB1, allowing us to assign them as singlet neutral or singlet charged excitons. In region IV, the X_2^- peak is a transition from CB2 in the presence of free carriers and is therefore a triplet charged exciton. Energetically, the triplet charged exciton can form with an electron in CB1 of either K valley in $MoSe_2$, but further studies are

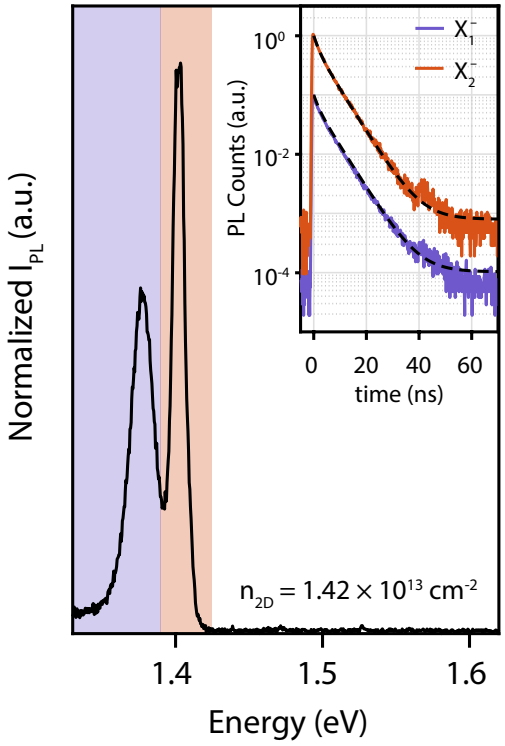

Figure 6.9: PL spectra for device A at $V_{tg} = 25V$ with the X_1^- and X_2^- regions shaded in purple and orange, respectively. Inset: Time-dependent PL measurements to determine the lifetime of X_1^- ($\tau_1 \sim 6.12$ ns) and X_2^- ($\tau_2 \sim 6.08$ ns) by spectrally filtering the energy range indicated. Dashed black lines are exponential fits.

required for a more detailed understanding. The emergence of X_2^- only after sufficient band filling can be explained by the relative dipole strengths of the singlet and triplet excitons.

The appearance of spectrally resolved exciton branches in region IV enables us to measure the lifetimes of these excitons. We spectrally isolate the two peaks obtained at $n_{2D} = 1.42 \times 10^{13}\text{cm}^{-2}$ (Fig. 6.9) and perform time-dependent PL (TDPL) measurements to find the lifetimes corresponding to X_1^- and X_2^- are $\tau_1 = 6.08 \pm 0.01$ ns and $\tau_2 = 6.12 \pm 0.02$ ns (Fig. 6.9 inset), respectively. The measured lifetimes are similar for the two species, but still 3 to 4 orders of magnitude longer than the typical lifetime of neutral or charged excitons in monolayer TMDs (~ 1 ps[32,33]). The similar lifetimes when the bands are filled with free carriers suggests the optical dipole strength of the two exciton

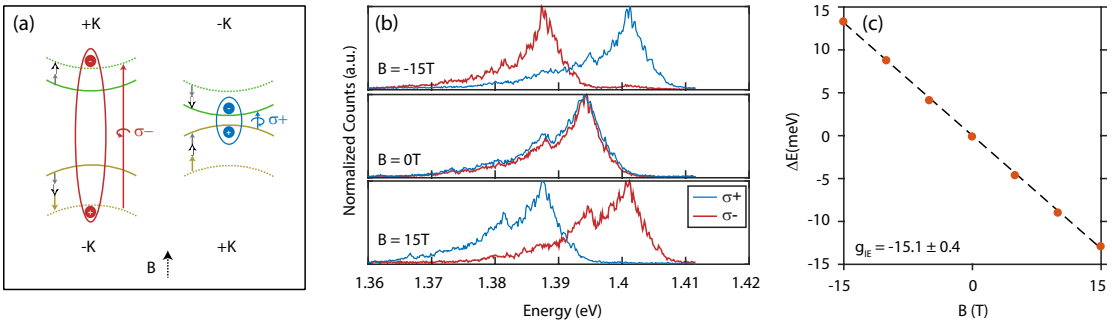

Figure 6.10: (a) Schematic diagram of the lower interlayer exciton transitions with B > 0 T for 60-degree alignment. The dotted green/yellow lines show the bands at B = 0 T and the solid green/yellow lines show the bands under magnetic field with the spin (grey), atomic orbital (yellow), and valley moment (white/black) directions indicated for each band. The +K (-K) valley of the valence band aligns with the -K (+K) valley of the conduction band. (b) Normalized polarization-resolved PL spectra in a 60-degree device at three different magnetic fields. (c) The extracted PL energy splitting as a function of magnetic field.

species are similar[40,87], consistent with theoretical calculations.

Despite being optically allowed, the spin-triplet exciton recombination must compete with the relaxation lifetime (τ_{relax}) of the electron from the upper to the lower $MoSe_2$ conduction band (CB2 and CB1, respectively). From studies on bright and dark excitons in WSe_2 [10], the τ_{relax}, attributed to spin-conserving intervalley scattering processes, has a time scale of $\sim$ 60 ps. Even at large doping, our X_1^- and X_2^- lifetimes are longer than τ_{relax} (Fig. 6.9), meaning observation of the X_2^- PL emission requires a quenching of τ_{relax} via Pauli blocking (Fig. 6.1(e)). This is in contrast with monolayer WSe_2, where the lifetime of the bright exciton $\sim$ 1 ps is shorter than τ_{relax}, allowing significant emission from the higher energy exciton. In 60-degree devices, theory calculates the upper transition to have a dipole strength $\sim$ 3 times stronger than the lower transition[40,87]. This could allow for the higher energy singlet transition to emit without quenching the relaxation process via Pauli blocking.

6.5 Confirming g-factors in 60-degree heterostructures

The 60-degree alignment case is also expected to have two bright transitions with the lowest energy transition having the $+K$ ($-K$) valley coupling to $\sigma+$ ($\sigma-$) polarized light. When applying magnetic field, the expected g-factor for the triplet exciton (lowest energy transition) is larger than even in the 0-degree stacked upper interlayer exciton transition, due to opposite signs in the valley moment contributions as well as the spin (Fig. 6.10(a)). When combining these two contributions, we expect a triplet g-factor of

$$g_{triplet}^{60-theory} = -\left(4 + 2\left(\frac{m_0}{m_h} + \frac{m_0}{m_e^{(1)}}\right) + 4\right) \approx -16.05, \tag{6.6}$$

for $m_e^{(1)} = 0.8\, m_0$ [20] and $m_h = 0.36 m_0$ [15].

We performed similar magneto-PL measurement in a separate 60-degree aligned sample and confirmed the selection rules and associated large triplet transition g-factor. In Figure 6.10(b), we show normalized polarization-resolved PL in a second sample (60-degree stacked) and see symmetric energy shifts with both magnetic field directions. We extract the energy splitting as a function of magnetic field (Fig. 6.10(c)) and measure a g-factor, $g_{triplet}^{60-stack} = -15.1 \pm 0.4$, in good agreement with the theoretical prediction and previous studies [65,57,62,87].

6.6 Control between singlet and triplet photoluminescence

With confirmation of the singlet and triplet states in devices A and B, we move to controlling the emission of the singlet and triplet. We find that the relative intensity of singlet and triplet exciton photoluminescence can be tuned by electrostatic doping and power of the laser excitation. Figures 6.11(a)-(b) show the power dependence of the normalized PL emission in devices A and B. The double peaked features near 1.34 eV and 1.37 eV in devices A and B, respectively, are attributed to CIEs

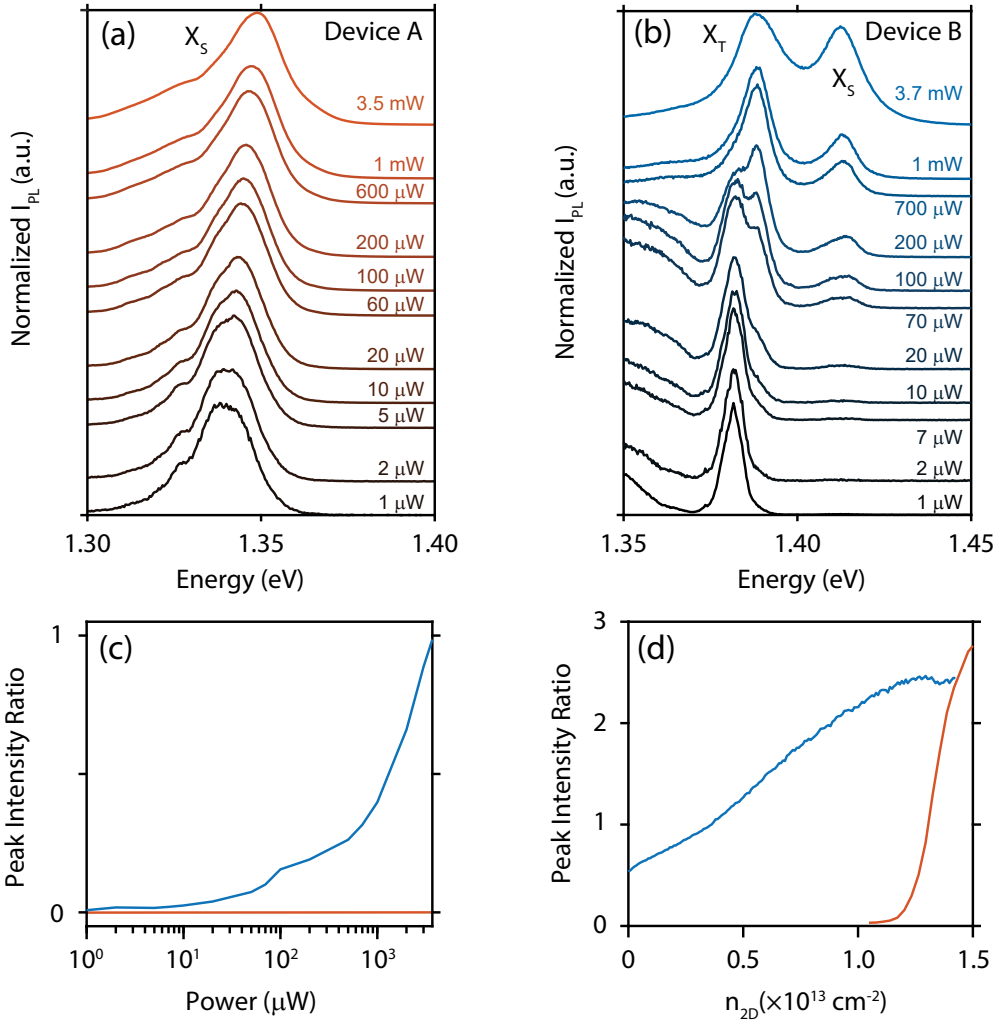

Figure 6.11: Tunable interlayer exciton species via excitation power and carrier density. (a)-(b) Power (P) dependence of the normalized photoluminescence (PL) spectra at $V_{tg} = \alpha V_{bg} = 0$ V for devices A and B, respectively. (c) Peak intensity ratio between the higher energy peak and the lower energy peak for device A (orange) and device B (blue) as a function of excitation power at $V_{tg} = \alpha V_{bg} = 0$ V. The higher energy peak does not appear at this carrier density in device A. (d) The same peak intensity ratio as a function of carrier density at P = 6 μW for device A (orange) and P = 100 μW for device B (blue).

due to changes in residual doping by the excitation power. We find that device A at neutral doping is always dominated by lower energy singlet emission without triplet emission even at high excitation powers. Device B even at neutrality, on the other hand, has a higher energy singlet peak ($\sim$ 1.42 eV) which becomes more prominent at higher powers. In the strongly non-equilibrium state at the largest excitation, the singlet and triplet emission are about similar intensity (Fig. 6.11(c)). While the excitation power can show limited range of singlet/triplet emission ratio, the electrostatic doping tuned by the gate can vary the triplet/singlet emission ratio in a wide range. Figure 6.11(d) shows that initially dominant singlet emission in device A turned to more than 70% triplet emission in the high doping range ($n_{2D} > 1.4 \times 10^{13}$ cm^{-2}), providing a singlet and triplet device where the emission of one state can be completely turned off. In device B, the inverse ratio can be tuned, with the singlet/triplet emission ratio varying between $0.5 - 2.5$ over a similar carrier density range. Thus, the $MoSe_2/WSe_2$ heterostructure provides a platform for fully tunable singlet-triplet exciton emission via electrical gates, excitation power, and the stacking registry.

6.7 Electrical generation of singlet and triplet

In Chapter 4, we showed electroluminescence (EL) of interlayer excitons and controlled the EL dynamics in device A. In our search for singlet and triplet excitons, we have realized better control of the forward-bias current with bias voltage (V_{ds}) and gate voltage ($V_{tg} = \alpha V_{bg}$). This resulted in a better understanding of the EL emission and then full control of the singlet or triplet EL emission in device B.

Utilizing the electrical contacts in WSe_2 and $MoSe_2$ layers, we can operate the device as a gate tunable atomically thin *p-n* diode [14], where the interlayer tunneling current across the heterostructure interface can generate singlet and triplet exciton emission. Fig. 6.12(a) shows the current (I_{ds}) vs. drain-source voltage (V_{ds}) curve at $V_{tg} = \alpha V_{bg} = 10$ V, where $\alpha = 1.4$, for device B, demonstrat-

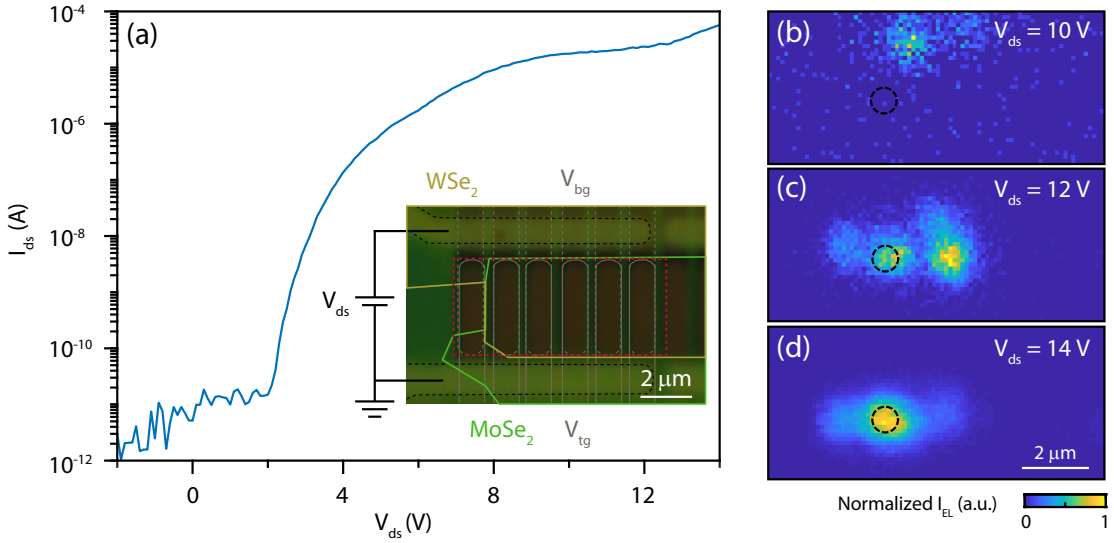

Figure 6.12: Electrical generation of singlet and triplet exciton species in device B. (a) I-V characteristics of the device B at $V_{tg} = \alpha V_{bg} = 10$ V, where $\alpha = 1.4$ is based on the h-BN thicknesses. Inset: Optical image of the sample with yellow (green) lines indicating WSe_2 ($MoSe_2$) area, gray solid (dashed) lines indicating V_{tg} (V_{bg}), black dashed lines outlining the contacts, and the red dashed rectangle indicating the sample area of interest in (b)-(d). (b)-(d) Spatial maps of normalized electroluminescence (EL) generated from the sample when in forward bias (V_{ds} = 10, 12 and 14 V). The black dashed circle indicates the collection spot for the spectra in Figs. 6.14 and 6.15.

ing rectifying diode behavior as expected for a type-II aligned heterostructure. Figs. 6.12(b)-(d) show the spatial distribution of the electroluminescence (EL) emission from the red outlined area of the heterostructure (Fig. 6.12(a) inset) under the same gate conditions at different V_{ds} in the high bias regime. We find that the spatial distribution of the emission is inhomogeneous, presumably due to disorders in the channel and the lateral gaps between the gate structures. The emission position shifts sensitively with V_{ds} and V_{tg} (see Fig. F.5), which tune the current distribution in the channel.

Fig. 6.13(a) shows all the electrodes that are controlled via the measurement circuit. Device B has multiple overlapping top and bottom gates, separated by about 300 nm, that span the width of the sample. These gates allow for electric field and high-density doping control of the heterostructure region. Both WSe_2 and $MoSe_2$ have pre-patterned contacts (yellow and green dashed lines, respectively) and have a corresponding contact gate (dashed grey line). The contact gates create a highly

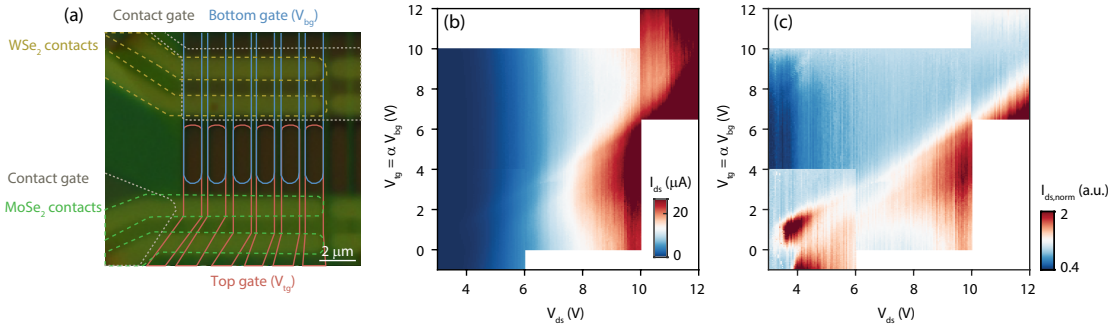

Figure 6.13: (a) Optical image of Device B with all active gates and contacts outlined. (b) Drain-source current (I_{ds}) as a function of drain-source voltage (V_{ds}) curve and gate voltages ($V_{tg} = \alpha V_{bg}$). (c) Same map as (b) but normalized to background current (I_{ds} at $V_{tg} = \alpha V_{bg} = 10$ V).

doped region of the monolayer to reduce contact resistances, allowing efficient doping and *p-n* diode transport.

We drive the device with (V_{ds}) and separately tune the density using ($V_{tg} = \alpha V_{bg}$) to observe current across the $MoSe_2/WSe_2$ heterojunction (Fig. 6.13(b)). However, the device also has areas of the *p-n* heterostructure sample that have disconnected (electrically floating) gates. As seen in Figure 6.13(b), there is current that is independent of the gate voltage, which we attribute to background current through the sample outside of our region of interest. We remove this effect by normalizing the I_{ds} map to the I_{ds} vs. V_{ds} curve taken at $V_{tg} = \alpha V_{bg} = 10$ V, which except for the highest V_{ds}, shows no apparent gate-dependent features. From the normalized map in Fig. 6.13(c), we find the V_{ds} range where we observe EL (Figs. 6.12(b)-(d)) corresponds to the onset of the current through the gated sample region. The EL is observed in the heterostructure at lower combinations of V_{ds} and V_{tg} as well, which is demonstrated in Figures 6.14(a)-(c) in the following section.

6.8 Full switching between singlet and triplet electroluminescence

Figures 6.14(a)-(b) show the EL spectra collected at a fixed location of the sample (marked by dashed black circle in Figs. 6.12(b)-(d)) for various gate and bias configurations (along the dotted and dashed

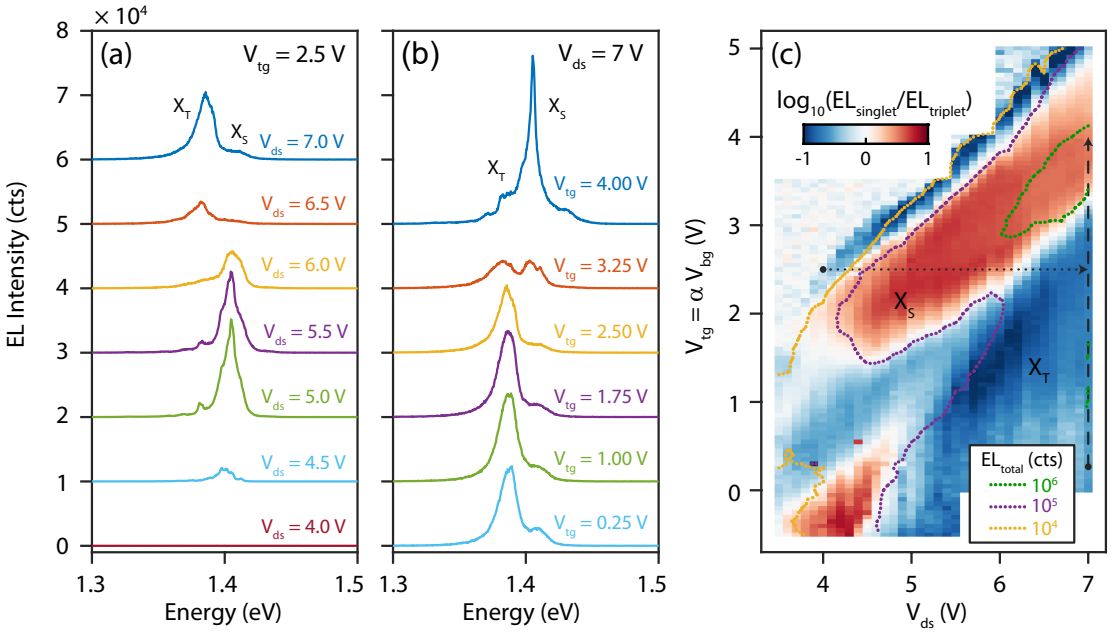

Figure 6.14: (a) EL spectra as a function of V_{ds} at fixed $V_{tg} = \alpha V_{bg} = 2.5$ V. (b) EL spectra as a function of $V_{tg} = \alpha V_{bg}$ at fixed $V_{ds} = 7$ V. (c) The log of the ratio between the integrated EL emission from singlet and triplet interlayer excitons as a function of V_{ds} and $V_{tg} = \alpha V_{bg}$ showing voltage regions with singlet and triplet dominant emission. The colored dotted lines show contours of the total integrated EL. The black dotted and dashed lines correspond to the linecuts for spectra in (a) and (b), respectively.

line in Fig. 6.14(c), respectively). We demonstrate complete tunability between singlet and triplet exciton EL emission as a function of V_{ds} and V_{tg}. Fig. 6.14(c) maps out the log of the ratio between the integrated singlet and triplet emission as a function of V_{ds} and V_{tg}, showing voltage conditions where either the singlet or triplet emission is dominant. The ratio of the EL emission between singlet and triplet, or triplet and singlet, approaches as large as 10:1. The observed switching is accompanied by enhancements in the total EL emission, which we discuss below, but further studies are required to fully understand the gate-dependence. We have demonstrated electrical generation that can be gate-tuned to be dominated by either singlet or triplet exciton emission, demonstrating an LED with selectable emission between opposite spin and polarizability characteristics.

In Figure 6.13(c), we showed that when the background current due to uncontrolled areas of the

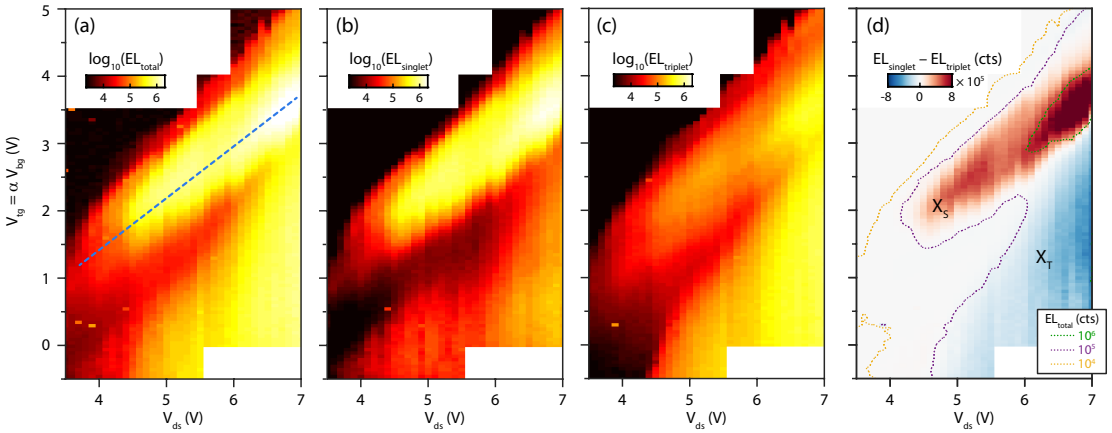

Figure 6.15: (a) Total integrated electroluminescence (EL) counts as a function of V_{ds} and $V_{tg} = \alpha V_{bg}$. (b) EL counts vs. V_{ds} and $V_{tg} = \alpha V_{bg}$ when integrated over the higher energy singlet interlayer exciton energy range. (c) Same EL map but for the lower energy triplet interlayer exciton. (d) The difference in the integrated EL emission from singlet (b) and triplet (c) interlayer excitons as a function of V_{ds} and $V_{tg} = \alpha V_{bg}$, showing regions with dominant exciton emission. The colored dotted lines show contours of the total integrated EL.

sample are removed, the I_{ds} through the gated regions of the sample is dependent on both V_{ds} and $V_{tg} = \alpha V_{bg}$. Similarly, the largest total integrated electroluminescence (EL) counts (Fig. 6.15(a)) from this area of the sample (black circles in Figs. 6.12(b)-(d)) occur at the same V_{ds} and $V_{tg} = \alpha V_{bg}$ conditions. Figures 6.15(b)-(c) show the integrated EL contribution from the singlet interlayer exciton (1.396 − 1.474 eV) and the triplet interlayer exciton (1.323 − 1.393 eV), respectively. In Fig. 6.15(d), we plot the difference in the integrated EL singlet and triplet emission, showing regions where singlet (red regions) or triplet (blue regions) emission are dominant. We also observe strong enhancement in the total EL along the blue-dashed line in Fig. 6.15(a), corresponding mostly to emission from the higher energy singlet interlayer excitons (Fig. 6.15(b)).

The origin behind the enhancement and voltage dependence remains a mystery. The observations are consistent with resonant band tunneling between the $MoSe_2$ and WSe_2 conduction bands, where the upper conduction band of $MoSe_2$ would be in resonance with the WSe_2 conduction band before the lower conduction band of $MoSe_2$. In previous studies on $MoSe_2$/h-BN/WSe_2 heterostructures,

current and EL enhancements have been attributed to interlayer exciton coherence[66]. Further studies are needed to fully understand the origin of the enhancement and the switching of the EL emission. These enhancements in EL and the work from Wang, Z. et al.[66] gave a strong motivation to pursue the possibility of a condensate in electrically generated interlayer excitons, which we discuss in Chapter 8.

6.9 Conclusion

Our capability of gate tuning to access the higher conduction band with opposite spin allows us to create charged excitons with singlet and triplet spin configurations and opposite chiral light coupling. The observation of the elusive triplet interlayer exciton state allows for the stacking configuration to be used in choosing the lowest energy spin state of the interlayer exciton. We demonstrate control of singlet and triplet interlayer exciton emission via electrostatic doping, optical pump power, and injection current. The observation of these states under the presence of charges means circularly polarized light coupling in singlet and triplet excitons can switch between fermionic and bosonic character, which could be utilized in novel quantum devices. Electrical generation of tunable singlet and triplet excitons in TMD heterostructures, combining long EL lifetime[14] with local gate engineering[143], paves the way towards independently controlling chiral, valley, and spin quantum states in valleytronic devices.

Question everything. Learn something. Answer nothing.

Euripides

7

Charged interlayer excitons under magnetic fields

External magnetic fields can be a powerful tool for studying the spin and valley characteristics in condensed matter systems. In semiconducting TMD heterostructures, magnetic fields can be used to break the valley degeneracy and understand the valley Zeeman effect of

interlayer excitons. Based on our studies of the singlet and triplet interlayer excitons, we proceeded to study the magnetic field behavior of the interlayer excitons as a function of free carrier doping. In both intralayer and interlayer exciton studies, charged exciton species have been shown to form in the presence of free carriers [42,43,14,144]. However, the nature of the formed charged interlayer excitons and their g-factors are not well understood. While previous studies use the single particle band shifts to attribute singlet or triplet charged interlayer excitons [77,87,144], they did not touch on the potential interactions due to the charges under magnetic field, which are present in the monolayer cases [145,45,22,20,146].

In this chapter, we study the g-factors of neutral and charged interlayer excitons in $MoSe_2/WSe_2$ heterostructure devices and reveal details in the g-factor and valley populations under magnetic fields. We use electrostatic gates to study how these properties are tuned by free carrier density. Finally, we use magnetic fields at high electron doping to confirm that the interlayer excitons are formed from the second conduction band electrons of the $MoSe_2$ K-valley with a spin-orbit splitting of ~ 20 meV.

7.1 Circularly polarized interlayer exciton species

In these studies, we use an h-BN encapsulated, 0-degree aligned $WSe_2/MoSe_2$ device with top and bottom gates and electrically transparent contacts (Fig. 3.1), as described in Chapter 3. To reduce the electric field effects from carrier density effects, we use a single-gate doping scheme, which we describe in detail in Appendix D. Since this device has $MoSe_2$ as the top layer and WSe_2 as the bottom layer, we apply V_{bg} for $V_g < 0$ V and V_{tg} for $V_g > 0$ V such that the doped layer screens the electric field between the layers [14], as discussed in Chapter 4.

We perform circular polarization dependent photoluminescence (PL) measurements under different out-of-plane magnetic fields (B) using a cross-polarization measurement scheme (Appendix B.4). This setup minimizes the polarization dependent response of the system and allows the extraction of the valley information of the PL due to the negative circular polarizability of the singlet interlayer exci-

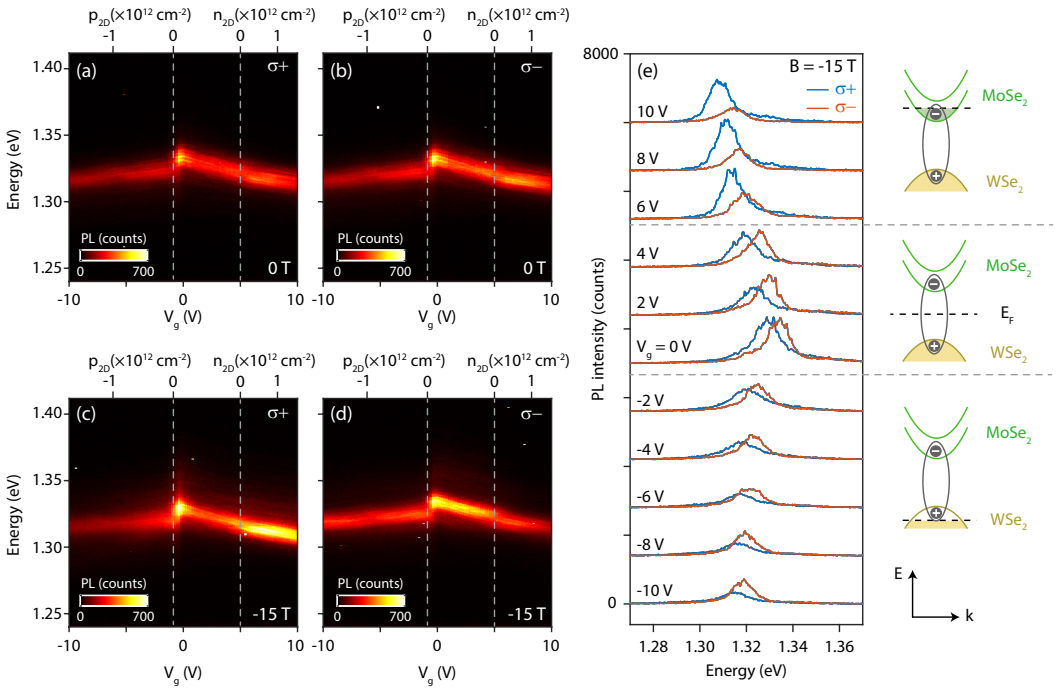

Figure 7.1: Polarization resolved PL as a function of carrier density. (a)-(b) Cross-polarized PL measurements at B = 0 T for $\sigma+$ and $\sigma-$ collection as a function of V_g. V_g is either the V_{tg} or V_{bg} depending on the sign of the applied voltage as described in the text. The corresponding carrier density is calculated via a parallel-plate capacitor model. (c)-(d) Same measurements but at B = $-$15 T. (e) Representative spectra taken in 2 V steps from (c)-(d). The spectra are offset by 700 counts. The grey dashed lines in (a)-(e) separate the different doping regimes as schematically drawn in the band structure diagrams. The dashed black line in the diagrams is the Fermi level.

tons[77,62,87,40]. All measurements are performed with an excitation wavelength of 660 nm and power of 15μW at 5 K. In Figure 7.1(a)-(b), we show the circular polarization dependent PL spectra at $B = 0$ T. We observe discontinuities in the PL energy position at $V_g \approx -1.4$ and 5 V, which are attributed to the $p-$ and $n-$doped charged interlayer excitons (grey dashed lines). The right- and left-handed circularly polarized PL emission, $\sigma+$ and $\sigma-$, respectively, do not show any significant differences in spectral energy or PL intensity, which is expected due to time reversal symmetry at zero magnetic field*. In Figure 7.1(c)-(d), we present the same measurement under a magnetic field of $B = -15$

*If the circular polarizability were measured instead, we would observe a difference in the polarizability response, which gives information on the ability to maintain valley polarization. In the cross-polarization setup, the $\sigma+$ and $\sigma-$ measurements are symmetric as it gives information on the valleys rather than the polarizability.

T. Figure 7.1(e) shows representative spectra of the circularly polarized PL in 2V steps where we find significant differences between the $\sigma+$ and $\sigma-$ PL emission. First, we observe an energy shift between the $\sigma+$ and $\sigma-$ emission. While the magnitude of energy shifts seem to vary, the sign of the shifts remains constant throughout the V_g range and are consistent with the expected Zeeman splitting of the singlet interlayer exciton[77] as described in Chapter 6. Second, we find the relative PL intensities of the $\sigma+$ and $\sigma-$ emission are strongly modulated with V_g, switching between $\sigma+$ or $\sigma-$ dominated emission in the $p-$ and $n-$doped regimes.

7.2 Valley polarization

To understand the polarization dependent intensity changes, we perform similar measurements at various B and compare the $\sigma+$ and $\sigma-$ PL intensity. The PL intensity will be proportional to the density of excitons that couple to a given circular polarization. Based on the singlet interlayer exciton selection rules[40,138,87], $\sigma-$ ($\sigma+$) polarized emission couples to the $+K$ ($-K$) valley and we can calculate the valley polarization[145,147] as

$$P_{(+K,\sigma-)} = \frac{I_{\sigma-} - I_{\sigma+}}{I_{\sigma-} + I_{\sigma+}}. \tag{7.1}$$

In Figure 7.2(a), we show the calculated valley polarization as a function of V_g at $B = -15$, 0, and 15 T (additional data in Appendix Fig. F.6). For $B = 15$ T, we observe a strong $-K$ valley polarization ($P_{(+K,\sigma-)} < 0$) when in the $p-$doped regime and strong $+K$ valley polarization ($P_{(+K,\sigma-)} > 0$) in the $n-$doped regime. The neutral interlayer exciton in the undoped regime switches between $+K$ and $-K$ valley polarization. We measure the opposite behavior for $B = -15$ T, consistent with time-reversal symmetry of the K valleys. Importantly, this behavior is minimally present ($|P_{+K,\sigma-}| < 0.05$) in the absence of magnetic field ($B = 0$ T). Valley polarization at $B = 0$ T is attributed to drifts in the system's response to the two circular polarizations, which is only removed via a normalization factor at a single gate value. The valley polarization measurements gives insight into the formation of the

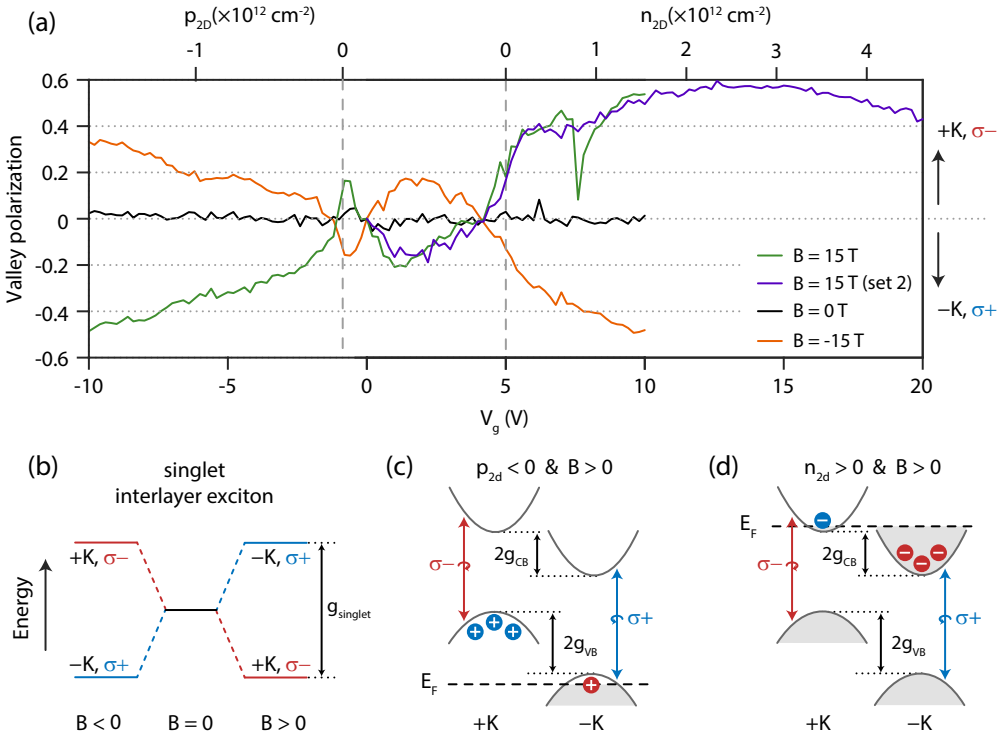

Figure 7.2: (a) Valley polarization = $\frac{I_{\sigma-} - I_{\sigma+}}{I_{\sigma-} + I_{\sigma+}}$ as a function of V_g for different magnetic fields (B). Positive (negative) valley polarization corresponds to +K(-K) valley polarization. Data set 2 (purple) shows similar behavior but over a larger n-doping range. (b) Singlet interlayer exciton splittings under magnetic fields show the lowest energy state. (c) Band diagram of the conduction band and valence band splittings for B > 0 when p-doping, leading to valley polarization of the free holes in the +K valley. (d) Similar band diagram for n-doping, leading to valley polarization of free electrons in the -K valley.

neutral and charged interlayer excitons in the two valleys.

In the undoped region without free charges, PL emission is dominated by neutral interlayer excitons. The Zeeman splitting will break the valley degenerate singlet interlayer exciton state and as shown in Figure 7.2(b). For $B > 0$ T, $\sigma-$ emission ($+K$ valley) will be the lowest energy state and so we expect a larger $+K$ valley polarization. While we observe a stronger $+K$ valley polarization near the band edges for $B > 0$ T (Fig. 7.2(a)), the behavior switches in the center of the band gap. Consistent with time-reversal symmetry of the K valleys, we observe the inverse behavior for $B < 0$ T. We rule out the electric field playing a major role as the valley polarization does not seem to be affected

by measurements where only the electric field is modulated (Section 7.4). One explanation of this behavior could be unoccupied in-gap states [148], which could affect the radiative and non-radiative decay processes differently in the separate valleys once the valley degeneracy is broken. Ultimately, the variations in neutral regime are not well understood and should be subject for future studies.

In the presence of free carriers, the valley polarizations differ for the $p-$ and $n-$doped regimes, but both change monotonically with increasing doping. This implies the charged interlayer exciton populations are modulated by the charges rather than the energy of the excitonic states. The valley polarization of the free carriers can be characterized by the effective g-factor, g_n, of the band (n = CB, VB)

$$g_n = \frac{\Delta E_Z}{2\mu_B B} = g_{spin} + g_K + g_l, \tag{7.2}$$

where $g_{spin} = 1$ is the spin contribution, $g_K = m_0/m^*$ is the valley Berry curvature contribution (m^* is the effective mass of the band), and $g_l = 0$ or 2 is the orbital contribution. This results in an effective g-factor of $g_{CB} = 2.25$ for the $MoSe_2$ conduction band ($m_e = 0.8m_0$ [20]) and $g_{VB} = 5.85$ the WSe_2 valence band ($m_h = 0.35m_0$ [15]). In Figures 7.2(c)-(d), we show schematics of the Zeeman splitting of the conduction and valence bands with $p-$ and $n-$doping. From the band structure schematic, we see that the electrons and holes will be polarized in opposite valleys for a given magnetic field. In the valence band (Fig. 7.2(c)), for $B > 0$ T we expect to find a greater density of holes in the $+K$ valley. Due to Pauli exclusion, charged interlayer exciton species are predicted to bind with the free carriers in the opposite valley [42,145,149,144]. Thus, a large valley polarized hole density in the $+K$ valley would form a charged interlayer exciton that emits $\sigma+$ polarized light via the excitonic transition in the $-K$ valley. Indeed, we observe increasing $\sigma+$ polarized emission ($-K$ valley polarization) in the $p-$doped regime. Similarly, in the $n-$doped regime for $B > 0$, electrons are polarized in the $-K$ valley, which forms charged interlayer excitons that have brighter $\sigma-$ ($+K$ valley) emission. The behavior is flipped for $B < 0$, consistent with time-reversal symmetry. Thus, we find the observed valley polarization of

the charged interlayer exciton is determined by the valley polarization of the associated bound charge.

We note the $n-$doped regime has larger valley polarization, which persists up to $n_{2D} \approx 3 \times 10^{12}$ cm^{-2} before decaying (Fig. 7.2(a)). Assuming the decay begins once the valley polarized bands reach an equilibrium, we can estimate the single particle g-factor,

$$g_{CB}^{exp} = \frac{1}{2\mu_B B} \frac{\pi \hbar^2}{\nu m_e} n_{2D} \cdot f_v, \tag{7.3}$$

where $\nu = 1$ is the degeneracy, $m_e = 0.8 m_0$ is the effective electron mass[20], and the valley fraction $f_v = I_{\sigma-}/(I_{\sigma-} + I_{\sigma+}) = \frac{1}{2}(P_{(+K,\sigma-)} + 1)$, which estimates the fraction of charges that fill the lower Zeeman split conduction band. From this approximation, we extract a $g_{CB}^{exp} \approx 3.9$, which is in reasonable agreement with the calculated $g_{CB} = 2.25$. The larger g_{CB}^{exp} is expected considering previous measurements show 2-3 times larger effective g-factors than the calculated values both in WSe_2 holes[22,146] and $MoSe_2$ electrons[20].

7.3 Charged interlayer exciton g-factors

We now discuss the interlayer exciton g-factor in the presence of free charges. From the circularly polarized PL measurements, we can measure the PL energy of $\sigma+$ and $\sigma-$ emission, corresponding to Zeeman shifts in the K valleys. We define the neutral and charged interlayer exciton Zeeman splitting as the difference between these energies

$$\Delta E_Z = E_{\sigma+} - E_{\sigma-}. \tag{7.4}$$

Fig. 7.3 shows ΔE_Z for various B. The Zeeman shift is expected to shift linearly proportional to the magnetic field

$$\Delta E_Z = g_{singlet} \mu_B B, \tag{7.5}$$

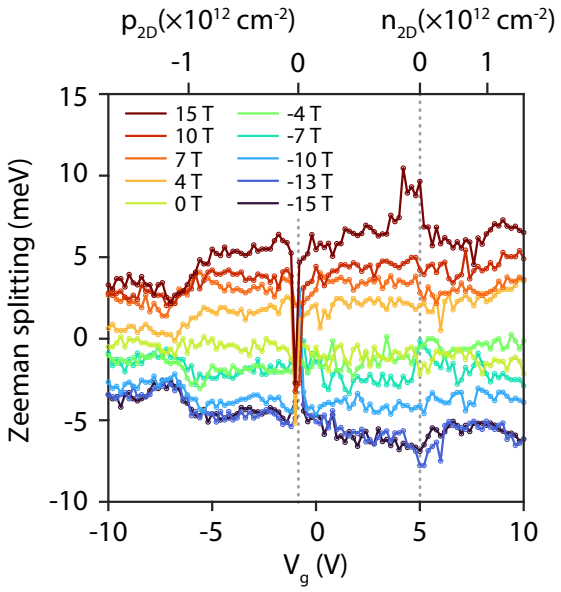

Figure 7.3: Interlayer exciton Zeeman splitting for different magnetic fields. Grey dashed lines indicate where free carrier doping begins determined from the onset of the charged interlayer excitons.

which we can fit to determine the neutral and charge interlayer exciton g-factor. Figure 7.4 shows the extracted the $g_{singlet}(V_g)$ from linearly fitting the Zeeman shift for the various B. We also show a second data set with a larger density range where we assume the g-factor is linear for a single $B = 15$ T measurement (purple). We observe significant modulation in the measured $g_{singlet}(V_g)$ with free carrier density. In the $p-$doped regime, we observe a flat $g_{singlet}(V_g) \approx 6$ until reaching a critical density of $p_{2D} \approx -1 \times 10^{12}$ cm^{-2} where $g_{singlet}(V_g)$ drops to around 4. In the $n-$doped regime, the behavior is more subtle, with an increase of the $g_{singlet}(V_g)$ to around 8 at around $n_{2D} \approx 1.5 \times 10^{12}$ cm^{-2} before steadily decreasing at larger densities. We focus on the features that occur near $\sim \pm 1 \times 10^{12}$ cm^{-2} and discuss two possible mechanisms. In the end, the results are not well understood yet and require further studies to understand the subtleties in the data.

First, we consider a single particle band model. In the simple picture, $g_{singlet}$ can be considered as a combination of single particle band shifts of the $MoSe_2$ conduction band and the WSe_2 valence

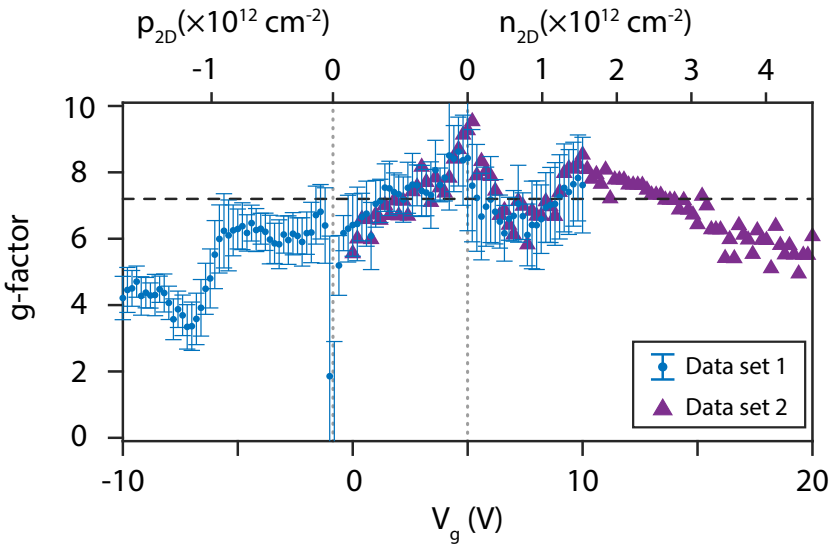

Figure 7.4: Interlayer exciton g-factor vs free carrier density extracted from linear fits to the Zeeman shift at various B fields. Grey dotted lines indicate where free carrier doping begins determined from the onset of the charged interlayer excitons. The black dashed line indicates the single particle calculated $g_{singlet}$.

bands[†]:

$$g_{singlet} = 2(g_{VB} - g_{CB}). \tag{7.6}$$

Using the calculated values in the previous section, we expect a g-factor shift $g_{singlet} = 7.2$ (dashed black line in Fig. 7.4). The measured g-factor is consistent with this calculated value in the neutral regime, but the simple picture cannot describe the density dependence.

Previous measurements of the single particle g-factors have shown enhancements near the band edge in both the WSe_2 valence band[22,146] and the $MoSe_2$ conduction band[20]. These enhancements are attributed to the scaling of the Coulomb interaction energy, which are strongly enhanced at lower densities where the screening effects are reduced. If both g_{VB} and g_{CB} are enhanced at the band edge, the effects could cancel out at low carrier densities. As the electron or hole density is increased though, the enhanced g-factor could be reduced in one of the bands, leading to a density dependence in the g-

[†]This is equivalent to the calculation done in Section 6.3

factor. The enhancements at very low densities could be suppressed by the presence of a finite density of interlayer excitons or disorders near the bottom of the bands, which could explain the saturation in the g-factor at finite doping in the $p-$doped regime. While this could explain $g_{singlet}$ decreasing in the $p-$doped regime and the small increase in the $n-$doped regime, it contradicts with the steady decrease in $g_{singlet}(V_g)$ above $n_{2D} \approx 2 \times 10^{12}$ cm^{-2}.

Alternatively, we note that the critical density for the decrease (increase) in the $p-(n-)$ doped g-factor is constant with respect to the magnetic field (Fig. 7.3). This rules out magnetic field induced quantum states such as Landau level formation or paramagnetism[45], which should shift the critical density as a function of B. The puzzling behavior could be related to crystallization of the free carriers. Generalized Wigner crystal states have been shown to exist by either matching the carrier density in each layer, such as in h-BN separated $MoSe_2$ homobilayers[150], or at partial fillings of the moiré unit cell in WSe_2/WS_2 heterobilayers[151,152,153,154]. We can estimate the moiré density (one charge per moiré unit cell) as

$$n_0 = \frac{2}{L_M^2\sqrt{3}} \tag{7.7}$$

where $L_M = \frac{a}{\sqrt{((a-a')/a)^2+\theta^2}}$ is the moiré length scale determined by the twisting angle θ and lattice mismatch, and a is the larger of the lattice constants. Using the lattice constants for $MoSe_2$ ($a = 0.319$ nm)[15] and WSe_2 ($a' = 0.316$ nm)[15] and an estimated $\theta \approx 0.81°$ (Appendix C.1), we get $n_0 \approx 1 \times 10^{12}$ cm^{-2}, closely matching the density at which we observe dips in the g-factor. Strong interactions at half-filling of the moiré band ($n_{2D} = n_0$) could result in an increase in the effective mass of carriers. The suppression of the g-factor in the $p-$doped region would correspond to a 3-fold increase in the effective hole mass near this density. The details of how the generalized Wigner crystal state manifests with respect to the interlayer excitons though is still an open question and would be a promising avenue for exploring charged exciton crystals.

We briefly discuss the large Zeeman splittings near the band edges. At high magnetic fields, the

opposite valley polarization for the neutral and charged interlayer exciton makes distinguishing the charged interlayer exciton onset difficult to identify (Fig. 7.1(c)-(d)). This is further compounded by the charged interlayer exciton binding energy being smaller than the linewidth of exciton emission. Thus, for example, the observed "enhancements" at the band edges for $B < 0$ are from comparing the neutral interlayer exciton emission from $\sigma-$ with the charged interlayer exciton emission in $\sigma+$. Further studies with a narrower linewidth sample could reveal a paramagnetic charged interlayer exciton state similar to observations in monolayers[45].

7.4 Dual-gate mapping of valley polarization and exciton g-factor

In the single-gate measurements, once the layer becomes degenerately doped, we can largely exclude electric field contributions to the PL emission (Appendix D). To confirm, this we measure the circularly polarized PL at $B = 15$ T as a function of both V_{tg} and V_{bg}. This allows us to separate the electric field and carrier density components in the undoped regime and also allows us to measure over a larger range of carrier densities. In Figure 7.5(a)-(b), we show the extracted exciton g-factor and valley polarization as a function of both gates. In Figure 7.5(c)-(d), we show the same data as a function of the electric field and carrier density (calculated based on Appendix D). Immediately, we can see the carrier density has a greater effect than the electric field. The defining features discussed in the previous sections such as the drop in the g-factor in the $p-$doped regime (yellow dashed line) and the valley polarization (grey dotted lines) are dictated by the onset of the free carrier doping rather than the electric field modulation. While finer tuning may occur due to the electric field, they are not the dominant effects observed in these measurements.

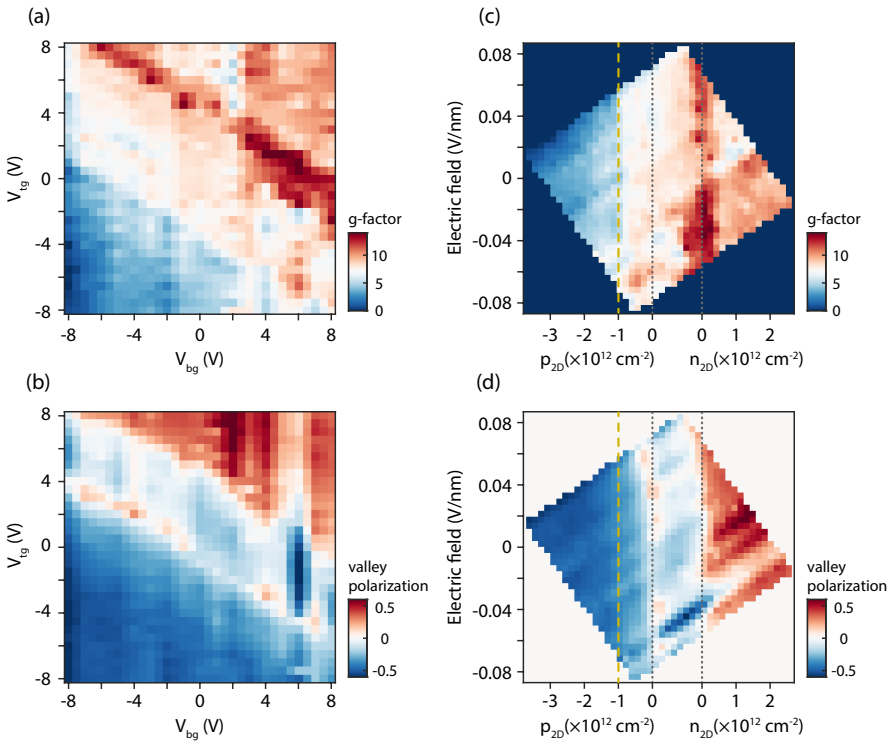

Figure 7.5: 2D gate scans of the g-factor and valley polarization at B = 15 T. (a) Interlayer exciton g-factor as a function of V_{tg} and V_{bg}. (b) Interlayer exciton valley polarization as a function of V_{tg} and V_{bg}. (c)-(d) Same as (a)-(b) except shown as electric field and carrier density dependence. Note the electric field values change once a layer begins to be doped. Grey dotted lines correspond to the onset of the charged interlayer exciton emission. Yellow dashed line indicates the drop in the g-factor.

7.5 Extracting the spin-orbit conduction band splitting

We further explore the charged interlayer exciton behavior upon reaching the second conduction band. The emergence of the spin-triplet interlayer exciton at high density was shown in Chapter 6. In Figure 7.6(a), we show the density dependence of the maximum PL intensity and find the triplet interlayer exciton overtakes the singlet interlayer exciton upon reaching $n^*_{2D} \approx 1.3 \times 10^{13}$ cm^{-2}. Using n^*_{2D} and taking the effective mass of the first conduction band to be $m_e^{(1)} = 0.8\, m_0$ [20] in units of bare electron mass (m_0), we calculate the energy separation between the spin-orbit split $MoSe_2$ conduction band

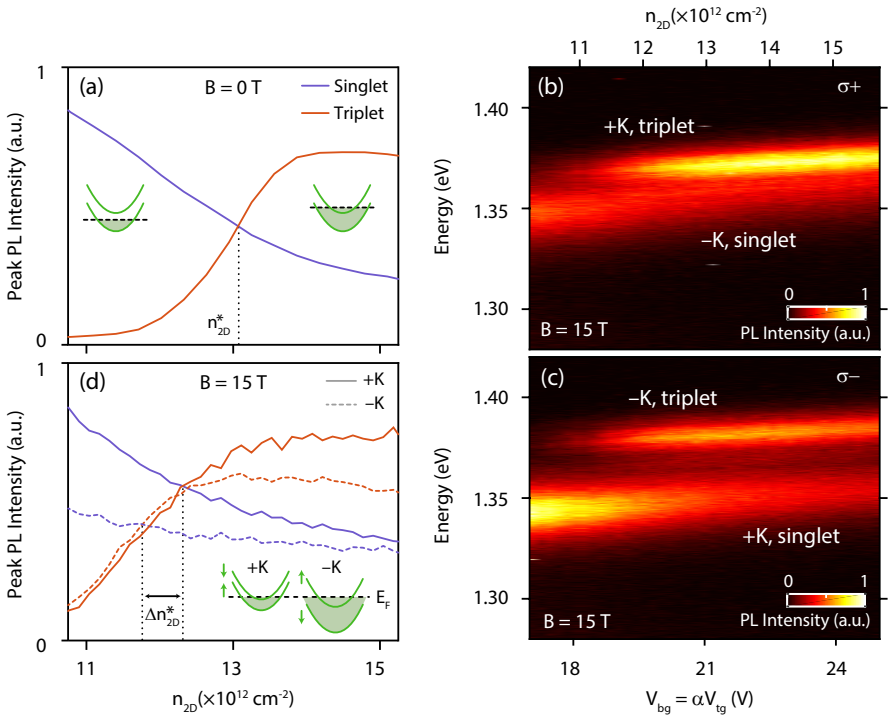

Figure 7.6: (a) PL peak intensity as a function of n_{2D} at B = 0 T (extracted from Fig.6.1(e)). Dotted black line indicates the cross over density n^*_{2D}. Left (right) inset: band filling before (after) the triplet state is brightened. (b) Photoluminescence (PL) spectra with $\sigma+$ collection using a cross-polarization measurement scheme at B = 15 T vs $V_{bg} = \alpha V_{tg}$. The corresponding carrier density is on the top x-axis. (c) Same as (b) for $\sigma-$ collection. (d) PL peak intensity as a function of n_{2D} for B = 15 T. The black dotted lines correspond to the singlet-triplet crossovers. Inset: Zeeman splitting of the conduction band states.

minima:

$$\Delta E_{CB} = \frac{\pi\, n^*_{2D}\, \hbar^2}{\nu\, m_e^{(1)}} \approx 19.5 \text{ meV}, \tag{7.8}$$

where we use $\nu = 2$ for the K-valley degeneracy factor. The estimated ΔE_{CB} is consistent with theoretically calculations [139,15], but smaller than previous experimental values [20].

In Figure 7.6(b)-(c), we use a dual-gating scheme (Appendix D) to measure the circularly polarized PL emission near the singlet to triplet transition at $B = 15$ T. We observe the singlet and triplet interlayer excitons shift in opposite directions for $\sigma+$ and $\sigma-$ polarized PL emission, consistent with the sign of the expected g-factors. Thus, we can label the PL peaks in the $\sigma+$ polarized light as singlet

(triplet) excitons from the $-K$ ($+K$) valley. In Figure 7.6(d), we plot the maximum PL intensity of the four exciton species and observe a shift in n^*_{2D} for the $\pm K$ valleys. The shift in density, $\Delta n^*_{2D} = n^*_{2D}(-K) - n^*_{2D}(+K) = 0.55 \times 10^{12}$ cm^{-2}, corresponds to an energy splitting of $\Delta E = 0.42$ meV, assuming a degeneracy of 4 at this density as the energy scales should be comparable to the temperature ($T = 5$ K). This energy splitting should correspond to the single band splitting of the second conduction band (CB2)

$$\Delta E_{Z,CB2} = 2(g_K - g_S)\,\mu_B\,B = 0.43 \text{ meV} \tag{7.9}$$

where g_K and g_S are the valley and spin contributions as defined earlier. We note that the flipped spin in the second conduction band of $MoSe_2$ results in a smaller Zeeman splitting than in the first conduction band (inset of Fig. 7.6(d)). Indeed, we find the measured value agrees very well with the single band splitting of the second conduction band.

7.6 Conclusion

In summary, we have measured the neutral and charged interlayer excitons under magnetic fields and observed carrier density dependent valley polarization and effective exciton g-factors. We also showed through the onset of the triplet exciton, we can extract the $MoSe_2$ conduction band splitting. Moreover, we can extract the splitting of the second conduction band under magnetic field, which is consistent with the expected single particle splitting. While parts of the charged interlayer exciton behavior can be explained by several different theories, including enhanced single particle g-factors or generalized Wigner crystallisation, a conclusive explanation cannot be made as of now. Still, we find these studies to be a strong motivation for further exploring the interlayer excitons under magnetic fields. The interplay between the charged interlayer excitons and the quantum hall states or generalized Wigner crystal states in these materials could provide an interesting platform for optically

coupling to states that are normally probed purely via transport.

If you do not believe you can do it then you have no chance at all.

Arsène Wenger

8

Toward the Interlayer Exciton Condensate

A strong motivation for studying dipolar exciton gases is the theoretical prediction for creating a Bose-Einstein condensate (BEC)[113,73,132,83]. For interlayer excitons in transition metal dichalcogenide (TMD), the predicted condensate temperature can be as large as $T = 100$ K. Furthermore, the interlayer excitons have since been shown to have a wide range of tunability in their emission energy[13,14], spin-polarization[64,65,137,77], and diffusion characteristics[14,155].

Once realized, the interlayer exciton BEC would provide a rich platform for exploring BEC physics in the solid state.

Previous reports have used coherence measurements, along with other transport and optical signatures, to claim evidence for the interlayer exciton condensate[66,67]. In this chapter, we will outline our efforts to realize the interlayer exciton condensate, which combines elements of both of the previous studies. Specifically, we aim to electrically generate the interlayer excitons by tuning the interlayer bias (as discussed in Chapter 6) in a $MoSe_2$/h-BN/WSe_2 heterostructure. We observe clear evidence of interlayer excitons forming between the further separated layers, with a larger dipole moment[120] and darker emission. Furthermore, we observe a resonance in the interlayer current when tuning the bias and relative carrier densities corresponding to a strong enhancement in the electroluminescence. Finally, we present second-order coherence, $g^{(2)}(\tau)$, measurements of the interlayer excitons that show evidence towards an interlayer exciton condensate.

8.1 Interlayer excitons with increased dipole moment

We focus our studies on a dual-gated, h-BN encapsulated $MoSe_2$/h-BN/WSe_2 heterostructure (details in Appendix C). Figure 8.1(a) shows the schematic of the device and the electrical circuit. Each layer has Pt contacts with matching contact gate areas, allowing for transparent injection of the free carriers. A single layer of h-BN is placed between the active $MoSe_2$ and WSe_2 layers, providing a tunneling barrier that weakly decouples the layers, but not enough that interlayer excitons cannot form. A corner of the device does not have the h-BN spacer, allowing us to compare the optical behavior for the two regions. In Figure 8.1(b), we show an optical microscope image of the device with the $MoSe_2$, WSe_2, and h-BN spacer outlined.

We characterize the device with photoluminescence (PL) spectroscopy using a laser wavelength of 660 nm and excitation power of 20μW at different spatial locations. In Figure 8.1(c), we show the

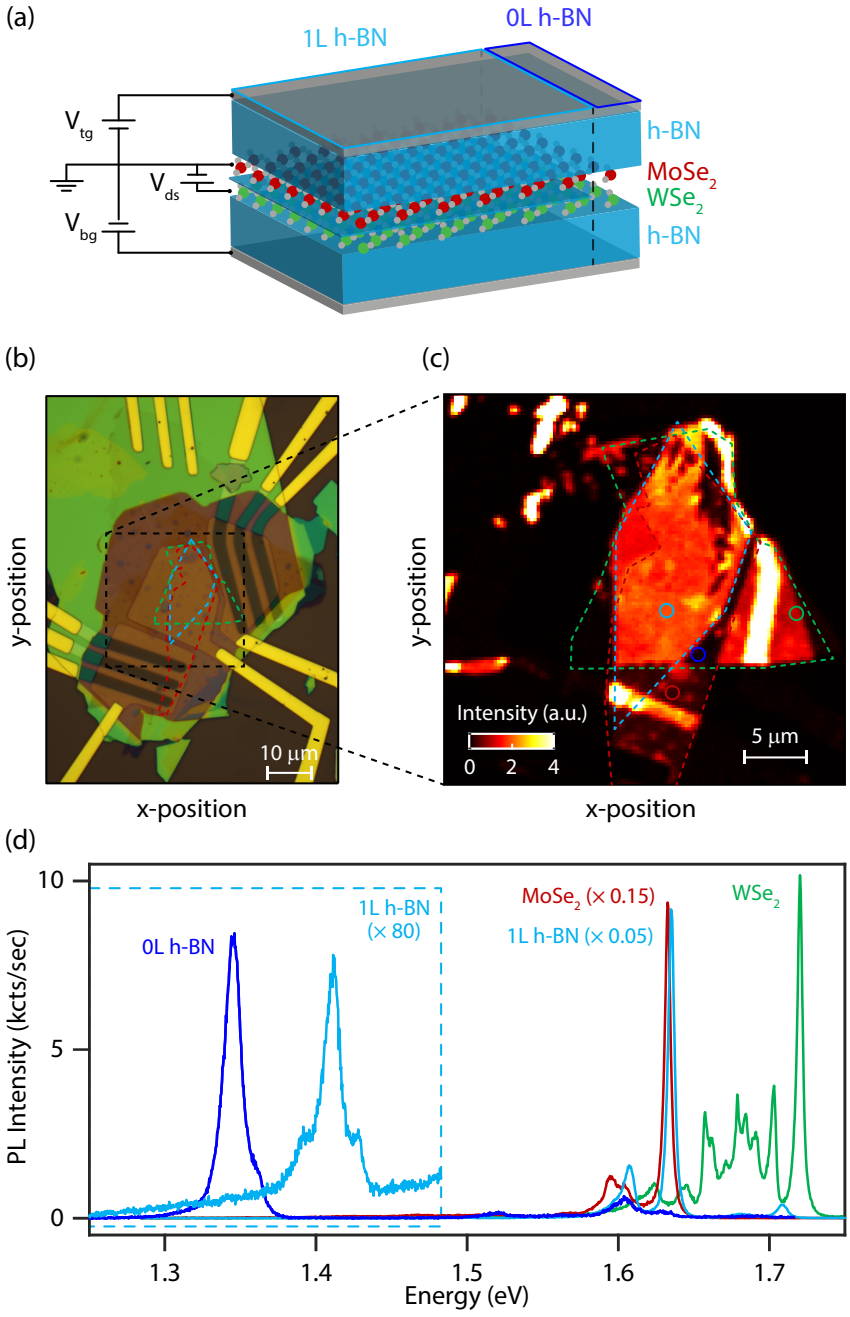

Figure 8.1: Photoluminescence from $MoSe_2$/h-BN/WSe_2 heterostructure. (a) Schematic of the device showing the circuit and outlining the regions where there is 1L or 0L of h-BN spacer. (b) Optical image of the device with $MoSe_2$ (red), WSe_2 (green), and single layer h-BN layer (teal) outlined. (c) Scanning PL spatial map in the area marked by the black dashed line in (b). (d) PL spectra from representative positions marked in the PL map in (c).

spatial PL emission from the black dashed area outlined in Figure 8.1(a). We observe suppressed PL emission in the 0L h-BN area, but strong emission from the monolayer $MoSe_2$ (dashed red area) and WSe_2 (dashed green area) layers as well as the area with the h-BN spacer (dashed teal line). Figure 8.1(d) shows the spectra from 4 representative positions (circles in Fig. 8.1(c)). In the monolayer regions, we observe intralayer exciton emission from the $MoSe_2$ (red) and WSe_2 (green) separately. We note that the emission is dominated by the excitons, which indicate less defects in the materials. In the heterostructure 0L h-BN region (blue), the layers are directly touching and we observe interlayer excitons. The fast charge transfer and prominent interlayer exciton emission explains the quenching of the PL emission in the spatial map. In the heterostructure region with 1L h-BN (teal), the h-BN layer suppresses charge transfer so that significant intralayer exciton recombination occurs. Still, we observe a peak at 1.41 eV, a lower energy than the intralayer transitions but higher than the interlayer exciton emission from the 0L region $\sim$ 1.35 eV.

To confirm the interlayer nature of the lower energy excitonic emission in the 1L region, we measure the PL as a function of the electric field. We apply oppositely polarized voltages scaled by the top and bottom h-BN thicknesses ($V_{tg} = -\alpha V_{bg}$, where $\alpha = 0.714$ is the ratio between the top and bottom h-BN layer thicknesses), which applies only an electric field without electrostatically doping the layers (details in Appendix D). In Figures 8.2(a)-(b), we present the electric field dependent PL spectra in the 0L h-BN and 1L h-BN regions, respectively. Interestingly, we observe a larger shift in the in the 1L h-BN region. We calculate the electric field (E_{bs}) as

$$E_{bs} = \frac{\varepsilon_{hBN}}{\varepsilon_{eff}} \cdot \frac{V_{tg} - V_{bg}}{t_{total}}, \tag{8.1}$$

where ε_{eff} is the effective dielectric felt in the TMD heterostructure and t_{total} is the combined top and bottom h-BN thickness. For the 0L h-BN, we assume $\varepsilon_{eff} = \varepsilon_{TMD} = 7.2$ as the interlayer exciton will be primarily within the TMD layers. For the 1L h-BN, we use $\varepsilon_{eff} = \varepsilon_{h-BN} = 3.9$ as the h-BN

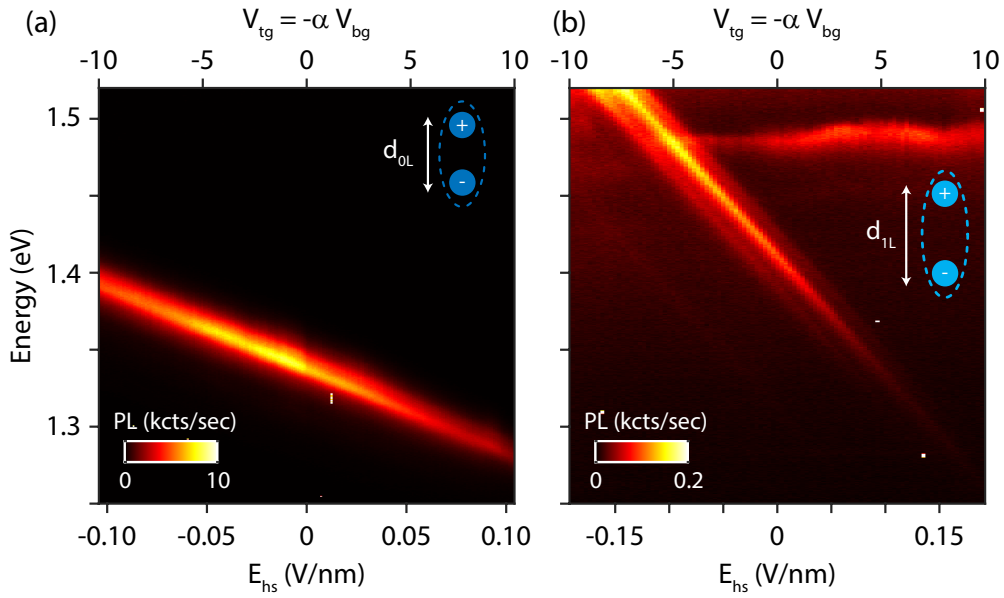

Figure 8.2: Electric field dependent PL emission in the (a) 0L and (b) 1L heterostructure regions. The emission energy is tuned by the linear Stark effect. Insets: interlayer exciton with smaller or larger electron hole separation for the 0L and 1L h-BN regions, respectively.

spacer will make up a large portion of the effective dielectric. We note that this is an overestimation and the actual ε_{eff} will have contributions from both the TMD and h-BN layers. We expect the interlayer exciton energy to shift due to the linear Stark effect:

$$\Delta E_{IE} = -e\, d\, E_{bs}, \tag{8.2}$$

where ΔE_{IE} is the interlayer exciton energy shift, e is the electron charge and d is the interlayer distance. From the slope of the shifts, we obtain $d_{0L} = 0.55$ nm and $d_{1L} = 0.76$ nm. The difference in the interlayer distance is close to the expected thickness of a single layer of h-BN $\sim$ 0.3 nm. The discrepancy is likely due to the overestimation of the electric field in the 1L h-BN case. Nevertheless, this confirms that the low energy emission peak in the 1L h-BN are interlayer excitons with a larger dipole moment. The higher energy of the 1L h-BN interlayer exciton emission at $E_{bs} = 0$ V/nm is

consistent with a weaker binding energy expected for a greater interlayer distance separation[74], which we can extract to be $\sim$ 60 meV. We note that the lifetime of the interlayer excitons in the 1L h-BN area should also be significantly longer, which is suggested by the significantly darker interlayer PL.

8.2 Electrical transport characteristics

To electrically generate the interlayer excitons, we first characterize the transport properties of the device. We apply a bias voltage (V_{ds}) on the WSe_2 layer while grounding the $MoSe_2$ layer and simultaneously compensating any changes in the carrier density with a combination of the top and bottom gates, $V_{tg} = \alpha V_{bg}$ (details in Appendix D). Figure 8.3(a) shows the interlayer current (I_{ds}) as a function of V_{ds} and $V_{tg} = \alpha V_{bg}$. We can drive current when the Fermi level (E_F) is tuned into the conduction band of the $MoSe_2$ or the valence band of the WSe_2 (Fig. 8.3(a) top and bottom insets). However, we also observe a strong enhancement in I_{ds} along a line matching $V_{ds} \approx 0.56 V_{tg}$, which should be when the Fermi level is in the gap (Fig. 8.3(a) middle inset). In Figures 8.3(b)-(c), we take linecuts along constant $V_{tg} = \alpha V_{bg}$ or constant V_{ds} and find unconventional behavior in the I_{ds} curves. For constant $V_{tg} = \alpha V_{bg}$, the I_{ds} increases smoothly until reaching a plateau. For a range of $\sim$ 1 V, the I_{ds} remains constant before increasing again. For constant V_{ds}, the I_{ds} shows a sharp cusp at a critical doping density. The observed behavior is not consistent with the expected transport behavior in a type-II heterojunction. The I_{ds} vs V_{ds} curves are expected to show rectifying *p-n* diode behavior. For the I_{ds} vs $V_{tg} = \alpha V_{bg}$ curves, we expect larger current when the heterostructure is doped and no current when the Fermi level is within the gap.

There are two possible explanations for the peculiar behavior. If the Fermi level is tuned within the gap such that the electron density (n) and hole density (p) are matched, the formation of interlayer excitons could enhance tunneling between the layers beyond the non-interacting single particle picture[66]. This is supported by the gate voltage dependence, which tunes the charge carrier density.

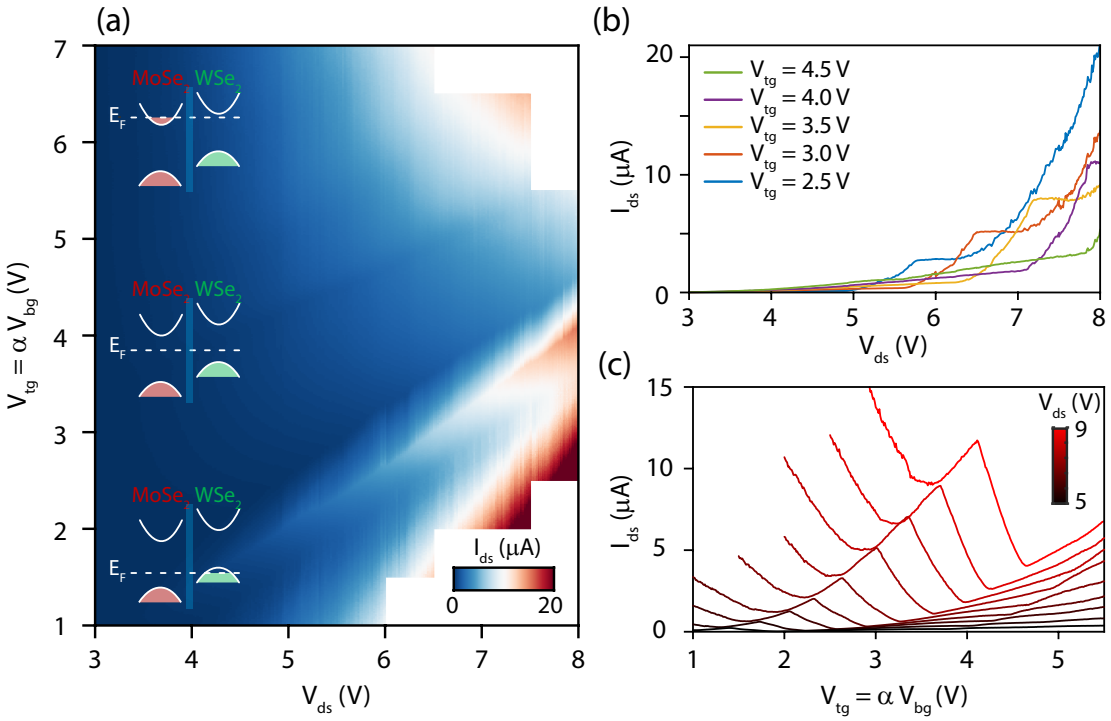

Figure 8.3: Interlayer current as a function of bias and gate. (a) Current (I_{ds}) as a function of the bias voltage (V_{ds}) and gate voltage ($V_{tg} = \alpha V_{bg}$). Inset: Band diagram of the heterostructure at various Fermi levels at roughly the corresponding $V_{tg} = \alpha V_{bg}$. (b) I_{ds} vs V_{ds} linecuts along constant $V_{tg} = \alpha V_{bg}$ lines showing plateaus in the current. (c) I_{ds} vs $V_{tg} = \alpha V_{bg}$ linecuts at constant V_{ds} showing a cusp in the total current.

In this picture, the sharp cusp in I_{ds} as a function of $V_{tg} = \alpha V_{bg}$ (Fig. 8.3(c)) corresponds to the $n = p$ condition where we observe the maximum current. At larger $V_{tg} = \alpha V_{bg}$, the heterostructure becomes p- or n-doped and we observe single particle current. When changing the V_{ds} (Fig. 8.3(b)), we are tuning both the charge density and the total carriers injected into the heterostructure. For fixed $V_{tg} = \alpha V_{bg}$, the tunneling current will increase with V_{ds} until the $n = p$ condition is reached, after which the current plateaus because it is limited by the minority carrier (in this configuration, electrons). While a thicker h-BN layer would completely isolate the two layers except for this interaction induced tunneling, due to the 0L h-BN region, we find I_{ds} eventually increases again after plateauing with V_{ds}.

An alternative explanation is due to limitations in the injection current. If the contact resistances are large and the Fermi levels in the $MoSe_2$, WSe_2, and heterostructure regions are not independently controlled, the total current can be dependent on the rates at which the different regions reach equilibrium rather than the interlayer tunneling rate between the two layers[156]. This injection limited current can describe the cusp-like behavior when the bands are inverted by an interlayer bias, which is incorrectly assumed by the electrostatic model in earlier experimental work[66]. Our devices have relatively transparent contacts to both $MoSe_2$ and WSe_2 with separate gates in the heterostructure and the monolayer regions, which should mitigate this behavior. Furthermore, we do not observe an inversion of the electron and hole bands in our device as we will show in our absorption and electroluminescence data in the following sections. Thus, the intriguing transport behavior cannot be trivially described by the injection limited current model. Instead, in our measurements, we observe large background currents when the Fermi level is tuned to match the doping layer in the monolayer regions (either *n*- or *p*- doping), which could be closer to the injection limited current picture. We note that this occurs away from the $n = p$ condition and appears to be a separate effect. Regardless, while the contact resistances should be greatly reduced compared to other works[66] and the electrostatic conditions are not the same as for the trivial injection current limited theory[156], it is still possible our observations are due to an alternative effect rather than enhanced tunneling mediated by interlayer exciton formation.

8.3 Tuning the carrier density

To understand the bias voltage effect on the carrier density, we use the intralayer exciton absorption spectra to measure the change in the doping in the sample. In Figure 8.4(a), we show the optical reflection contrast in the 1L h-BN region as a function of the dual-gate tuned $V_{tg} = \alpha V_{bg}$ (details in Appendix D) for $V_{ds} = 0$ V. The two strong reflection features at 1.67 eV and 1.73 eV correspond to the intralayer exciton energies in the $MoSe_2$ and WSe_2, respectively. For a range of gate voltages

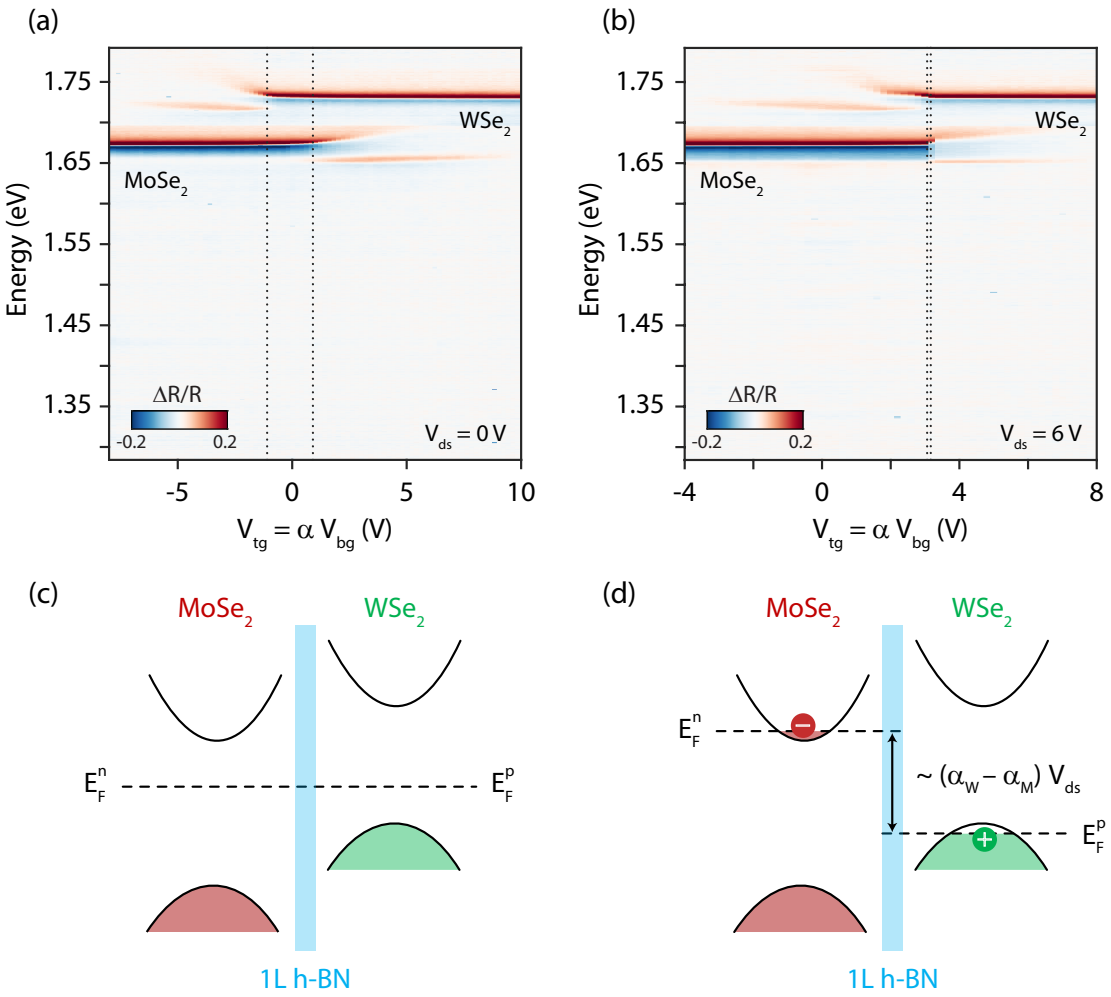

Figure 8.4: Reflection at finite bias voltage. (a) Reflection spectra as a function of $V_{tg} = \alpha V_{bg}$ at $V_{ds} = 0$ V. Black dashed lines indicate the intrinsic regime determined by a 60% drop in the reflection intensity. (b) Same measurement but at $V_{ds} = 6$ V shows a much narrower intrinsic region. (c) Band diagram in the undoped regime for $V_{ds} = 0$ V, where the electron and hole Fermi levels (E_F^n and E_F^p, respectively) are tuned together by the gate voltage. (d) Band diagram for $V_{ds} > 0$ V, where V_{ds} and $V_{tg} = \alpha V_{bg}$ tune the Fermi energies of the two layers separately. Due to only 1L h-BN, the interlayer bias is scaled by α_M and α_W in the $MoSe_2$ and WSe_2 layers.

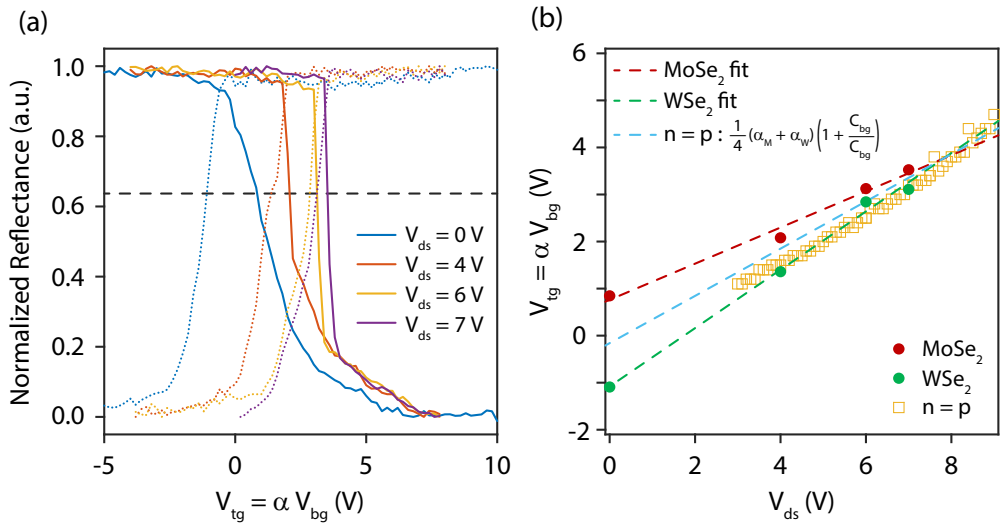

Figure 8.5: Analysis of the reflection spectra (a) Linecut of the $MoSe_2$ (solid) and WSe_2 (dotted) exciton resonance in the reflectance vs V_{tg} spectra at various V_{ds}. Dashed black line ≈ 0.63 is the cutoff for determining the beginning of the layer doping. (b) Fitted V_{tg} at the start of the n- (red) and p-doping (green) regimes from (a). Dashed lines are the fits to the electrostatic model. Blue dashed is the expected n=p condition from the calcuations using the fit values. Yellow squares show the n=p condition determined from the transport measurements.

(between the black dotted lines), we can observe neutral exciton reflection features from both layers indicating the quasi-Fermi level (E_F) is in the gap. The exciton feature give way to trions for p-doping in WSe_2 or n-doping in the $MoSe_2$. When we apply a bias voltage of $V_{ds} = 6$ V (Fig. 8.4(b)), the range of gate voltages where the layers are undoped becomes small. Schematics of the band alignment under both bias conditions are shown in Figures 8.4(c)-(d). For $V_{ds} = 0$ V, the Fermi level of the two layers are tuned together by the gate voltages. For $V_{ds} > 0$ V, the interlayer bias tunes the relative Fermi level between the layers. Equivalently, with forward bias ($V_{ds} > 0$), V_{ds} tunes the relative band alignment between the layers to create a flat band condition allowing current to flow. Since the layers are coupled across the h-BN layer and we have finite contact resistances, we assume the voltage on the two layers are not perfectly equilibrated with the contacts and are scaled by a factor of α_M and α_W for the $MoSe_2$ and WSe_2, respectively. The difference in the quasi-Fermi level in each layer would then be proportional to $(\alpha_W - \alpha_M) V_{ds}$.

In Figure 8.5(a), we take linecuts of the $MoSe_2$ (dotted lines) and WSe_2 (solid lines) exciton reflectance resonances for several bias voltages and extract the $V_{tg} = \alpha V_{bg}$ required to begin doping the layers. We use a cutoff intensity of 0.63, corresponding to approximately $1/e$ drop in intensity. We show the extracted values in Figure 8.5(b) where we observe different slopes for the two layers, indicating a bias induced interlayer electric field. We fit the values to our electrostatic model (Appendix D), obtaining $\alpha_M = 0.45$ and $\alpha_W = 0.73$. From the linear fits, we expect at $V_{ds} \approx 8$ V, the actual interlayer bias will be equivalent to the gap. This is consistent with our observations in the transport measurements (Fig. 8.3(a)), where we no longer observe an insulating regime between the electron and hole doped regimes. We use the fitted α_M and α_W to plot the expected slope for the density matched condition ($n = p$) and find reasonable agreement with the $n = p$ condition extracted from the transport measurements (yellow squares).

We note that in the ideal case where the interlayer resistance is the dominant effect, each layer would be equilibrated to their respective leads giving $\alpha_M = 0$ and $\alpha_W = 1$. While this is not the case, we are also not completely contact resistance limited where we expect $\alpha_M = \alpha_W$. Since the layers are not completely isolated though, we will not be able create an equilibrium density of charge carriers in each layer, such as in experiments with thicker h-BN spacer layers[66,157]. This is expected given the finite interlayer exciton recombination rates indicated by charge transfer across the layers. The lower resistance between the layers could be due to having only a single layer of h-BN spacer or having a region of the sample without the h-BN spacer, although the transport measurements imply these limitations may be in different doping regimes.

8.4 Theory of second-order coherence

The second-order coherence function, $g^{(2)}(\tau)$, quantifies the intensity fluctuations as a function of time delay and is referred to as the degree of second-order coherence. Physically it is measuring the

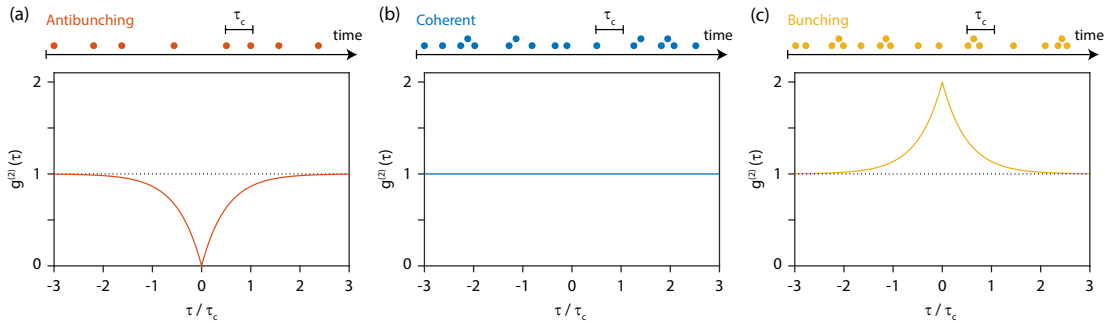

Figure 8.6: (a) Second-order coherence, $g^{(2)}(\tau)$, for antibunching case: $g^{(2)}(0) < 0$. For single-photon emitters such as atoms, photons can only be emitted one at a time. (b) $g^{(2)}(\tau) = 1$ for a coherent light source. Photon number follows a Poisson distribution and photons emit randomly in time. (c) For a thermal or chaotic light source, $g^{(2)}(0) > 1$. The photons exhibit bunching due to intensity fluctuations from the source. The coherence time τ_c indicates the time scale for the photon in antibunching case and intensity fluctuations in the bunching case.

probability of detecting two photons with a time delay, τ, which describes the correlation between these photons. In the classical description, the second-order coherence is defined as

$$g^{(2)}(\tau) = \frac{\langle I(t)I(t+\tau)\rangle}{\langle I(t)\rangle}, \tag{8.3}$$

where I is the light intensity (proportional to the number of photons) and t is time.

The second order coherence at $\tau = 0$ can indicate the type of photon statistics that is present. In single photon emitters, only a single photon can emit at a given a time, which means the probability of measuring a photon at $\tau = 0$ will be 0. This is described as photon antibunching and will result in $g^{(2)}(0) = 0$ (Fig. 8.6(a)). For a coherent light source, we expect a Poisson distribution of the number of photons, or photons emitting randomly in time. In this case, we expect a constant $g^{(2)}(\tau) = 1$ for all time delays (Fig. 8.6(b)).

For an incoherent light source, due to intensity fluctuations at the source, photon bunching occurs, or $g^{(2)}(0) > 1$ (Fig. 8.6(c)). In the classical case with Lorentzian broadened chaotic light, we expect

$$g^{(2)}(\tau) = 1 + |g^{(1)}(\tau)|^2 = 1 + e^{-2|\tau|/\tau_c}, \tag{8.4}$$

where $g^{(1)}(\tau)$ is the first order coherence function and τ_c is the coherence time of the light. For practical measurements, the linewidth of incoherent light sources are often very broad, and thus, τ_c can be shorter than the detection limit. Great efforts must be made to detect $g^{(2)}(0) > 1$ for incoherent light sources [158].

When the light approaches a phase transition from incoherent to coherent light, critical fluctuations in the intensity could result in measurable bunching at $g^{(2)}(0)$ with an enhancement in τ_c [66,159]. Specifically, $g^{(2)}(0)$ can be enhanced and τ_c can greatly exceed the expected coherence time for a given linewidth of the EL emission as well as the detection limit. Thus, observation of $g^{(2)}(0) > 1$ followed by a sharp drop to $g^{(2)}(0) = 1$ as we change the pump power or injection current can be indicative of a quantum phase transition. This behavior has been shown in lasing transitions in lasers [160,161] and exciton-polariton systems [162,163].

8.5 Quantum fluctuations in electrically generated interlayer excitons

With a more comprehensive understanding of the carrier density, we turn to the electrical generation of the interlayer excitons. In Figure 8.7(a), we apply $V_{ds} = 6.2$ V at the $n = p$ condition and collect spectrally filtered electroluminescence (EL) around 1.41 eV, the energy for the 1L h-BN interlayer excitons. We find that the EL emission extends across large parts of the 1L h-BN region but is brightest at the corner of the heterostructure along the shortest path from the WSe_2 to the $MoSe_2$ monolayers. We observe EL emission even when filtering the 0L h-BN energy ($\sim$ 1.35eV) due to the spectral tails of the EL. In Figure 8.7(b), we measure the spectrally filtered EL as a function of V_{ds} and $V_{tg} = \alpha V_{bg}$ from a spot near the center of the heterostructure (white circle in Fig. 8.7(a)), avoiding spectral leakage from the 0L h-BN interlayer excitons. We only observe EL along a narrow condition near the $n = p$ condition, consistent with the cusp appearing in $I_{ds}(V_{tg})$ in our transport measurements.

In Figure 8.8(a), we show the EL spectra from the 1L h-BN region of the sample for various bias

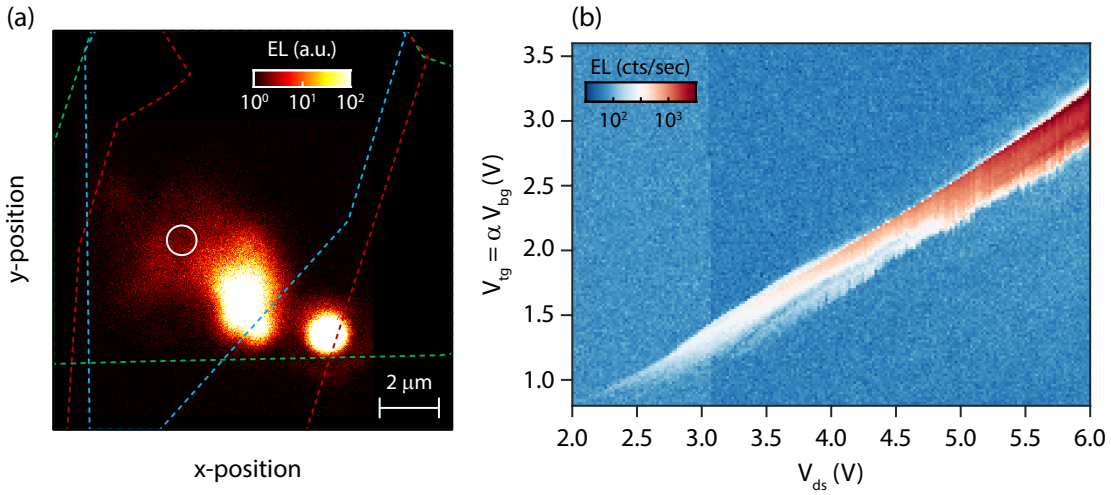

Figure 8.7: (a) Electroluminescence (EL) map for $V_{ds} = 6.2V$ at the $n = p$ condition. The EL is spectrally filtered for the 1L h-BN interlayer excitons. White circle indicates the collection for the following EL measurements. (b) EL counts as a function of V_{ds} and $V_{tg} = \alpha V_{bg}$ from the white circle in (a) showing a narrow range for EL counts. The EL closely follows the $n = p$ condition observed in the transport measurements.

voltages along the $n = p$ condition. We observe two peaks (IX_1 and IX_2) near 1.41 eV, corresponding to interlayer excitons in the 1L h-BN area, with a separation of $\sim$ 13 meV. The interlayer exciton energies do not shift significantly supporting the fact that the band alignment remains largely unchanged. We also observe EL from the intralayer exciton peaks, most prominently from the $MoSe_2$ exciton (X^0_M) and trion (X^-_M). In Figure 8.8(b), we use a Hanbury Brown-Twiss interferometer setup (details in Appendix B) to measure the second order coherence function ($g^{(2)}(\tau)$, where τ is the time delay) of the combined IX_1 and IX_2 peak as a function of V_{ds}. Interestingly, we observe photon bunching ($g^{(2)}(0) > 1$) for a range of V_{ds} indicating bias-voltage induced critical quantum fluctuations[66]. Above or below this voltage range, $g^{(2)}(0) = 1$. The observation of $g^{(2)}(0) = 1$ can be due to a decrease in the coherence time (τ_c) below the detection limit[162] ($\sim$ 300 ps), or, more fascinatingly, due to a coherent state or condensate where the EL statistics is Poissonian.

In Figure 8.8(c), we show the Gaussian fitted peak intensities of IX_1, IX_2, X^-_M, and X^0_M to understand the evolution of the excitonic peaks with the bias voltage. We also show the measured current

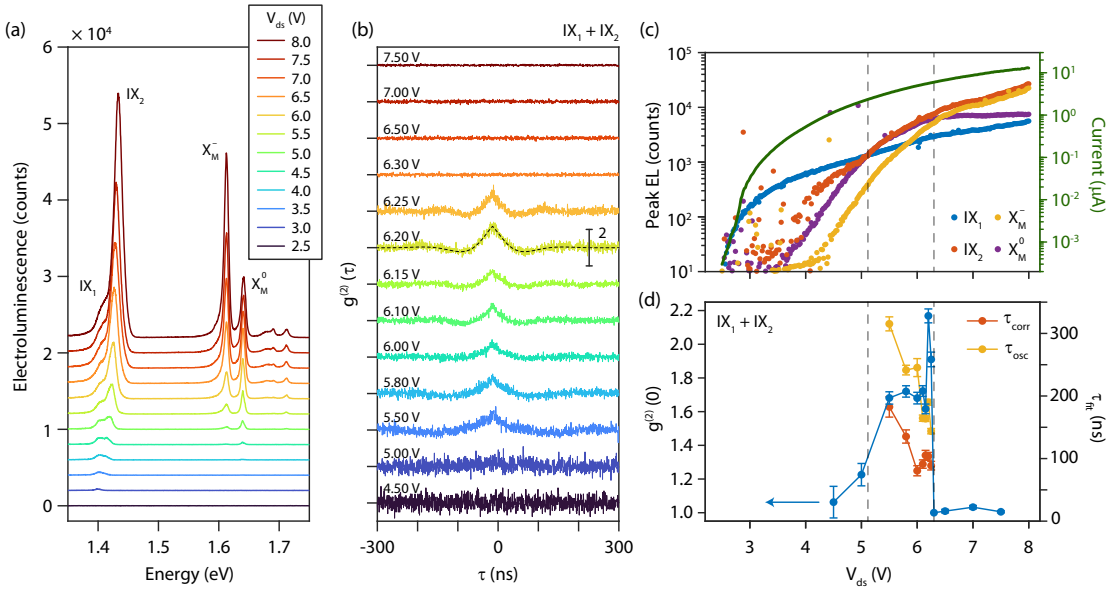

Figure 8.8: (a) Electroluminescence (EL) spectra for various V_{ds} along the $n = p$ condition. Each spectra is offset by 2×10^3 counts. Two interlayer exciton peaks in 1L h-BN area (IX_1 and IX_2) and the $MoSe_2$ trion (X_M^-) and exciton (X_M^0) peaks are used in later analysis. (b) EL intensity correlation function, $g^{(2)}(\tau)$, from the IX_1 and IX_2 peaks at various V_{ds}. Each curve is offset by 2. Black dashed line shows a representative fit to the $g^{(2)}(\tau)$. (c) Fitted peak intensity for IX_1, IX_2, X_M^- and X_M^0 as a function of V_{ds}. Right axis: corresponding current (I_{ds}). (d) Fitted $g^{(2)}(0)$ from (b) as a function of V_{ds} showing EL fluctuations for a range of V_{ds} before rapidly decreasing back to 1. Right axis: The fitted time scales τ_{corr} and τ_{osc}.

(I_{ds}) over the same range. We find that the IX_1 peak and I_{ds} scale similarly with the V_{ds}. However, the onset of IX_2 occurs at a larger V_{ds} and eventually overtakes IX_1 in intensity at $V_{ds} \approx 5$ V. For the intralayer peaks, X_M^- overtakes X_M^0 when the X_M^0 peak intensity abruptly saturates at $V_{ds} \approx 6.3$ V. We note that the current does not have any defining features at these critical voltages. In Figure 8.8(d), we show the fitted $g^{(2)}(0)$ as a function of the bias voltage. We find critical EL intensity fluctuations ($g^{(2)}(0) > 1$) are only present between the two critical voltages discussed above. This suggests the onset of IX_2 is important for observing the $g^{(2)}(0) > 1$, while the saturation of the X_M^0 coincides with the sharp decrease in $g^{(2)}(0)$.

The observation of $g^{(2)}(0) > 1$ for a small range of V_{ds} suggest the EL intensity fluctuations might be induced by a phase transition, which disappear upon reaching the condensate phase[66,162]. Unlike

in previous EL coherence measurements[66], the critical fluctuations in our experiment originate from the interlayer excitons. Specifically, IX_2 appears to be the relevant interlayer exciton species, which coincides with the fluctuations. We speculate that IX_2 and IX_1 could be the interlayer exciton and charged interlayer exciton, respectively, where the energy splitting matches previous reports of the charged interlayer exciton binding energy[14,108]. In this case, only the exciton, a composite-boson, would follow Bose statistics and be able to form a condensate. Alternatively, IX_2 could be an entirely separate emission peak specific to the condensate. We also observe X_M^- intensity increasing across both critical voltages similar to IX_2. This could be an electron from the longer-lived condensate phase forming a trion with the shorter-lived intralayer exciton and enhancing recombination, similar to previous experiments[66]. The X_M^- emission would dominate recombination from the $MoSe_2$ once the condensate forms beyond the second critical V_{ds} when $g^{(2)}(0) = 1$, consistent with the observed plateau in the X_M^0 intensity.

The shape of the non-zero $g^{(2)}(\tau)$ can give us further insight on the time-scales involved in the intensity fluctuations. We fit the second-order coherence to a phenomenological equation (representative fit shown with a black dashed line in Fig. 8.8(b)):

$$g^{(2)}(\tau) = 1 + g^{(2)}(0)\, e^{-2|\tau|/\tau_{corr}} \cos\left(\frac{2\pi\tau}{\tau_{osc}}\right), \tag{8.5}$$

where τ_{corr} and τ_{osc} are the correlation and the oscillation timescales. We extract a $\tau_{corr} = 80 - 200$ ns and $\tau_{osc} = 150 - 300$ ns in the V_{ds} region where fluctuations are present. For an ideal thermal light source, we expect $\tau_{corr} = \tau_c$, which is determined by the radiative linewidth. However, for fluctuations induced by a phase transition, τ_{corr} can far exceed τ_c. In the fluctuation regime, the linewidth of IX_2 extracted from the EL spectra is approximately 12 meV (Fig. 8.9(b)), corresponding to $\tau_c \approx 27$ fs, nearly 7 orders of magnitude smaller than the measured τ_{corr}. Although the measured linewidth could have significant inhomogeneous broadening, the large discrepancy in the timescales suggests a phase

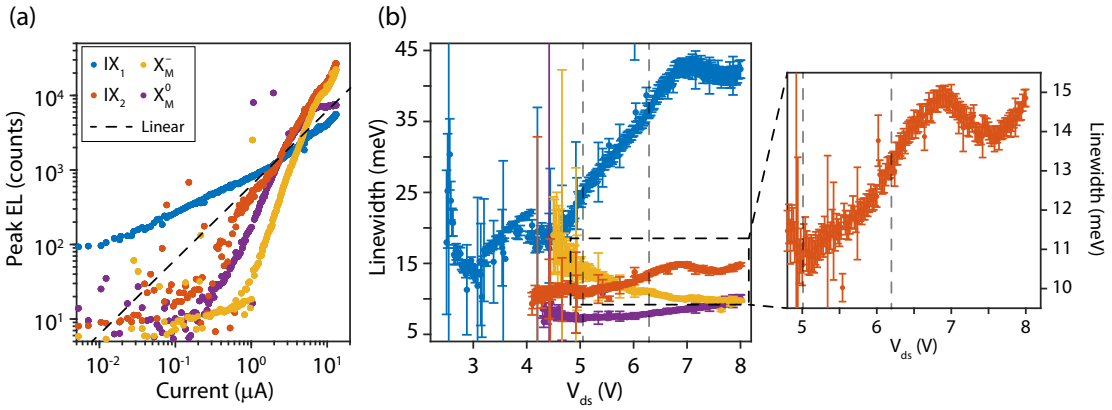

Figure 8.9: (a) Fitted peak EL as a function of the current (I_{ds}). The black dashed line indicates a linear dependence (power law of 1). (b) Fitted spectral linewidths as a function of V_{ds}. The grey dashed lines indicate the critical bias voltages discussed in the main text. Right: Zoomed in plot of the region outlined in the black dashed line showing the dip in linewidth.

transition induced enhancement in the correlation time of the EL*. We also comment on τ_{osc}, which indicates an exchange timescale in the EL fluctuations. The coupling energy scale, $E_{osc} = 2\pi\hbar/\tau_{osc} \sim 10$ neV, increases with the V_{ds} and is much smaller than any energy scale between the EL spectral features. Oscillations in $g^{(2)}(\tau)$, found in nanolasers, have been attributed to coherent oscillations between photons and carrier populations, which indicate the presence of a coherent field [160,161]. Since the interlayer excitons and resulting EL do not interact with an optical cavity in our system, any coherence and the corresponding oscillations must be from the interlayer excitons themselves. This is in contrast to lasing or exciton-polariton systems, which make use of an optical cavity to generate coherent light.

Finally, we discuss two additional supporting measurements that are consistent with a phase transition to an exciton condensate. Figure 8.9(a) shows the EL peak intensities as a function of the injection current (I_{ds}). We can see that IX_1 has a sublinear power law dependence with I_{ds}, while the other peaks all increase superlinearly. We find the power law scaling for IX_2 is $\sim$ 1.8 while the the intralayer excitons are as large as 2.3. The superlinear dependence is consistent with enhancements

*Conversely, for $\tau_c \sim 100$ ns, the radiative linewidth would need to be 3 neV, or 7 orders of magnitude smaller than the measured linewidths.

in the recombination rate across the phase transition [162], but could also be explained by other two photon processes such as Auger recombination. In Figure 8.9(b), we show the extracted linewidths from the EL spectra. When the excitons condense, we expect them to increasingly occupy the ground state, reducing their linewidth. Intriguingly, we find the linewidth increases for all of the peaks except for X_M^-. This is another indication that X_M^- recombination may be inheriting coherence properties. Furthermore, for a critical $V_{ds} \approx 7.5$, we find a slight decrease in the linewidth for all 4 peaks. In exciton-polariton systems, the spectral linewidth decreases significantly above the threshold power, because the linewidth upon is determined by the photon in the cavity [162,66]. While we do not observe such a sharp transition, it is not fully expected because the spectral linewidth, even in the pure exciton condensate, can still be limited by disorder and other broadening mechanisms in the system. Nonetheless, these observations may give us information about the phase transition which is clearly marked by the EL intensity fluctuations.

8.6 Conclusion

The experiments presented in this chapter strongly suggest that a phase transition occurs when tuning the V_{ds} along the $n = p$ condition. The intensity fluctuations in EL, measured via the second-order coherence function, cannot be explained by trivially incoherent light. Other supporting evidence such as the injection current dependence and extracted coherence times also suggest a transition may be occurring in this system. However, conclusively claiming an exciton condensate will require further experiments. The measurement of first-order spatial coherence, $g^{(1)}(x_1, x_2)$, where x_1 and x_2 are the spatial positions, would be a strong indication of the interlayer exciton condensate. The macroscopic occupation of the ground-state would enhance of the spatial coherence length far beyond the thermal de Broglie wavelength [81,164]. Performing first-order and second-order coherence measurements at varying temperatures should show the behavior disappear above the degeneracy temperature, which

we expect is on the order of 10s of Kelvin. Such experiments were performed in GaAs double quantum wells [165,81,82], but used laser excitations, which still draws concerns on the degree of laser-induced coherence. The realization of coherent EL emission mediated by only the excitonic states would be unrefutable evidence for the interlayer exciton condensate. While such an achievement would be monumental in its own right, the realization of the interlayer exciton BEC would open many new avenues for applications and novel studies of the exciton BECs.

The search for truth is more precious than its possession.

Albert Einstein

9

Conclusion: The future for interlayer excitons

Interlayer excitons are composite bosons with a permanent out-of-plane dipole moment. In this thesis, we have outlined many of the unique properties of the interlayer excitons and explored their phase diagram. We have used novel optoelectronic devices to control the interlayer

exciton properties, including their emission energies, lifetimes, and polarization properties. In Chapter 5, we have shown that the Mott transition is reached at large exciton densities, setting the upper bound for working in the exciton limit. In Chapter 8, we have shown promising results towards realizing an purely electrically generated interlayer exciton condensate. Once realized, interlayer excitons in the TMD heterostructures will be a promising candidate for fundamental physics and applications research. The interlayer exciton condensates will have many of the unique spin and valley properties which could be used to study two-fluid condensates. The introduction of charged interlayer excitons could also explore the interplay between fermionic and bosonic statistics near a condensate phase. In terms of applications, the realization of a high temperature condensate could lead to excitonic routers and transistors that maintain phase coherence.

One aspect that has not been discussed in depth in this thesis is the formation of moiré potentials [140,166,167,53,168,152,71,169,62,170,171,172,144,173]. Small twisting angles in the active layers can give rise to strong interactions that can modify the band structure and form spatially periodic potentials in the materials. This can be utilized to create spatially periodic arrays of interlayer excitons for use in studies of topological excitons or creating model exciton solids. In a sense, we can perform similar experiments as in cold atom BECs with optical traps to model a condensed matter systems with a solid-state system. One requirement for such experiments would be the realization of the interlayer exciton condensate. Another important consequence of the moiré potentials is the emergence of strongly correlated physics. In both twisted TMD and graphene heterostructures, unconventional superconductivity and correlated insulating states have been observed [174,175,176,177,151,153]. The interactions of optically active interlayer excitons and these correlated states could be an exciting direction of research.

Combining the potential for high condensate temperatures, rich correlated physics, and the relative ease of using 2D materials, the interlayer excitons in TMD heterostructure can be a promising area of research for many years. The work presented here lays the foundation for these exciting directions, which will hopefully bear fruit in fundamental understandings in condensed matter systems.

A

Fabrication details

This appendix will discuss fabrication details mentioned in the main chapters. Rather than a comprehensive step-by-step guide, it will different recipes and guides as well as specific tips and tricks for fabricating devices. In the end, mastering of the fabrication techniques will be dependent on the materials and stack design, which each person and project will need to develop. In a sense, true mastery is realizing that certain steps will require some artistic ingenuity.

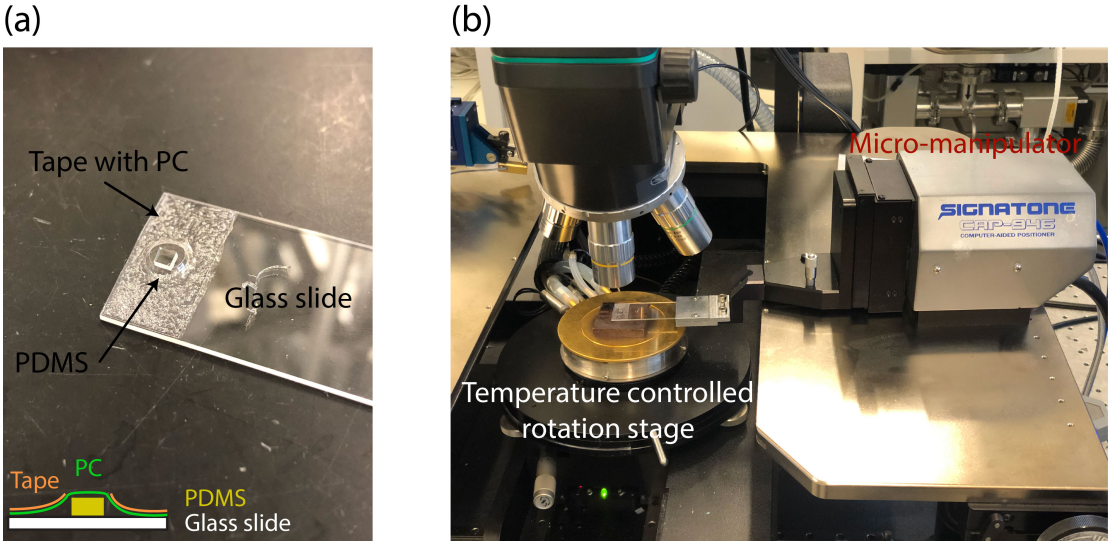

Figure A.1: (a) Photo of a prepared transfer slide with a cube of PDMS and scotch tape with PC on a glass slide. Inset: schematic of the transfer slide. (b) Photo of the transfer stage with the electrically-controlled micro-manipulator which holds the transfer slide. The sample is placed on the temperature controlled rotation stage.

A.1 PC TRANSFER DETAILS

The stamp we use for stacking the layers is based on polycarbonate (PC or PolyBisphenol A carbonate), which has a glass transition temperature around 150°. We begin by placing a cube of homemade polydimethylsiloxane (PDMS), which is a flexible gel that supports the PC film, on a glass slide. We prepare the PC film by pressing two glass slides together with the liquid PC between them. By sliding the glass slides apart, we get thin films of PC. We cut a strip of the PC that is on the glass slide, and pick it up using scotch tape with a hole punched in it. We can then align the PC in the hole of the scotch tape to the PDMS. Finally, we bake the completed transfer slide at $\sim 140°$, or at least the temperature anticipated during the pick up steps, to help the PC remain on the PDMS. Without this baking step, the PC could adhere to the SiO_2 substrate better than the PDMS and drop off prematurely. In Figure A.1(a), we show the finished transfer slide where the PC is held down on the PDMS by the tape. An alternative method is to cut a small piece of PC and place it on top of the PDMS using a tweezer. While

the drop off temperature is lower with this method, the PC can accidentally fall off the PDMS during intermediate steps, which the tape method avoids.

Figure A.1(b) shows the transfer stage in the Kim lab. Once the stamp is prepared, we attach it to the micro-manipulator to begin stacking. For the pickup steps, we place the glass slide at a small angle to better define the starting point of the wavefront. We place the substrate with the first flake (usually a top h-BN layer) on the temperature controlled rotation stage, which is held down via vacuum. For the first pick-up, we generally increase the temperature to between 90° and 120° C so that the PC can conform well to the outline of the h-BN layer. We control the wavefront with either the stage temperature or the computer-controlled z motor height. We note that the temperature controlled wavefront can be a slower, but more controlled process because the wavefront will gradually expand as more of the PC touches the surface. Once the h-BN layer is fully covered, we can begin to pull back the PC film. Generally, the temperature is set to no lower than 70° to 80° C to maintain the stickiness of the PC film. If the wavefront will not retract back over the flake as the temperature is lowered, the z height of the manipulator can be raised to slowly remove the film. This method is effective at picking up flakes below $\sim$ 70 nm, and higher temperatures will be required for flakes that are thicker or particularly stubborn to pick up.

For the subsequent layers, we align the top stack with the flake of interest and then lower the PC film to pick up the subsequent layers. A similar process is used except the stage does not need to go as high in temperature. Generally, a temperature between 50° to 80° C will be sufficient for the PC wavefront to be reliably controllable with the temperature and stage height. To minimize any chances of oxidation-type defects on the TMDs, we generally use the minimum temperature that is controllable. At temperatures lower than 40° C, the wavefront can jump across the flake of interest and is not advised to be used.

For the final drop off, we will set the angle of the glass slide to be as flat as possible, which increases the wavefront speed, but guarantees better alignment, less sliding, and better adhesion of the PC to

the substrate. We lower the stack on the area of interest, usually in the center of alignment marks or aligned to pre-patterened contacts and the bottom gate, at an intermediate temperature where the wavefront can be controlled. Then we raise the temperature until the PC film begins to melt. This usually occurs between 170° and 180° C. At this point, we can slowly raise the z height of the micromanipulator until the edges of the PC film begin to tear. If the temperature is sufficiently high, the PC film will have melted onto the SiO_2 substrate and the transfer slide will liftoff. If the temperature is not high enough, the PC film will stretch and the entire film could violently retract back. If it appears the film is doing this, it is advisable to go to higher temperature to allow the PC to melt. The alternative method without using the tape method only requires a temperature of around 140° C for the PC film to adhere to the SiO_2 and come off of the PDMS. However, in general the tape method is more reliable for removing the PC film at the final step rather than during intermediate steps.

A.2 Cleanroom recipes

This section will include the electron beam lithography recipes used and general tips for cleanroom lithography steps.

A.2.1 Electron beam lithography designs

We design our device designs using AutoCAD and optical images of the device. For the bottom gates and Pt contacts, we usually use pre-patterned alignment marks which are written using either electron beam (e-beam) lithography or optical lithography. Since the alignment markers can be larger than 1μm, minimizing distortion is more important than resolution of the writing. We generally use numbers at each alignment mark which makes finding the area of interest easier in both the lithography steps and in the optical setup.

One tip for device design is for any features on top of h-BN to have rounded edges rather than

sharp edges. The sharp edges on the insulating substrate result in build up of charges resulting in small cracks or whiskers at these edges. These cracks generally are difficult to see and will extend out to the nearest metallic surface creating shorts that become apparent after metal evaporation. By having smooth turns in the design, this effect is mitigated. If this is unavoidable, an expensive alternative is to use AQUASAVE. AQUASAVE is a conductive layer that is spun at 2000 RPM and generally not baked, which helps with non-conducting surfaces. It should be removed with 60 seconds in water before the development process.

A.2.2 General electron beam lithography recipe

For most e-beam lithography steps, unless specifically specified, this standard recipe is used. It has the most versatility in terms of quick liftoff, decent resolution, and allows for up to $\sim$ 250 nm of metal evaporation without issues. It can also withstand up to at least 10 minutes of h-BN etching if step 2 is repeated.

Generally if this recipe fails, it will be due to small feature sizes (< 300 nm), long etching requirements, or large metal evaporation heights. One can try taking tricks from either the PdAu gate recipe or the Pt contact recipe to improve results. Another possibility is expired PMMA - the expiration date for PMMA is usually only 1 year after the date of purchase. While the e-beam will certainly last longer than this, unsolvable lithography problems have magically disappeared upon using a fresh bottle of e-beam resist.

1. Spin 495 A6 PMMA for at 4000 RPM for 1 minute. Bake sample at 1800 C for 2 minutes on hot plate.

2. Spin 950 A6 PMMA for at 4000 RPM for 1 minute. Bake sample at 1800 C for 2 minutes on hot plate. (For long etching steps requiring multiple exposures to O_2 plasma, a second top layer can be added by repeating this step again).

3. Write the design using e-beam lithography tool of choice:

    - For Raith:
        - Small features: 500 μC/cm^2 at 30 μm aperture gives quick write times for relatively small features (> 500 nm).
        - Large features: 500 μC/cm^2 at 120 μm aperture with resolution of $\sim$ 1 μm.
    - For Elionix:
        - Small features: Write with 1 nA with 50,000 dots and a dose time 2 (0.06) μs/dot.
        - Large features: Write with 10 or 20 nA at 50,000 dots and a dose time 0.2 or 0.1 μs/dot.

4. Develop the PMMA:

    - For writes on h-BN or other highly resistive substrates, develop with a 3:1 mixture of freezer-chilled IPA:H_2O for 2 minutes. This is a slower (less harsh) development process that aids in preventing cracks in the PMMA mask when writing on resistive substrates.
    - For all other writes (such as SiO_2), develop with a 1:3 mixture of MIBK:IPA for 1 minute. This process is faster and I believe gives cleaner development of the PMMA. This can be critical for processes require flat surfaces (such as the back gate).

5. Etch or evaporate metals.

6. Remove the PMMA (or metal lift-off) overnight by leaving the sample in acetone.

    - This process can be accelerated by putting the beaker with acetone on a hot plate at 55° C for a few hours. This can be as short as 1-2 hours if it is the double layer resist in this recipe.

- When removing the PMMA, one can spray with an acetone spray bottle or a plastic pipette. The acetone spray bottle is harsher but generally safe unless the 2D flakes are not well attached to the surface.

A.2.3 Palladium gold (PdAu) alloy gate recipe

There are a few tricks for achieving flat and bottom gates with very small feature sizes. The first suggestion is to mainly use the Elionix as the high accelerating voltage (125 kV) is helpful for writing designs reliably. The second is to use the thinner e-beam resist. The thinner e-beam resist places the design closer to the surface giving less chances for shadowing in higher resolution designs. Finally, the final trick is the evaporation. The PdAu gates are evaporated with a thermal evaporator. Aligning the long axis of the fine features to the thermal evaporator boat minimizes the chances for bunny ears and uneven gate shapes. The last step is especially important for small features such as quantum dot gates.

This gate recipe was originally created with the idea of creating quantum dot gates. These designs generally have long aspect ratios with gate width and separation may be less than 100 nm. This is generally the best design when creating designs with small feature sizes as this allows for the acetone to flow between the gates and lift off the unwanted PMMA. Gate designs, such as circular holes in a metal gate, will have harder times lifting off. This was tried but required sonication of the sample to get the circles to lift off (not recommended with a heterostructure in place and should be treated as a last resort for lift off). The final suggestion is to write an array of these gates if possible. Since it is a bottom gate, generally there is room to create many versions of these bottom gates (at least 3x3). This gives a higher chance of finding a set of bottom gates that will be flat enough to be used for a device.

1. Spin 495 A2 PMMA for at 4000 RPM for 1 minute. Bake sample at 1800 C for 2 minutes on hot plate.

2. Spin 950 A2 PMMA for at 4000 RPM for 1 minute. Bake sample at 1800 C for 2 minutes on

hot plate.

3. Write the design using e-beam lithography tool of choice (Elionix is recommended):

    - For Raith: 500 μC/cm^2 at 30 μm aperture gives quick write times for relatively small features (> 500 nm).
    - For Elionix, small (ultra fine) features: Write with 1 nA (300 pA) with 50,000 (500,000) dots and a dose time 2 (0.6) μs/dot.

4. Develop the PMMA immediately before placing in the thermal evaporator:

    - For writes on h-BN or other highly resistive substrates, develop with a 3:1 mixture of freezer-chilled IPA:H_2O for 2 minutes. This is a slower (less harsh) development process that aids in preventing cracks in the PMMA mask when writing on resistive substrates.
    - For all other writes (such as on SiO_2), develop with a 1:3 mixture of MIBK:IPA for 1 minute.

5. Evaporate Cr (1 nm) / PdAu (9 nm) in a thermal evaporator with a chamber pressure in the low 10^{-7} Torr. Use rates between 0.2 - 0.5 Å/s for the Cr layer and 0.5 - 1 Å/s for the PdAu layer.

    - Align the long axis of the gate design with the axis of the evaporation boat and place the PdAu boat closest to the center holder (directly underneath the chip). This reduces any chances of a shadow which can contribute to asymmetric gate shapes or bunny ears.
    - Thermal evaporation of PdAu (similar to Pd) can be extremely volatile with the evaporation rate going from 0.1 to 2 Å/s in a flash. Patience in increasing the current across the boat and increasing it "adiabatically" is important to minimize these jumps. It is possible

reach a meta-stable condition between 0.5 and 1 Å/s long enough to evaporate the gate thickness.

- The evaporation rates have trade-offs although I generally aim for the lowest rate in the suggested ranges. If slower, it can increase the chance of creating a dirty film because the rate becomes closer to the rate of "junk" evaporation. Faster rates can be worse as the film may not be as uniform. Since our goal is to create a very flat film, we generally err on the side of lower evaporation rates.

6. Liftoff in a beaker of acetone overnight. In the morning (or $\sim$ 10 hours later) spray the gates with acetone and let the sample soak for a additional 1-2 hours. Repeat the acetone spray again to remove any remaining metal. This allows for the PMMA that is between two long, narrowly separated gates to get removed by acetone flow.

A.2.4 Platinum TMD contact recipe

The Pt contact recipe was developed to solve p-type contacts in the WSe_2. The recipe uses weak O_2 plasma to try to clean the h-BN surface before evaporating. The PMMA recipe can be replaced with 495 A4 and 950 A6 if the feature sizes will be larger than 1 μm as it is a little bit safer for the O_2 plasma etch. The A2 recipe can achieve finer resolution and could be preferred. It is also preferred to use the Raith as the lower accelerating voltage (30 kV) may have more back-scattering which could create a larger undercut. This undercut is thought to reduce the amount of bunny ears.

1. Spin 495 A2 (A4) PMMA for at 4000 RPM for 1 minute. Bake sample at 1800 C for 2 minutes on hot plate.

2. Spin 950 A2 (A6) PMMA for at 4000 RPM for 1 minute. Bake sample at 1800 C for 2 minutes on hot plate.

3. Write the design using e-beam lithography tool of choice (Raith is preferred):

    - For Raith: 500 μC/cm^2 at 30 μm aperture gives quick write times for relatively small features ($\sim$ 500nm).
    - For Elionix: Write with 1 nA with 50,000 dots and a dose time 2 μs/dot.

4. Develop the PMMA. Since the Pt contacts are usually on h-BN bottom layers, this is usually a 3:1 mixture of freezer-chilled IPA:H_2O for 2 minutes. If they are directly on SiO_2, a 1:3 mixture of MIBK:IPA for 1 minute may be better.

5. Lightly clean the contact areas by doing an O_2 plasma cleaning step of 15 seconds at 40% power at 40 sccm (RIE-9).

6. Evaporate Cr (1 nm) / Pt (19 nm) in the e-beam evaporator with a chamber pressure in the low 10^{-7} Torr (default with lab's Evap2 evaporator). Use rates of 0.2 Å/s for the Cr layer and 0.1 Å/s for the Pt layer.

    - Turn on the Peltier cooling voltage sources (which lower the stage temperature by around 40°) or change chilling water temperature to be 5° C before the Pt evaporation step. Pt requires very high e-beam currents to evaporate and the chamber will heat up to high temperatures. Without changing at least the chilling water temperature, the PMMA will crack and the evaporation will not lift off.
    - For the heating reason mentioned above, we do not evaporate at a rate higher than 0.1 Å/s.

7. Liftoff in a beaker of acetone overnight. In the morning (or $\sim$ 10 hours later) spray the contacts with acetone and let the sample soak for a additional 1-2 hours. Repeat the acetone spray again to remove any remaining metal.

B

The Optical Setups

In this appendix, the optical setups, the logic behind their design, and the relevant equipment will be discussed. This should allow one to put together the optical setups used for the experiments in this thesis. Each experiment had issues in their initial setup that will be briefly discussed in each section to hopefully save a future researcher some time. All of the knowledge gathered in this appendix is owed to strong collaborations with other optics experts in the Kim, Lukin, and Park groups at Harvard.

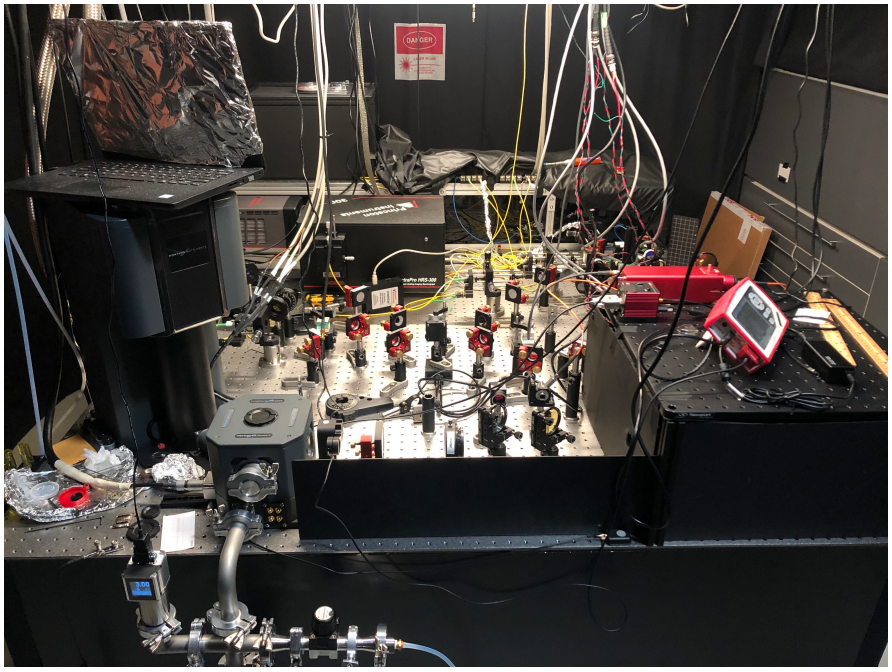

Figure B.1: Photo of the 4f confocal microscope setup in the Kim lab.

B.1 The optical setup: 4f confocal microscope

Optical measurements were performed using a 4f scanning confocal microscopy setup. Figure B.1 shows a picture of the setup, including a Montana instruments, closed-loop 4K optical cryostat, the optical paths, Princeton instruments spectrometer and camera, and M2 tunable continuous wave laser (inside long black box).

There are two primary reasons for using a 4f scanning confocal microscope for our measurements, rather than a simpler 4f confocal system. The first is the ability to measure exciton diffusion in our samples, which occurs readily given the long lifetimes and dipole repulsion at high exciton densities. The second is to generate scanning maps of the photon counts throughout the sample without moving the often hysteretic low-temperature piezo stages.

When performing photoluminescence (PL) or electroluminesence (EL) measurements, we either

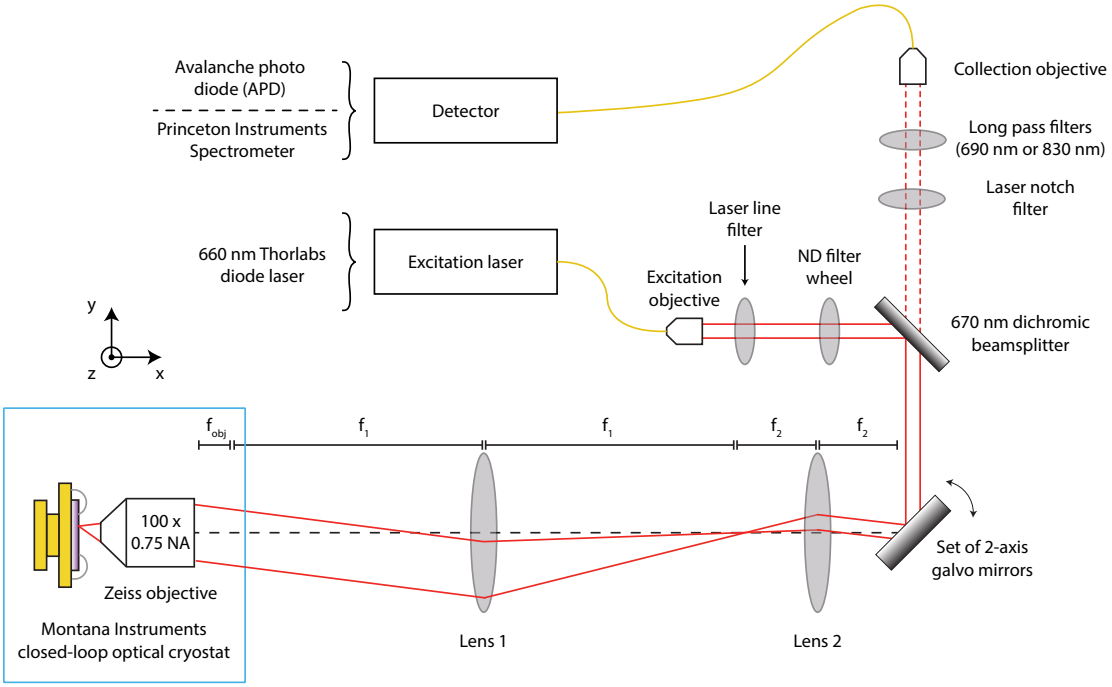

Figure B.2: Scanning 4f confocal microscope setup when operating in photoluminescence or electroluminescence measurements. The two lenses, with focal lengths f_1 and f_2, combined with the scanning galvo mirrors allow us to select any point on the sample. We fiber couple the excitation and collection paths. We excite the sample with a 660 nm diode laser and direct the collection into either an avalanche photo diode (APD) or a spectrometer to measure the luminescence.

excite excitons in the sample using a laser or generate them by passing current across our heterostructure device. The setup is designed such that the beam size coming out of the cryostat objective is magnified to match the collection or excitation objectives. Since there is a third lens in the path (the two lenses and the sample objective), the tilted angle of the galvo mirror is mapped to a spatial point on the sample. This is demonstrated in Fig. B.2. We can then steer the beam using the galvo mirrors so that we can collect anywhere within our sample, limited by the size of the mirrors and lenses.

We fiber couple the excitation and collection paths, allowing us to change them without major realignment. We generally excite the sample with a 660 nm diode laser (other excitation sources are described in the text) and direct the collection into either an avalanche photo diode (APD) or a Prince-

ton Instruments spectrometer and camera to measure the luminescence. Each collection instrument has its advantages.

APDs (Appendix B.7.1) are well known for counting single photons in very low count rate samples, such as quantum dots. They also have the advantage of very fast readout times, allowing one to perform time-resolved measurements. In the experiments in this thesis, we collect light into the APDs for creating scanning confocal images, for time-resolved PL or EL measurements, and coherence measurements. They are generally more efficient in terms of counts per second than the spectrometer so light can also be filtered by band-pass filters and sent into the APD for quicker, diagnostic measurements. For time-resolved measurements for extracting lifetime or degrees of coherence, the APD is our only option.

The optical parts are selected with the consideration of matching the size of the beam to the back aperture of the objective (mode-matching) near the interlayer exciton wavelength. The beam size (D) needed to optimally couple light between for these two parts is

$$D = \frac{4f\lambda}{\mathrm{MFD}\pi} \tag{B.1}$$

where f is the focal length, λ is the light wavelength, and MFD is the mode field diameter of the fiber. For our system, using a Thorlabs 780 nm single mode fiber and an Olympus 10x objective, we get $D = 3.896$ mm. We compare this to the size of the back of the objective

$$D_{obj} = 2f\mathrm{NA} = 2\frac{L_{tube}}{M}\,\mathrm{NA}, \tag{B.2}$$

where L_{tube} is the obejctive's tube length, M is the magnification, and NA is the numerical aperture. For the Zeiss objective, we have a magnification of 100x and a tube length of 165mm. Thus, we get $D_{obj} = 2 \cdot 1.65\ \mathrm{mm} \cdot 0.75 = 2.475$ mm for the size of the back objective. So to match the two beam

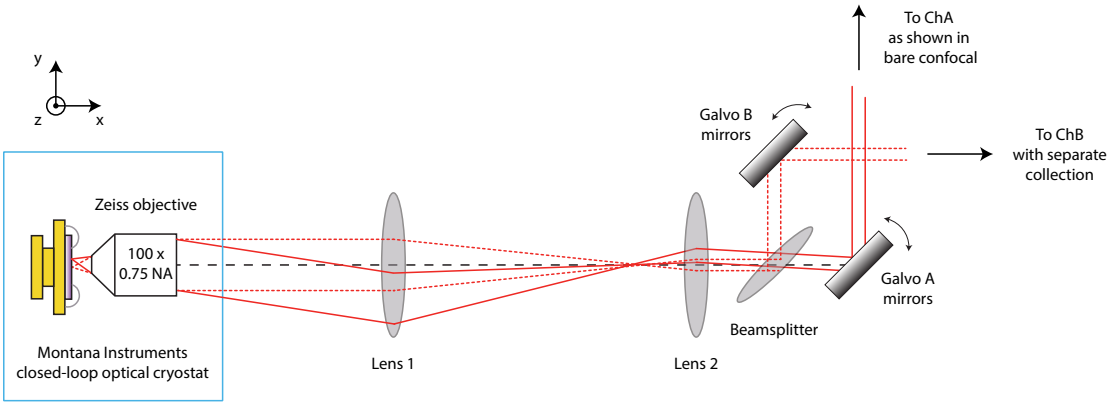

Figure B.3: Double galvo setup for two separate channels for the confocal microscope. The same setup as the single galvo confocal except a beamsplitter is placed to allow for two separate galvos.

sizes in our system, we choose lenses of focal length 250 mm and 400 mm, which magnifies the beam.

B.2 Double galvo confocal setup

Our setup includes an additional set of galvos on the second path, labeled path B in (Fig. B.3). Importantly, we use a pellicle beamsplitter to split the beam paths. The thickness of the pellicle is thin such that different angles of the galvo mirrors do not significantly misalign the beam path. This allows the use of two separate sets of scanning mirrors for two separately controlled paths. The main motivation for the second path is to control the excitation and collection paths independently in diffusion measurements. We also use the second path for any extraneous measurement setups such as the polarization setup (Section B.4) or the first order coherence measurements (Section B.6).

B.3 White light reflection imaging

The setup can be modified for spatial imaging by adding beamsplitters into the path between the two lenses (Fig. B.4). By inserting the beamsplitters here, the two lenses provide a real space image at the camera. We use this configuration to get a spatial reflection image of the sample using a broadband

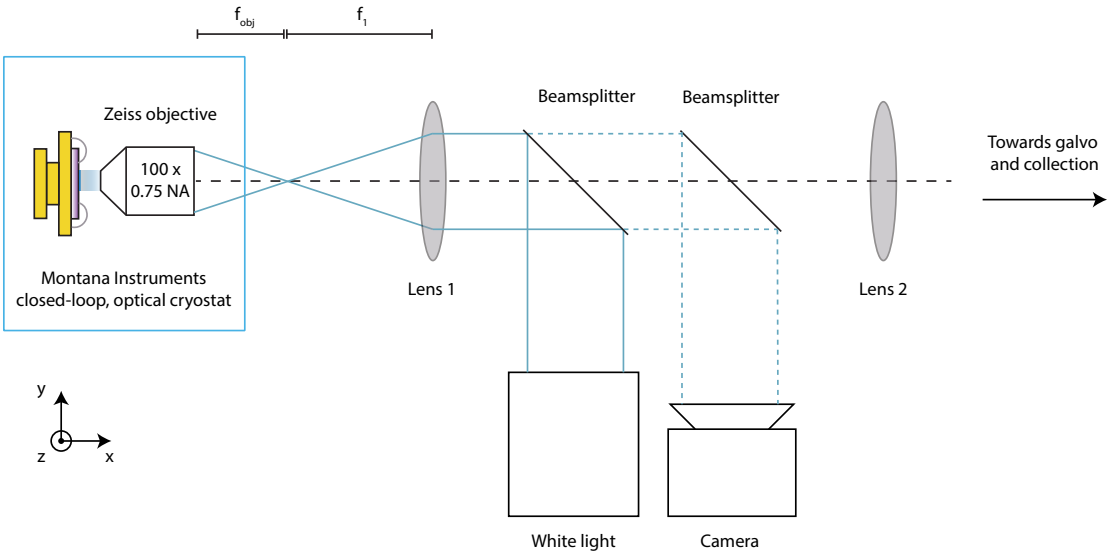

Figure B.4: For the white light imaging setup, we place beamsplitters between the lenses to add a white light lamp and camera. This allows for white light reflection real-space imaging.

white light source. This is important for identifying the sample location and roughly focusing the laser beam spot. The white light source can also be inserted for performing broadband absorption measurements as it will uniformly illuminate the sample area. A similar measurement could be done with an additional lens in order to perform k-space imaging.

B.4 Circular polarization

In this section, we discuss circular polarization measurements. One important discussion point is brought to light here, which is the naming convention of the circular polarization in TMD literature. Having lost many hours with these considerations, I believe it is important to enlighten the confused reader here. If one considers circularly polarized light reflecting off of a mirror (the same behavior as the intralayer excitons), we expect the opposite polarization as the incoming light (Fig. B.5). In this sense, it would be accurate to describe this as circular cross-polarization. However, in the literature, the polarization behavior is described as if it were a transmission measurement, perhaps due to tra-

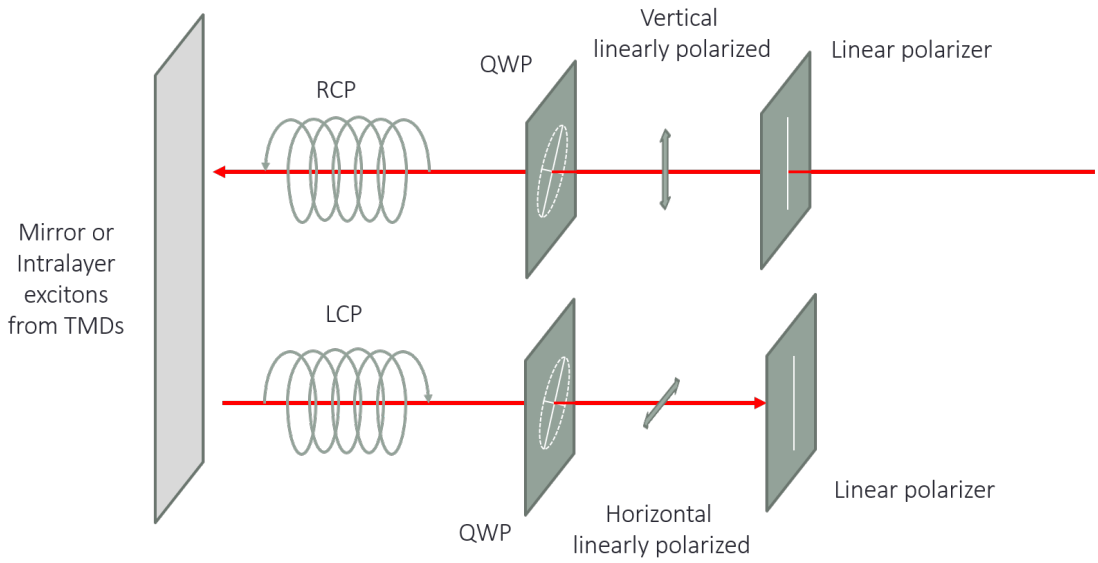

Figure B.5: A demonstration of the behavior of circular polarization when reflecting through a mirror. The right circular polarized (RCP) light created by the quarter wave plate (QWP) will reflect and turn into left circular polarized (LCP) light. Upon returning through the setup the light will be blocked by the initial linear polarizer.

ditional optics experiments. In Figure B.6, we see the emission polarization of the monolayer TMD in both directions. The selection rules (and the coupling to the K valley), in the crudest description, actually determine the circular rotation of the light, while the handedness is determined by the light propagation direction. Thus, a true cross-polarization measurement (which is allowed in the reflection from a mirror) is described as a co-polarized measurement. This will be true in almost all TMD literature and in this thesis. This means, for example, $\sigma+$ excitation and $\sigma+$ collection, the expected behavior for the bright exciton in monolayer TMDs defined as co-polarized, is measured by having the excitation and collection linear polarizers perpendicular to each other. The "cross-polarized" measurement scheme (Section B.4.2) is named according to the literature convention and the measurement setup actually has the linear polarizers parallel in alignment (also as seen in Fig. B.5), which blocks out the monolayer or trivial reflection signal.

For polarizability measurements, or general polarization measurements, we place the quarter wave

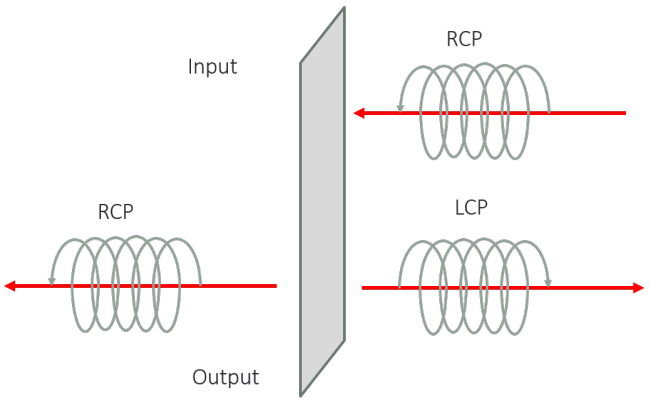

Figure B.6: A comparison of the circular polarization in transmission or reflection of a mirror or monolayer TMD. The rotation direction will be the same as the oscillating dipole looks identical from either side. However, the propagation direction will dictate the label of right circular (RCP) or left circular polarized (LCP) light.

plate (QWP) in the common path as close to the objective as possible. Most optical parts maintain linear polarization well, but do not maintain circular polarization nearly as well. In this setup, the circularly polarized light only goes through the objective, which is the minimum number of optical parts to travel through. The linear polarizers are placed after the beamsplitter but before the galvos. The galvo mirrors may introduce some rotation and are usually avoided for this reason. In this way, we can change both the excitation and collection polarizers separately. We note that the dichroic mirror used for our co-aligned confocal setup is the main culprit for ruining the polarization so this method avoids changing the polarization afterwards. Because the system may have biases towards s (perpendicular) and p (parallel) polarizations, in order to accurately get the polarizability of the sample, it is important to measure all four combinations, i.e. exciting with $\sigma\pm$ and collecting with $\sigma\pm$. One can then use this for removing the biases of the optical setup.

B.4.1 Polarizability setup

The PL intensity signal can be considered as $I_{PL}^{excitation/collection} = I_{sample}^{excitation/collection} I_{system}^{collection}$, where $I_{sample}^{excitation/collection}$ and $I_{system}^{collection}$ are the sample and system dependent signal with a given excitation and

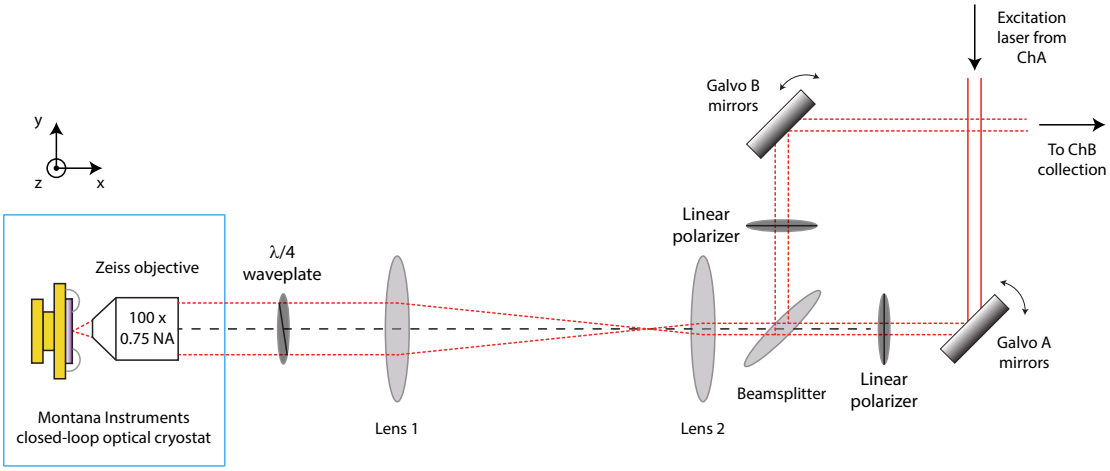

Figure B.7: Optical polarization setup where the quarter wave plate ($\lambda/4$ or QWP) is placed as close to the sample at 45 degrees from the fast and slow axes of the system. The linear polarizers (LP) choose an axis to either measure cross- or co- circular polarized measurements.

collection polarization. The degree of circular polarization can be defined as

$$\mathrm{DOCP} = \frac{I^{co}_{sample} - I^{cross}_{sample}}{I^{co}_{sample} + I^{cross}_{sample}}, \tag{B.3}$$

which is only dependent on the sample. In order to extract the DOCP, we can define the co- and cross-polarization in terms of the measured signal:

$$\begin{aligned} I^{co}_{sample} &= I^{\sigma+/\sigma+}_{sample} = I^{\sigma-/\sigma-}_{sample} \\ &= \frac{I^{\sigma+/\sigma+}_{PL}}{I^{\sigma+}_{system}} = \frac{I^{\sigma-/\sigma-}_{PL}}{I^{\sigma-}_{system}} \\ &= \sqrt{\frac{I^{\sigma+/\sigma+}_{PL}\, I^{\sigma-/\sigma-}_{PL}}{I^{\sigma+}_{system}\, I^{\sigma-}_{system}}} \end{aligned} \tag{B.4}$$

and

$$\begin{aligned} I_{sample}^{cross} &= I_{sample}^{\sigma+/\sigma-} = I_{sample}^{\sigma-/\sigma+} \\ &= \frac{I_{PL}^{\sigma+/\sigma-}}{I_{system}^{\sigma-}} = \frac{I_{PL}^{\sigma-/\sigma+}}{I_{system}^{\sigma+}} \\ &= \sqrt{\frac{I_{PL}^{\sigma+/\sigma-}\, I_{PL}^{\sigma-/\sigma+}}{I_{system}^{\sigma+}\, I_{system}^{\sigma-}}}. \end{aligned} \tag{B.5}$$

By plugging in Eq. B.4 and B.5, we can remove the system contribution from the DOCP. We show the resultant equation for the DOCP given all four measurements are taken:

$$\mathrm{DOCP} = \frac{\sqrt{I_{PL}^{\sigma+/\sigma+}\, I_{PL}^{\sigma-/\sigma-}} - \sqrt{I_{PL}^{\sigma+/\sigma-}\, I_{PL}^{\sigma-/\sigma+}}}{\sqrt{I_{PL}^{\sigma+/\sigma+}\, I_{PL}^{\sigma-/\sigma-}} + \sqrt{I_{PL}^{\sigma+/\sigma-}\, I_{PL}^{\sigma-/\sigma+}}}. \tag{B.6}$$

B.4.2 Cross-polarized measurement setup

An alternative and quicker measurement for the polarization-resolved PL (but no polarizability) is to place the quarter-wave plate ($\lambda/4$ or QWP) and the linear polarizer in the common path together and rotating the QWP by 90 degrees for the two measurements. In this case, only cross-polarized measurements can be taken, which for IEs still provides significant signal given lower polarizability. However, the advantage of this measurement scheme is that the system response for the intensity of the excitation and collection will remain constant for all measurements, allowing a quicker and more reliable measurement of the $\sigma\pm$ emission. Without a magnetic field, the K-valleys are degenerate and the response should be trivial. However, when measuring the response from the separate K-valleys under magnetic fields, this measurement scheme can be used to quickly and accurately characterize the PL emission energy and intensity from each K-valley. This measurement scheme is used in Chapters 6 and 7 to extract the IE g-factors and valley polarization.

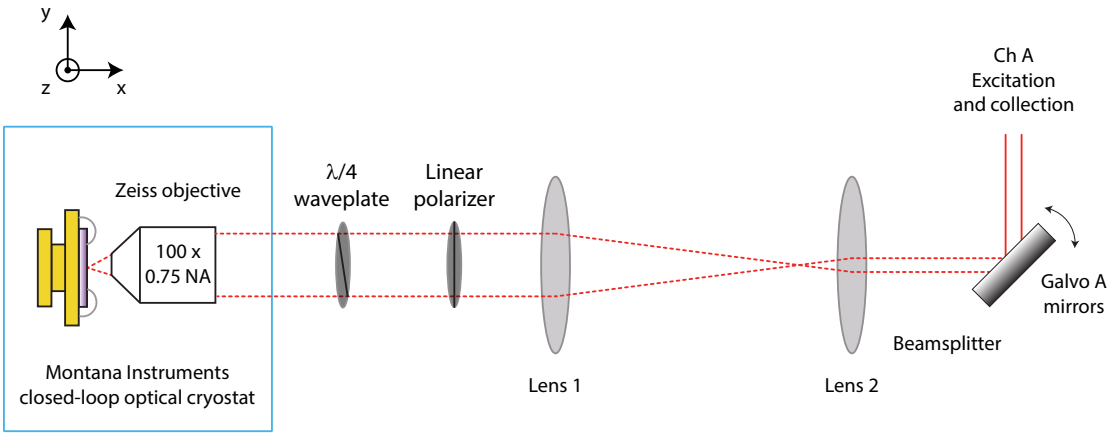

Figure B.8: Optical polarization setup where the quarter wave plate ($\lambda/4$ or QWP) and a single linear polarizer (LP) are placed in the common path closest to the sample. It will always measure the cross-polarization.

B.5 $g^{(2)}(\tau)$ MEASUREMENT SETUP

For the $g^{(2)}(\tau)$ measurements, we employ a Hanbury-Brown and Twiss (HBT) interferometer setup (Fig B.9). The emission is fiber-coupled and sent to a 50:50 fiber beamsplitter. The two arms of the fiber-splitter are sent to two identical fiber-coupled APDs (details in Appendix B.7.1). For PL or EL measurements of interlayer excitons, the slow APDs (APD A/B) are used for these measurements. The output pulses of the APDs are connected to the Picoharp (Appendix B.7.2) via BNC cables into the channel 0 and 1 counters. Using the Picoharp software, we run time-tagged time-resolved (TTTR) measurements that count every incoming photon from both channels and their time stamp. We post-process the correlation between all photons to extract the $g^{(2)}(\tau)$ second-order coherence. These measurements can be employed for observing bunching due to quantum fluctuations in phase transitions as in Chapter 8 or for anti-bunching in single photon emitters.

While relatively simple in design, we experienced a few major issues during the setup. The first is that the APDs may have a large radiation footprint, much larger than the encasing of the module. To solve this issue, we were required to separate the APD spatially by at least the length of the short-

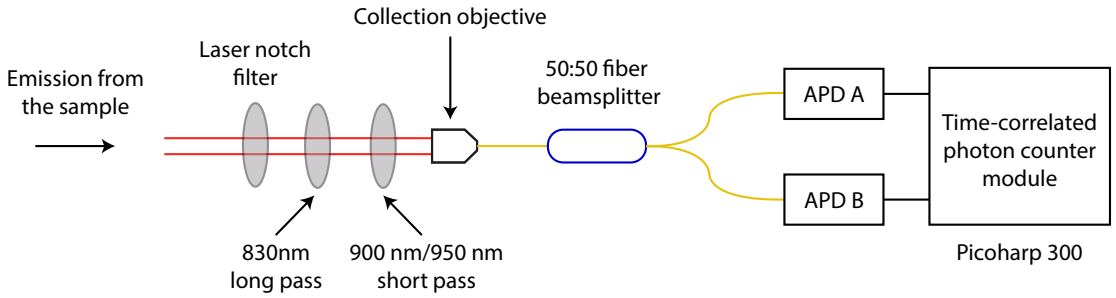

Figure B.9: Hanbury-Brown and Twiss setup for $g^{(2)}(\tau)$ measurements. The collection is split by a 50:50 beamsplitter and sent to two separate APDs. The APDs signal is sent to a Picoharp (photon counter) which time marks each photon count.

axis of our optical table (4 feet). In addition, the radiation appears to be the greatest in the plane of the detector (perpendicular to the fiber input) so the APDs are placed so their position is in series (not parallel). The second issue we experienced is re-emitted IR wavelength photons. We observed bunching of photons at $\tau = \pm 50$ ns, implying correlations. This photon bunching would move with the center delay time (by lengthening one arm). We believe the origin of this issue is the improved photodetecting efficiency for APD A and B in the NIR regime. This could increase the number of re-emitted photons from the APD. To solve this, we inserted a shortpass filter in the path to cut out wavelengths longer than the emission wavelength.

Once the extraneous $g^{(2)}(\tau)$ signatures were removed, we tested the second order coherence setup by measuring across the lasing transition of a 660 nm Thorlabs diode laser. We observe intensity fluctuations in the $g^{(2)}(\tau)$ signal when the diode laser is driven near the lasing transition (Fig. B.10(a)). In Figure B.10(b), we show the fitted $g^{(2)}(0)$ for the various laser currents and observe clear signatures of a lasing transition. Below lasing, the coherence time is broader than our detection limit and we measure $g^{(2)}(\tau) = 1$. When approaching the lasing transition, we observe $g^{(2)}(0) > 1$ due to quantum fluctuations. Interestingly, we also observe oscillations, which could be due to population exchange with the optical cavity [160,161]. Above the lasing threshold of around 60 mA, the second-order coherence returns to $g^{(2)}(\tau) = 1$ indicating coherent light emission (Section 8.4).

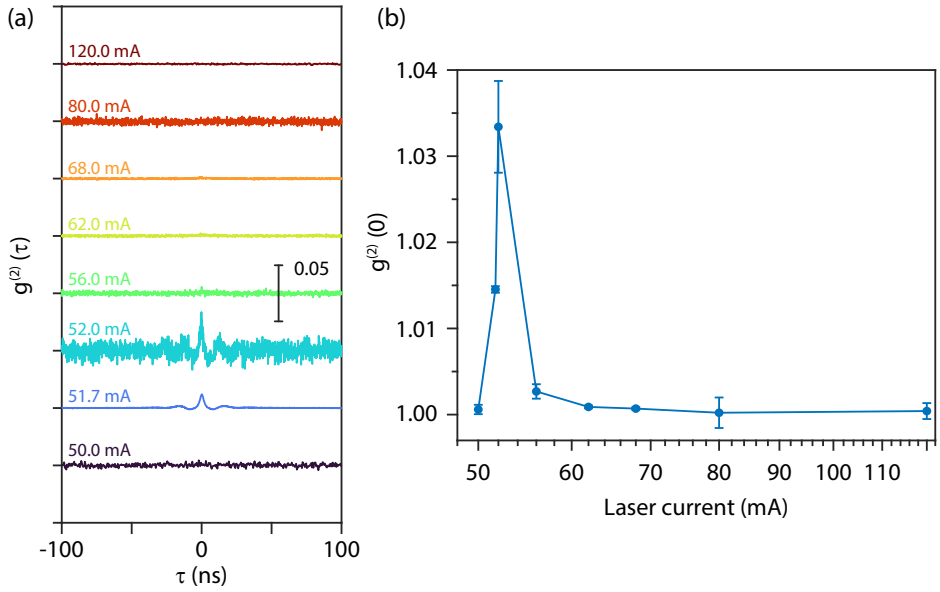

Figure B.10: Hanbury-Brown and Twiss $g^{(2)}(\tau)$ of a diode laser across the lasing transition. (a) $g^{(2)}(\tau)$ for various diode laser currents showing intensity fluctuations near the lasing transition. Lasing occurs at around 60 mA. (b) The fitted $g^{(2)}(0)$ for various laser currents. $g^{(2)}(0)$ returns to 1 above the lasing transition.

B.6 $g^{(1)}(\tau)$ MEASUREMENT SETUP

While we do not present any first-order coherence measurements in this thesis, we have prepared an interferometer for these measurements in the future. For the $g^{(1)}(\tau)$ measurements, we built a Mach-Zehnder interferometer. Figure B.11 shows the interferometer setup used, which is built on ChB, allowing the galvos to still select our sample position. There are two arms, which are initially measured out to be the same length. One arm has a retroreflector (an optical element designed to send the light back with some small displacement) placed on a motorized stage in the path, which can be used to control path length. The path length translates to a delay in the two arms, which can be continuously changed with the motorized stage with step sizes as small as $\sim$ 200 nm and a full range of 12 mm. Even with its approximate homing accuracy of 1 μm, the stage should have a minimum time resolution of 5 fs. This setup can also be used for $g^{(1)}(\tau, x)$ measurements by collecting from a different position

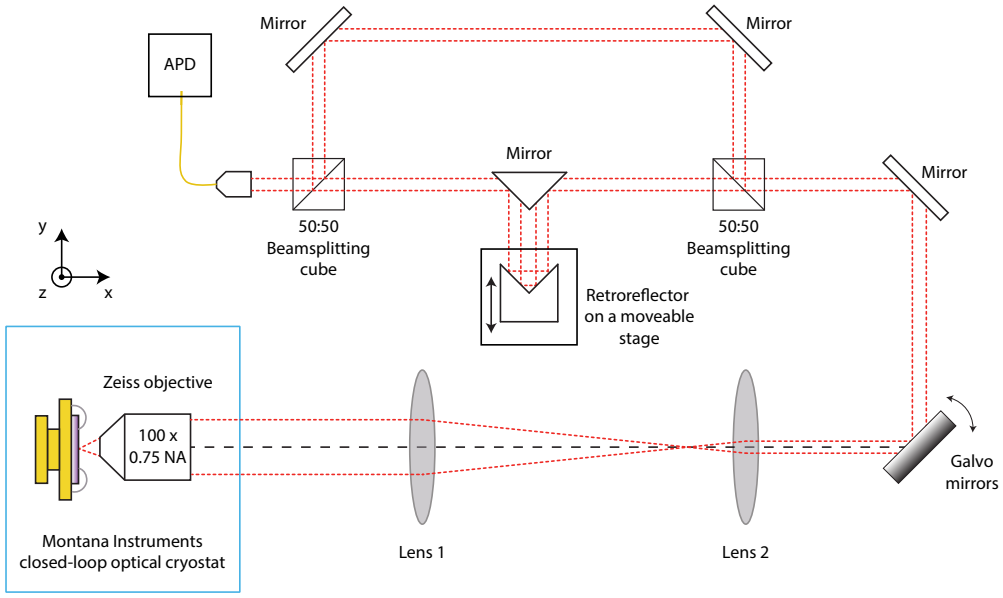

Figure B.11: Mach-Zehnder setup for $g^{(1)}(\tau)$ measurements. The collection is sent split into two arms by a beamsplitter, where one arm has a stage which controls the retroreflector position. This translates to a change in the interferometer arm length and a delay time in the measurement.

with the second arm. Initial measurements had issues due to dispersion caused by the retroreflector. The main cause was retroreflector was not hollow and the input signal was broader than the measured coherence signal. To remedy this, a hollow reflecting retroreflector was installed instead.

In order to test the quality of our coherence measurements, we began with measuring the behavior of the most obtainable coherence light sources in our lab: the lasers. We reflect the laser from the sample into the interferometer setup where the light is split into the two arms before being sent into the same photon counter (an APD). We move the retroreflector, while measuring the APD counts, and observe interference oscillations in the total counts. We are able to achieve a visibility of close to 0.7, which could be improved by further alignment of the interferometer (Fig. B.12(a)). These oscillations persist up to the maximum range of our motor stepper ($\sim$ 12 mm). Furthermore, in Figure B.12(b), we can look at the first-order coherence visibility of an incoherent light source with a 10 nm bandpass filter. In this case, the coherence length is significantly smaller and we observe the

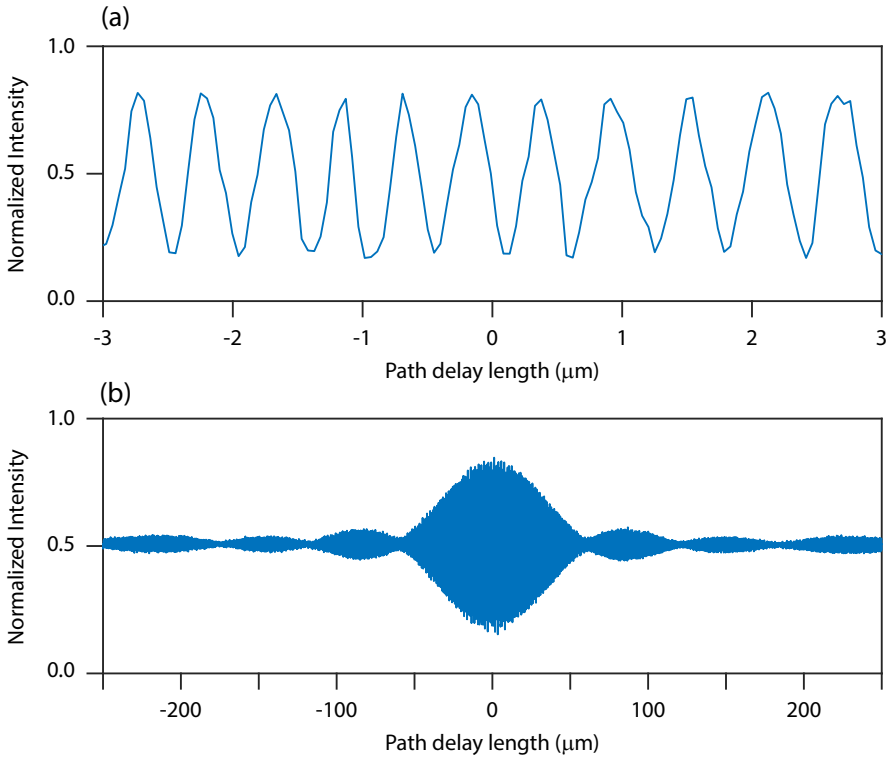

Figure B.12: (a) Normalized laser coherence fringes measured in the $g^{(1)}(\tau)$ Mach-Zehnder interferometer. (b) Normalized coherence fringes of an incoherent light source with a 10 nm bandpass filter with a finite decay length.

oscillations decay as a function of the delay length. We also observe the signal has nodes along the path length to the square shape of the bandpass. These measurements serve as a demonstration of the interferometer setup, which will be used for future temporal and spatial coherence measurements.

B.7 Optics Parts list

Here we list a few key instruments or parts that are in the optical set up which are critical for the measurements in this thesis. Hopefully, this can serve as a guide for future confocal setups or to refer to for finding old instruments.

B.7.1 Avalanche photo diode (APD)

At the time of this thesis, we have three APDs available for use. We have two Excilitas single photon counting modules (SPCM-900-14-FC), which we call "slow APDs." The slow APDs (APD A and B) are specifically screened at 900 nm to have high photon detection efficiency (*sim* 45%). They are spec'd with an output pulse width of 10 ns, output pulse height of 2.2 V, dead time of 22 ns, maximum dark counts of 100 counts per second. For interlayer exciton measurements near the NIR range, we expect lifetimes of at least 1 ns and emission wavelengths between 850 - 950 nm so these APDs are ideal for these measurements. We also have a "fast APD" with around 30 ps resolution, which is less efficient in this NIR range.

B.7.2 Picoharp 300

For all time-resolved photon counting or correlation measurements (except for first order coherence), we use the Picoharp 300, a picosecond histogram accumulating real–time processor. The Picoharp has two channels, channel 0 (Ch0) and channel 1 (Ch1), which are independent and each have a time resolution of 4 ps. In measurements with a trigger, Ch0 is the trigger input and Ch1 is the main measurement input. In EL lifetime and PL lifetime measurements, the laser pulse output trigger or voltage modulation trigger output are used for Ch0 and the emission APD counts are used for Ch0. In the $g^{(2)}(\tau)$, the two APD outputs gets sent into each channel and the two channels are treated identically.

B.7.3 Spectrometer

In early measurements, we use a Princeton Instruments spectrometer with a PIXIS:256BR camera. In more recent measurements, the camera is upgraded to the BLAZE:400HR camera. The BLAZE:400HR is a particularly powerful camera bought specifically for its improved efficiency in

the NIR range and larger number of pixels. This allows for efficient collection of the interlayer exciton emission and larger area for imaging. The spectrometer has three gratings installed: a 300, 600, and 1200 grooves/mm with either 1 μm or 750 nm Blaze wavelength. These allow for courser measurements with broadband collection or finer measurements. The measurements are generally performed by fiber coupling into the spectrometer, but has a manual slit that can be opened for performing imaging directly with the camera.

B.7.4 Other parts

A rough list of the important optical components in our setup are listed here.

- Zeiss custom vacuum compatible 100X objective, 0.75NA, 4mm working distance (additional spec's on Montana Instruments website)
- Thorlabs 660 nm, pigtailed laser diode with a single-mode fiber (LP660-SF40).
- Thorlabs 705 nm, pigtailed laser diode with a single-mode fiber (LP705-SF15).
- M2 laser with tunable wavelength from 700 to 1050 nm with output powers up to 5 W. Pump laser of 532 nm, which can be free-space coupled.
- Most mirror mounts are from Radiant Dyes (MDI-HS-2-3025-1/4"-20). The mounts are smooth in alignment and stable over long periods of time (similar quality for half the price of Thorlabs or Newport's high quality mounts).
- All mirrors are broadband dielectric mirrors from Newport (10Q620BB.HR2). They have broadband reflection from either 350 - 1100 nm or 650 - 1100nm wavelengths and are ideal for the NIR measurements. After switching to these mirrors, we realized the interlayer excitons were present in many of our samples.

C

Device Details

The glory of the science will often overlook the details of the materials. There are a few important devices that were essential for the making of this thesis. Some are created with the help of fellow graduate students or very talented undergraduate students. Credit is noted here when that is the case. We will label them here as they are described in the chapters and provide details of the device.

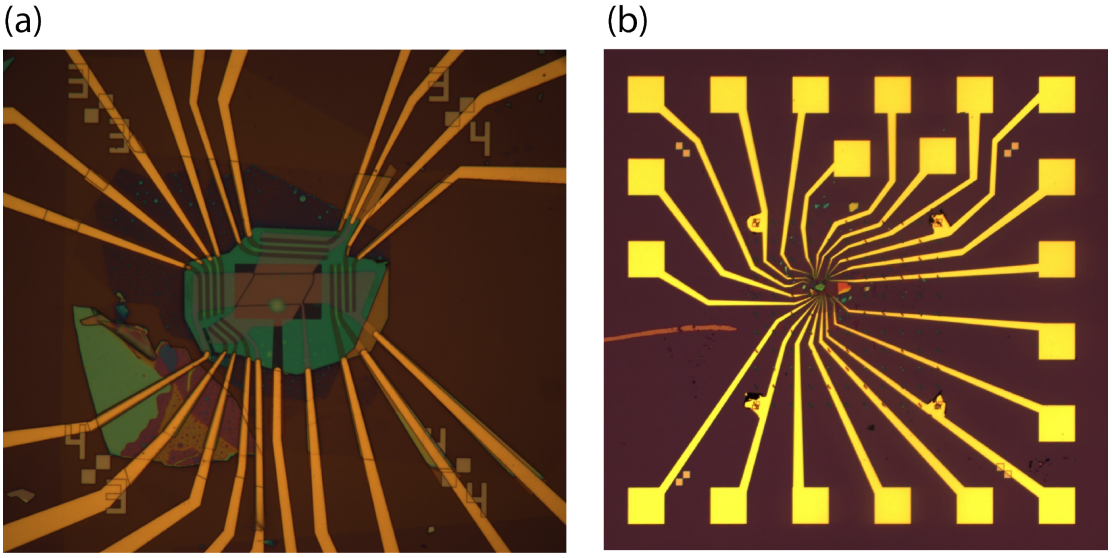

Figure C.1: Optical images of S49 (a) 100x image (b) 2.5x image.

C.1 S49 or Device A

One of the first devices created with bright interlayer excitons, S49 played an important part in the search for interlayer excitons. It is the primary device in Chapters 4 and 7, and referred to as device A in Chapter 6. The device image is in Figure C.1 It is a 0-degree heterostructure that has a Cr/PdAu bottom gate with Cr/Pd top gates. The device encapsulated by top and bottom h-BN with thicknesses of 70 nm and 114 nm, respectively. The WSe_2 contacts are made with Cr (1 nm)/Pt (19 nm) and the $MoSe_2$ contacts are made with Cr (1 nm)/Pt (9 nm). The TMD layers are CVT grown crystals sourced from HQ Graphene (commercial company). The approximate angle between the stacked layers is $< 2^\circ$, based on second harmonic generation (SHG) measurements (Figure 3.6). The optical images have conflicting clean edges so the relative angle extracted this way ranges from $\Delta\theta \approx 0.81^\circ - 2.7^\circ$. The h-BN thicknesses are also the basis for discussion on device electrostatics in Appendix D. This device was fabricated with the help of Kateryna Pistunova.

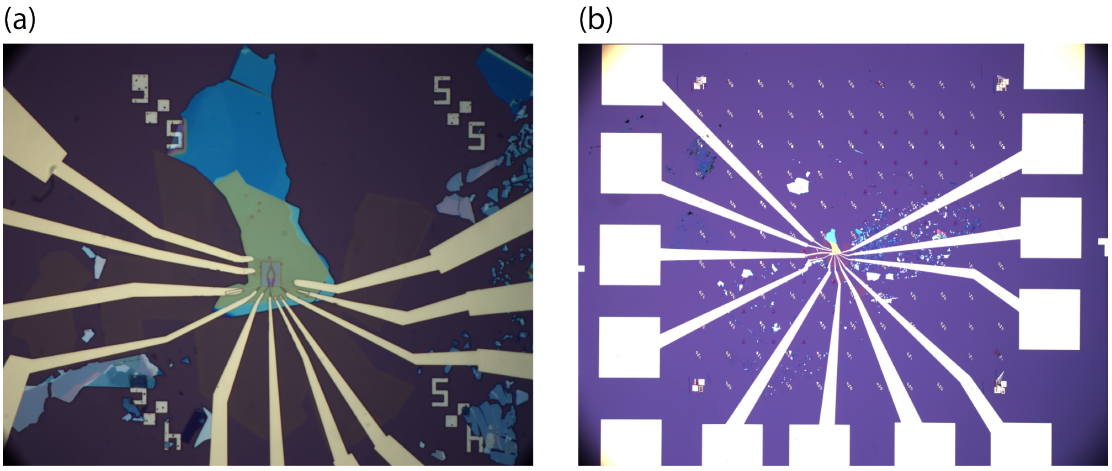

Figure C.2: Optical images of AJ28 (a) 100x image (b) 10x image.

C.2 AJ28 or Diamond Trap

The "Diamond" trap was the main device for trapping as shown in Chapter 5. The device image is shown in Figure C.2. The $MoSe_2$, WSe_2, and hBN layers are prepared via mechanical exfoliation on 285 nm SiO_2 substrates. The $MoSe_2$ and WSe_2 bulk crystals are grown via the flux method. The hBN thicknesses are 36.2 nm and 59.1*nm* for the top and bottom h-BN, respectively. The stack is assembled by picking up each layer starting with the top hBN. The final stack is placed on ultra-flat Cr/PdAu alloy (1 nm / 9 nm) bottom gates written on a 285 nm SiO_2 substrate. The wire gate width ($\sim$ 250 nm) and outer gate separations ($\sim$ 500 nm) are measured via scanning electron microscopy (SEM) images (Figure 5.2(b)). The same gates are evaporated on top of the completed heterostructure. Edge contacts were fabricated by reactive ion etching parts of the monolayer region with O_2/CHF_3/Ar gas mixture and then evaporating Cr / Au leads (5 nm / 120nm). It should be noted these contacts are not sufficient for electronic transport but can be used for electrostatic doping measurements. The top stack was prepared by Kateryna Pistunova.

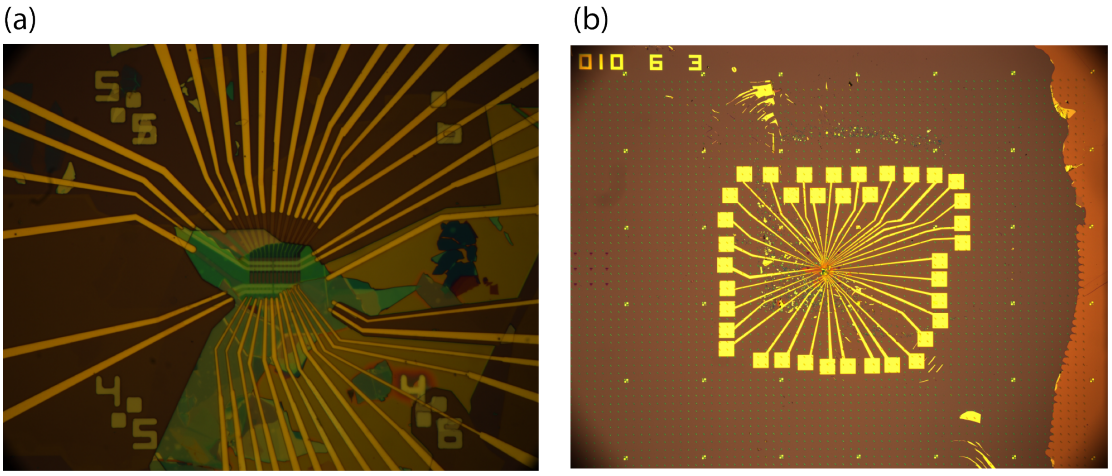

Figure C.3: Optical images of AJ41 (a) 100x image (b) 2.5x image.

C.3 AJ41 or Device B

AJ41 or Device B was originally designed for trapping with 13 spatially aligned top and bottom wire gates. They are 1 μm-wide Cr (1 nm) / PdAu (9 nm) top and bottom gates with a separation of 200 nm. The device image is shown in Figure C.3. The trapping turned out to be less effective in this device and instead became a useful for studying the spin-singlet and triplet interlayer excitons (Chapter 6). The layers in device B are aligned by the natural edges of the sample. With the knowledge of 60-degree alignment from our experiments, the relative angle of device B extracted from the clean edge for each layer in the optical images is $\Delta\theta \approx 58.76°$. It is a 60-degree aligned heterostructure. It is encapsulated with 100 nm top h-BN and 70 nm bottom h-BN. Both the WSe_2 contacts and the $MoSe_2$ contacts are made with Cr (1 nm)/Pt (19 nm). They each have contact gates made of Cr (1 nm) / PdAu (9 nm), but the gate placements are not ideal for the $MoSe_2$ due to the device geometry. The TMD layers are flux-grown crystals sourced from Jim Hone's group at Columbia University.

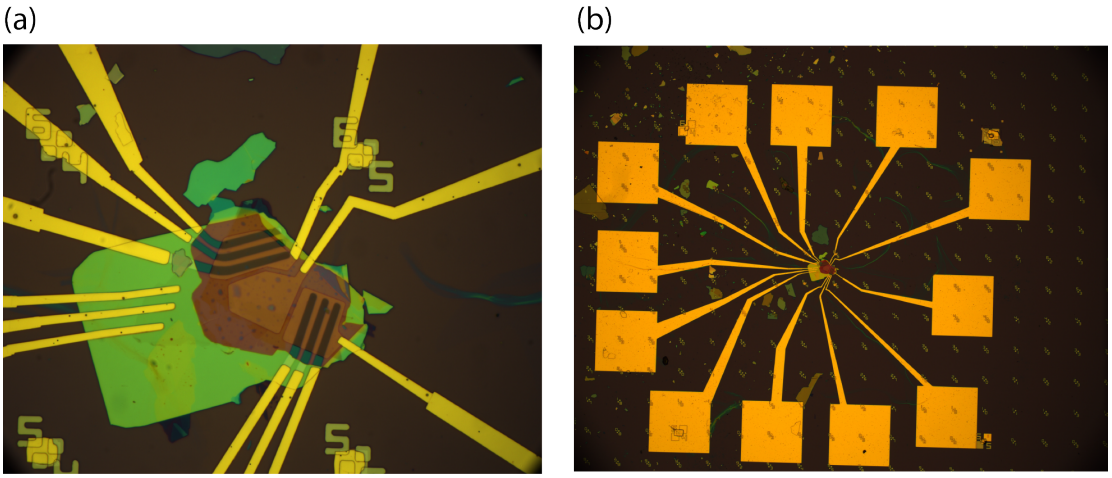

Figure C.4: Optical images of Achilles (a) 100x image (b) 2.5x image.

C.4 Achilles

Achilles is the device discussed in Chapter 8 and shown again in Figure C.4. The device is a top (52 nm) and bottom (75 nm) h-BN encapsulated $MoSe_2$/1L-hBN/WSe_2 heterostructure with a graphite bottom gate and Pd top gates. The TMD flakes were mechanically exfoliated from flux-grown bulk crystals Jim Hone's group at Columbia University. The spacer h-BN layer is verified to be a a single layer based second harmonic generation (SHG). The layers are stacked using a dry transfer technique and placed down on pre-patterned Cr (1 nm)/Pt (19 nm) contacts. The top gates and contact gates are made of Cr (1 nm) / Pd (9 nm), and are thin enough to be optically transparent. During the measurements, the contact gates on the $MoSe_2$ (WSe_2) layers are kept at $+10$ (-10) V to dope the monolayer regions allowing transparent injection of electrons (holes). This device was fabricated by Andrés M. Mier Valdivia.

D

Electrostatics in Interlayer Exciton Heterostructures

In this Appendix, we discuss the details behind the electrostatic calculations for our $MoSe_2/WSe_2$ heterostructures. There are two important considerations were made that differ from graphene or bilayer graphene samples: (1) the finite difference in the interlayer dielectric. The transition metal dichalcogenide (TMD) layers have a different dielectric constant compared to the encapsulating h-BN which

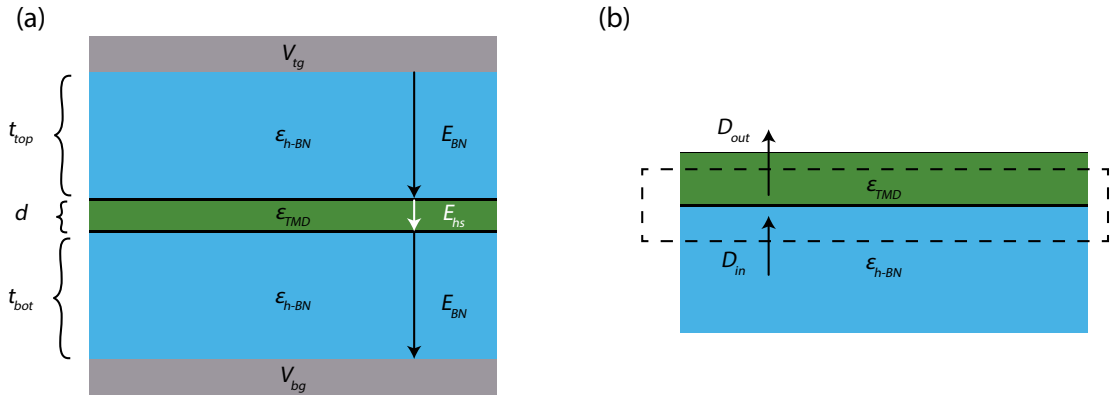

Figure D.1: (a) Schematics of the device structure and definition of variables for electric field in the TMD. (b) Gaussian pillbox schematic.

change the electric field that the interlayer exciton will feel. (2) the two layers will become degenerately doped at different gate voltages. This can have important consequences when considering the net electric field that exists between layers. In other words, the top and bottom gate are not symmetric.

D.1 Electric field only configuration

We first discuss creating only an electric field between the layers. The values used in this section are for the device in Chapter 4 or device A in Chapter 6.

In a parallel plate capacitor with a single slab of material in between, the electric field can be defined to be the ratio between the voltage difference and the distance between the parallel plates. When there is a thin sheet of material with a different dielectric constant as in Figure D.1(a), the electric field within this sheet will be effectively smaller. Let us define the top and bottom h-BN thicknesses to be $t_{total}/2$ and the thickness of the TMD to be d, where $d \ll t_{total}$. We can start by drawing a Gaussian pillbox (Figure D.1(b)), where the displacement field into and out of the box will be equal (there are no free charges):

$$\varepsilon_{h-BN} E_{BN} = D_{in} = D_{out} = \varepsilon_{TMD} E_{hs} \tag{D.1}$$

$$E_{BN} = \frac{\varepsilon_{TMD}}{\varepsilon_{h-BN}} E_{hs} \tag{D.2}$$

where E_{BN} and E_{HS} are the electric fields in the h-BN and TMD layer respectively. Now if we integrate the electric field along a straight line from the top to the bottom plate:

$$V_{bg} - V_{tg} = -\int_{top}^{bot} \vec{E_{Field}} \cdot \vec{dl} = -\left(E_{BN} \cdot (t_{top} + t_{bot}) + E_{hs} \cdot d\right) \tag{D.3}$$

We can use Eq. D.2 and $t_{total} = t_{top} + t_{bot}$ to get an expression for E_{hs}:

$$V_{bg} - V_{tg} = -\left(\left(\frac{\varepsilon_{TMD}}{\varepsilon_{h-BN}} E_{hs}\right) \cdot t_{total} + E_{hs} \cdot d\right) \tag{D.4}$$

$$E_{hs} = (V_{tg} - V_{bg})/(\frac{\varepsilon_{TMD}}{\varepsilon_{h-BN}} \cdot t_{total} + d) = \frac{V_{tg} - V_{bg}}{t_{total}} / \left(\frac{\varepsilon_{TMD}}{\varepsilon_{h-BN}} + \frac{d}{t_{total}}\right) \tag{D.5}$$

Because of our initial assumption, $d \ll t_{total}$, to first order, we can ignore the second term in the denominator. Therefore, we can define the electric field felt by the interlayer excitons (E_{hs}) to be:

$$E_{hs} = \frac{V_{tg} - V_{bg}}{t_{total}} \cdot \left(\frac{\varepsilon_{h-BN}}{\varepsilon_{TMD}}\right) \tag{D.6}$$

where V_{tg} is the top gate voltage, V_{bg} is the bottom gate voltage, $\varepsilon_{h-BN} = 3.9$ and $\varepsilon_{TMD} = 7.2$[178] are the dielectric constants for h-BN and TMD, and $t_{total} = 184$ nm is the total h-BN thickness. This allows us to calculate E_{hs} and extract the electron hole separation (d) from the linear Stark shift:

$$\Delta Energy = p \cdot E_{hs} = edE_{hs} \tag{D.7}$$

where $\vec{p}$ is the dipole moment and e is the electron charge.

Along with the electric field, there will be electrostatic doping due to the gate voltages. We define the carrier density doping due to the two gates in the intrinsic regime to be:

$$n = \frac{C_{tg}\, V_{tg}}{e} + \frac{C_{bg}\, V_{bg}}{e} - n_0 \tag{D.8}$$

where $C_{tg} = \varepsilon_{h-BN}/t_{top}$ and $C_{bg} = \varepsilon_{h-BN}/t_{bot}$ are the capacitances per unit area for the top and bottom gates, e is electron charge, and n_0 is the density of in-gap states needed to be filled before filling the conduction band. In order to avoid electrostatic doping of the TMDs, we use

$$V_{tg} = -\alpha V_{bg} \tag{D.9}$$

with $\alpha = t_{top}/t_{bottom} = 0.614$, where $t_{top} = 70$ nm and $t_{bottom} = 114$ nm are the top and bottom h-BN thicknesses respectively. When Eq. D.9 is inserted into Eq. D.8, we get no change in doping due to the electrostatic gates. This gate configuration is defined to be only changing the electric field without changing the doping level in the TMD layers and is confirmed from our absorption measurements as shown in Fig. 4.1(b).

D.2 Dual-gate configuration

Here, we would like to introduce the electrostatics of our dual-gated doping scheme. Here we will describe the electrostatics for our heterostructure ($MoSe_2$ on top) while controlling both gates. The same analysis can be considered with the inverted heterostructure (WSe_2 on top).

Let's begin with the following definitions (Figure D.2): $C_{TMD} = \frac{\varepsilon_{TMD}}{d}$ is the capacitance per unit area of the TMD layers, $C_{tg} = \frac{\varepsilon_{h-BN}}{t_{top}}$ and $C_{bg} = \frac{\varepsilon_{h-BN}}{t_{bot}}$ are the electrostatic capacitances per unit area of the top and bottom gates, $C_{q,\,tg}$ and $C_{q,\,bg}$ are the quantum capacitances per unit area associated with the top and bottom gates, μ_m and μ_w are the chemical potentials of the $MoSe_2$ and WSe_2 layers,

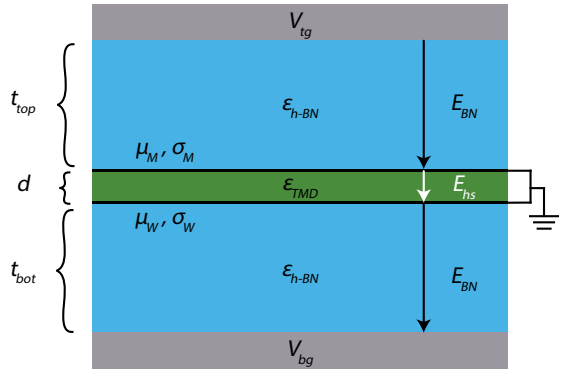

Figure D.2: Schematic of the device structure and definition of variables for dual-gating and doping in the TMD.

μ_m^0 and μ_w^0 are the chemical potentials at which the $MoSe_2$ and WSe_2 layers begin to be doped, σ_m and σ_w are the carrier densities in the $MoSe_2$ and WSe_2 layers, and d is the interlayer distance. From here we can set up a system of equations to solve for the chemical potentials:

$$\begin{cases} \sigma_m = \varepsilon_{TMD} E_{hs} - \varepsilon_{h-BN} E_{top} \\ \sigma_w = \varepsilon_{h-BN} E_{bot} - \varepsilon_{TMD} E_{hs} \end{cases} \tag{D.10}$$

$$\begin{cases} t_{top} E_{top} = V_{tg} - \mu_m \\ t_{bot} E_{bot} = \mu_w - V_{bg} \\ d E_{hs} = \mu_m - \mu_w \end{cases} \tag{D.11}$$

$$\begin{cases} \sigma_m = -C_{q,tg}(\mu_m - \mu_m^0) \\ \sigma_w = -C_{q,bg}(\mu_w - \mu_w^0) \end{cases} \tag{D.12}$$

where Eqs. D.10 are Gauss's law for $MoSe_2$ and WSe_2 layers, Eqs. D.11 are the electric field between each layer, and Eqs. D.12 describe the effects of quantum capacitance. When solving these equations

for E_{bs}, we get the following expression:

$$\begin{aligned} E_{bs} &= \frac{\mu_m - \mu_w}{d} \\ &= \frac{1}{d} \frac{\left(C_{q,bg} + C_{bg}\right)\left(C_{tg}\, V_{tg} + C_{q,\,tg}\,\mu_m^0\right) - \left(C_{q,\,tg} + C_{tg}\right)\left(C_{bg}\, V_{bg} + C_{q,\,bg}\,\mu_w^0\right)}{\left(C_{q,\,tg} + C_{tg} + C_{TMD}\right)\left(C_{q,bg} + C_{bg} + C_{TMD}\right) - C_{TMD}^2} \end{aligned} \tag{D.13}$$

We can simplify this equation by making approximations on the values of the capacitances. From plugging in the relevant numbers for the capacitances,

$$C_{TMD} = \frac{\varepsilon_{TMD}}{d} \cong \frac{7.2\varepsilon_0}{0.6\text{ nm}} \sim 12\,\varepsilon_0\,\text{nm}^{-1} \tag{D.14}$$

$$C_{tg/bg} = \frac{\varepsilon_{h-BN}}{t_{top/bot}} \cong \frac{3.9\varepsilon_0}{100\text{ nm}} \sim 4\times10^{-2}\,\varepsilon_0\,\text{nm}^{-1} \tag{D.15}$$

where $\varepsilon_{h-BN} = 3.9$ and $\varepsilon_{TMD} = 7.2$ [178] are the dielectric constants for h-BN and TMD, we can make the approximation that

$$C_{TMD} \gg C_{tg/bg} \tag{D.16}$$

The quantum capacitance will depend on whether we are in an intrinsic or doping regime:

$$\begin{aligned} C_q &\cong 0 && \text{(intrinsic)} \\ C_q &= \frac{e^2\, m^*}{\pi\,\hbar^2} = 4\,\frac{m^*\,\varepsilon_0}{m_0\,a_0} \sim 10^2\,\varepsilon_0\,nm^{-1} && \text{(doped)} \end{aligned} \tag{D.17}$$

where m^* is the effective mass of the relevant band, m_0 is the bare electron mass, and a_0 is the Bohr radius. The expression for the quantum capacitance includes the valley degeneracy, while assuming that only a single a single spin component per valley is occupied. This is valid at low doping, as in our experiments, where the Fermi energy is below (above) the second conduction (valence) band, which is split by spin-orbit coupling. When either layer is doped, then we can also make the approximation

that

$$C_q \gg C_{tg/bg}. \tag{D.18}$$

Then using the approximations in Eq. D.16, we can simplify the electric field expression from Eq. D.13 to be

$$E_{bs} \cong \frac{1}{d} \frac{\left(C_{q,bg} + C_{bg}\right)\left(C_{tg} V_{tg} + C_{q,\,tg}\,\mu_m^0\right) - \left(C_{q,\,tg} + C_{tg}\right)\left(C_{bg} V_{bg} + C_{q,\,bg}\,\mu_w^0\right)}{C_{TMD}\left(C_{q,\,tg} + C_{q,bg} + C_{tg} + C_{bg}\right)}. \tag{D.19}$$

In the intrinsic regime, where $\mu_M = \mu_W = 0$ and $C_{q,bg} \cong C_{q,tg} \cong 0$, we recover the electric field from Eq. D.6. In the doped regime, our expression becomes more complicated. First, we define the chemical potential to be

$$\mu_m \cong \mu_w \cong \frac{1}{C_{bg} + C_{tg}}(C_{bg} V_{bg} + C_{tg} V_{tg}) \tag{D.20}$$

when the given layer is in the doped regime. Let us consider the case for n-doping. If we define the gate voltages required to reach the conduction band edge when combined as V_{tg}^e and V_{bg}^e (experimentally we can begin doping with an arbitrary combination of top and bottom gates), then we define this chemical potential as

$$\mu_m^0 \cong \frac{1}{C_{bg} + C_{tg}}(C_{bg} V_{bg}^e + C_{tg} V_{tg}^e). \tag{D.21}$$

The corresponding electric field at these gate voltages will be

$$E_{Field}^e = \frac{V_{tg}^e - V_{bg}^e}{t_{total}} \cdot \left(\frac{\varepsilon_{h-BN}}{\varepsilon_{TMD}}\right). \tag{D.22}$$

We know from our experimental results that for n-doping, only the $MoSe_2$ layer becomes doped. Thus, we can assume $\mu_w^0 \cong 0$ and $C_{q,bg} \cong 0$. Using this assumption and Eqs. S22 and S24, with some

algebra, we obtain the expression

$$E_{bs} \cong E^{e}_{Field} + \frac{\varepsilon_{h-BN}}{\varepsilon_{TMD}} \frac{1}{t_{bot}} (\Delta V^{e}_{bg} - \frac{C_{tg}}{C_{q,tg}} \Delta V^{e}_{tg} + \frac{C_{tg}}{C_{q,tg}} V^{e}_{tg}) \quad \text{(n-doped)} \tag{D.23}$$

where $\Delta V^{e}_{bg} = V^{e}_{bg} - V_{bg}$ and $\Delta V^{e}_{tg} = V^{e}_{tg} - V_{tg}$ are the voltages applied once the layer is doped. A similar calculation can be done for the p-doping regime to get:

$$E_{bs} \cong E^{h}_{Field} - \frac{\varepsilon_{h-BN}}{\varepsilon_{TMD}} \frac{1}{t_{top}} (\Delta V^{h}_{tg} - \frac{C_{bg}}{C_{q,bg}} \Delta V^{h}_{bg} + \frac{C_{bg}}{C_{q,bg}} V^{h}_{bg}) \quad \text{(p-doped)} \tag{D.24}$$

where $e \rightarrow h$ corresponds to discussing hole doping in the WSe_2 valence band.

Although we see that the last term in both Eqs. D.23 and D.24 is a discontinuity in electric field from the intrinsic regime to a doped regime, this term can be ignored because $\frac{C_{tg}}{C_{q,tg}} V^{e}_{g} \sim 10^{-4}$V in our measurements, which corresponds to an energy shift of $\sim 0.3\,\mu$eV, significantly smaller than our interlayer exciton linewidth $\sim$ 10 meV. Therefore, we can ignore this final term and any observable jumps in exciton energy cannot be attributed to an abrupt change in electric field.

D.2.1 Special case: Single-gated

When using a single gate for the heterostructure, because of the gate structure and screening from either the $MoSe_2$ or WSe_2 layer, the applied electric field will differ depending on the doping level. We consider special cases of Eqs. D.6, D.23, and D.24, to obtain expressions for the electric field when sweeping a single gate. When sweeping the top gate only and fixing $V_{bg} = 0$:

$$E_{bs} = \begin{cases} \frac{\varepsilon_{h-BN}}{\varepsilon_{TMD}} (\frac{V^{h}_{tg}}{t_{total}} + \frac{\Delta V^{h}_{tg}}{t_{top}}) & V_{tg} < V^{h}_{tg} \quad \text{(p-doped)} \\ \frac{\varepsilon_{h-BN}}{\varepsilon_{TMD}} (\frac{V_{tg}}{t_{total}}) & V^{h}_{tg} < V_{tg} < V^{e}_{tg} \quad \text{(intrinsic)} \\ \frac{\varepsilon_{h-BN}}{\varepsilon_{TMD}} (\frac{V^{e}_{tg}}{t_{total}}) & V^{e}_{tg} < V_{tg} \quad \text{(n-doped)} \end{cases} \tag{D.25}$$

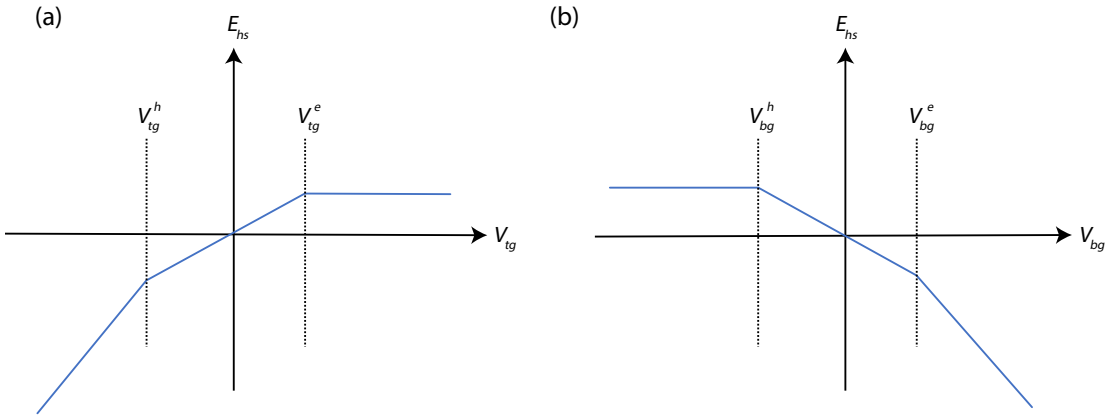

Figure D.3: Representation of electric field as a function of a single gate as described in Eq. D.25 (a) and Eq. D.26 (b).

When sweeping the bottom gate only and fixing $V_{tg} = 0$:

$$E_{hs} = \begin{cases} \frac{\varepsilon_{h-BN}}{\varepsilon_{TMD}}\left(\frac{V_{bg}^{h}}{t_{total}}\right) & V_{bg} < V_{bg}^{h} \quad \text{(p-doped)} \\ -\frac{\varepsilon_{h-BN}}{\varepsilon_{TMD}}\left(\frac{V_{bg}}{t_{total}}\right) & V_{bg}^{h} < V_{bg} < V_{bg}^{e} \quad \text{(intrinsic)} \\ \frac{\varepsilon_{h-BN}}{\varepsilon_{TMD}}\left(\frac{V_{bg}^{e}}{t_{total}} - \frac{\Delta V_{bg}^{e}}{t_{bot}}\right) & V_{bg}^{e} < V_{bg} \quad \text{(n-doped)} \end{cases} \tag{D.26}$$

The V_{tg} (V_{bg}) sweeping configuration allows for n- (p-) doping without changing electric field in the TMD for one doping direction. This allows us to explore the doping response of the interlayer exciton peaks without the Stark effect. A visual representation of the electric fields for the two special cases is shown in Figure D.3. Thus, these electrostatic conditions provide the basis for using separate single gates for understanding the doping behavior in Chapters 4 and 7.

The carrier density when using a single gate is simply an extension of Eq. D.8 for only a single gate:

$$n = \frac{C_g V_g}{e} - n_0 \tag{D.27}$$

where $g = tg, bg$ is either the top gate or the bottom gate chosen for doping.

D.2.2 Special case: Dual-gate with same polarity ($V_{tg} = \alpha\, V_{bg}$)

We can also apply a symmetric gating configuration where $V_{tg} = \alpha\, V_{bg}$ with ($\alpha = t_{top}/t_{bottom}$). To understand the electric field applied in this configuration, we summarize the electric field felt by the heterostructure (Eqs. D.6, D.23, and D.24) in the intrinsic and doped regimes as derived above:

$$\begin{aligned} E_{hs} &= \tfrac{V_{tg}-V_{bg}}{t_{total}} \cdot \left(\tfrac{\varepsilon_{h-BN}}{\varepsilon_{TMD}}\right) \quad \text{(intrinsic)} \\ E_{hs} &\cong E^{e}_{Field} + \tfrac{\varepsilon_{h-BN}}{\varepsilon_{TMD}} \tfrac{\Delta V^{e}_{bg}}{t_{bot}} \quad \text{(n-doped)} \\ E_{hs} &\cong E^{h}_{Field} - \tfrac{\varepsilon_{h-BN}}{\varepsilon_{TMD}} \tfrac{\Delta V^{h}_{tg}}{t_{top}} \quad \text{(p-doped)} \end{aligned} \tag{D.28}$$

where V^{e}_{bg} is the initial back gate voltage necessary to begin electron doping the sample, $\Delta V^{e}_{bg} = V^{e}_{bg} - V_{bg}$ is the voltage applied once the layer is doped, $t_{total} = t_{top} + t_{bot}$, and $E^{e}_{Field} = \tfrac{V^{e}_{tg}-V^{e}_{bg}}{t_{total}} \cdot \left(\tfrac{\varepsilon_{h-BN}}{\varepsilon_{TMD}}\right)$ is the electric field before the sample becomes doped (with $e \to h$ to describe holes and $bg \to tg$ to describe the top gate). If we plug in our gating condition of $V_{tg} = \alpha\, V_{bg}$ into the above solutions, we find that once the sample is doped we have a reduced electric field, which is the same for both positive and negative applied gate voltage:

$$E_{hs} = \begin{cases} E^{h}_{Field} + \tfrac{\varepsilon_{h-BN}}{\varepsilon_{TMD}} \tfrac{\Delta V^{h}_{tg}}{t_{top}} & V_{tg} < V^{h}_{tg} \text{ or } V_{bg} < V^{h}_{bg} \quad \text{(p-doped)} \\ \tfrac{\varepsilon_{h-BN}}{\varepsilon_{TMD}} \tfrac{t_{top}-t_{bot}}{t_{total}} \tfrac{V_{tg}}{t_{top}} & V^{h}_{tg} < V_{tg} < V^{e}_{tg} \text{ and } V^{h}_{bg} < V_{bg} < V^{e}_{bg} \quad \text{(intrinsic)} \\ E^{e}_{Field} - \tfrac{\varepsilon_{h-BN}}{\varepsilon_{TMD}} \tfrac{\Delta V^{e}_{tg}}{t_{top}} & V^{e}_{tg} < V_{tg} \text{ or } V^{e}_{bg} < V_{bg} \quad \text{(n-doped)} \end{cases} \tag{D.29}$$

The main advantage of the dual-gated scheme is to achieve higher densities. We calculate the charge density based on the parallel plate capacitor model when using the $V_{tg} = \alpha\, V_{bg}$ gating scheme:

$$n = \frac{\varepsilon_{h-BN}}{t_{top}} \Delta V^{e}_{tg} + \frac{\varepsilon_{h-BN}}{t_{bottom}} \Delta V^{e}_{bg} = 2\frac{\varepsilon_{h-BN}}{t_{top}} \Delta V^{e}_{tg} \tag{D.30}$$

with ε_{h-BN} being the dielectric constant and n being the electron density. Replacing $e \rightarrow h$ gives a similar expression for the hole density (p). Thus, we get twice the density achievable with a single gate allowing us to reach densities on the order of 10^{13} cm^{-2}.

Note that in Figure 6.3, we use a different gate scheme where $V_{bg} = \alpha V_{tg}$, due to gate leakage issues. However, the electrostatics should only differ by geometric factors. For the ease of the reader, we provide the applied density in this configuration by substituting $V_{bg} = \alpha V_{tg}$ into the capacitor model to get

$$n = \frac{\varepsilon_{h-BN}}{t_{top}} \Delta V_{tg}^{e} + \frac{\varepsilon_{h-BN}}{t_{bottom}} \Delta V_{bg}^{e} = (1+\alpha^2) \frac{\varepsilon_{h-BN}}{t_{top}} \Delta V_{tg}^{e} \approx 1.38 \frac{\varepsilon_{h-BN}}{t_{top}} \Delta V_{tg}^{e}, \tag{D.31}$$

which was still large enough to reach the highly doped regime.

D.3 Electrostatics in heterostructures with h-BN spacer

In this section, we discuss the electrostatics in the $MoSe_2$/h-BN/WSe_2 heterostructure devices. For simplicity, we begin with the case when the h-BN spacer perfectly insulates the two active TMD layers, which is also briefly discussed in Wang, et al.[66]. Figure D.4(a) shows a schematic of the device with a top gate (V_{tg}), bottom gate (V_{bg}), and a bias voltage (V_{ds}) on the WSe_2 layer. In this case, we can consider the electrostatically doping electrons in the $MoSe_2$

$$n = \frac{C_{tg}}{e} V_{tg} + \frac{C_{bg}}{e} V_{bg} - n_0 \tag{D.32}$$

or holes in the WSe_2

$$p = -\left[\frac{C_{tg}}{e} (V_{tg} - V_{ds}) + \frac{C_{bg}}{e} (V_{bg} - V_{ds}) \right] - p_0, \tag{D.33}$$

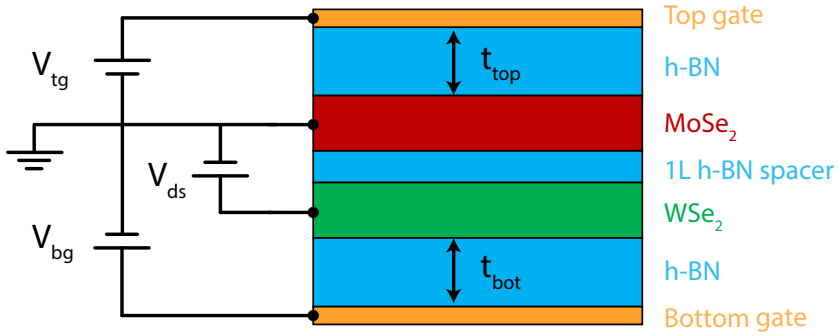

Figure D.4: Schematic of the device with h-BN spacer, which perfectly isolates the two layers. The bias voltage (V_{ds}) and the gate voltages (V_{tg} and V_{bg}) are used to control the density in the device.

where n_0 and p_0 are the net density required between V_{tg} and V_{bg} to begin doping the layers and $C_{tg/bg} = \varepsilon_{h-BN}/t_{top/bot}$ is the gate dielectric capacitance. In our experiments we apply $V_{tg} = \alpha V_{bg}$ where $\alpha = C_{bg}/C_{tg}$. Rewriting the equations, we find

$$n = 2\frac{C_{tg}}{e}V_{tg} - n_0, \tag{D.34}$$

$$p = -\left[2\frac{C_{tg}}{e}V_{tg} - \frac{(C_{tg}+C_{bg})}{e}V_{ds}\right] - p_0. \tag{D.35}$$

We discuss three special cases. The first is when the total electron density is 0:

$$\begin{aligned} n = 2\tfrac{C_{tg}}{e}V_{tg} - n_0 = 0 \\ V_{tg} = \tfrac{e}{2C_{tg}}n_0. \end{aligned} \tag{D.36}$$

Since the $MoSe_2$ is controlled solely by the gates, we simply tune the gates to reach the $n = 0$ condition.

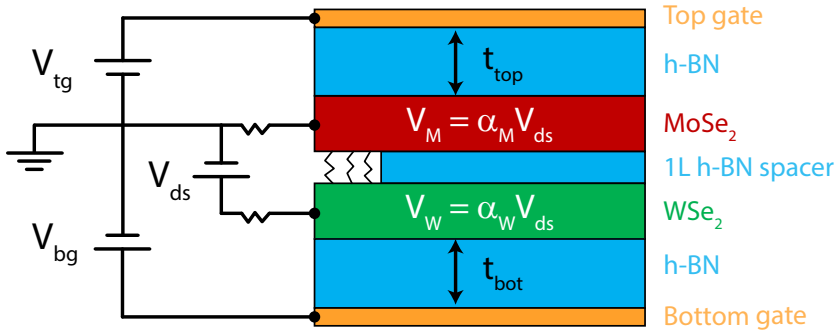

Figure D.5: Schematic of the device with h-BN spacer, used in our experiments. Contact resistances and resistance between the layers (labeled as resistors) will weakly couple the two layers affecting the electrostatics.

To have the total hole density be 0

$$p = 2\frac{C_{tg}}{e}V_{tg} - \frac{(C_{tg}+C_{bg})}{e}V_{ds} - p_0 = 0$$
$$V_{tg} = \tfrac{1}{2}(1 + \frac{C_{bg}}{C_{tg}})V_{ds} + \frac{e}{2C_{tg}}p_0. \tag{D.37}$$

For the WSe_2 layer, we must match V_{ds} and the V_{tg} in order to reach the $p = 0$ condition. The final condition we discuss is the $n = p$ condition:

$$n - p = 0$$
$$\left[2\frac{C_{tg}}{e}V_{tg} - n_0\right] + \left[2\frac{C_{tg}}{e}V_{tg} - \frac{(C_{tg}+C_{bg})}{e})V_{ds} - p_0\right] = 0 \tag{D.38}$$
$$4C_{tg}V_{tg} - (C_{tg} + C_{bg})V_{ds} - \frac{e}{2C_{tg}}n_0 - \frac{e}{2C_{tg}}p_0 = 0$$
$$V_{tg} = \frac{1}{4}(1 + \frac{C_{bg}}{C_{tg}})V_{ds} + \frac{e}{2C_{tg}}n_0 + \frac{e}{2C_{tg}}p_0. \tag{D.39}$$

We see that the behavior is straight-forward, where the $n = p$ condition scales with half of the slope of the $n = 0$ and $p = 0$ conditions.

While the above equations work well for a perfectly insulating h-BN layer, we must modify it to fit the data in our device. The device discussed in Chapter 8 has only a single layer of h-BN spacer and also an area with no h-BN spacer, which will act as an electrical short between the layer. Since the two layers may pass current, the voltage on the $MoSe_2$ and WSe_2 layers will scale with the resistances between the contacts and between the two layers. While modeling the entire circuit is difficult, we can create a phenomenological model where the voltage on the $MoSe_2$ (V_M) and WSe_2 (V_W) are scaled by a scaling factor $V_M = \alpha_M V_{ds}$ and $V_W = \alpha_W V_{ds}$, respectively. Figure D.4 shows the schematic for this model. In this case, our equations above will be modified to be

$$\begin{aligned} n &= \left[\tfrac{C_{tg}}{e}(V_{tg} - V_M) + \tfrac{C_{bg}}{e}(V_{bg} - V_M)\right] - n_0, \\ p &= -\left[\tfrac{C_{tg}}{e}(V_{tg} - V_W) + \tfrac{C_{bg}}{e}(V_{bg} - V_W)\right] - p_0. \end{aligned} \tag{D.40}$$

We can simplify this to show that

$$\begin{aligned} n &= \left[2\tfrac{C_{tg}}{e}V_{tg} - \tfrac{(C_{tg}+C_{bg})}{e}\alpha_M V_{ds}\right] - n_0, \\ p &= -\left[2\tfrac{C_{tg}}{e}V_{tg} - \tfrac{(C_{tg}+C_{bg})}{e}\alpha_W V_{ds}\right] - p_0. \end{aligned} \tag{D.41}$$

In this case, we see the $MoSe_2$ layer gets tuned by V_{ds} due to the weak coupling between the layers. We can now show the $n = 0, p = 0$, and $n = p$ conditions for this adjusted model

$$\begin{aligned} V_{tg} &= \tfrac{\alpha_M}{2}(1 + \tfrac{C_{bg}}{C_{tg}})V_{ds} + \tfrac{e}{2C_{tg}}n_0 && n = 0 \text{ condition} \\ V_{tg} &= \tfrac{\alpha_W}{2}(1 + \tfrac{C_{bg}}{C_{tg}})V_{ds} + \tfrac{e}{2C_{tg}}p_0 && p = 0 \text{ condition} \\ V_{tg} &= \tfrac{(\alpha_W+\alpha_M)}{4}(1 + \tfrac{C_{bg}}{C_{tg}})V_{ds} + \tfrac{e}{2C_{tg}}n_0 + \tfrac{e}{2C_{tg}}p_0 && n = p \text{ condition} \end{aligned} \tag{D.42}$$

which we use to fit the reflection data in Chapter 8. We note some specific cases for this model. If the two layers are completely isolated, we would expect $\alpha_W = 1$ and $\alpha_M = 0$, recovering the original equations. If the two layers are shorted to each other, then $\alpha_W = \alpha_M$, resulting in the same solution for all three conditions. In this case, the ratio between the contact resistances would determine the lateral (rather than vertically across the heterostructure) drop in the voltage in the heterostructure.

E

Supplementary Theoretical discussions

This appendix includes more detailed theoretical discussions, which are more loosely summarized in the main chapters of this thesis.

E.1 Theoretical description of interaction driven diffusion

We now derive a simple model for the diffusion of excitons that takes into account electrostatic interactions. Excitons that are generated with a rate $R(\mathbf{r}, t)$ per unit area and recombine with rate γ satisfy

the continuity equation

$$\frac{\partial n(r,t)}{\partial t} + \nabla \cdot J(r,t) = R(r,t) - \gamma n(r,t) \tag{E.1}$$

$$\frac{\partial n(r,t)}{\partial t} + \nabla \cdot J(r,t) = R(r,t) - \gamma n(r,t) \tag{E.2}$$

where $n(\mathbf{r},t)$ is the exciton density, and $\mathbf{J}(\mathbf{r},t)$ the exciton current density. We assume that the excitons are locally in equilibrium such that

$$\mathbf{J}(\mathbf{r},t) = \frac{\tau}{m} n(\mathbf{r},t)\left[-\nabla\mu(r,t) + F(\mathbf{r},t)\right], \tag{E.3}$$

where τ is the momentum relaxation time, m the exciton mass, $\mu(\mathbf{r},t)$ the local chemical potential, and $F(\mathbf{r},t)$ a local force. The chemical potential is to be determined self-consistently to match the local density. For a non-interacting Bose gas in two dimensions, we have

$$\mu = k_B T ln\left[1 - e^{-n(\mathbf{r},t)/n_c}\right], \tag{E.4}$$

where $n_c = mk_BT/(\pi\hbar^2)$, having accounted for valley degeneracy.

Interactions between excitons are taken into account via the force term. For a rigid exciton, the net electric field is given by the difference of the field acting on the hole and the electron, i.e. $E = E_h - E_e$. If no in-plane external field is applied, the only contribution to the electric field is generated by the excitons themselves. By approximating each exciton as a positive and a negative point charge separated by the layer separation d, we can express the potential energy as

$$U(r,t) = \frac{e^2}{2\pi\varepsilon}\int d^2r\prime n(r',t)\left(\frac{1}{|r-r'|} - \frac{1}{\sqrt{|r-r'|^2+d^2}}\right). \tag{E.5}$$

Together with $F = -\nabla U$, Eqs. E.1 – E.5 form a set of nonlinear integro-differential equations for the exciton density $n(r,t)$. While these equations may be tractable numerically, it is desirable to make further simplifications. In particular, we note that the exciton density is expected to vary only weakly over the length scale $d \approx 0.6$ nm, which enables us to approximate the integral in Eq. E.5 by $U(\mathbf{r},t) \approx e^2 d n(\mathbf{r},t)/\varepsilon$. This expression has the simple interpretation of the potential inside a parallel plate capacitor, where the charge density is allowed to slowly vary in space. In Section 4.3, the same expression was used to estimate the exciton density from the observed blue shift of the PL resonance. We substitute this result back into Eq. E.1 to obtain

$$J(r,t) = -D\left[\frac{n(r,t)/n_c}{e^{n(r,t)/n_c}-1} + \frac{n(r,t)}{n^*}\right]\nabla n(r,t), (37) \tag{E.6}$$

where $D = kT\tau/m$ and $n^* = \varepsilon k_B T/(e^2 d)$. By substituting back into Eq. E.2, we thus arrive at the nonlinear diffusion equation

$$\frac{\partial n(r,t)}{\partial t} - D\nabla\cdot\left[\left(\frac{n(r,t)/n_c}{e^{n(r,t)/n_c}-1} + \frac{n(r,t)}{n^*}\right)\nabla n(r,t)\right] = R(r,t) - \gamma n(r,t). \tag{E.7}$$

In the limit of vanishing density, the above model reduces to conventional single-particle diffusion with diffusion constant D. Single particle diffusion is suppressed for densities approaching n_c as the occupation of the zero momentum state is enhanced by the Bose occupation factor. At the same time, repulsion between the excitons leads to increasing diffusion with increasing density. At temperature 4 K, using $d = 0.6$ nm, $\varepsilon = \varepsilon_0$, $m \approx m_e$, we have $n^* \approx 3\times 10^9\, cm^{-2}$ and $n_c \approx 5\times 10^{11}$ cm^{-2}.

We note that the above treatment ignores a number of important effects. We neglect short-range correlations that arise due to interactions in the exciton fluid, which have been predicted to significantly affect the interaction induced blue shift [113]. We further ignore the role of dielectric screening, which plays an important role in determining the exciton binding energy [113,179]. While these effects

may modify the value of n^*, we expect Eq. E.6 to remain valid to a good approximation. Finally, we have ignored the possibility of temperature gradients as well as interactions between excitons and phonons, which have been proposed to play an important role in monolayer TMDs[29].

We now consider a Gaussian pump profile given by

$$R(r) = \gamma n^* A e^{-2r^2/w_0^2}. \tag{E.8}$$

The dimensionless constant A quantifies the density of excitons in units of n^* generated at the center of the beam per exciton lifetime. By defining the diffusion length $l^2 = D/\gamma$, $\widetilde{n} = n/n^*$, and $\tau = \gamma t$, Eq. E.6 can be concisely written as

$$\frac{\partial \widetilde{n}(r,t)}{\partial \tau} - l^2 \frac{1}{r}\frac{\partial}{\partial r}\left[r\left(\frac{\alpha \widetilde{n}(r,t)}{e^{\alpha \widetilde{n}(r,t)} - 1} + \widetilde{n}(r,t) \right) \frac{\partial \widetilde{n}(r,t)}{\partial r} \right] = A e^{-2r^2/w_0^2} - \widetilde{n}(r,t), \tag{E.9}$$

where $\alpha = n^*/n_c$, and we assumed that the boundary and initial conditions are cylindrically symmetric such that there is no angular dependence at any time. Based on our estimate above, we set $\alpha = 0.01$ for all numerical simulations below. To explore the exciton dynamics quantitatively, we define the width

$$w(t) = \sqrt{\langle r^2(t) \rangle} = \left[\frac{\int d^2 r\, |r|^2 n(r,t)}{\int d^2 r\, n(r,t)} \right]^{1/2}. \tag{E.10}$$

The steady-state width as a function of the amplitude A is shown for three different values of the diffusion length l in Figure E.1. For $A \ll 1$, the diffusion term due to interaction is negligible and $\alpha \widetilde{n}(r,t)/(e^{\alpha \widetilde{n}(r,t)} - 1) \approx 1$, such that the width is given by $w \approx \sqrt{w_0^2/2 + 4l^2}$. In this regime, the steady-state density is given by $n(r) \propto \int d^2\mathbf{r}\, R(|\mathbf{r} - \mathbf{r}'|)\, K_0(r'/l)$, where K_0 is the modified Bessel function, which asymptotically approaches

$$n \sim \frac{e^{-r/l}}{\sqrt{r/l}} \tag{E.11}$$

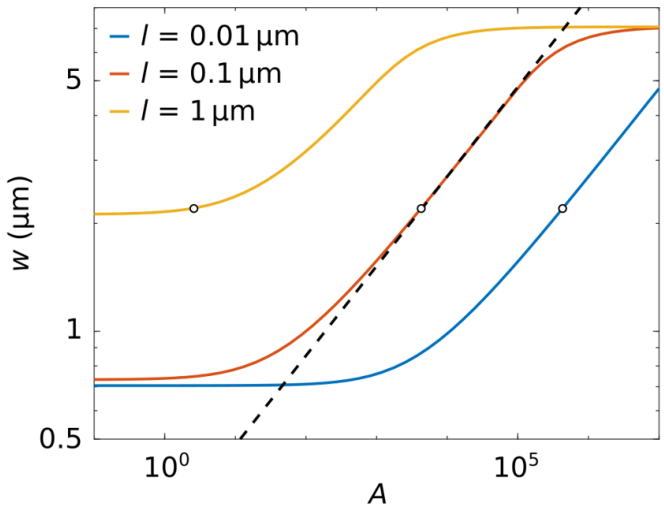

Figure E.1: Steady-state width as a function of the pump amplitude A for three different values of the diffusion length. The simulation was performed with Gaussian beam waist $w_0 = 1\,\mu$m on a disk of radius $10\,\mu$m with hard wall boundary conditions. The dashed line indicates the scaling $w \propto A^{1/4}$, corresponding to $D_{eff} \propto A^{1/2}$, which is the behaviour expected at high power in the absence of finite size effects. The circles indicate the parameters for which time dependence is plotted in Figure E.2.

when $r, l \gg w_0$. The effect of interaction driven diffusion becomes apparent when $A \sim max(1, w_0^2/l^2)$. For A much greater than this value, the width scales as $w \propto A^{1/4}$ until finite size effects start to matter. We can associate the width with an effective diffusion constant $D_{eff} = (w^2/4 - w_0^2/8)\,\gamma$, which corresponds to the diffusion constant in a linear model that would reproduce the same steady-state width. At high power, in the absence of finite size effects, we expect $D_{eff} \propto A^{1/2}$.

This behavior is in qualitative agreement with the experimental observation of increased diffusion at high power. Nonlinear diffusion also provides a potential explanation for the fact that only little diffusion is observed after the laser has been switched off: As the exciton population decays, the effective diffusion constant decreases. This effect is evident in the plots of the exciton density as a function of time in Figure E.2, where the exciton generation rate is set to zero at $\gamma t = 10$. For $\gamma t < 10$, the amplitude A was chosen such that the steady state width is $2.2\,\mu$m for all three values of the diffusion length, corresponding to the circles in Figure E.1. There is little diffusion at late times when the steady-state

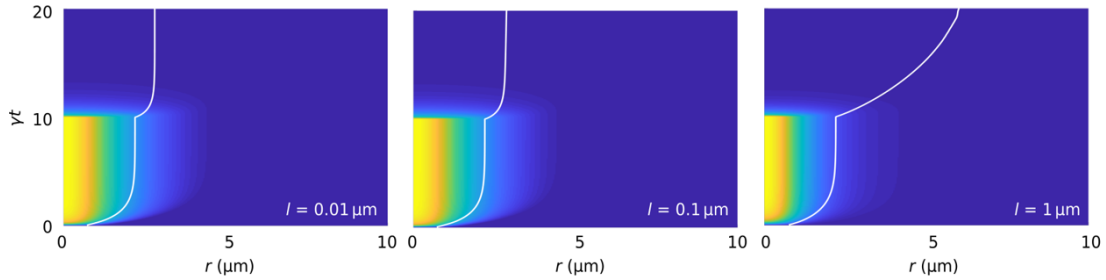

Figure E.2: Exciton density as a function of time and distance from the beam center for three different values of the diffusion length. The white line indicates the width as defined by Eq. E.10. The amplitude is chosen such that the steady-state width is $2.2\,\mu m$. All remaining computational parameters are the same as in Figure E.1.

width is dominated by the interaction term ($l = 0.01\,\mu$ m and $l = 0.1\,\mu$ m), whereas conventional single particle diffusion is significant for $l = 1\,\mu$ m.

E.2 Modeling of diffraction limited spot size and the trap alignment

We attempt to reproduce the 0.95μm diffusion full-width half-max (FWHM) by including two parameters that can increase spatial broadening. The first is the possibility of slight defocusing from the ideal diffraction limited spot at the emission wavelength of 900 nm. We model the diffraction limited spot size as the Airy pattern, or a Fraunhofer diffraction pattern:

$$I(x,\lambda) = I_0 \left(\frac{2J_1(2\pi \frac{x}{\lambda} \mathrm{NA})}{2\pi \frac{x}{\lambda} \mathrm{NA}} \right)^2 . \tag{E.12}$$

where J_1 is the Bessel function of the first order, NA is the numerical aperture of the objective (0.75), x is the spatial coordinate, and λ is the collection wavelength. We vary λ with the assumption that our spot size is not diffraction limited.

The second parameter we adjust is possible misalignment of the top and bottom gates (x_{offset}). We roughly model the two gates as adjustable square-wave potentials with a width of 500 nm and falling edges with a characteristic length scale, $x_{\mathrm{edge}} = t_{hBN}$, where t_{hBN} is the corresponding hBN thick-

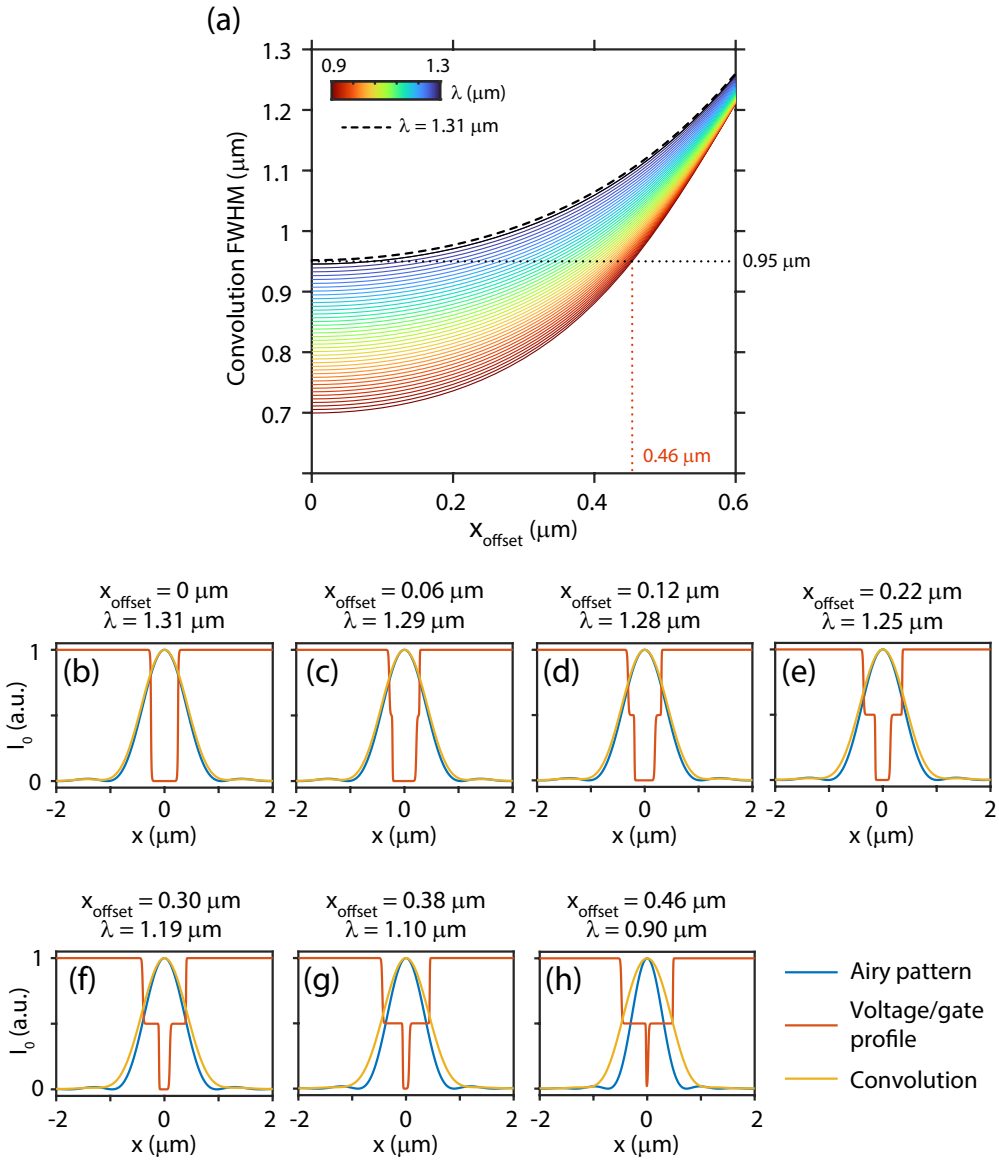

Figure E.3: (a) The convolution FWHM for various x_{offset} and the diffraction limited spot size (governed by the wavelength λ). There are many solutions that could result in a FWHM in the experiment. Black dotted line is the convolution FWHM of 0.95μm. Red dotted line is the trap width if we are diffraction limited at 900 nm and the black dashed line is the diffraction limited wavelength if we had no gate offset. (b)-(h) Representative convolutions for various x_{offset} and λ that result in a FWHM of $\sim 0.95\mu$m. Based on the voltage profiles, we can make an estimate of the misalignment and spot size broadening contributions.

ness. We use this length scale as a rough measure of the fringing fields from the gates. This takes the functional form:

$$V(x, x_{\text{offset}}) = \frac{V_0}{4}\left[\tanh\left(\frac{x + (0.25 + x_{\text{offset}})}{x_{\text{edge}}/4}\right) - \tanh\left(\frac{x - (0.25 - x_{\text{offset}})}{x_{\text{edge}}/4}\right)\right.$$
$$\left. + \tanh\left(\frac{x + (0.25 - x_{\text{offset}})}{x_{\text{edge}}/4}\right) - \tanh\left(\frac{x - (0.25 + x_{\text{offset}})}{x_{\text{edge}}/4}\right)\right]. \quad \text{(E.13)}$$

We assume $n_{IE} \propto V_0 - V(x, x_{\text{offset}})$. We then convolute the Airy function with n_{IE} for varying values of λ and x_{offset} to get a simulated spatial distribution of the IEs. Figure E.3 shows the FWHM of the convolution for varying parameters. We first note the extremes. If we are truly diffraction limited ($\lambda = 0.9\mu$m), the top and bottom gates would be offset by 0.46μm (red dotted line). If $x_{\text{offset}} = 0$, then our beam spot is equivalent to a diffraction limited spot at $\lambda = 1.31\mu$m (black dashed line). Realistically, there are likely contributions from both that broaden our measured FWHM. Figures E.3(b)-(h) show representative curves along the convolution FWHM = 0.95μm line (black dotted line). We do not see any evidence of E_{og} majorly affecting the energy of the excitons in the trap (Fig. E.3(e)-(h)). This strongly suggests a rough upper bound $x_{\text{offset}} < 0.20\mu$m, but that our spot size is broader than the diffraction limit.

F

Additional Supplementary Data

Included in this Appendix are supplementary data figures organized by chapter. This data, while less polished, form an important part of the story for explaining the rich physics behind the interlayer excitons in the $MoSe_2/WSe_2$ platform. Hopefully, the odd data set here may shed some light on important physics in the future.

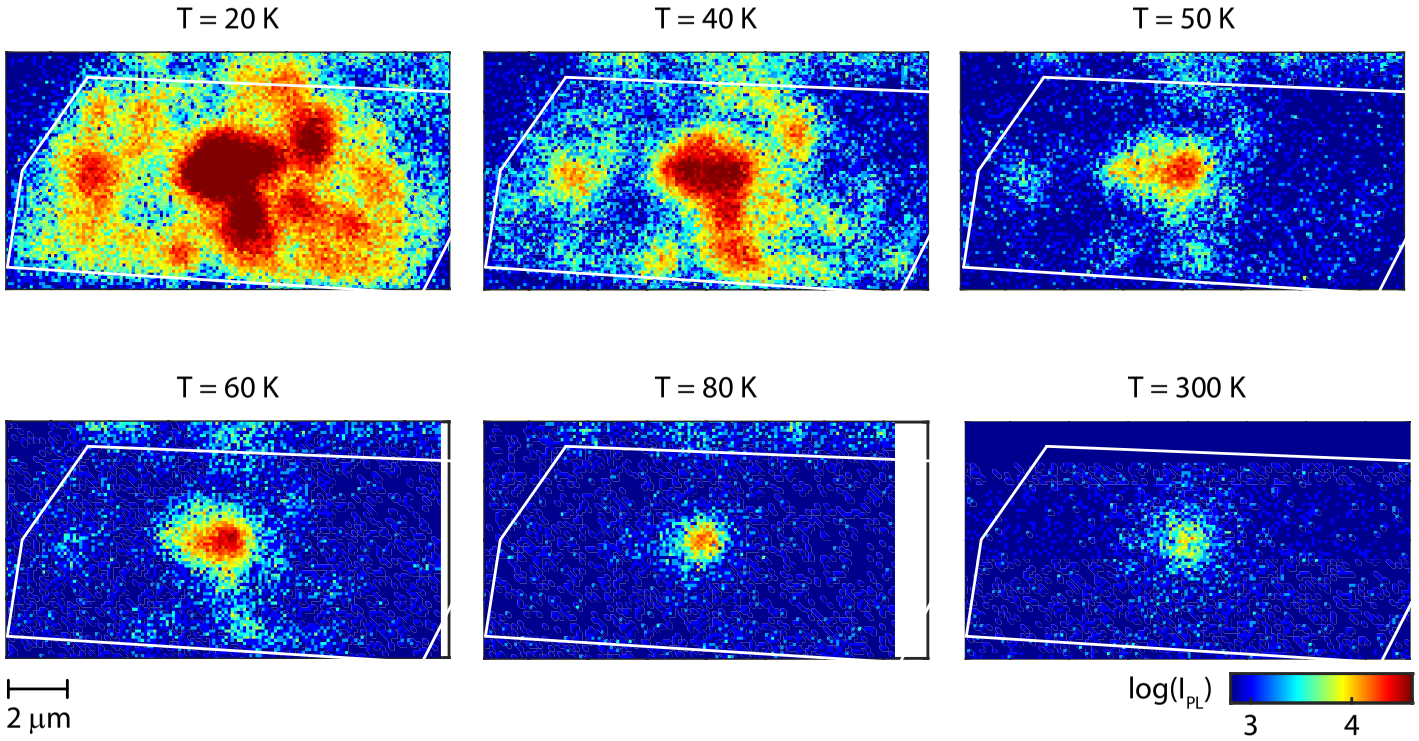

Figure F.1: Temperature dependent log PL intensity (I_{PL}) exciton diffusion maps with continuous wave excitation P = 550 μW at the center of the sample. The white lines define the heterostructure region.

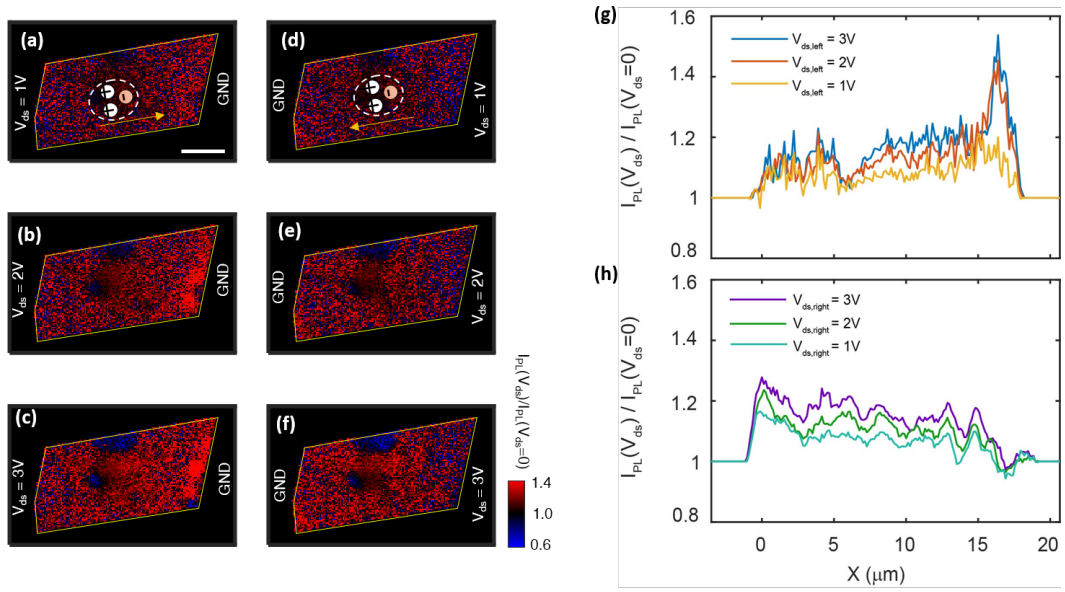

Figure F.2: (a)-(c) Normalized spatial dependence of I_{PL} under different V_{ds}'s applied on the left side for p-doped charged interlayer excitons (CIEs). We normalized I_{PL} by $I_{PL}(V_{ds})/I_{PL}(V_{ds} = 0)$. We observed a larger population of charged IEs near the right WSe_2 electrode by increasing V_{ds}. (d)-(f) Same as (a)-(c) except for switched V_{ds} direction. (g)-(h) vertical average linecut of the normalized I_{PL} for data from (a)-(c) and (d)-(f) respectively, vs. X for different V_{ds}. For (a) and (d) V_{bg} = -3.375V, for (b) and (e) V_{bg} = -1.25V and for (c) and (f) V_{bg} = 0.875V while V_{tg} = 0 in all the cases. The WSe_2 contact top gates were kept at -13V during this measurement.

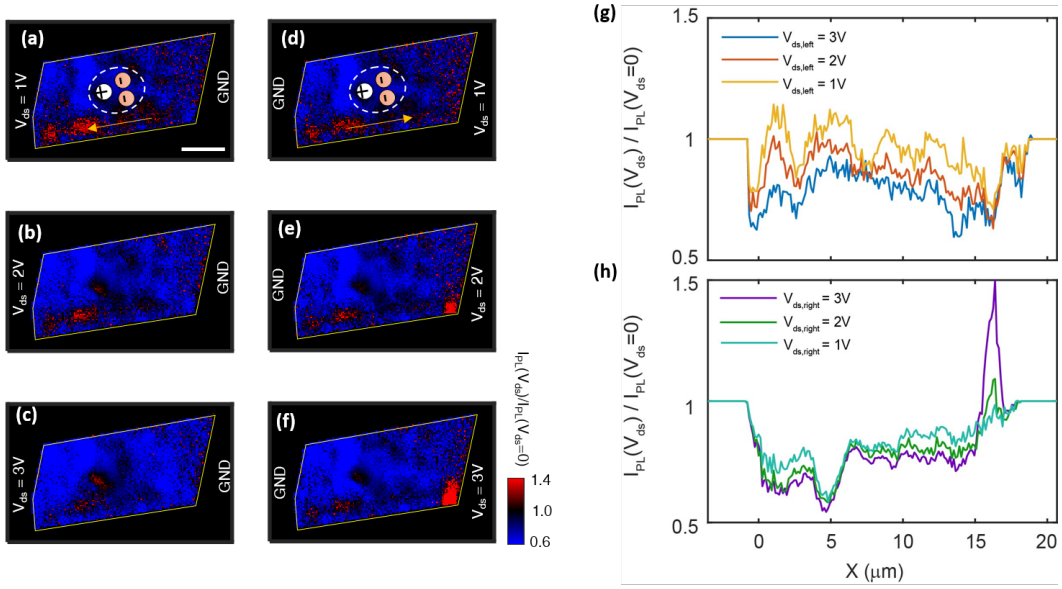

Figure F.3: (a)-(c) Normalized spatial dependence of I_{PL} under different V_{ds}'s applied on the left side for n-doped charged interlayer excitons (CIEs). We normalized I_{PL} by $I_{PL}(V_{ds})/I_{PL}(V_{ds} = 0)$. (d)-(f) Same as (a)-(c) except for switched V_{ds} direction. (g)-(h) vertical average linecut of the normalized I_{PL} for data from (a)-(c) and (d)-(f) respectively, vs. X for different V_{ds}. For (a) and (d) V_{tg} = 1.6 V, for (b) and (e) V_{tg} = 3.2 V and for (c) and (f) V_{tg} = 4.8 V while V_{bg} = 0 in all the cases. The WSe_2 contact top gates were kept at -13 V and the $MoSe_2$ contact top gates were kept at 13 V during this measurement.

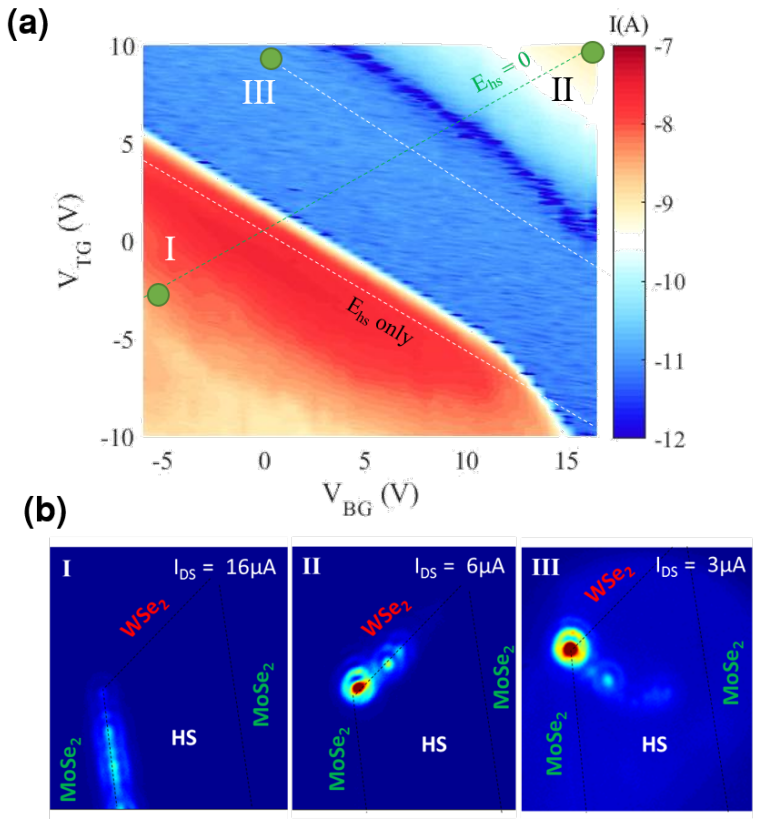

Figure F.4: (a) I_{ds} vs. V_{tg} and V_{bg} (with V_{ds} = -3V) on $MoSe_2$ and grounded WSe_2. The white dashed line represents the compensated electric field line where V_{bg} = 10.37 V - αV_{tg} and α is defined in Appendix D. We label three regimes which correspond to p-doped (region I), n-doped (region II) and intrinsic (region III). (b) Spatial dependent electroluminescence maps taken in the labeled regimes (I, II, III).

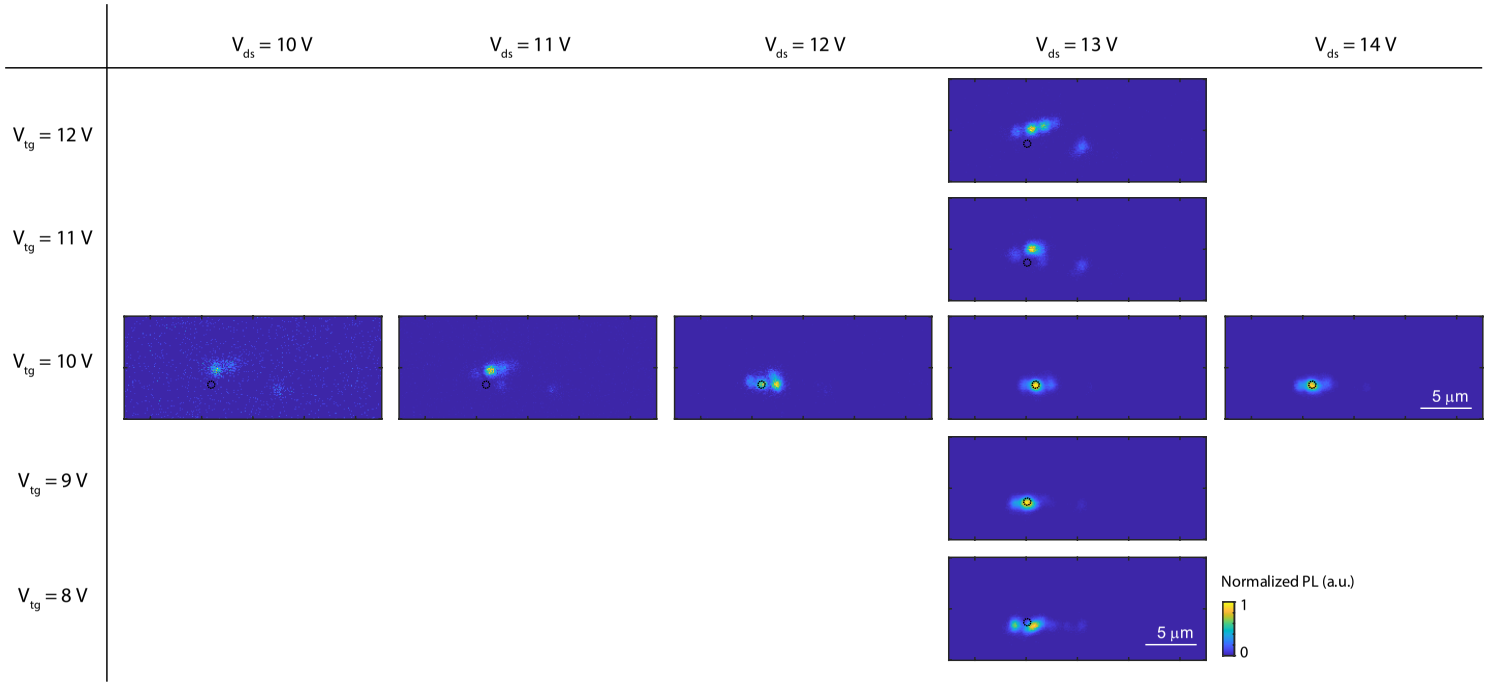

Figure F.5: Electroluminescence (EL) map of the sample at different V_{ds} for $V_{tg} = \alpha V_{bg}$ = 10 V and at different $V_{tg} = \alpha V_{bg}$ for V_{ds} = 13 V. Tuning either V_{ds} or V_{tg} away from the optimal point shifts the EL position away from the designated collection spot in the heterostructure. This optimal position occurs at the onset of current through the gated region, as described in Fig. 6.13.

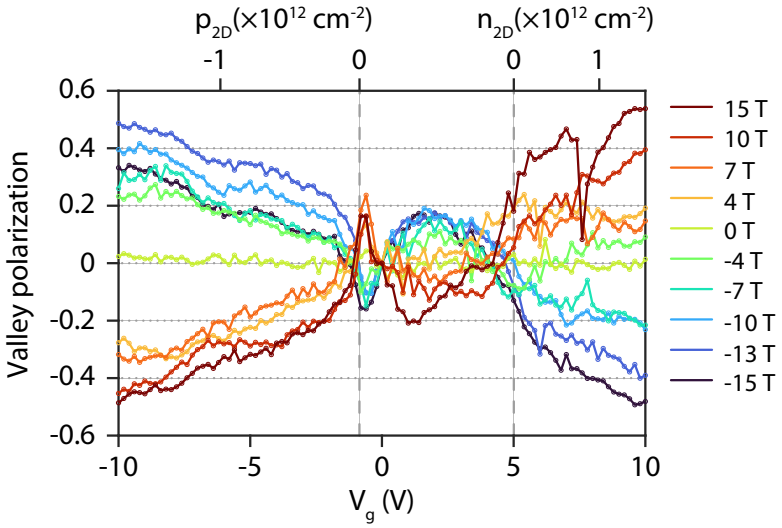

Figure F.6: Valley polarization = $\frac{I_{\sigma-}-I_{\sigma+}}{I_{\sigma-}+I_{\sigma+}}$ as a function of V_g for different magnetic fields (B). Positive (negative) valley polarization corresponds to +K(-K) valley polarization.

References

[1] Yuanbo Zhang, Yan-Wen Tan, Horst L. Stormer, and Philip Kim. Experimental observation of the quantum Hall effect and Berry's phase in graphene. *Nature*, 438(7065):201–204, 2005.

[2] K. S. Novoselov, A. K. Geim, S. V. Morozov, D. Jiang, Y. Zhang, S. V. Dubonos, I. V. Grigorieva, and A. A. Firsov. Electric field in atomically thin carbon films. *Science*, 306(5696):666–669, 2004.

[3] K. S. Novoselov, A. K. Geim, S. V. Morozov, D. Jiang, M. I. Katsnelson, I. V. Grigorieva, S. V. Dubonos, and A. A. Firsov. Two-dimensional gas of massless Dirac fermions in graphene. *Nature*, 438(7065):197–200, 2005.

[4] R. F. Frindt. Single crystals of MoS_2 several molecular layers thick. *Journal of Applied Physics*, 37(4):1928–1929, 1966.

[5] L. C. Upadhyayula, J. J. Loferski, A. Wold, W. Giriat, and R. Kershaw. Semiconducting properties of single crystals of N- and P-type tungsten diselenide (WSe2). *Journal of Applied Physics*, 39(10):4736–4740, 1968.

[6] W J Schutte, J L De Boer, and F Jellinek. Crystal structures of tungsten disulfide and diselenide. *Journal of Solid State Chemistry*, 70(2):207–209, 1987.

[7] Kin Fai Mak, Changgu Lee, James Hone, Jie Shan, and Tony F. Heinz. Atomically Thin MoS_2: A New Direct-Gap Semiconductor. *Physical Review Letters*, 105(13):136805, 2010.

[8] Andrea Splendiani, Liang Sun, Yuanbo Zhang, Tianshu Li, Jonghwan Kim, Chi Yung Chim, Giulia Galli, and Feng Wang. Emerging photoluminescence in monolayer MoS_2. *Nano Letters*, 10(4):1271–1275, 2010.

[9] You Zhou, Giovanni Scuri, Dominik S. Wild, Alexander A. High, Alan Dibos, Luis A. Jauregui, Chi Shu, Kristiaan de Greve, Kateryna Pistunova, Andrew Y. Joe, Takashi Taniguchi, Kenji Watanabe, Philip Kim, Mikhail D. Lukin, and Hongkun Park. Probing dark excitons in atomically thin semiconductors via near-field coupling to surface plasmon polaritons. *Nature Nanotechnology*, 12(9):856–860, 2017.

[10] Xiao-Xiao Zhang, Yumeng You, Shu Yang Frank Zhao, and Tony F. Heinz. Experimental Evidence for Dark Excitons in Monolayer WSe_2. *Physical Review Letters*, 115(25):257403, 2015.

[11] Y J Zhang, T Oka, R Suzuki, J T Ye, and Y Iwasa. Electrically switchable chiral light-emitting transistor. *Science*, 344(6185):725–728, 2014.

[12] Chul Ho Lee, Gwan Hyoung Lee, Arend M. Van Der Zande, Wenchao Chen, Yilei Li, Minyong Han, Xu Cui, Ghidewon Arefe, Colin Nuckolls, Tony F. Heinz, Jing Guo, James Hone, and Philip Kim. Atomically thin p-n junctions with van der Waals heterointerfaces. *Nature Nanotechnology*, 9(9):676–681, 2014.

[13] Pasqual Rivera, John R. Schaibley, Aaron M. Jones, Jason S. Ross, Sanfeng Wu, Grant Aivazian, Philip Klement, Kyle Seyler, Genevieve Clark, Nirmal J. Ghimire, Jiaqiang Yan, D. G. Mandrus, Wang Yao, and Xiaodong Xu. Observation of long-lived interlayer excitons in monolayer $MoSe_2$–WSe_2 heterostructures. *Nature Communications*, 6(1):6242, 2015.

[14] Luis A. Jauregui, Andrew Y. Joe, Kateryna Pistunova, Dominik S. Wild, Alexander A. High, You Zhou, Giovanni Scuri, Kristiaan De Greve, Andrey Sushko, Che-Hang Yu, Takashi Taniguchi, Kenji Watanabe, Daniel J. Needleman, Mikhail D. Lukin, Hongkun Park, and Philip Kim. Electrical control of interlayer exciton dynamics in atomically thin heterostructures. *Science*, 366(6467):870–875, 2019.

[15] Andor Kormányos, Guido Burkard, Martin Gmitra, Jaroslav Fabian, Viktor Zólyomi, Neil D. Drummond, and Vladimir Fal'ko. K.P Theory for Two-Dimensional Transition Metal Dichalcogenide Semiconductors. *2D Materials*, 2(2):022001, 2015.

[16] K. Kosmider, J W González, and J Fernández-Rossier. Large spin splitting in the conduction band of transition metal dichalcogenide monolayers. *Physical Review B - Condensed Matter and Materials Physics*, 88(24):245436, 2013.

[17] Xiaobo Lu, Xiaoqin Li, and Li Yang. Modulated interlayer exciton properties in a two-dimensional moiré crystal. *Physical Review B*, 100(15):155416, 2019.

[18] Masaru Onga, Yijin Zhang, Toshiya Ideue, and Yoshihiro Iwasa. Exciton Hall effect in monolayer MoS_2. *Nature Materials*, 16(12):1193–1197, 2017.

[19] G. Aivazian, Zhirui Gong, Aaron M. Jones, Rui-Lin Chu, J. Yan, D. G. Mandrus, Chuanwei Zhang, David Cobden, Wang Yao, and X. Xu. Magnetic control of valley pseudospin in monolayer WSe_2. *Nature Physics*, 11(2):148–152, 2015.

[20] Stefano Larentis, Hema C.P. Movva, Babak Fallahazad, Kyounghwan Kim, Armand Behroozi, Takashi Taniguchi, Kenji Watanabe, Sanjay K Banerjee, and Emanuel Tutuc. Large effective mass and interaction-enhanced Zeeman splitting of K-valley electrons in $MoSe_2$. *Physical Review B*, 97(20):201407(R), 2018.

[21] Babak Fallahazad, Hema C.P. Movva, Kyounghwan Kim, Stefano Larentis, Takashi Taniguchi, Kenji Watanabe, Sanjay K. Banerjee, and Emanuel Tutuc. Shubnikov-de Haas Oscillations of High-Mobility Holes in Monolayer and Bilayer WSe_2: Landau Level Degeneracy, Effective Mass, and Negative Compressibility. *Physical Review Letters*, 116(8):1–5, 2016.

[22] Martin V. Gustafsson, Matthew Yankowitz, Carlos Forsythe, Daniel Rhodes, Kenji Watanabe, Takashi Taniguchi, James Hone, Xiaoyang Zhu, and Cory R. Dean. Ambipolar Landau levels and strong band-selective carrier interactions in monolayer WSe_2. *Nature Materials*, 17(5):411–415, 2018.

[23] Akash Laturia, Maarten L. Van de Put, and William G Vandenberghe. Dielectric properties of hexagonal boron nitride and transition metal dichalcogenides: from monolayer to bulk. *npj 2D Materials and Applications*, 2(1):6, 2018.

[24] Charles. Kittel. *Introduction to Solid State Physics*. Wiley, 2005.

[25] Gang Wang, Alexey Chernikov, Mikhail M. Glazov, Tony F. Heinz, Xavier Marie, Thierry Amand, and Bernhard Urbaszek. Colloquium: Excitons in atomically thin transition metal dichalcogenides. *Reviews of Modern Physics*, 90(2):21001, 2018.

[26] Nevill F. Mott. Metal-Insulator Transition. *Reviews of Modern Physics*, 40(4):677–683, 1968.

[27] Yiling Yu, Guoqing Li, and Linyou Cao. Exciton Mott transition in two-dimensional semiconductors. *arXiv*, 2007.11509, 2020.

[28] L. V. Keldysh. Coulomb interaction in thin semiconductor and semimetal films. *JETPL*, 29:658, 1979.

[29] Timothy C. Berkelbach, Mark S. Hybertsen, and David R. Reichman. Theory of neutral and charged excitons in monolayer transition metal dichalcogenides. *Physical Review B*, 88(4):045318, 2013.

[30] Alexey Chernikov, Timothy C. Berkelbach, Heather M. Hill, Albert Rigosi, Yilei Li, Ozgur Burak Aslan, David R. Reichman, Mark S. Hybertsen, and Tony F. Heinz. Exciton binding energy and nonhydrogenic Rydberg series in monolayer WS_2. *Physical Review Letters*, 113(7):076802, 2014.

[31] M. M. Glazov, E. L. Ivchenko, G. Wang, T. Amand, X. Marie, B. Urbaszek, and B. L. Liu. Spin and valley dynamics of excitons in transition metal dichalcogenide monolayers. *Physica Status Solidi (B) Basic Research*, 252(11):2349–2362, 2015.

[32] C. Robert, D. Lagarde, F. Cadiz, G. Wang, B. Lassagne, T. Amand, A. Balocchi, P. Renucci, S. Tongay, B. Urbaszek, and X. Marie. Exciton radiative lifetime in transition metal dichalcogenide monolayers. *Physical Review B*, 93(20):205423, 2016.

[33] Maurizia Palummo, Marco Bernardi, and Jeffrey C. Grossman. Exciton radiative lifetimes in two-dimensional transition metal dichalcogenides. *Nano Letters*, 15(5):2794–2800, 2015.

[34] Haining Wang, Changjian Zhang, Weimin Chan, Christina Manolatou, Sandip Tiwari, and Farhan Rana. Radiative lifetimes of excitons and trions in monolayers of the metal dichalcogenide MoS_2. *Physical Review B*, 93(4):045407, 2016.

[35] Giovanni Scuri, You Zhou, Alexander A. High, Dominik S. Wild, Chi Shu, Kristiaan De Greve, Luis A. Jauregui, Takashi Taniguchi, Kenji Watanabe, Philip Kim, Mikhail D. Lukin, and Hongkun Park. Large Excitonic Reflectivity of Monolayer $MoSe_2$ Encapsulated in Hexagonal Boron Nitride. *Physical Review Letters*, 120(3):037402, 2018.

[36] Anshul Kogar, Melinda S Rak, Sean Vig, Ali A Husain, Felix Flicker, Young Il Joe, Luc Venema, Greg J. MacDougall, Tai C Chiang, Eduardo Fradkin, Jasper van Wezel, and Peter Abbamonte. Signatures of exciton condensation in a transition metal dichalcogenide. *Science*, 358(6368):1314–1317, 2017.

[37] Xiaomeng Liu, Kenji Watanabe, Takashi Taniguchi, Bertrand I. Halperin, and Philip Kim. Quantum Hall drag of exciton condensate in graphene. *Nature Physics*, 13(8):746–750, 2017.

[38] J. I.A. Li, T. Taniguchi, K. Watanabe, J. Hone, and C. R. Dean. Excitonic superfluid phase in double bilayer graphene. *Nature Physics*, 13(8):751–755, 2017.

[39] J. P. Eisenstein and A. H. MacDonald. Bose–Einstein condensation of excitons in bilayer electron systems. *Nature*, 432(7018):691–694, 2004.

[40] Hongyi Yu, Gui Bin Liu, and Wang Yao. Brightened spin-triplet interlayer excitons and optical selection rules in van der Waals heterobilayers. *2D Materials*, 5(3):035021, 2018.

[41] C. Robert, B. Han, P. Kapuscinski, A. Delhomme, C. Faugeras, T. Amand, M. R. Molas, M. Bartos, K. Watanabe, T. Taniguchi, B. Urbaszek, M. Potemski, and X. Marie. Measurement of the spin-forbidden dark excitons in MoS_2 and $MoSe_2$ monolayers. *Nature Communications*, 11(1):4037, 2020.

[42] Kin Fai Mak, Keliang He, Changgu Lee, Gwan Hyoung Lee, James Hone, Tony F. Heinz, and Jie Shan. Tightly bound trions in monolayer MoS_2. *Nature Materials*, 12(3):207–211, 2012.

[43] Jason S. Ross, Sanfeng Wu, Hongyi Yu, Nirmal J. Ghimire, Aaron M. Jones, Grant Aivazian, Jiaqiang Yan, David G. Mandrus, Di Xiao, Wang Yao, and Xiaodong Xu. Electrical control of neutral and charged excitons in a monolayer semiconductor. *Nature Communications*, 4(1):1474, 2013.

[44] Zefang Wang, Kin Fai Mak, and Jie Shan. Strongly Interaction-Enhanced Valley Magnetic Response in Monolayer WSe_2. *Physical Review Letters*, 120(6):66402, 2018.

[45] Patrick Back, Meinrad Sidler, Ovidiu Cotlet, Ajit Srivastava, Naotomo Takemura, Martin Kroner, and Atac Imamoğlu. Giant Paramagnetism-Induced Valley Polarization of Electrons in Charge-Tunable Monolayer $MoSe_2$. *Physical Review Letters*, 118(23):237404, 2017.

[46] D. Sanvitto, F. Pulizzi, A. J. Shields, P. C.M. Christianen, S. N. Holmes, M. Y. Simmons, D. A. Ritchie, J. C. Maan, and M. Pepper. Observation of charge transport by negatively charged excitons. *Science*, 294(5543):837–839, 2001.

[47] Richard Schmidt, Tilman Enss, Ville Pietilä, and Eugene Demler. Fermi polarons in two dimensions. *Physical Review A - Atomic, Molecular, and Optical Physics*, 85(2):105301, 2012.

[48] Meinrad Sidler, Patrick Back, Ovidiu Cotlet, Ajit Srivastava, Thomas Fink, Martin Kroner, Eugene Demler, and Atac Imamoglu. Fermi polaron-polaritons in charge-tunable atomically thin semiconductors. *Nature Physics*, 13(3):255–261, 2017.

[49] Yuanyue Liu, Paul Stradins, and Su-Huai Wei. Van der Waals metal-semiconductor junction: Weak Fermi level pinning enables effective tuning of Schottky barrier. *Science Advances*, 2(4):e1600069, 2016.

[50] Hailong Chen, Xiewen Wen, Jing Zhang, Tianmin Wu, Yongji Gong, Xiang Zhang, Jiangtan Yuan, Chongyue Yi, Jun Lou, Pulickel M. Ajayan, Wei Zhuang, Guangyu Zhang, and Junrong Zheng. Ultrafast formation of interlayer hot excitons in atomically thin MoS_2/WS_2 heterostructures. *Nature Communications*, 7(1):12512, 2016.

[51] Jens Kunstmann, Fabian Mooshammer, Philipp Nagler, Andrey Chaves, Frederick Stein, Nicola Paradiso, Gerd Plechinger, Christoph Strunk, Christian Schüller, Gotthard Seifert, David R. Reichman, and Tobias Korn. Momentum-space indirect interlayer excitons in transition-metal dichalcogenide van der Waals heterostructures. *Nature Physics*, 14(8):801–805, 2018.

[52] Mitsuhiro Okada, Alex Kutana, Yusuke Kureishi, Yu Kobayashi, Yuika Saito, Tetsuki Saito, Kenji Watanabe, Takashi Taniguchi, Sunny Gupta, Yasumitsu Miyata, Boris I. Yakobson, Hisanori Shinohara, and Ryo Kitaura. Direct and Indirect Interlayer Excitons in a van der Waals Heterostructure of $hBN/WS_2/MoS_2/hBN$. *ACS Nano*, 12(3):2498–2505, 2018.

[53] Chenhao Jin, Emma C. Regan, Aiming Yan, M. Iqbal Bakti Utama, Danqing Wang, Sihan Zhao, Ying Qin, Sijie Yang, Zhiren Zheng, Shenyang Shi, Kenji Watanabe, Takashi Taniguchi, Sefaattin Tongay, Alex Zettl, and Feng Wang. Observation of moiré excitons in WSe_2/WS_2 heterostructure superlattices. *Nature*, 567(7746):76–80, 2019.

[54] Ouri Karni, Elyse Barré, Sze Cheung Lau, Roland Gillen, Eric Yue Ma, Bumho Kim, Kenji Watanabe, Takashi Taniguchi, Janina Maultzsch, Katayun Barmak, Ralph H Page, and Tony F Heinz. Infrared Interlayer Exciton Emission in MoS_2/WSe_2 Heterostructures. *Physical Review Letters*, 123(24), 2019.

[55] Zumeng Huang, Yuanda Liu, Kévin Dini, Qinghai Tan, Zhuojun Liu, Hanlin Fang, Jin Liu, Timothy Liew, and Weibo Gao. Robust Room Temperature Valley Hall Effect of Interlayer Excitons. *Nano Letters*, 20(2):1345–1351, 2020.

[56] Pasqual Rivera, Kyle L. Seyler, Hongyi Yu, John R. Schaibley, Jiaqiang Yan, David G. Mandrus, Wang Yao, and Xiaodong Xu. Valley-polarized exciton dynamics in a 2D semiconductor heterostructure. *Science*, 351(6274):688–691, 2016.

[57] Philipp Nagler, Mariana V. Ballottin, Anatolie A. Mitioglu, Fabian Mooshammer, Nicola Paradiso, Christoph Strunk, Rupert Huber, Alexey Chernikov, Peter C.M. Christianen, Christian Schüller, and Tobias Korn. Giant magnetic splitting inducing near-unity valley polarization in van der Waals heterostructures. *Nature Communications*, 8(1):1551, 2017.

[58] Alberto Ciarrocchi, Dmitrii Unuchek, Ahmet Avsar, Kenji Watanabe, Takashi Taniguchi, and Andras Kis. Polarization switching and electrical control of interlayer excitons in two-dimensional van der Waals heterostructures. *Nature Photonics*, 13(2):131–136, 2019.

[59] Wei Ting Hsu, Li Syuan Lu, Po Hsun Wu, Ming Hao Lee, Peng Jen Chen, Pei Ying Wu, Yi Chia Chou, Horng Tay Jeng, Lain Jong Li, Ming Wen Chu, and Wen Hao Chang. Negative circular polarization emissions from $WSe_2/MoSe_2$ commensurate heterobilayers. *Nature Communications*, 9(1):1356, 2018.

[60] Bastian Miller, Alexander Steinhoff, Borja Pano, Julian Klein, Frank Jahnke, Alexander Holleitner, and Ursula Wurstbauer. Long-Lived Direct and Indirect Interlayer Excitons in van der Waals Heterostructures. *Nano Letters*, 17(9):5229–5237, 2017.

[61] Aubrey T. Hanbicki, Hsun Jen Chuang, Matthew R. Rosenberger, C. Stephen Hellberg, Saujan V. Sivaram, Kathleen M. McCreary, Igor I. Mazin, and Berend T. Jonker. Double Indirect Interlayer Exciton in a $MoSe_2/WSe_2$ van der Waals Heterostructure. *ACS Nano*, 12(5):4719–4726, 2018.

[62] Kyle L. Seyler, Pasqual Rivera, Hongyi Yu, Nathan P. Wilson, Essance L. Ray, David G. Mandrus, Jiaqiang Yan, Wang Yao, and Xiaodong Xu. Signatures of moiré-trapped valley excitons in MoSe2/WSe2 heterobilayers. *Nature*, 567(7746):66–70, 2019.

[63] Jue Wang, Jenny Ardelean, Yusong Bai, Alexander Steinhoff, Matthias Florian, Frank Jahnke, Xiaodong Xu, Mackillo Kira, James Hone, and X.-Y. Zhu. Optical generation of high carrier densities in 2D semiconductor heterobilayers. *Science Advances*, 5(9):eaax0145, 2019.

[64] Long Zhang, Rahul Gogna, G. William Burg, Jason Horng, Eunice Paik, Yu-Hsun Chou, Kyounghwan Kim, Emanuel Tutuc, and Hui Deng. Highly valley-polarized singlet and triplet interlayer excitons in van der Waals heterostructure. *Physical Review B*, 100(4):041402(R), 2019.

[65] Tianmeng Wang, Shengnan Miao, Zhipeng Li, Yuze Meng, Zhengguang Lu, Zhen Lian, Mark Blei, Takashi Taniguchi, Kenji Watanabe, Sefaattin Tongay, Dmitry Smirnov, and Su-Fei Shi. Giant Valley-Zeeman Splitting from Spin-Singlet and Spin-Triplet Interlayer Excitons in $WSe_2/MoSe_2$ Heterostructure. *Nano Letters*, 20(1):694–700, 2020.

[66] Zefang Wang, Daniel A Rhodes, Kenji Watanabe, Takashi Taniguchi, James C Hone, Jie Shan, and Kin Fai Mak. Evidence of high-temperature exciton condensation in two-dimensional atomic double layers. *Nature*, 574(7776):76–80, 2019.

[67] Lukas Sigl, Florian Sigger, Fabian Kronowetter, Jonas Kiemle, Julian Klein, Kenji Watanabe, Takashi Taniguchi, Jonathan J. Finley, Ursula Wurstbauer, and Alexander W. Holleitner. Signatures of a degenerate many-body state of interlayer excitons in a van der Waals heterostack. *Physical Review Research*, 2(4):042044, 2020.

[68] Xiaoping Hong, Jonghwan Kim, Su-Fei Shi, Yu Zhang, Chenhao Jin, Yinghui Sun, Sefaattin Tongay, Junqiao Wu, Yanfeng Zhang, and Feng Wang. Ultrafast charge transfer in atomically thin MoS_2/WS_2 heterostructures. *Nature Nanotechnology*, 9(9):682–686, 2014.

[69] Frank Ceballos, Matthew Z. Bellus, Hsin Ying Chiu, and Hui Zhao. Ultrafast charge separation and indirect exciton formation in a MoS_2-$MoSe_2$ van der waals heterostructure. *ACS Nano*, 8(12):12717–12724, 2014.

[70] Zefang Wang, Yi-Hsin Chiu, Kevin Honz, Kin Fai Mak, and Jie Shan. Electrical Tuning of Interlayer Exciton Gases in WSe_2 Bilayers. *Nano Letters*, 18(1):137–143, 2018.

[71] Giovanni Scuri, Trond I. Andersen, You Zhou, Dominik S. Wild, Jiho Sung, Ryan J. Gelly, Damien Bérubé, Hoseok Heo, Linbo Shao, Andrew Y. Joe, Andrés M. Mier Valdivia, Takashi Taniguchi, Kenji Watanabe, Marko Lončar, Philip Kim, Mikhail D. Lukin, and Hongkun Park. Electrically Tunable Valley Dynamics in Twisted WSe_2/WSe_2 Bilayers. *Physical Review Letters*, 124(21):217403, 2020.

[72] Junho Choi, Matthias Florian, Alexander Steinhoff, Daniel Erben, Kha Tran, Dong Seob Kim, Liuyang Sun, Jiamin Quan, Robert Claassen, Somak Majumder, Jennifer A. Hollingsworth, Takashi Taniguchi, Kenji Watanabe, Keiji Ueno, Akshay Singh, Galan Moody, Frank Jahnke, and Xiaoqin Li. Twist Angle-Dependent Interlayer Exciton Lifetimes in van der Waals Heterostructures. *Physical Review Letters*, 126(4):47401, 2021.

[73] M. M. Fogler, L. V. Butov, and K. S. Novoselov. High-temperature superfluidity with indirect excitons in van der Waals heterostructures. *Nature Communications*, 5(1):4555, 2014.

[74] M. Van Der Donck and F M Peeters. Interlayer excitons in transition metal dichalcogenide heterostructures. *Physical Review B*, 98(11):115104, 2018.

[75] Yuanda Liu, Kévin Dini, Qinghai Tan, Timothy Liew, Kostya S. Novoselov, and Weibo Gao. Electrically controllable router of interlayer excitons. *Science Advances*, 6(41):eaba1830, 2020.

[76] Dmitrii Unuchek, Alberto Ciarrocchi, Ahmet Avsar, Kenji Watanabe, Takashi Taniguchi, and Andras Kis. Room-temperature electrical control of exciton flux in a van der Waals heterostructure. *Nature*, 560(7718):340–344, 2018.

[77] Andrew Y Joe, Luis A Jauregui, Kateryna Pistunova, Andrés M Mier Valdivia, Zhengguang Lu, Dominik S Wild, Giovanni Scuri, Kristiaan De Greve, Ryan J Gelly, You Zhou, Jiho Sung, Andrey Sushko, Takashi Taniguchi, Kenji Watanabe, Dmitry Smirnov, Mikhail D Lukin, Hongkun Park, and Philip Kim. Electrically controlled emission from singlet and triplet exciton species in atomically thin light-emitting diodes. *Physical Review B*, 103(16):L161411, 2021.

[78] Jason S. Ross, Pasqual Rivera, John Schaibley, Eric Lee-Wong, Hongyi Yu, Takashi Taniguchi, Kenji Watanabe, Jiaqiang Yan, David Mandrus, David Cobden, Wang Yao, and Xiaodong Xu. Interlayer Exciton Optoelectronics in a 2D Heterostructure p-n Junction. *Nano Letters*, 17(2):638–643, 2017.

[79] M. H. Anderson, J. R. Ensher, M. R. Matthews, C. E. Wieman, and E. A. Cornell. Observation of Bose-Einstein Condensation in a Dilute Atomic Vapor. *Science*, 269(5221):198–201, 1995.

[80] Wolfgang Ketterle and N. J. van Druten. Bose-Einstein condensation of a finite number of particles trapped in one or three dimensions. *Physical Review A - Atomic, Molecular, and Optical Physics*, 54(1):656–660, 1996.

[81] A. A. High, J. R. Leonard, A. T. Hammack, M. M. Fogler, L. V. Butov, A. V. Kavokin, K. L. Campman, and A. C. Gossard. Spontaneous coherence in a cold exciton gas. *Nature*, 483(7391):584–588, 2012.

[82] A. A. High, J. R. Leonard, M. Remeika, L. V. Butov, M. Hanson, and A. C. Gossard. Condensation of excitons in a trap. *Nano Letters*, 12(5):2605–2609, 2012.

[83] Bishwajit Debnath, Yafis Barlas, Darshana Wickramaratne, Mahesh R. Neupane, and Roger K. Lake. Exciton condensate in bilayer transition metal dichalcogenides: Strong coupling regime. *Physical Review B*, 96(17):174504, 2017.

[84] Avinash Rustagi and Alexander F. Kemper. Theoretical Phase Diagram for the Room-Temperature Electron-Hole Liquid in Photoexcited Quasi-Two-Dimensional Monolayer MoS_2. *Nano Letters*, 18(1):455–459, 2018.

[85] Yiling Yu, Alexander W. Bataller, Robert Younts, Yifei Yu, Guoqing Li, Alexander A. Puretzky, David B. Geohegan, Kenan Gundogdu, and Linyou Cao. Room-Temperature Electron–Hole Liquid in Monolayer MoS_2. *ACS Nano*, 13(9):10351–10358, 2019.

[86] Trevor B. Arp, Dennis Pleskot, Vivek Aji, and Nathaniel M. Gabor. Electron–hole liquid in a van der Waals heterostructure photocell at room temperature. *Nature Photonics*, 13(4):245–250, 2019.

[87] Tomasz Woźniak, Paulo E. Faria Junior, Gotthard Seifert, Andrey Chaves, and Jens Kunstmann. Exciton g factors of van der Waals heterostructures from first-principles calculations. *Physical Review B*, 101(23):235408, 2020.

[88] C. R. Dean, A. F. Young, I. Meric, C. Lee, L. Wang, S. Sorgenfrei, K. Watanabe, T. Taniguchi, P. Kim, K. L. Shepard, and J. Hone. Boron nitride substrates for high-quality graphene electronics. *Nature Nanotechnology*, 5(10):722–726, 2010.

[89] Yilei Li, Yi Rao, Kin Fai Mak, Yumeng You, Shuyuan Wang, Cory R. Dean, and Tony F. Heinz. Probing symmetry properties of few-layer MoS_2 and h-BN by optical second-harmonic generation. *Nano Letters*, 13(7):3329–3333, 2013.

[90] Wei Ting Hsu, Zi Ang Zhao, Lain Jong Li, Chang Hsiao Chen, Ming Hui Chiu, Pi Shan Chang, Yi Chia Chou, and Wen Hao Chang. Second harmonic generation from artificially stacked transition metal dichalcogenide twisted bilayers. *ACS Nano*, 8(3):2951–2958, 2014.

[91] Xuan Hu, Poya Yasaei, Jacob Jokisaari, Serdar Öğüt, Amin Salehi-Khojin, and Robert F. Klie. Mapping Thermal Expansion Coefficients in Freestanding 2D Materials at the Nanometer Scale. *Physical review letters*, 120(5):055902, 2018.

[92] Sandeep Kumar Singh, M. Neek-Amal, S. Costamagna, and F. M. Peeters. Thermomechanical properties of a single hexagonal boron nitride sheet. *Physical Review B*, 87(18):184106, 2013.

[93] Qiran Cai, Declan Scullion, Wei Gan, Alexey Falin, Shunying Zhang, Kenji Watanabe, Takashi Taniguchi, Ying Chen, Elton J. G. Santos, and Lu Hua Li. High thermal conductivity of high-quality monolayer boron nitride and its thermal expansion. *Science Advances*, 5(6):eaav0129, 2019.

[94] Duhee Yoon, Young Woo Son, and Hyeonsik Cheong. Negative thermal expansion coefficient of graphene measured by raman spectroscopy. *Nano Letters*, 11(8):3227–3231, 2011.

[95] Yuval Ronen, Thomas Werkmeister, Danial Haie Najafabadi, Andrew T. Pierce, Laurel E. Anderson, Young Jae Shin, Si Young Lee, Young Hee Lee, Bobae Johnson, Kenji Watanabe, Takashi Taniguchi, Amir Yacoby, and Philip Kim. Aharonov–Bohm effect in graphene-based Fabry–Pérot quantum Hall interferometers. *Nature Nanotechnology*, 2021.

[96] L. V. Butov, A. L. Ivanov, A. Imamoglu, P. B. Littlewood, A. A. Shashkin, V. T. Dolgopolov, K. L. Campman, and A. C. Gossard. Stimulated scattering of indirect excitons in coupled quantum wells: Signature of a degenerate Bose-gas of excitons. *Physical Review Letters*, 86(24):5608–5611, 2001.

[97] Monique Combescot, Roland Combescot, and François Dubin. Bose-Einstein condensation and indirect excitons: A review. *Reports on Progress in Physics*, 80(6):66501, 2017.

[98] I Schwartz, D Cogan, E R Schmidgall, Y Don, L Gantz, O Kenneth, N H Lindner, and D Gershoni. Deterministic generation of a cluster state of entangled photons. *Science*, 354(6311):434–437, 2016.

[99] E Poem, Y Kodriano, C Tradonsky, N H Lindner, B D Gerardot, P M Petroff, and D. Gershoni. Accessing the dark exciton with light. *Nature Physics*, 6(12):993–997, 2010.

[100] A. A. High, A. K. Thomas, G. Grosso, M. Remeika, A. T. Hammack, A. D. Meyertholen, M. M. Fogler, L. V. Butov, M. Hanson, and A. C. Gossard. Trapping Indirect Excitons in a GaAs Quantum-Well Structure with a Diamond-Shaped Electrostatic Trap. *Physical Review Letters*, 103(8):087403, 2009.

[101] A. A. High, A. T. Hammack, L. V. Butov, L. Mouchliadis, A. L. Ivanov, M. Hanson, and A. C. Gossard. Indirect excitons in elevated traps. *Nano Letters*, 9(5):2094–2098, 2009.

[102] A. T. Hammack, M. Griswold, L. V. Butov, L. E. Smallwood, A. L. Ivanov, and A. C. Gossard. Trapping of Cold Excitons in Quantum Well Structures with Laser Light. *Physical Review Letters*, 96(22):227402, 2006.

[103] L. V. Butov, C. W. Lai, A. L. Ivanov, A. C. Gossard, and D. S. Chemla. Towards Bose–Einstein condensation of excitons in potential traps. *Nature*, 417(6884):47–52, 2002.

[104] R Rapaport, Gang Chen, D Snoke, Steven H Simon, Loren Pfeiffer, Ken West, Y Liu, and S Denev. Charge Separation of Dense Two-Dimensional Electron-Hole Gases: Mechanism for Exciton Ring Pattern Formation. *Physical Review Letters*, 92(11):117405, 2004.

[105] L Wang, I Meric, P Y Huang, Q. Gao, Y Gao, H Tran, T Taniguchi, K Watanabe, L M Campos, D A Muller, J Guo, P Kim, J Hone, K L Shepard, and C. R. Dean. One-Dimensional Electrical Contact to a Two-Dimensional Material. *Science*, 342(6158):614–617, 2013.

[106] Ki Kang Kim, Allen Hsu, Xiaoting Jia, Soo Min Kim, Yumeng Shi, Mildred Dresselhaus, Tomas Palacios, and Jing Kong. Synthesis and Characterization of Hexagonal Boron Nitride Film as a Dielectric Layer for Graphene Devices. *ACS Nano*, 6(10):8583–8590, 2012.

[107] Zefang Wang, Liang Zhao, Kin Fai Mak, and Jie Shan. Probing the Spin-Polarized Electronic Band Structure in Monolayer Transition Metal Dichalcogenides by Optical Spectroscopy. *Nano Letters*, 17(2):740–746, 2017.

[108] Igor V Bondarev and Maria R Vladimirova. Complexes of dipolar excitons in layered quasi-two-dimensional nanostructures. *Physical Review B*, 97(16):165419, 2018.

[109] Aaron M. Jones, Hongyi Yu, John R. Schaibley, Jiaqiang Yan, David G. Mandrus, Takashi Taniguchi, Kenji Watanabe, Hanan Dery, Wang Yao, and Xiaodong Xu. Excitonic luminescence upconversion in a two-dimensional semiconductor. *Nature Physics*, 12(4):323–327, 2016.

[110] Gleb Finkelstein, Hadas Shtrikman, and Israel Bar-Joseph. Negatively and positively charged excitons in quantum wells. *Physical Review B - Condensed Matter and Materials Physics*, 53(4):R1709–R1712, 1996.

[111] K Kheng, R. T. Cox, Merle Y. d' Aubigné, Franck Bassani, K Saminadayar, and S Tatarenko. Observation of negatively charged excitons *X* in semiconductor quantum wells. *Physical Review Letters*, 71(11):1752–1755, 1993.

[112] Murray A. Lampert. Mobile and Immobile Effective-Mass-Particle Complexes in Nonmetallic Solids. *Physical Review Letters*, 1(12):450–453, 1958.

[113] B. Laikhtman and R. Rapaport. Exciton correlations in coupled quantum wells and their luminescence blue shift. *Physical Review B - Condensed Matter and Materials Physics*, 80(19), 2009.

[114] A L Ivanov. Quantum diffusion of dipole-oriented indirect excitons in coupled quantum wells. *Europhysics Letters (EPL)*, 59(4):586–591, 2002.

[115] S. V. Lobanov, N. A. Gippius, and L. V. Butov. Theory of condensation of indirect excitons in a trap. *Physical Review B*, 94(24):245401, 2016.

[116] Philipp Nagler, Gerd Plechinger, Mariana V Ballottin, Anatolie Mitioglu, Sebastian Meier, Nicola Paradiso, Christoph Strunk, Alexey Chernikov, Peter C M Christianen, Christian Schüller, and Tobias Korn. Interlayer exciton dynamics in a dichalcogenide monolayer heterostructure. *2D Materials*, 4(2):25112, 2017.

[117] L. V. Butov, L. S. Levitov, A. V. Mintsev, B. D. Simons, A. C. Gossard, and D. S. Chemla. Formation Mechanism and Low-Temperature Instability of Exciton Rings. *Physical Review Letters*, 92(11):117404, 2004.

[118] Xiaodong Xu, Wang Yao, Di Xiao, and Tony F. Heinz. Spin and pseudospins in layered transition metal dichalcogenides. *Nature Physics*, 10(5):343–350, 2014.

[119] Kin Fai Mak, Keliang He, Jie Shan, and Tony F. Heinz. Control of valley polarization in monolayer MoS_2 by optical helicity. *Nature Nanotechnology*, 7(8):494–498, 2012.

[120] Dmitrii Unuchek, Alberto Ciarrocchi, Ahmet Avsar, Zhe Sun, Kenji Watanabe, Takashi Taniguchi, and Andras Kis. Valley-polarized exciton currents in a van der Waals heterostructure. *Nature Nanotechnology*, 14(12):1104–1109, 2019.

[121] Roland Gillen and Janina Maultzsch. Interlayer excitons in $MoSe_2/WSe_2$ heterostructures from first principles. *Physical Review B*, 97:165306, 2018.

[122] Mathieu Alloing, Mussie Beian, Maciej Lewenstein, David Fuster, Yolanda González, Luisa González, Roland Combescot, Monique Combescot, and François Dubin. Evidence for a Bose-Einstein condensate of excitons. *EPL (Europhysics Letters)*, 107(1):10012, 2014.

[123] G. Rossbach, J. Levrat, G. Jacopin, M. Shahmohammadi, J.-F. Carlin, J.-D. Ganière, R. Butté, B. Deveaud, and N. Grandjean. High-temperature Mott transition in wide-band-gap semiconductor quantum wells. *Physical Review B*, 90(20):201308, 2014.

[124] M Stern, V Garmider, V Umansky, and I. Bar-Joseph. Mott Transition of Excitons in Coupled Quantum Wells. *Physical Review Letters*, 100(25):256402, 2008.

[125] Gabija Kiršanskė, Petru Tighineanu, Raphaël S. Daveau, Javier Miguel-Sánchez, Peter Lodahl, and Søren Stobbe. Observation of the exciton Mott transition in the photoluminescence of coupled quantum wells. *Physical Review B*, 94(15):155438, 2016.

[126] Jue Wang, Qianhui Shi, En-Min Shih, Lin Zhou, Wenjing Wu, Yusong Bai, Daniel Rhodes, Katayun Barmak, James Hone, Cory R. Dean, and X.-Y Zhu. Diffusivity Reveals Three Distinct Phases of Interlayer Excitons in $MoSe_2/WSe_2$ Heterobilayers. *Physical Review Letters*, 126(10):106804, 2021.

[127] Andrey Sushko, Kristiaan De Greve, Madeleine Phillips, Bernhard Urbaszek, Andrew Y. Joe, Kenji Watanabe, Takashi Taniguchi, Alexander L. Efros, C. Stephen Hellberg, Hongkun Park, Philip Kim, and Mikhail D. Lukin. Asymmetric photoelectric effect: Auger-assisted hot hole photocurrents in transition metal dichalcogenides. *Nanophotonics*, 10(1):105–113, 2020.

[128] J. Binder, J. Howarth, F. Withers, M. R. Molas, T. Taniguchi, K. Watanabe, C. Faugeras, A. Wysmolek, M. Danovich, V. I. Fal'ko, A. K. Geim, K. S. Novoselov, M. Potemski, and A. Kozikov. Upconverted electroluminescence via Auger scattering of interlayer excitons in van der Waals heterostructures. *Nature Communications*, 10(1):2335, 2019.

[129] Weijie Li, Xin Lu, Sudipta Dubey, Luka Devenica, and Ajit Srivastava. Dipolar interactions between localized interlayer excitons in van der Waals heterostructures. *Nature Materials*, 19(6):624–629, 2020.

[130] Malte Kremser, Mauro Brotons-Gisbert, Johannes Knörzer, Janine Gückelhorn, Moritz Meyer, Matteo Barbone, Andreas V. Stier, Brian D. Gerardot, Kai Müller, and Jonathan J. Finley. Discrete interactions between a few interlayer excitons trapped at a $MoSe_2$–WSe_2 heterointerface. *npj 2D Materials and Applications*, 4(1):8, 2020.

[131] V. Negoita, D. Snoke, and K. Eberl. Huge density-dependent blueshift of indirect excitons in biased coupled quantum wells. *Physical Review B - Condensed Matter and Materials Physics*, 61(4):2779–2783, 2000.

[132] Feng-Cheng Wu, Fei Xue, and A. H. MacDonald. Theory of two-dimensional spatially indirect equilibrium exciton condensates. *Physical Review B*, 92(16):165121, 2015.

[133] G. Manzke, D. Semkat, and H. Stolz. Mott transition of excitons in gaas-gaalas quantum wells. *New Journal of Physics*, 14(9):095002, 2012.

[134] W. Liu, R. Butté, A. Dussaigne, N. Grandjean, B. Deveaud, and G. Jacopin. Carrier-density-dependent recombination dynamics of excitons and electron-hole plasma in *m*-plane InGaN/GaN quantum wells. *Physical Review B*, 94(19):195411, 2016.

[135] Kenichi Asano and Takuya Yoshioka. Exciton–Mott Physics in Two-Dimensional Electron–Hole Systems: Phase Diagram and Single-Particle Spectra. *Journal of the Physical Society of Japan*, 83(8):084702, 2014.

[136] A. A. High, E. E. Novitskaya, L. V. Butov, M. Hanson, and A. C. Gossard. Control of Exciton Fluxes in an Excitonic Integrated Circuit. *Science*, 321(5886):229–231, 2008.

[137] A. Delhomme, D. Vaclavkova, A. Slobodeniuk, M. Orlita, M. Potemski, D. M. Basko, K. Watanabe, T. Taniguchi, D. Mauro, C. Barreteau, E. Giannini, A. F. Morpurgo, N. Ubrig, and C. Faugeras. Flipping exciton angular momentum with chiral phonons in $MoSe_2/WSe_2$ heterobilayers. *2D Materials*, 7(4):041002, 2020.

[138] Fengcheng Wu, Timothy Lovorn, and A. H. MacDonald. Theory of optical absorption by interlayer excitons in transition metal dichalcogenide heterobilayers. *Physical Review B*, 97(3):035306, 2018.

[139] J. P. Echeverry, B. Urbaszek, T. Amand, X. Marie, and I. C. Gerber. Splitting between bright and dark excitons in transition metal dichalcogenide monolayers. *Physical Review B*, 93(12):121107(R), 2016.

[140] Hongyi Yu, Gui-Bin Liu, Jianju Tang, Xiaodong Xu, and Wang Yao. Moiré excitons: From programmable quantum emitter arrays to spin-orbit–coupled artificial lattices. *Science Advances*, 3(11):e1701696, 2017.

[141] G. Wang, L. Bouet, M. M. Glazov, T. Amand, E. L. Ivchenko, E. Palleau, X. Marie, and B. Urbaszek. Magneto-optics in transition metal diselenide monolayers. *2D Materials*, 2(3):034002, 2015.

[142] D. V. Rybkovskiy, I. C. Gerber, and M. V. Durnev. Atomically inspired k·p approach and valley Zeeman effect in transition metal dichalcogenide monolayers. *Physical Review B*, 95(15):155406, 2017.

[143] Ke Wang, Kristiaan De Greve, Luis A. Jauregui, Andrey Sushko, Alexander High, You Zhou, Giovanni Scuri, Takashi Taniguchi, Kenji Watanabe, Mikhail D. Lukin, Hongkun Park, and Philip Kim. Electrical control of charged carriers and excitons in atomically thin materials. *Nature Nanotechnology*, 13(2):128–132, 2018.

[144] Mauro Brotons-Gisbert, Hyeonjun Baek, Aidan Campbell, Kenji Watanabe, Takashi Taniguchi, and Brian D. Gerardot. Moiré-trapped interlayer trions in a charge-tunable $WSe_2/MoSe_2$ heterobilayer. *arXiv*, 2101.07747, 2021.

[145] Yilei Li, Jonathan Ludwig, Tony Low, Alexey Chernikov, Xu Cui, Ghidewon Arefe, Young Duck Kim, Arend M. van der Zande, Albert Rigosi, Heather M Hill, Suk Hyun Kim, James Hone, Zhiqiang Li, Dmitry Smirnov, and Tony F Heinz. Valley splitting and polarization by the zeeman effect in monolayer $MoSe_2$. *Physical Review Letters*, 113(26):266804, 2014.

[146] Qianhui Shi, En Min Shih, Martin V. Gustafsson, Daniel A. Rhodes, Bumho Kim, Kenji Watanabe, Takashi Taniguchi, Zlatko Papić, James Hone, and Cory R. Dean. Odd- and even-denominator fractional quantum Hall states in monolayer WSe_2. *Nature Nanotechnology*, 15(7):569–573, 2020.

[147] Hualing Zeng, Junfeng Dai, Wang Yao, Di Xiao, and Xiaodong Cui. Valley polarization in MoS2 monolayers by optical pumping. *Nature Nanotechnology*, 7(8):490–493, 2012.

[148] Kristen Kaasbjerg. Atomistic *T*-matrix theory of disordered two-dimensional materials: Bound states, spectral properties, quasiparticle scattering, and transport. *Physical Review B*, 101(4):045433, 2020.

[149] Gerd Plechinger, Philipp Nagler, Ashish Arora, Robert Schmidt, Alexey Chernikov, Andrés Granados del Águila, Peter C.M. Christianen, Rudolf Bratschitsch, Christian Schüller, and Tobias Korn. Trion fine structure and coupled spin–valley dynamics in monolayer tungsten disulfide. *Nature Communications*, 7(1):12715, 2016.

[150] You Zhou, Jiho Sung, Elise Brutschea, Ilya Esterlis, Yao Wang, Giovanni Scuri, Ryan J. Gelly, Hoseok Heo, Takashi Taniguchi, Kenji Watanabe, Gergely Zaránd, Mikhail D. Lukin, Philip Kim, Eugene Demler, and Hongkun Park. Signatures of bilayer Wigner crystals in a transition metal dichalcogenide heterostructure. *arXiv*, 2010.03037, 2020.

[151] Emma C. Regan, Danqing Wang, Chenhao Jin, M. Iqbal Bakti Utama, Beini Gao, Xin Wei, Sihan Zhao, Wenyu Zhao, Zuocheng Zhang, Kentaro Yumigeta, Mark Blei, Johan D. Carlström, Kenji Watanabe, Takashi Taniguchi, Sefaattin Tongay, Michael Crommie, Alex Zettl, and Feng Wang. Mott and generalized Wigner crystal states in WSe_2/WS_2 moiré superlattices. *Nature*, 579(7799):359–363, 2020.

[152] Yanhao Tang, Lizhong Li, Tingxin Li, Yang Xu, Song Liu, Katayun Barmak, Kenji Watanabe, Takashi Taniguchi, Allan H. MacDonald, Jie Shan, and Kin Fai Mak. Simulation of Hubbard model physics in WSe_2/WS_2 moiré superlattices. *Nature*, 579(7799):353–358, 2020.

[153] Yang Xu, Song Liu, Daniel A. Rhodes, Kenji Watanabe, Takashi Taniguchi, James Hone, Veit Elser, Kin Fai Mak, and Jie Shan. Correlated insulating states at fractional fillings of moiré superlattices. *Nature*, 587(7833):214–218, 2020.

[154] Bikash Padhi, R Chitra, and Philip W Phillips. Generalized Wigner crystallization in moiré materials. *Physical Review B*, 103(12):125146, 2021.

[155] Junho Choi, Wei-Ting Hsu, Li-Syuan Lu, Liuyang Sun, Hui-Yu Cheng, Ming-Hao Lee, Jiamin Quan, Kha Tran, Chun-Yuan Wang, Matthew Staab, Kayleigh Jones, Takashi Taniguchi, Kenji Watanabe, Ming-Wen Chu, Shangjr Gwo, Suenne Kim, Chih-Kang Shih, Xiaoqin Li, and Wen-Hao Chang. Moiré potential impedes interlayer exciton diffusion in van der Waals heterostructures. *Science Advances*, 6(39):eaba8866, 2020.

[156] Yongxin Zeng and A. H. MacDonald. Electrically controlled two-dimensional electron-hole fluids. *Physical Review B*, 102(8):085154, 2020.

[157] Liguo Ma, Phuong X. Nguyen, Zefang Wang, Yongxin Zeng, Kenji Watanabe, Takashi Taniguchi, Allan H. MacDonald, Kin Fai Mak, and Jie Shan. Strongly correlated excitonic insulator in atomic double layers. *arXiv*, 2104.05066, 2021.

[158] William E. Hayenga, Hipolito Garcia-Gracia, Hossein Hodaei, Christian Reimer, Roberto Morandotti, Patrick LiKamWa, and Mercedeh Khajavikhan. Second-order coherence properties of metallic nanolasers. *Optica*, 3(11):1187, 2016.

[159] V. Degiorgio and Marlan O. Scully. Analogy between the laser threshold region and a second-order phase transition. *Physical Review A*, 2(4):1170–1177, 1970.

[160] A. Lebreton, I. Abram, N. Takemura, M. Kuwata-Gonokami, I. Robert-Philip, and A. Beveratos. Stochastically sustained population oscillations in high-β nanolasers. *New Journal of Physics*, 15(3):033039, 2013.

[161] T Wang, G P Puccioni, and G L Lippi. Dynamical Buildup of Lasing in Mesoscale Devices. *Scientific Reports*, 5(1):15858, 2015.

[162] Hui Deng, Hartmut Haug, and Yoshihisa Yamamoto. Exciton-polariton Bose-Einstein condensation. *Reviews of Modern Physics*, 82(2):1489–1537, 2010.

[163] David Snoke and Peter Littlewood. Polariton condensates. *Physics Today*, 63(8):42–47, 2010.

[164] Tobias Damm, David Dung, Frank Vewinger, Martin Weitz, and Julian Schmitt. First-order spatial coherence measurements in a thermalized two-dimensional photonic quantum gas. *Nature Communications*, 8(1):158, 2017.

[165] L V Butov, A C Gossard, and D S Chemla. Macroscopically ordered state in an exciton system. *Nature*, 418(6899):751–754, 2002.

[166] Fengcheng Wu, Timothy Lovorn, and A H Macdonald. Topological Exciton Bands in Moiré Heterojunctions. *Physical Review Letters*, 118(14):147401, 2017.

[167] Chih-Kang Shih, Lain-Jong Li, Xibiao Ren, Chendong Zhang, Chuanhong Jin, Mei-Yin Chou, Chih-Piao Chuu, and Ming-Yang Li. Interlayer couplings, Moiré patterns, and 2D electronic superlattices in MoS_2/WSe_2 hetero-bilayers. *Science Advances*, 3(1):e1601459, 2017.

[168] Nan Zhang, Alessandro Surrente, Michał Baranowski, Duncan K. Maude, Patricia Gant, Andres Castellanos-Gomez, and Paulina Plochocka. Moiré Intralayer Excitons in a $MoSe_2/MoS_2$ Heterostructure. *Nano Letters*, 18(12):7651–7657, 2018.

[169] Trond I. Andersen, Giovanni Scuri, Andrey Sushko, Kristiaan De Greve, Jiho Sung, You Zhou, Dominik S. Wild, Ryan J. Gelly, Hoseok Heo, Damien Bérubé, Andrew Y. Joe, Luis A. Jauregui, Kenji Watanabe, Takashi Taniguchi, Philip Kim, Hongkun Park, and Mikhail D. Lukin. Excitons in a reconstructed moiré potential in twisted WSe_2/WSe_2 homobilayers. *Nature Materials*, 20:480–487, 2021.

[170] Kha Tran, Galan Moody, Fengcheng Wu, Xiaobo Lu, Junho Choi, Kyounghwan Kim, Amritesh Rai, Daniel A. Sanchez, Jiamin Quan, Akshay Singh, Jacob Embley, André Zepeda, Marshall Campbell, Travis Autry, Takashi Taniguchi, Kenji Watanabe, Nanshu Lu, Sanjay K. Banerjee, Kevin L. Silverman, Suenne Kim, Emanuel Tutuc, Li Yang, Allan H. MacDonald, and Xiaoqin Li. Evidence for moiré excitons in van der Waals heterostructures. *Nature*, 567(7746):71–75, 2019.

[171] H. Baek, M. Brotons-Gisbert, Z. X. Koong, A. Campbell, M. Rambach, K. Watanabe, T. Taniguchi, and B. D. Gerardot. Highly energy-tunable quantum light from moiré-trapped excitons. *Science Advances*, 6(37):eaba8526, 2020.

[172] Yusong Bai, Lin Zhou, Jue Wang, Wenjing Wu, Leo J. McGilly, Dorri Halbertal, Chiu Fan Bowen Lo, Fang Liu, Jenny Ardelean, Pasqual Rivera, Nathan R. Finney, Xu Chen Yang, D. N. Basov, Wang Yao, Xiaodong Xu, James Hone, Abhay N. Pasupathy, and X. Y. Zhu. Excitons in strain-induced one-dimensional moiré potentials at transition metal dichalcogenide heterojunctions. *Nature Materials*, 19(10):1068–1073, 2020.

[173] Sara Shabani, Dorri Halbertal, Wenjing Wu, Mingxing Chen, Song Liu, James Hone, Wang Yao, D N Basov, Xiaoyang Zhu, and Abhay N Pasupathy. Deep moiré potentials in twisted transition metal dichalcogenide bilayers. *Nature Physics*, 2021.

[174] Yuan Cao, Valla Fatemi, Ahmet Demir, Shiang Fang, Spencer L. Tomarken, Jason Y. Luo, Javier D. Sanchez-Yamagishi, Kenji Watanabe, Takashi Taniguchi, Efthimios Kaxiras, Ray C. Ashoori, and Pablo Jarillo-Herrero. Correlated insulator behaviour at half-filling in magic-angle graphene superlattices. *Nature*, 556(7699):80–84, 2018.

[175] Yuan Cao, Valla Fatemi, Shiang Fang, Kenji Watanabe, Takashi Taniguchi, Efthimios Kaxiras, and Pablo Jarillo-Herrero. Unconventional superconductivity in magic-angle graphene superlattices. *Nature*, 556(7699):43–50, 2018.

[176] Lei Wang, En Min Shih, Augusto Ghiotto, Lede Xian, Daniel A. Rhodes, Cheng Tan, Martin Claassen, Dante M. Kennes, Yusong Bai, Bumho Kim, Kenji Watanabe, Takashi Taniguchi,

Xiaoyang Zhu, James Hone, Angel Rubio, Abhay N. Pasupathy, and Cory R. Dean. Correlated electronic phases in twisted bilayer transition metal dichalcogenides. *Nature Materials*, 19(8):861–866, 2020.

[177] Zeyu Hao, A M Zimmerman, Patrick Ledwith, Eslam Khalaf, Danial Haie Najafabadi, Kenji Watanabe, Takashi Taniguchi, Ashvin Vishwanath, and Philip Kim. Electric field–tunable superconductivity in alternating-twist magic-angle trilayer graphene. *Science*, 371(6534):1133–1138, 2021.

[178] Kyounghwan Kim, Stefano Larentis, Babak Fallahazad, Kayoung Lee, Jiamin Xue, David C. Dillen, Chris M. Corbet, and Emanuel Tutuc. Band alignment in WSe_2-graphene heterostructures. *ACS Nano*, 9(4):4527–4532, 2015.

[179] Pierluigi Cudazzo, Ilya V. Tokatly, and Angel Rubio. Dielectric screening in two-dimensional insulators: Implications for excitonic and impurity states in graphane. *Physical Review B*, 84(8):085406, 2011.

Kim Lab photo taken on the Harvard Law quad behind the LISE building (2019).